Enhancing Microgrid Resilience Through Seamless Operation : From Design to P-HIL Demonstrator

Samuel Kamajaya

THÈSE

Pour obtenir le grade de

DOCTEUR DE L'UNIVERSITÉ GRENOBLE ALPES

École doctorale : EEATS - Electronique, Electrotechnique, Automatique, Traitement du Signal (EEATS)
Spécialité : Génie électrique
Unité de recherche : Laboratoire de Génie Electrique

Renforcer la Résilience des Micro-réseaux Grâce à une Transition *Seamless* — de la Conception au Démonstrateur P-HIL

Enhancing Microgrid Resilience Through Seamless Operation — from Design to P-HIL Demonstrator

Présentée par:

Samuel Kamajaya

Direction de thèse :

Raphael CAIRE ASSOCIATE PROFESSOR, Grenoble INP	Directeur de thèse
Sedik BACHA PROFESSOR, Université Grenoble Alpes	Co-directeur de thèse
Jerome BUIRE ASSOCIATE PROFESSOR, Grenoble INP	Co-encadrant de thèse

Rapporteurs :

Zhe CHEN
PROFESSOR, Aalborg Universitet
Andreas SUMPER
PROFESSOR, Universitat Politècnica de Catalunya

Thèse soutenue publiquement le **03 Mai 2024,** devant le jury composé de :

Zhe CHEN PROFESSOR, Aalborg Universitet	Rapporteur
Andreas SUMPER PROFESSOR, Universitat Politècnica de Catalunya	Rapporteur
Mohamed BENBOUZID PROFESSOR, Université de Brest	Président
Bertrand RAISON PROFESSOR, Grenoble INP	Examinateur
Adriana AGUILERA GONZALEZ ASSOCIATE PROFESSOR, Université de Bordeaux	Examinateur
Raphael CAIRE ASSOCIATE PROFESSOR, Grenoble INP	Directeur de thèse
Seddik BACHA PROFESSOR, Université Grenoble Alpes	Co-directeur de thèse
Jerome BUIRE ASSOCIATE PROFESSOR, Grenoble INP	Co-encadrant de thèse

Invités :

Jean WILD
Ingénieur Chercheur, Schneider Electric
Wedian YOUSSEF
Ingénieure Chercheuse, Schneider Electric

Abstract / Résumé

Abstract — As our world transitions to sustainable energy, microgrid integration, including decentralized PV and BESS, has seen substantial growth and widespread adoption, particularly in commercial and industrial buildings. This thesis focuses on enhancing BESS technology to ensure uninterrupted power supply to critical loads while maintaining regulatory compliance. In the event of grid loss, microgrids switch the supply to BESS. The research examines the requirement for a seamless transition that critical loads can tolerate during a grid loss, which results in a value of 10 ms. In order to meet this requirement, a fast and reliable method for detecting a loss of main is proposed. Additionally, various inverter control strategies have been developed to achieve seamless transitions from grid following to grid forming, ensuring disruption times due to grid loss in less than 10 ms while minimizing overvoltage. Moreover, an advance sequence of operation is proposed to ensure the grid code compliance and DERs operation during the transition. The research is validated by experimental prototypes and a small microgrid demonstrator using P-HIL, which increase technology readiness level.

Keywords: Microgrid, Resilience, Seamless Operation Control, Fast Detection, BESS

Résumé — À mesure que notre monde évolue vers une énergie durable, l'intégration des microgrids, comprenant le photovoltaïque décentralisé et les systèmes de BESS, a connu une croissance substantielle et une adoption généralisée, notamment dans les bâtiments tertiaires. Cette thèse se concentre sur l'amélioration de la technologie BESS afin de garantir une alimentation électrique ininterrompue aux charges critiques tout en respectant les règles de raccordement au réseau. En cas de perte de réseau, les microgrids basculent l'alimentation vers le BESS. La recherche examine l'exigence d'une transition que les charges critiques peuvent tolérer lors d'une perte de réseau, laquelle est définie par une durée maximale de 10 millisecondes. Pour répondre à cette exigence, une méthode rapide et fiable de détection d'une perte de réseau est proposée. De plus, diverses stratégies de contrôle d'onduleur ont été développées pour réaliser des transitions rapides du mode grid following a grid forming, garantissant des temps de perturbation dus à une perte de réseau de moins de 10 ms tout en minimisant les surtensions. De plus, une séquence d'opération avancée est proposée pour garantir la conformité au code réseau et le fonctionnement des DERs pendant la transition. La recherche est validée par des prototypes expérimentaux et démonstrateur petite échelle de microgrid utilisant P-HIL, ce qui augmente l'echelle de TRL.

Mots clés : Microréseau, Résilience, *Seamless* Contrôle, Détection Rapide,BESS.

Acknowledgements

First and foremost, I would like to express my sincere gratitude to my academic supervisior Raphael Caire, Seddik Bacha, and Jerome Buire, for the continuous support of my study and research, for their patience, motivation, and immense knowledge. Their guidance helped me in all the time of research and writing of this thesis.

I would also like to express my sincere appreciation to the esteemed members of the jury for their insightful comments and constructive feedbacks, but also for the hard questions which incented me to widen my research from various perspectives.

I am also deeply grateful to my industrial supervisor, Jean Wild, for providing me the opportunity to work on this project within Schneider Electric. His real-world insights have been instrumental in bridging the gap between academia and industry, enriching my thesis with practical relevance. I would also like to acknowledge Association Nationale Recherche Technologie (ANRT) for French CIFRE fellowship funding (n° 2020/1494) that made this industrial PhD possible.

I thank my fellow labmates in SYREL G2Elab for all the fun we have had in the last few years. Also, i extend this gratitude to my colleagues in Schneider Electric Micrgorid LoB, for enriching this thesis journey with practical knowledge. Additionally, I am grateful to my PPI Grenoble friends for their unwavering support and encouragement during my stay in France.

Last but not the least, I would like to thank my loving parents, the persistent support throughout this PhD journey has been my guiding light. My deepest thanks go to my dear wife Michelle for her love, ears, and patience during the long hours spent on research which kept me motivated and balanced.

This thesis would not have been possible without the support and understanding of my loved ones, to whom I owe my deepest gratitude.

Thank you all.

Contents

List of Acronyms

BESS	Battery Energy Storage System
CHP	Combine, Health, and Power
DDSRF	Decoupled Double Srf
DER	Distributed Energy Resource
DFT	Discrete Fourier Transform
DQ	Direct Quadrature
DSP	Digital Signal Processing
DVR	Dynamic Voltage Restorer
EKF	Extended Kalman Filter
EMC	Electro-Magnetic Compatibility
EU	European Union
EV	Electric Vehicle
FRT	Fault Ride Through
HVAC	Heating, Ventilation, and Air Conditioning
IT	Information Technology
LV	Low Voltage
PC	Personal Computer
PCC	Point of Common Coupling
PI	Proportional Integral
PLL	Phase Locked Loop
POC	Point of Connection
POW	Point of Wave
PR	Proportional Resonant
PV	Photovoltaic

RMS	Root Mean Squared
SoC	State of Charge
SoH	State of Health
SS	Static Switch
THD	Total Harmonic Distortion
UPS	Uninterrupted Power Supply
US	United States
VSC	Voltage Source Converter

Chapter 1

Microgrid for Small and Medium Buildings

Contents

1.1 Integration of Distributed Energy Resources

In response to the escalating climate crisis, the majority of nations worldwide have committed to achieving net zero emissions by the year 2050. This ambitious goal necessitates a transformation on our energy systems, shifting from fossil fuel reliance to sustainable and renewable

energy sources, such as wind, solar, and hydroelectric power. Moving towards the decarbonization, the clean energy technologies are projected to experience a significant surge by 2030. By the end of the next decade, the number of electric vehicles (EV) on the road worldwide is expected to increase nearly tenfold [1]. Concurrently, there is a growing trend towards utilizing electric heating systems, such as heat pumps, which are recognized for their efficiency and reduced environmental impact. From the generation side, Solar PV remains the main source of global renewable capacity expansion in 2023, ahead of wind power. In 2023, solar PV capacity experienced a 65% growth, with half of this expansion coming from distributed applications, including both residential and commercial systems [2]. Moreover, according to the International Energy Agency (IEA), the projected global expansion of solar photovoltaic (PV) capacity is estimated to reach 167.8 GW by 2024 in the accelerated scenario, accounting for almost half of global PV expansion as illustrated in Fig 1 [2].

The global electricity price increase in both wholesale and retail has made small solar PV systems appealing from an economic standpoint for both residential and commercial building. Geopolitical aspects also drive the policy environment for distributed solar PV systems to be installed rapidly [2]. Conversely, utility scaled systems require expensive and long process grid interconnection studies.

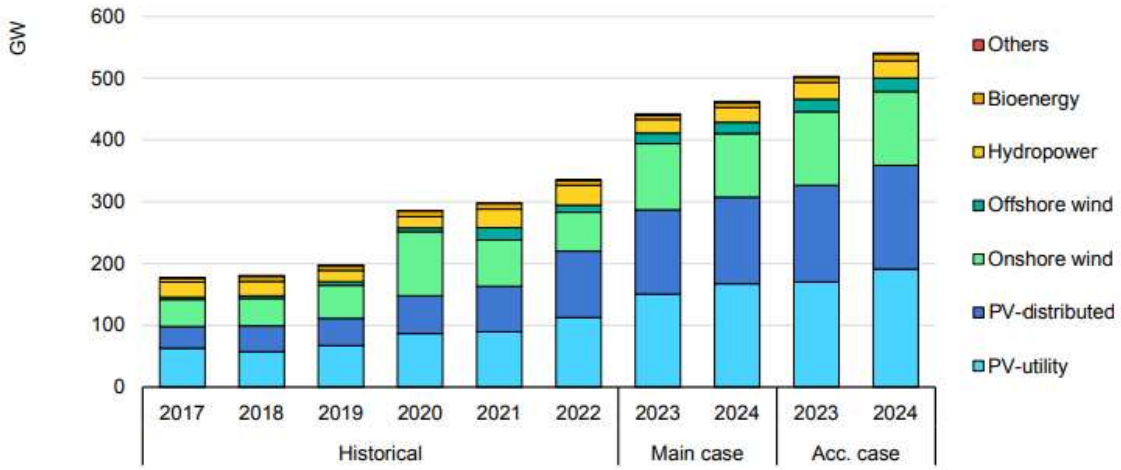

Figure 1.1: Net renewable electricity capacity additions [2].

The widespread installation of EV charging infrastructure and distributed solar PV will have a notable impact on grid infrastructure. In spite of this, the integration of EV charging and solar PV systems can be effectively achieved with the help of technologies such as microgrids.

The U.S. Department of Energy defines a microgrid as "group of interconnected loads and distributed energy resources (DER) with defined electrical boundaries forming a local electric power system at distribution voltage levels, which acts as a single controllable entity and is able to operate in either grid-connected or island mode" [3]. The microgrid concept offers

integration of distributed energy resource and operation with or without grid. From this definition, microgrid sizes can range from small sites, such as individual houses or buildings, to much larger areas like districts or entire islands. In this thesis, we will focus on low voltage (LV) microgrid applications for small and medium buildings.

Energy usage in buildings represents nearly 30% of global energy consumption [4]. Moreover, the energy needs from both building operations and construction are on an upward trajectory. In the absence of specific policy interventions, the energy demand in buildings might soar to approximately 70% by 2050. [4]. The survey in 2018, conducted by the U.S. Energy Information Administration (EIA) illustrates the distribution of energy consumption by fuel type for commercial buildings.

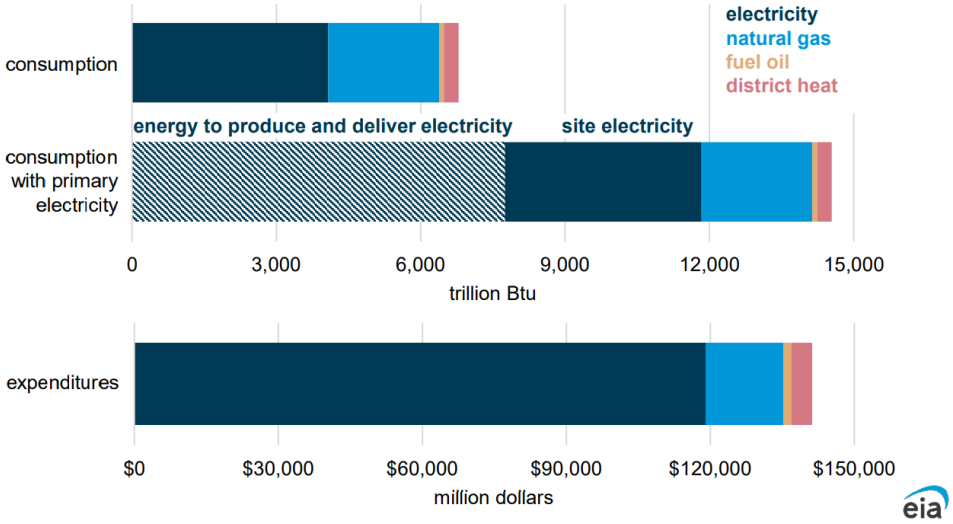

Figure 1.2: Building's energy consumption shares by fuel type [4].

As shown in Figure 1.2, the energy required to produce and transmit electricity is more than twice the amount of electricity that a building actually consumes. The electricity is produced by transforming the primary sources of energy such as nuclear, solar, wind, coal, and natural gas. In the United States, natural gas and coal serve as the predominant primary sources. The conversion of these fuels into electricity inherently involves certain inefficiencies, resulting in a notable loss of energy during the generation process. This loss can be attributed to factors like heat dissipation, transmission and distribution losses, and the thermodynamic limitations of the power plants.

Several strategies can be implemented to reduce this primary source consumption. Firstly, reducing it while optimizing the building energy efficiency by improving insulation, sealing air leaks, and using energy-efficient windows which can minimize heat losses or gain. Secondly, upgrading energy-efficient appliance can significantly reduce electricity usage, such as LED bulbs for lightning and heat pumps for heating. Thirdly, implementing smart energy management systems that automate and optimize energy usage based on occupancy, daylight, and

other factors which can lead to substantial energy savings. Additionally, promoting energy-conscious behavior among building occupants through awareness campaigns and education can also contribute to reducing energy consumption in buildings.

In the context of notable energy losses associated with the production and transmission of electricity, local renewable generation presents itself as a promising solution to improve even further the efficiency and resilience of buildings electrical installations. These small local generators, typically located behind the customer's meter, are known as distributed energy resources (DER). Examples of DERs include rooftop photovoltaic (PV) systems, wind turbines, combined heat power (CHP) units, and battery energy storage systems (BESS). In power systems, resilience is defined as the ability to withstand and recover from a disruptive event [5], [6]. Within microgrid context, the local generation enable backup power supply after a grid outage.

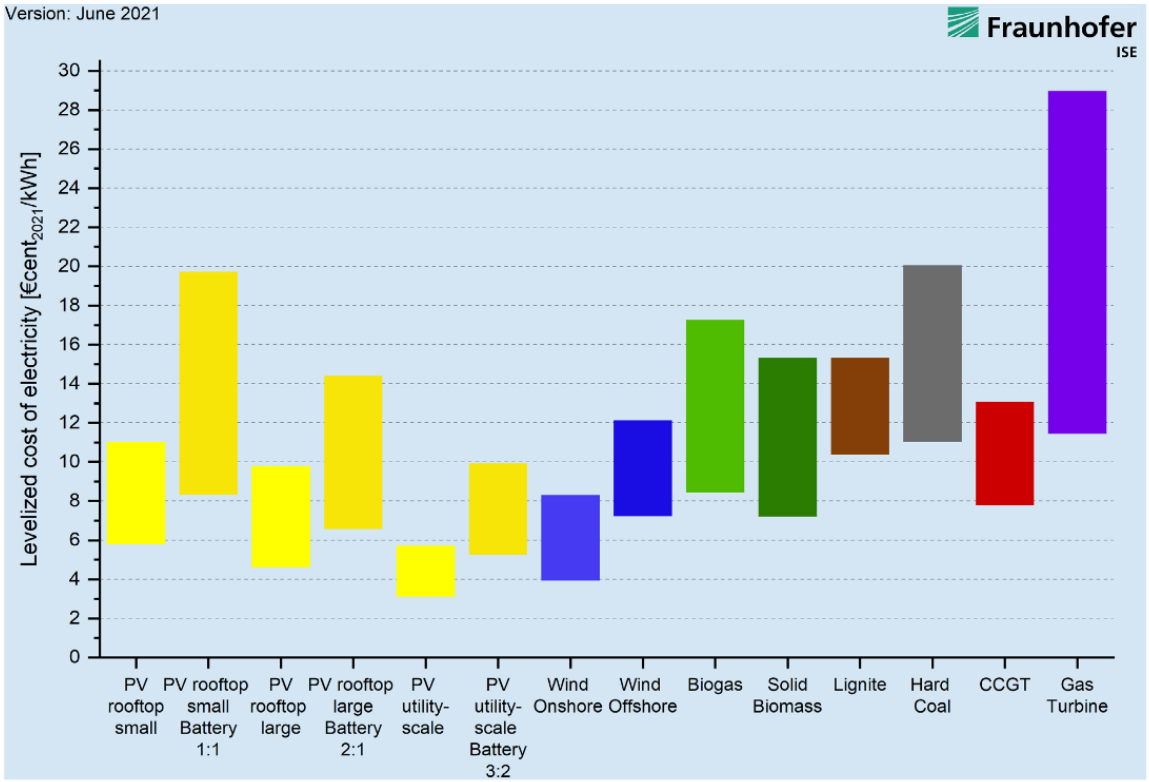

Figure 1.3: Levelized cost of electricity of various generation types in year 2021 [7].

Figure 1.3 presents the cost comparison of various generation systems. Among these, rooftop PV systems have gained significant adoption in the field. Nonetheless, from a practical standpoint, the deployment of photovoltaic panels, intended to generate energy equivalent to a building's consumption, may be constrained by the limited surface area available. It is worth noting that there exists a significant disparity in electricity consumption across buildings depending on the usage. Additionally, the daily and seasonal profiles of consumption and PV

production are rarely aligned. From a consumption perspective, the average certified building has a total annual electricity consumption of approximately 150 kWh/m^2. Nonetheless, it is common to encounter older tertiary buildings that surpass this value, consuming more than 300 kWh/m^2 annually [8]. Conversely, there are also highly efficient buildings that have achieved notable energy savings, with consumption levels as low as 37 kWh/m^2 [9]. From the PV production point of view, depending on the locations for example in France and in US the yearly average PV production are 270 kWh/m^2 and 350 kWh/m^2 respectively.[1] Considering the current trend in enhancing building efficiency, it is plausible to anticipate buildings with an energy demand as low as 50 kWh/m^2 in the foreseeable future. As such, if there are no shading issues caused by neighboring buildings, photovoltaic panels above five to seven-floors buildings could adequately meet their electricity needs. In most of the case, at least, consumers can lower their bills as electricity from PV systems is cheaper than utility rates.

The surface availability represents just one dimension of the challenge when integrating distributed PV systems. In residential districts or in smaller structures where roof space is sufficient, the increase of PV installations is still bounded by the PV hosting capacity. As the integration of PV systems into the LV distribution network intensifies, there emerges a potential risk of breaching operational parameters, predominantly attributed to overvoltage concerns. It is crucial to highlight that these overvoltage scenarios can be judiciously managed and mitigated through the strategic deployment [10] and control of BESS [11]. The integration of BESS not only facilitates energy storage but also underscores its instrumental role in maintaining grid stability and ensuring continuous operation when interfaced with significant PV installations.

A major challenge with PV production is its intermittency and dependence on solar availability; for example, it can only generate power during daylight hours. Additionally, PV output varies with the seasons. Therefore, achieving complete self-sufficiency without grid support requires storing excess PV energy for use during periods of low production. Figure 1.4 demonstrate how the BESS can improve self-sufficiency rate by enabling PV to be installed. In this example, we are using electricity dataset from Green-ER smart building [12].

This five-floors building houses part of the University of Grenoble Alpes and a research laboratory where this thesis is being carried out., is covering an area of 20,000 square meters. For illustration purposes, the PV profiles from this dataset is scaled to create the two scenarios. Let us consider a full week of typical sunny days in the summer season. In the scenario where no PV system is in place, the load consumption is met entirely through the grid. By introducing a 600 kWp PV system, the building can already attain a 44% level of self-sufficiency. However, in order to achieve complete self-sufficiency at 100%, it necessitates the installation of a substantially larger PV system with a capacity of 1,400 kWp, along with an 850 kW of 6 hours BESS. It is also important to note that this illustration only analyzes a

[1]The average PV production is derived from https://globalsolaratlas.info/

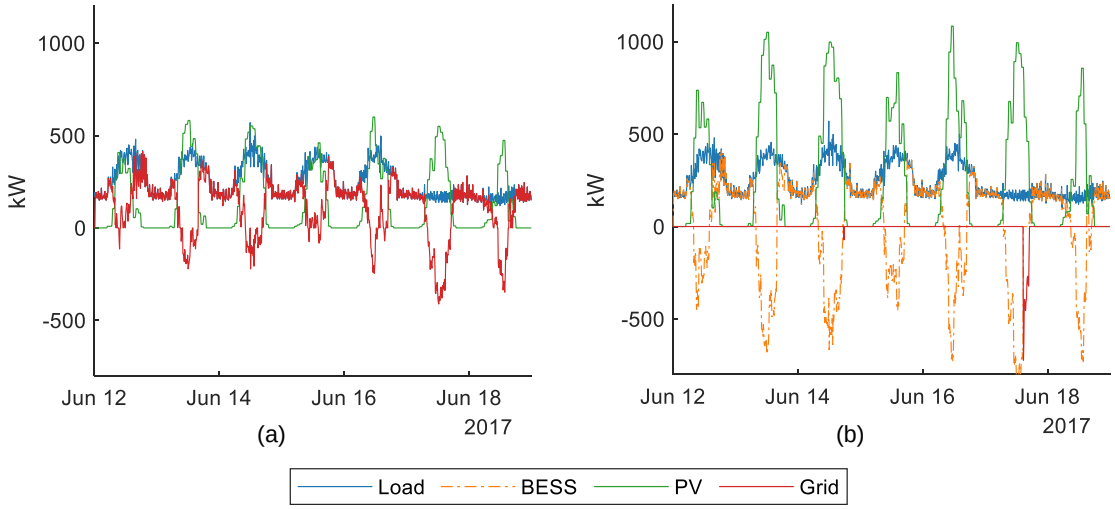

Figure 1.4: Illustration of impact on PV and BESS integration on GreEn-ER smart building's consumption profile. (a) case with only 600 kWp PV. (b) case with 1400 kWp PV and 850 kW of 6 hours BESS.

single week in the summer. Therefore, the self-consumption data does not accurately reflect seasonal changes throughout the year. Although the investment cost may appear substantial in this situation, there is a concrete example at the University of Queensland [13] where they successfully offset 100% of their electricity needs through the use of PV and BESS.

Another notable benefit of an on-site BESS is its ability to provide a reliable backup in the event of a power failure. This strengthens the system's overall reliability and resilience, ensuring consistent energy availability even during unforeseen challenges. Recent climatic extremities and unforeseen disasters have unveiled the vulnerabilities in our conventional power distribution systems, leading to colossal economic repercussions. The Texas power crisis in 2021 clearly demonstrate this, where electricity prices skyrocketed to an astonishing $9000 /MWh, burdening certain consumers with staggering bills, some witnessing a surge of up to $5000 within a mere span of five days [14]. Extending this scenario, consider a hypothetical four-day blackout impacting fifteen million crucial facilities nationwide. Such an event could lead to potential economic setbacks of over $700 billion [15]. While prolonged outages owing to large-scale disasters are perceived as low-frequency, high-impact events, even transient disruptions due to faults or power quality issues are not benign and can culminate in significant economic strains [16]. In response to these vulnerabilities, the United States took initiative-taking measures. By 2018, at least thirteen states had implemented or embraced policies promoting resilient microgrids to enhance grid stability during unexpected outages [15].

Several studies have highlighted the significant financial consequences of outages in major industries like data centers, manufacturing, retail, healthcare, and research institute [17] [18]. These outages can result in multi-million-dollar costs per event, underscoring their severe im-

pact on operations. According to a 2021 survey in US, 22% of companies that experienced outages reported losses of $100,000 or more for a typical outage. Shockingly, 80% of these companies faced such outages on a monthly basis, leading to an annual loss of at least $1.2 million [18]. Specifically, the average cost of a data center outage is estimated to be around $9,000 per minute [17]. For small commercial and industrial facilities, even momentary interruptions can cost to $200 per kW, while a one-hour outage can escalate costs to $300 per kW [19]. By adopting microgrids, businesses in these key sectors aim to bolster their energy resiliency, enhance operational continuity, and mitigate the substantial financial risks associated with downtime. This shift toward microgrid technology represents an initiative-taking approach to safeguarding their operations in the face of unexpected outages. Within this context, this thesis aims to enhance the resilience of microgrid supply through seamless operation of local DER, effectively protecting critical loads in the face of grid disruptions.

1.2 Distributed Energy Resources in Buildings

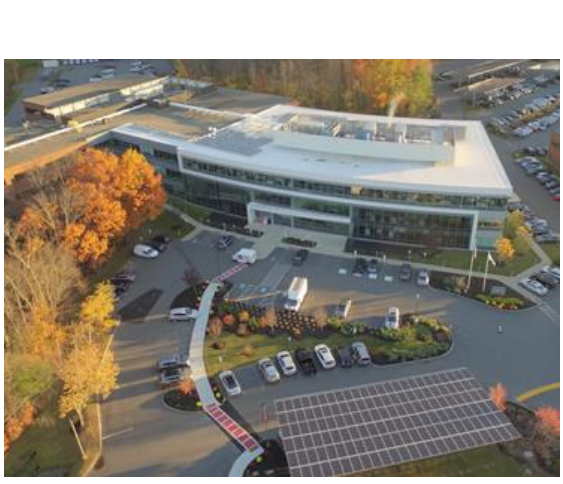
© Schneider Electric

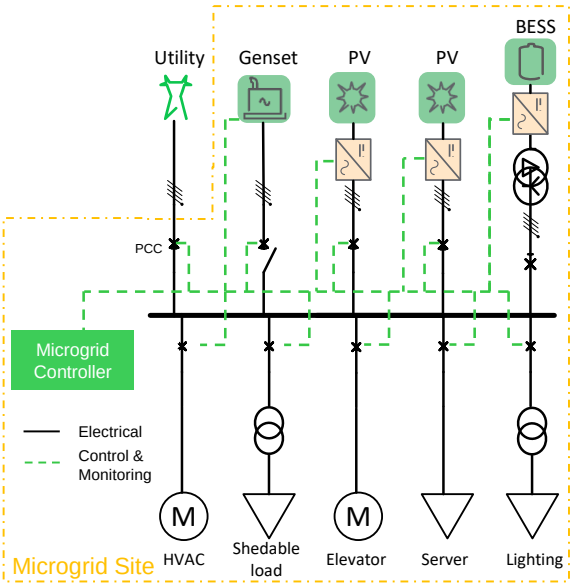

Figure 1.5: Example of microgrid and its typical schematic.

Currently, various types of distributed energy (re)sources (DERs) exist, including solar PV systems, wind turbines, small-scale combined heat and power or backup generators, fuel cells, and biomass systems. Traditionally, buildings were supplied solely by the utility grid

and relied on a generator set (Genset) for emergency power. Nowadays, distributed renewable energy resources such as PV and BESS are being integrated locally into customer sites. As a result, a microgrid controller is necessary to manage these DERs. Figure 1.5 illustrates a building equipped with microgrids, where the microgrid limit is bounded by the point of common coupling (PCC) [20]. The utility meter is installed at this point, with the upstream representing the utility grid and the downstream representing the local power system, or microgrid.

Understanding the characteristics of DERs is mandatory for controlling the microgrid. Classical DERs have two fundamental types of control: grid tie and grid forming. In section 3.2, a comprehensive and detailed explanation will be provided for each type of control.

Grid tie control In this mode, the DERs need to synchronize with the grid which acts as a voltage source. This syncrhonization is typically controlled using a Phase-Locked Loop (PLL). The primary objective of grid tie control is to inject active and reactive power into the grid in accordance with the grid voltage phase. From modeling perspective, this can be modeled as current sources. As it relies on the voltage source, if there are no voltage source existing on the system, the DER will stop working on this mode.

Grid forming Grid forming control establishes a voltage and frequency reference for the entire system instead of synchronizing with an external voltage source. The control loop in grid forming inverters focuses on regulating the voltage and frequency within the system. It actively adjusts its power output to maintain the desired voltage and frequency reference, making it crucial for the primary sources of some of the DERs to be dispatchable. If the consumed power exceeds the capacity of the DER, it will stop due to overload as it tries to maintain the imposed voltage and frequency. Additionally, operating grid forming sources in parallel requires advanced control to ensure power system stability [21].

1.2.1 Solar PV system

PV panels transform solar energy into DC electricity. The DC energy generated by the panels is then converted into AC electricity using inverters. The amount of power produced by the PV panels is determined by the strength of sunlight, often referred to as irradiance and PV panels voltages. To ensure optimal performance and power generation, it is possible to regulate the power output of the PV system by controlling the voltage (polarization) across the panels. As illustrates Figure 1.6 right the maximum power at given irradiance is achieved at different voltage. This process involves adjusting the panel voltage to achieve a state known as Maximum Power Point Tracking (MPPT). MPPT allows the PV system to operate at its highest efficiency by continuously monitoring and adjusting the panels voltage to maximize power production.

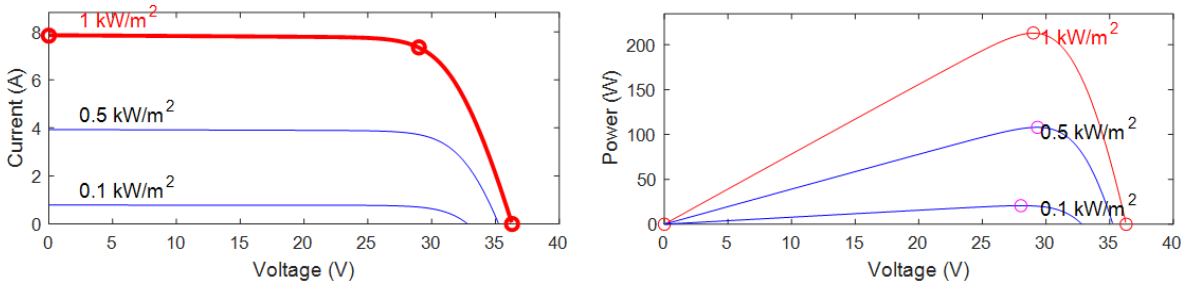

Figure 1.6: Characteristics of PV panel under different insolation conditions. (left) I–V characteristics, (right) P–V characteristics.

There are wide range of choices of PV panels in the market, typically ranges from 200 W to 400 W each. In many applications, the panels are connected in series to increase the voltage, this commonly referred as "string." Multiple string, often labeled as "array" can be connected in parallel to PV inverters, which convert the DC power into AC power. Additionally, there are various PV inverter topologies available that depend on factors such as the processing stages, phases, isolation requirements, and power rating of the PV system [22]. In the context of building rooftop applications, the PV system typically exceeds 10 kW in capacity, which the usage of three phase inverters is common.

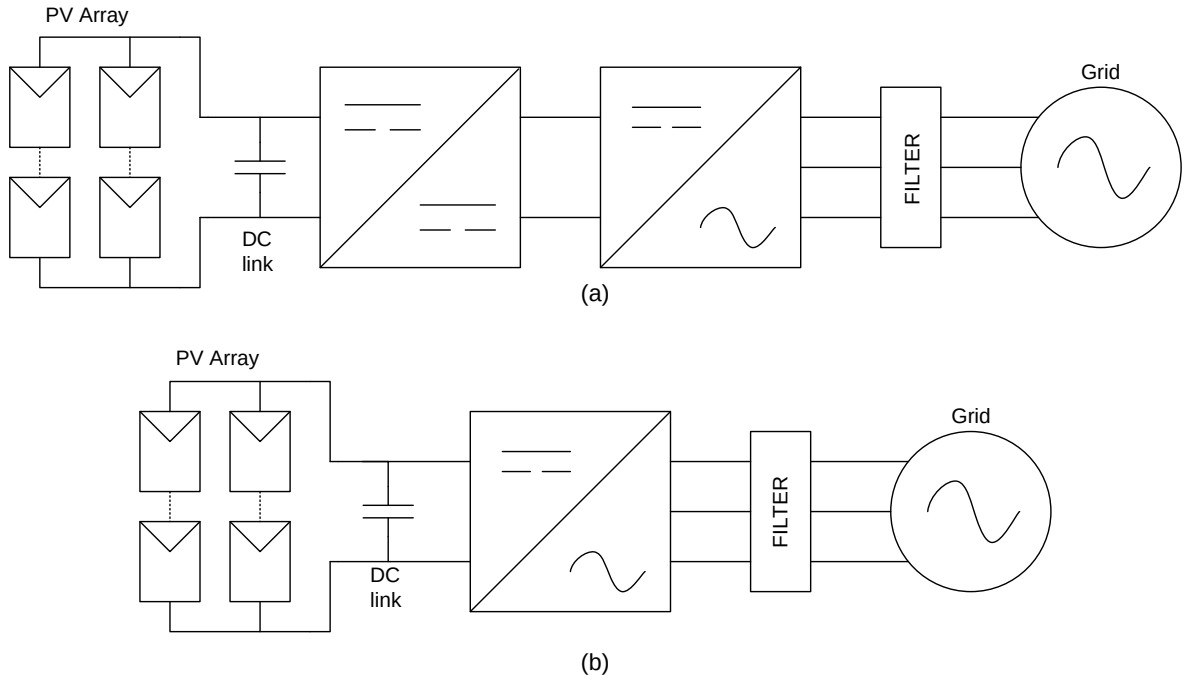

Figure 1.7: PV systems. (a) Two-stage inverter structure (b) Single-stage inverter structure

In single stage conversion topology, dc-dc stage is not present. Effectively, the inverter's

efficiency increases. However, the grid side inverters need to manage the MPPT which adding the control complexity. [23]. On the other hand, the dual stage use dc-dc stage to decouple MPPT and grid side inverter control. Although the inverter efficiency is reduced, the inverter can support multiple strings connected to independent MPPT which can optimize the PV production [22].

1.2.2 Battery Energy Storage Systems

1.2.2.1 Batteries technologies

Lithium-ion, sodium-sulfur, lead-acid, and redox flow batteries are the primary electrochemical technologies utilized in grid applications. To evaluate battery energy storage technologies, the following criteria must be considered: power density, energy density, efficiency, life cycles, calendar life, capital cost, maintenance cost, commercial maturity, and safety [24]. Figure 1.8 shows a comparison of the relevant battery technologies.

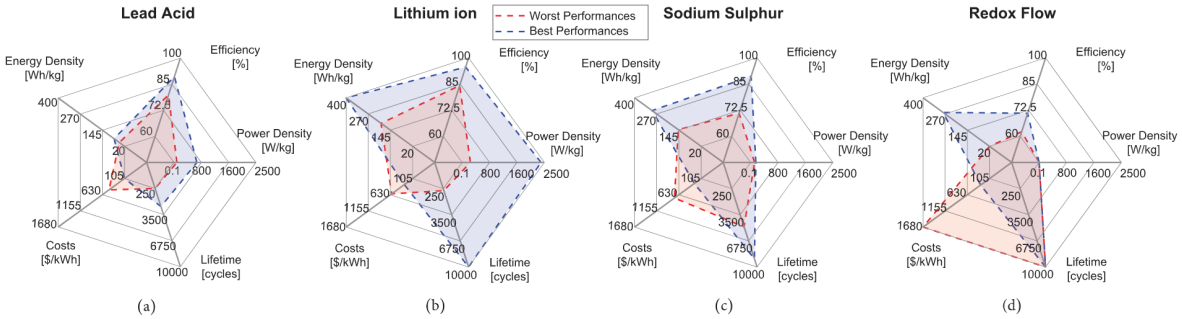

Figure 1.8: Performances of different electrochemical battery technologies: (a) Lead Acid, (b) Lithium ion, (c) Sodium Sulphur, and (d) Flow Battery [25]

Lead Acid was invented in 19th century by french physicist Gaston Planté, marked as the first rechargeable battery technology. Today, they are recognized as a well-established technology, noted for their affordability, with cell costs ranging between $50 to $600 per kilowatt-hour, and a commendable efficiency rate of 80-90%. However, they fall short in terms of cycle durability—reaching up to 2500 cycles—which is relatively low when compared to alternative technologies. Additionally, they have a modest energy density of 20-30 Wh/kg.

Sodium-sulfur (NaS) batteries emerged from a collaborative development effort between NGK Insulators Ltd. and Tokyo Electric Power Company (TEPCO). These batteries are distinguished by their high operational temperature, approximately three hundred degrees Celsius also, and exhibit a respectable efficiency exceeding 80%. They also boast a substantial energy density, situated between 150 and 240 Wh/kg, alongside an

extended cycle lifespan that can reach up to 4500 cycles. NaS battery technology has been successfully implemented in grid-connected energy storage applications, serving as a counterbalance to the variable nature of power generation from renewable energy sources.

Redox Flow (RF) batteries adopt a unique approach compared to other battery types, where one or both of the active materials are dissolved in the electrolyte solution, which is then stored in external tanks [26]. The electrolytes that flow through the cathode and anode are separated by a membrane. This membrane allows specific ion to pass through, thus facilitating the oxidation-reduction (redox) reaction.

A notable advantage of RF batteries is the ability to independently adjust their power and energy capacities. The power (kW) of the system is determined by the size of the membrane electrodes, whereas the energy storage capacity (kWh) is determined by the concentration and total volume of the electrolyte. Therefore, the energy storage can easily be adjusted from few hours to days, depending on the application [27]. RF batteries typically have lower energy densities, ranging from 35 to 60 Wh/kg, and efficiencies that can reach up to 85% [28].

A significant advantage of RF batteries is their longevity and resilience to depth of discharge [29], free from the cycle life constraints seen in other battery types. The vanadium redox flow battery technology is mature and has been commercially deployed for grid-scale storage [27]. Although, theoretically, vanadium redox flow battery has exceptionally long operating life, its sharp degradation due to electrolyte imbalance and the fairly expensive ion-exchange membrane are some of the significant challenges [28].

Lithium-ion batteries are widely used in consumer electronics and electric vehicle applications [30] due to their high energy density and cycling performance. They typically consist of a graphite anode and a lithium metal oxide cathode. Various cathode materials are used to characterize the cells, such as lithium cobalt oxide-based $LiCoO_2$, lithium nickel manganese oxide-based $LiNi_xMn_yCo_zO_2$ [NMC], lithium nickel cobalt aluminum oxide-based $LiNi_xCo_yAl_zO_2$ [NCA], and lithium iron phosphate-based $LiFePO_4$ [LFP]. The Li-ion battery technology demonstrates impressive round-trip cell efficiency, near to 100% [31]. However, the global efficiency which includes power conversion system and auxiliaries is about 65% to 85% depending on the operation power [32]. These batteries also exhibit high energy density, typically ranging from 100 to 200 Wh/kg [28]. Furthermore, their long lifetime can reach up to 10,000 cycles at 80% depth of charge [33]. It is worth noting that the cell temperature significantly impacts the battery's lifetime, as it is a critical factor in the degradation process [32]. For a comprehensive understanding of the performance differences among various Li-ion chemistries, please refer to Figure 1.9. As seen in the picture the LFP has higher lifetime, but lower efficiency compares to the other two. NMC stands out in power density, while NCA has better energy density. Furthermore, LFP has much better thermal stability and is therefore safer [34].

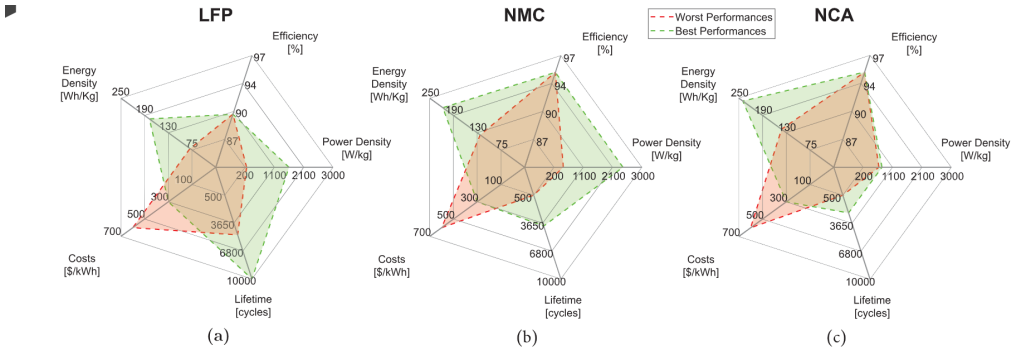

Figure 1.9: Performances of different Li-ion battery technologies: (a) Lithium iron phosphate, (b) Lithium nickel manganese cobalt, and (c) Lithium nickel aluminum cobalt [25]

Furthermore, the battery voltage varies depending on factors, such as state of charge and current values, as illustrated in Figure 1.10. These characteristics must be taken into account when designing a BESS.

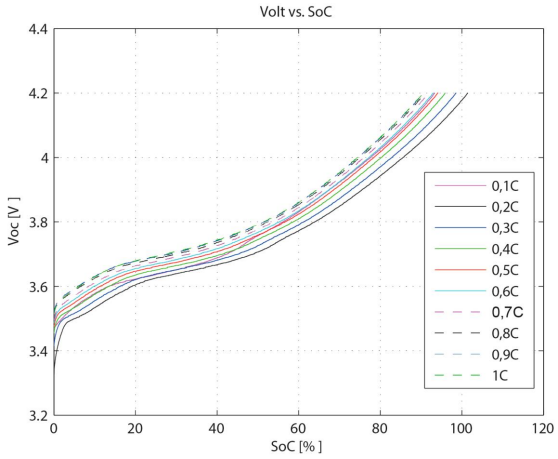

Figure 1.10: Battery voltage and SoC relationship during the charge process at different current values. [35]

1.2.2.2 Energy Storage Power Conversion System

The connection of battery storages to the microgrid is made through power converters. Figure 1.11 shows the schematic of battery energy storage system, which consist of battery pack, dc link, converter, and filter. In addition, battery management system is needed to manage the battery pack, along with the local controller to manage the whole battery energy storage system. Depending on the application, to increase the power of the system, converters can be paralleled. This allows for multiple possible topologies, such as parallel power trains, modular multilevel cascaded converters, and more [36].

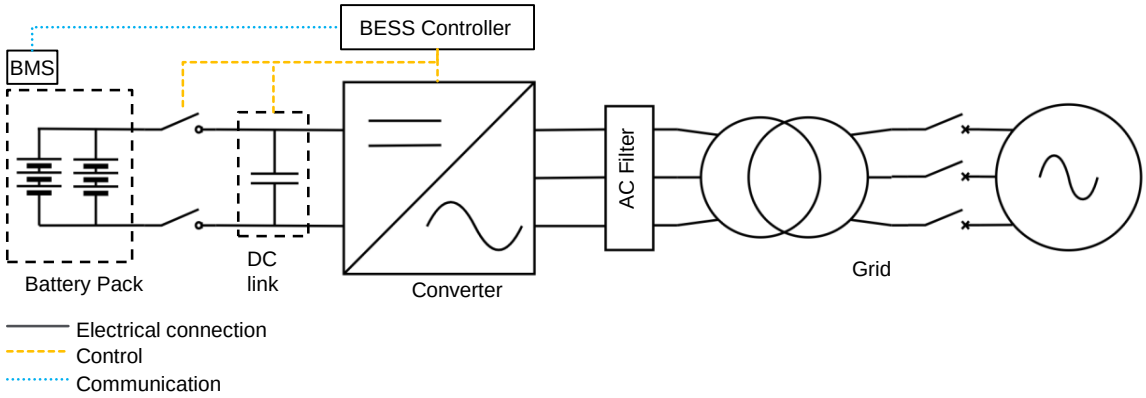

Figure 1.11: Schematic of battery energy storage system

Batteries are stacked in series to attain the desired voltage level for conversion, thereby eliminating the need for an extra dc/dc converter, hence improving efficiency, and reducing the cost. The battery pack is connected with dc link through disconnection switch. A dc link is mainly capacitor to reduce the voltage ripples caused by converter switching. Consequently, the implementation of a pre-charging circuit becomes necessary to eliminate the inrush current to the capacitor upon connection, thereby extending the lifespan of the capacitor. De-energizing circuit can also be added for safety purposes.

1.2.2.3 Battery Management System

Battery pack consist of multiple battery module is usually integrated with battery management system (BMS). The primary objective of a BMS is to ensure the safe and optimal operation of batteries throughout their lifecycle [35]. One of the key responsibilities of the BMS is to manage the charging and discharging processes of the battery. It controls the flow of current to and from each battery cells, preventing overcharging, deep discharging, and other potentially damaging conditions. This not only protects the battery from premature degradation but also ensures its longevity and sustained performance. Moreover, the BMS plays a crucial role in maintaining the balance among individual cells within a battery pack. Cell imbalances can occur due to variations in capacity, internal resistance, or aging. The BMS actively monitors the voltage levels of each cell and implements balancing mechanisms to equalize the charge distribution, thereby maximizing the overall capacity and extending the battery pack's lifespan. Another critical aspect of the BMS is its role in ensuring the safety of the battery and its surroundings. It incorporates various protection mechanisms to prevent thermal runaway [37], overtemperature, overvoltage, undervoltage, and short circuits. These safeguards not only preserve the battery's integrity but also minimize the risk of fire, explosion, or other hazardous situations. In addition, the BMS incorporates advanced algorithms and predictive models to accurately estimate the battery's state of charge (SoC) and state of health (SoH). BMS also communicates to the local controller to give the operating limit value such as max

charge and max discharge power.

1.2.2.4 DC/AC Converter

Bidirectional voltage source converters (VSC) are essential components that interface BESS with the electrical grid. These converters efficiently transform the dc power from the batteries into high-quality ac power suitable for grid injection, and they can also convert ac back to dc for storage. However, the efficiency of the BESS is compromised by the VSC due to inherent switching and conduction losses, highlighting the need for optimization in converter design. There are several converter topologies illustrated in Fig 9, such as (a) two level VSC, (b)

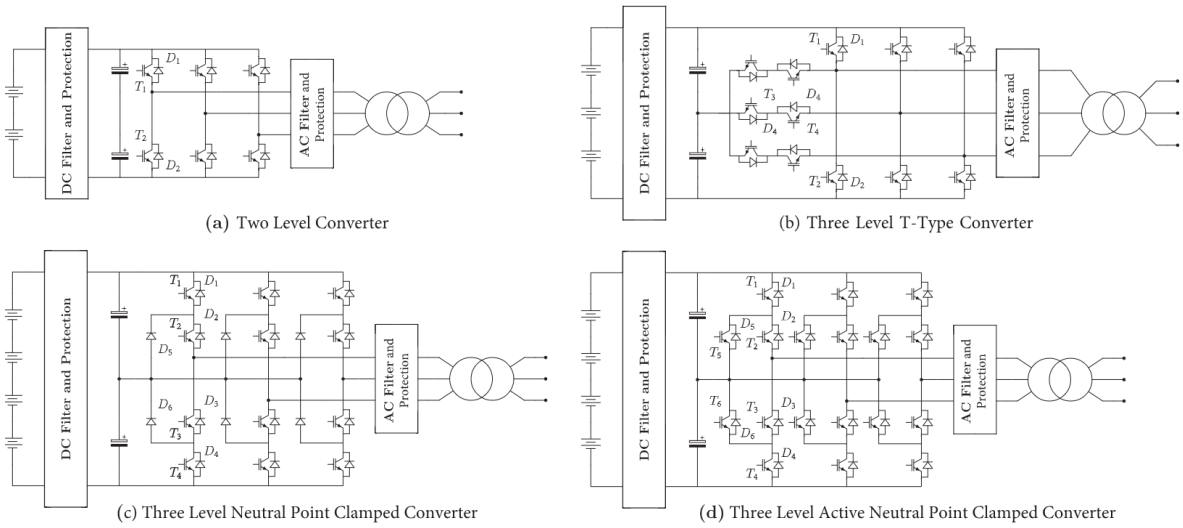

Figure 1.12: Different converter topology [25]

three level T-type, (c) Neutral Point Clamped (NPC), and (d) Active Neutral Point Clamped (ANPC). Each topologies have its own advantages and drawbacks. The Two-Level Voltage Source Converter (VSC) operates with two voltage levels ($+V_{dc}$ and $-V_{dc}$), commonly used but has higher harmonic distortion and switching losses. The Three Level T-type Converter offers three voltage levels ($+V_{dc}$, 0, and $-V_{dc}$), reducing harmonic content and improving waveform quality compared to the two-level VSC. The Neutral Point Clamped (NPC) Converter provides multiple voltage levels using capacitors. Finally, the ANPC converter is an enhanced version of the NPC converter that further reduces switching losses, improves efficiency, and provides higher voltage levels. However providing improved efficiency, requires additional active switches, which adds complexity to the control and increases the overall system cost. The design of these converters is further influenced by the varying voltage of the battery, which changes according to the state of charge as shown previously in Figure 1.10. In addition, a minimum of 700 V dc is needed to produce three phase 230 V ac rms value. Conversely, the voltage must not exceed the upper limit of 1500 V DC, which is the threshold for LV system.

1.2.3 Diesel Generator

Diesel generators are often used in situations where the grid is unavailable to provide a backup power source. These diesel generators offer several advantages in microgrid applications, such as providing short-circuit power and the ability to generate power for extended periods of time. However, it is important to note that efforts are being made to minimize the reliance on diesel generators in microgrids due to environmental concerns, with a focus on incorporating renewable energy sources and energy storage technologies to achieve a more sustainable and resilient power supply.

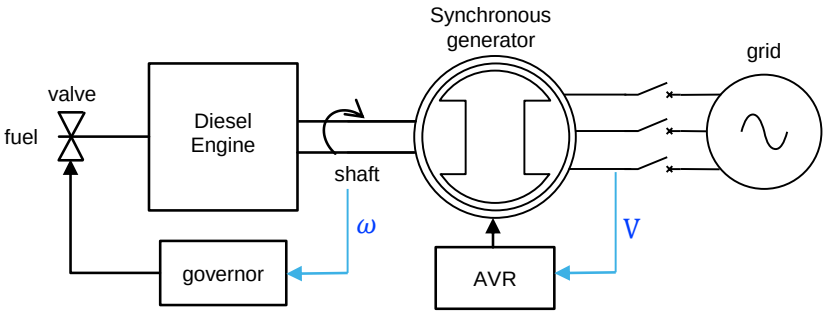

Figure 1.13: Diesel generator schematic

A diesel generator combines a diesel engine and a synchronous generator to convert mechanical power into electrical power. The diesel engine provides the mechanical power, which is then converted to electrical power by the synchronous generator. The speed of the generator is controlled by a governor, which regulates fuel injection to adjust the rotor speed. To maintain the output voltage of the generator within a certain range, an automatic voltage regulator (AVR) is used to change the excitation current of the synchronous generator.

For the performance of generating sets (Gensets), ISO 8528 specifies various classes that relate to the allowable deviation in frequency and voltage, recovery time, and other performance characteristics under different operating conditions. The standard defines genset performance according to the following classes:

Class G1 : This class is generally considered to have the least stringent requirements regarding voltage and frequency stability. Gensets in this class are typically used in applications where the connected equipment can tolerate a wider variation in voltage and frequency.

Class G2 : With more stringent requirements than Class G1, generators within the G2 category provide enhanced voltage and frequency stability, often comparable to that of commercial public utilities. They demonstrate improved transient response to load variations.

Class G3 : This class has the strictest requirements for voltage and frequency stability of

these three classes. Gensets in this class are designed for applications that require a high quality of power with minimal deviations, such as data centers or hospitals.

Class G4 : This class represents the highest level of performance and is designed for specific applications. Performance criteria are typically defined through a mutual agreement between the customer and the manufacturer.

Furthermore, Table 1.1 elaborates on the operational thresholds for each class, encompassing aspects such as transient voltage, frequency fluctuation, and recovery durations. In combustion engine, the power is related to its break mean effective pressure (BMEP), thus the genset electrical performances are also dependent to this values.

Table 1.1: Genset performance class comparison

Parameter		**Unit**	**Performance Class**			
			G1	G2	G3	G4
Frequency deviation	steady state	%	± 2.5	± 1.5	± 0.5	*
	100% to 0% load decrease	%	$\leq +18$	$\leq +12$	$\leq +10$	*
	BMEP** load increase	%	≤ -15	≤ -10	≤ -7	*
Frequency recovery time		s	≤ 10	≤ 5	≤ 3	*
Voltage deviation	Steady-state	%	± 10	± 10	± 1	*
	100% to 0% load decrease	%	$\leq +35$	$\leq +25$	$\leq +20$	*
	BMEP** load increase	%	≤ -25	≤ -20	≤ -15	*
Voltage recovery time		s	± 10	± 6	± 4	*

Note: *customer specified performance. **load increase is based on BMEP step loading

1.2.4 Various types of electrical loads in buildings

In buildings, electrical loads refer to the devices, equipment, and systems that consume electrical power. The fundamental purpose of power grid is to provide a high quality to electrical loads, knowing the nature of electrical loads will help us to understand the needs of microgrid. There are several types of loads in building:

- **Lighting:** LED (Light Emitting Diode) bulbs and CFL (Compact Fluorescent Lamps) are two prominent lighting technologies that is commonly used. LEDs, leveraging semiconductors to emit light, consume less electricity, and outlast traditional incandescent bulbs. CFLs operate differently, exciting mercury vapor to emit light. Both, distinct from traditional incandescent bulbs, function as nonlinear loads.
- **HVAC:** Heating, Ventilation, and Air Conditioning (HVAC) systems consume a significant amount of electrical power in buildings. This includes air conditioning units, fans,

pumps, boilers, and other HVAC equipment.

- **Power Outlets:** These loads consist of electrical outlets used for plugging in devices such as computers, printers, chargers, appliances, and other equipment.
- **Appliances and Equipment:** This category includes various electrical appliances found in buildings, such as refrigerators, microwaves, ovens, washing machines, dryers.
- **IT:** Buildings with extensive IT infrastructure have specific loads related to servers, switches, routers, UPS (Uninterruptible Power Supply) systems, and other networking devices.
- **Elevators or Lifts:** Buildings with multiple floors often have electrical loads associated with elevators, escalators, and lifts used for vertical transportation. Some elevators now come equipped with battery-powered emergency power sources [38] [39]. This battery also can be used to increase efficiency by using energy recovery mechanism [40]
- **Security Systems:** Security devices like CCTV cameras, access control systems, fire alarms, sprinkler systems and surveillance equipment also contribute to the electrical load in a building.
- **Electric Vehicle Chargers:** With the rise of electric vehicles, buildings have dedicated charging stations that add to the electrical load.

While electrical loads are known to consume energy, it is important to consider the inherent flexibility of controllable loads. In fact, controllable loads can be equated to generators due to their ability to provide valuable flexibility. The integration of generation into the power grid has a comparable effect on power balance as reducing consumption. One example of this is to take advantage of off-peak pricing by charging electric vehicles and water heater during those times. Future developments, such as "vehicle-to-grid" applications, could allow electric vehicles to feed power back into the grid as needed, essentially turning them into bi-directional energy storage systems [41]. By classifying loads based on their flexibility, we can differentiate between flexible and non-flexible loads.

Moreover, among these loads, certain ones are more critical than others. Critical loads demand a prominent level of reliability and uninterrupted power supply, being essential for safety, health, security, or crucial operations. Examples include servers, IT networks, and emergency life-saving equipment. These critical loads underscore the importance of reliable power management.

In our study, we utilize the dataset of the GreenEr campus building [12] as a representative example. Our objective is to analyze how various loads consume energy. By examining the consumption curves derived from this dataset, we can estimate the peak power consumption for each specific category of load as illustrated in Figure 1.14. This analysis is crucial as it

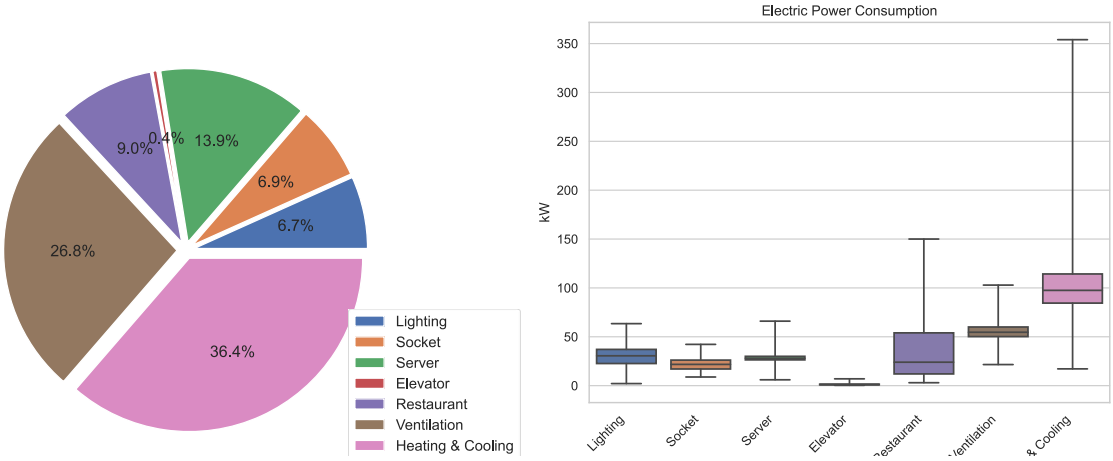

Figure 1.14: Electricity consumption of GreenEr buildings. (a) yearly consumption (b) power distribution during working hours.

allows us to calculate approximate figures for the minimum power requirement necessary for emergency backup systems. Understanding these requirements is essential for ensuring that the backup systems are adequately designed to handle power needs during unforeseen outages or emergencies, thus maintaining continuous operation and safety.

This building is energized through two transformers of 2 MVA. From this example we can see that for short outages, we need only to supply the server, socket and lighting, which totaled only 200 kW. When outages duration is longer, some ventilation should also be powered on along with some air conditioning for the comfort of occupants.

1.3 Microgrid Architecture and Operation Modes

1.3.1 Microgrid Architecture

Microgrids can be primarily classified into three categories based on the system architecture and voltage characteristics

AC microgrid The AC microgrid is the most common architecture type in microgrid systems. Its notable advantage lies in its compatibility with the existing electrical installation and mass market appliances. Within the AC microgrid, DC-AC inverters play a critical role in converting DC power, generated from DER such as PV and BESS, into AC power. However, this architecture also presents certain challenges, particularly due to the inverters that are crucial for ensuring the delivery of high-quality AC currents.

These inverters must effectively eliminate harmonics and prevent instability in the power supply.

DC microgrid Due to advancements in DC renewable energy sources, research in the area of DC microgrids is gaining momentum. Additionally, a significant number of DC loads, which account for around 30% of the generated AC power, pass through a converter before being utilized [42]. DC microgrids offer several benefits, making them an attractive option in certain contexts. They enable direct connection of BESS and reduce the need for multiple power conversions, thereby improving overall system efficiency. Renewable energy resources can be seamlessly integrated into DC microgrids. Furthermore, power converter loss and operating costs are minimized in DC systems, as they typically require only a simple inverter unit connected to the AC main grid. However, DC microgrids also have drawbacks. Most current load units are designed for AC power, making a solely DC distribution network less feasible. Voltage transformation in DC systems is generally less efficient than in AC systems. Moreover, protection in DC systems is more challenging because there is no zero-crossing zone. Unlike ac microgrid, dc microgrid is still in adoption stage. Several demonstration sites are already up and running such as an industry [43] or an island [44]

Hybrid AC-DC microgrid As mentioned previously, the involvement of DC/AC and AC/DC converters escalates equipment costs. To address these issues, a hybrid AC-DC microgrid architecture has been proposed, combining architectures of DC and AC microgrids. This hybrid system incorporates the advantages of both, including minimized conversion losses, reduced equipment costs, and the ability to supply reliable and high-quality power to diverse loads. However, the structure of hybrid AC/DC microgrids is complex. Therefore, the coordinated control strategies must be thoroughly investigated.

1.3.2 Mode of operations

Unlike traditional power systems, a microgrid is capable of functioning in two distinct modes: either as connected to the grid or in an islanded mode as represented in Figure 1.15

Grid-connected mode In this operational mode, the microgrid maintains a connection to the main grid. This connection is indicated by the closed state of the point of common coupling breaker, allowing the main grid to supply electricity to loads. Additionally, DER within the microgrid have the ability to provide various services to the grid, such as peak shaving, frequency regulation, renewable energy smoothing, and reactive power support.

Islanded mode Whenever a disturbance or fault occurs on the main grid, the microgrid operates independently from the main utility grid, becoming an isolated entity that

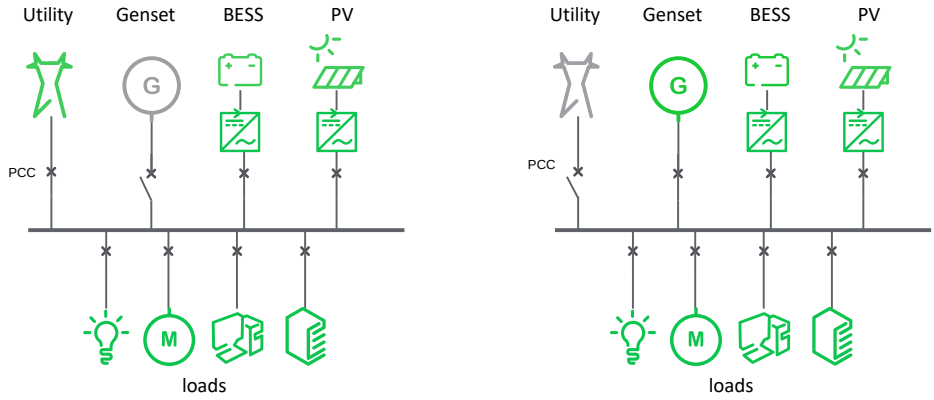

Figure 1.15: Microgrid operation mode. (a) grid connected mode. (b) islanded mode.

ensures a power supply to the local loads. The microgrid relies on its own DER to sustain a reliable and superior power supply. This mode is essential for improving the power system's resilience, especially in areas susceptible to grid disruptions or in remote locations with limited grid connectivity.

Transition between modes

When microgrid transition from one mode to another, a set of sequence of operation must be performed like controlling breaker, starting, or stopping the DER. This operation is ensured by microgrid controller through industrial communication protocols. The IEEE 2030.7 standards [45] specify a minimum transition function that need to be considered as represented in Figure 1.16.

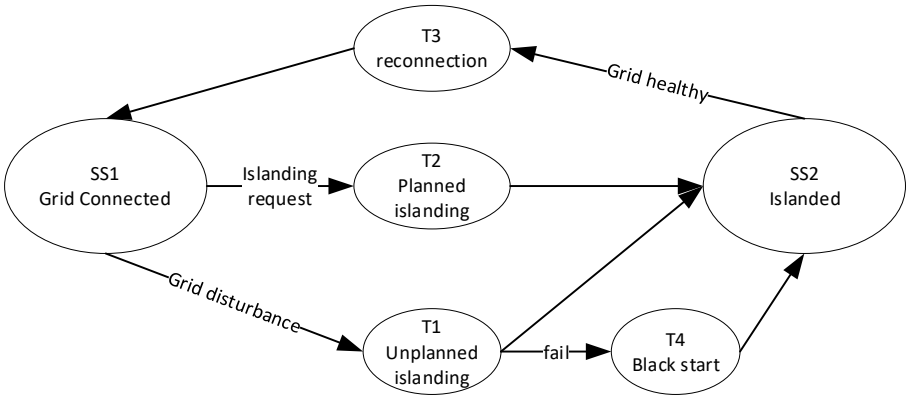

Figure 1.16: Microgrid operation mode. (a) grid connected mode. (b) islanded mode.

Unplanned Islanding – T1 When the microgrid controller detects a disturbance in the main grid, it disconnects the microgrid from the main grid. DER such as BESS or

gensets, form a local power system to maintain a continuous power supply to the loads. Simultaneously, non-critical loads are shed to prevent overloading of the DER. Additionally, protection devices and DER parameters are adjusted accordingly.

Planned islanding – T2 Even though the main grid is available, operators may occasionally initiate an islanding sequence for testing or maintenance reasons. Unlike unplanned islanding, in this scenario, the microgrid controller has time to balance local production and consumption before disconnecting from the main grid, thereby ensuring a smoother transition.

Grid reconnection – T3 When the grid becomes available and stable, the microgrid initiates grid reconnection transition. The local grid-forming generators need to synchronize their phase with the grid before closing the point of common coupling breaker, as reclosing out-of-phase can cause serious damage to local generators and protection equipment. Immediately after the breaker is closed, the DER must switch to grid-following mode.

Black Start – T4 When an unplanned transition fails or a blackout occurs in islanding mode, the microgrid performs a black start capability. During this transition, the microgrid controller disconnect non-critical loads and restarts the available DER. Once a stable generation source is available, loads can be reconnected one at a time according to priority.

Moreover, earthing system or commonly known grounding in United States plays crucial roles to ensure safety in the microgrid. Appendix A provides insight of these earthing systems in both grid connected and islanded mode.

1.4 Classical solution for grid outage

As mentioned previously, the grid outages or even a small grid disturbance have significant impact on business operations. Traditionally, the building is backed up by generator set and the uninterrupted power supply (UPS) for each critical load. A UPS is a device that provides emergency power to a load when the input power source, typically the main electricity grid, fails. Its primary function is to bridge the gap between the onset of a power failure and the point at which a backup generator can come online, or to provide sufficient time for a safe shutdown of critical equipment. In terms of operation, a UPS typically has two modes of operations: normal and battery. Some UPS technologies, such as double conversion systems, offer an additional normal mode, known as high efficiency bypass mode. Furthermore, these systems are designed to seamlessly switch between normal, bypass, and battery modes, ensuring consistent power delivery. Depending on their dependence on the input power source, UPS systems can be categorized into three classes:

- Voltage and Frequency Dependent (VFD)
- Voltage Independent (VI)
- Voltage and Frequency Independent (VFI)

Additionally, UPS can be classified by its dynamic output performance which describes the output voltage variations of UPS during transient.

1.4.1 UPS Dynamic performance class

As per IEC 62040-3 standard, the UPS dynamic performance class is assessed with two configurations: firstly, during changes in operating mode. Secondly, during the load step application. Voltage variations fall into one of three classifications:

- Class 1: No interruption with ±30% voltage regulation in <4 ms. This kind of performance is required by sensitive critical loads.
- Class 2: Up to 1 ms of interruption with ±20% voltage regulation in <10 ms. This performance is accepted by most types of critical loads.
- Class 3: Up to 10 ms of interruption with +10%, -20% voltage regulation in <100 ms. This performance is accepted for general information technology (IT) purposes.

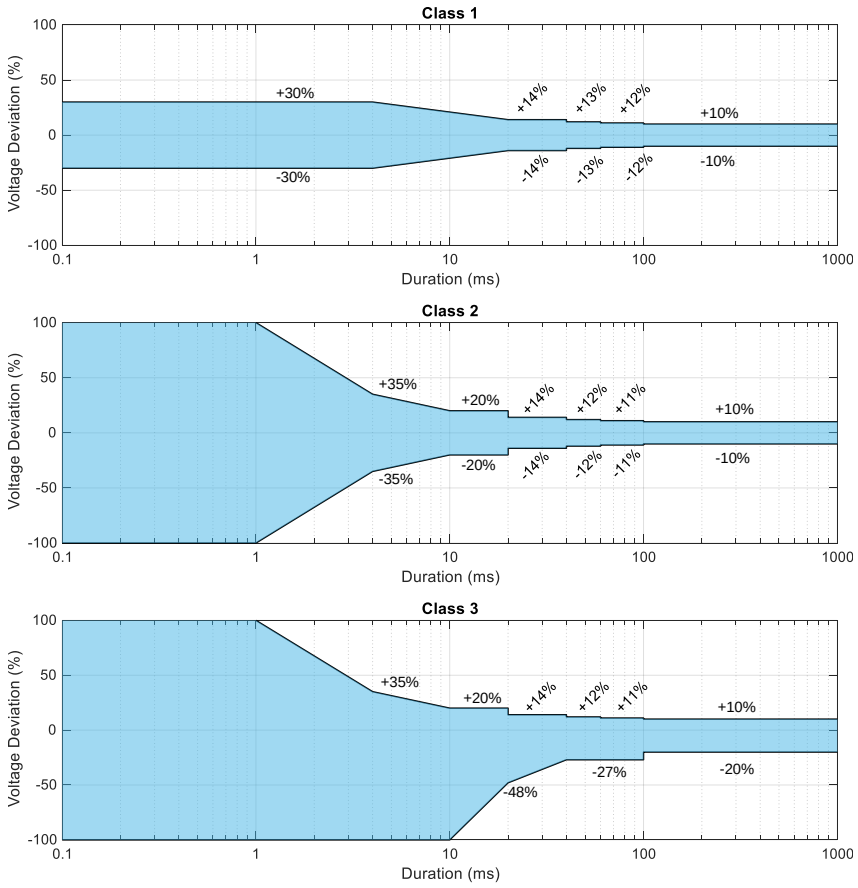

Figure 1.17: UPS dynamic output performance classes [46]

1.4.2 UPS topology

UPS use similar component with BESS. In this section we present the UPS topology to compare the similarity with BESS. IEC 62040-3 standard distinguish three types of UPS topologies: passive standby, line interactive and double conversion. These terms refer to UPS operation with respect to utility power i.e. the distribution system upstream of the UPS. Figure 1.18 shows the difference of UPS topology

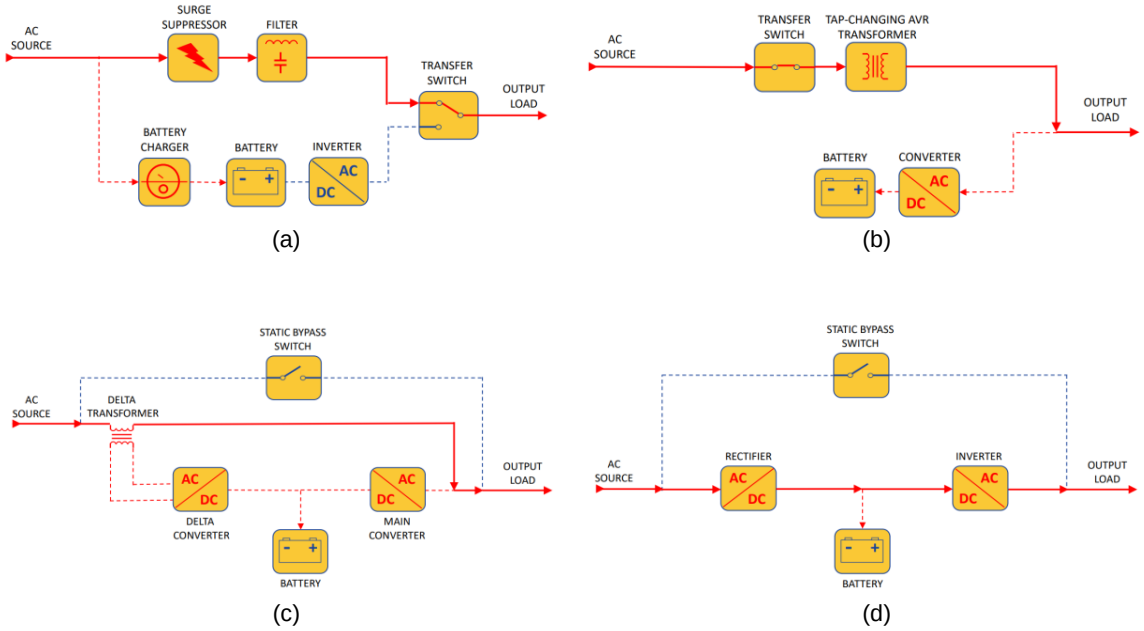

Figure 1.18: UPS dynamic output performance classes [46]

Standby UPS topology (Figure 1.18a) is the most basic type, where the UPS is on standby and kicks in only when it detects a power failure. It's suitable for less critical applications. This topology is often referred as off-line UPS.

Series Line-interactive UPS topology (Figure 1.18b) offers more advanced features, such as voltage regulation. It is often used in small business and consumer applications. This system consist of a static switch, a series inductor, a bi-directional converter, and battery. In normal mode of operation, AC/DC converter is connected in parallel with the load and charges the battery while regulating the output voltage. In stored-energy mode of operation, the bi-directional converter operates as an inverter and supplies the load from the battery set. The transfer switch disconnects the AC line in order to prevent back feed from the inverter.

Series-parallel line-interactive UPS topology (Figure 1.18c), also known as delta conver-

sion UPS consist of two bi-directional converters. In this topology, the delta converter is connected in series with the AC input line and rated at about 20% of the output power of the UPS. The main bidirectional converter is connected in parallel to the load and rated at 100% of the output power [47].

Double-conversion UPS topology (Figure 1.18d) This type provides the highest level of power quality and protection. Here, power always runs through the UPS, completely isolating the attached equipment from the main power supply. This is ideal for sensitive and critical equipment. In fact, almost all UPS which more than 50 kVA rating is using this topology.

1.5 Thesis objective: Enhancing microgrid supply resilience through seamless operation

Even though the UPS system is widely used as a solution for power supply issues, microgrid emerges to offer an islanding function to provide electricity for local loads during longer grid outages. Recently, many building owners has been investing on microgrid technology. They

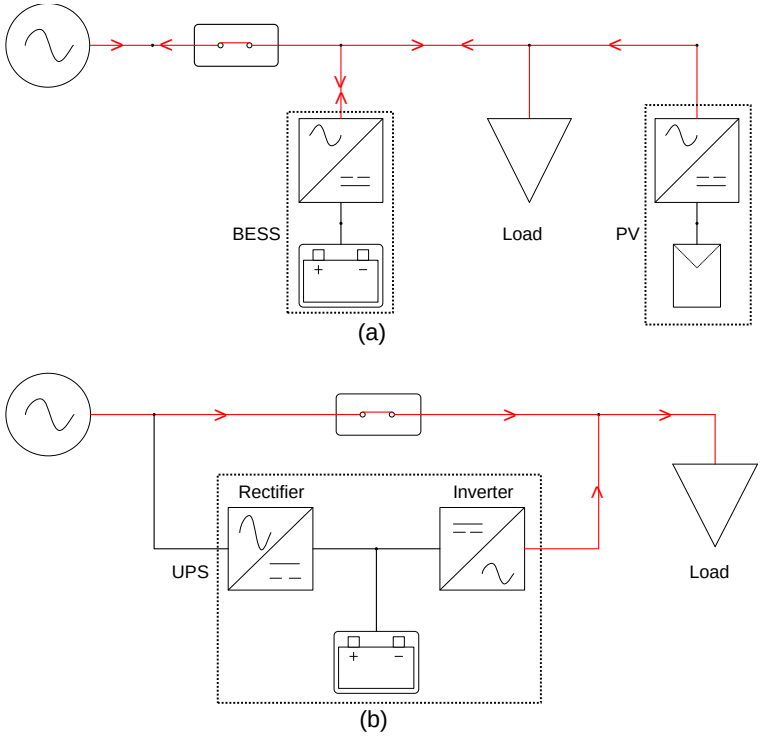

Figure 1.19: Different operation of (a) microgrid with BESS. (b) UPS in bypass mode

have been demanding higher resilience requirement for certain application over time. However, the latest technology of microgrid islanding function cannot ensure the preservation of critical

loads in the event of a fault in the utility grid (further referred as loss of grid). Examination of both solutions (UPS and microgrid) shows that they share the same approach and components i.e., the detection of grid disturbances leads to a switch-over to batteries.

In double conversion UPS systems, the normal "bypass" mode ensures that the load is primarily powered by the AC source through a static bypass switch. At the same time, the inverter can operate in parallel to inject current for power factor correction. However, when the UPS detects a disturbance or interruption in the AC source, the static switch opens, and the inverters take over by providing sinusoidal voltage waveforms directly to the output load. This ensures a continuous and uninterrupted power supply to the load.

These principles can be applied to microgrids equipped with BESS and static switches, which enable a smooth transition from grid-connected mode to islanding mode. However, there are a number of challenges that need to be addressed due to nature of microgrid that have source and loads, unlike the UPS that has only loads. Therefore, to enable smooth transition within the microgrid system by leveraging BESS, the following questions should be addressed:

Q-1 **How fast islanding transition should be done?**
When disruptions occur on utility side such as momentary interruption, or voltage sag, the operation of critical load may be impacted. Under such circumstances, it is imperative for microgrids to isolate from the main grid promptly to ensure a continuous power supply to these critical loads. Compared to classical solutions, as previously discussed, the minimal performance guaranteed by Class 3 UPS limits interruptions on the load side to last only 10ms. However, the adoption of 10 milliseconds as the threshold for transition necessitates careful consideration. This is because some DERs such as local sources have obligation imposed by the grid code [48], [49] to stay connected for certain duration during the fault, providing support to the upstream network. Firstly, this thesis delves into the permissible duration for seamless transitions that satisfies the needs of critical loads while maintain the compliance with the grid code.

Q-2 **How to assess the decision to island?**
Achieving microgrid islanding transition with such performance is challenging. Firstly, we need to reliably detect the grid problem in less than half electrical cycle. The conventional relay protection works classically with phasor measurement, thus needs a full cycle wave e.g. 16.67 or 20 ms for 60 Hz and 50 Hz systems, respectively. A downstream fault can create a voltage sag which leads to a false detection. Secondly, this thesis investigates the main technical challenges on how to detect the grid outage in order of milliseconds with a good precision for unplanned islanding decision.

Q-3 **How to disconnect the microgrid?**

Once a grid outage is detected, the microgrid needs to isolate itself from the main grid to supply critical loads locally. Conventionally, this is typically done using circuit breakers. However, the mechanical opening of circuit breakers takes around 50ms. For faster opening performance, power electronic based switch such as thyristor based static switch is used. The thyristor based static switch needs to wait until the zero-crossing current for tripping the circuit [50]. Which is why the opening of static switch in microgrid cannot be instant. However, if we are able to control this current, forcing it to zero, the opening will be faster. Moreover, in microgrid system, the operation of multiple DER during the transient must be investigated thoroughly thus grid code constrains is respected. Thirdly, thesis specifically address the control of whole microgrid system during transient.

Q-4 **How to establish DER seamless operation?**
After the fault isolation, the microgrid needs to establish its own voltage and frequency references to operate independently. Thus, the DER capable of being grid forming such as BESS need to change its operation from grid connected to islanded mode. The seamless transition between grid connected and island modes had been achieved in several academic research [51] [52]. By using static switch (STS), some research teams shown promising results with transfer time with less than one fundamental electric cycle. However, the proposed solutions face several challenges in real life. During grid faults, the voltage at PCC will be brought down by the grid, creating inverter current overload during transient. Consequently, the inverter control needs to be able to compensate the disturbance for local loads supply. Lastly, thesis focuses on improving the dynamics of BESS during transition due to grid fault.

1.6 Principals scientific contributions

We have listed some of the principal contributions in this work. More detailed contributions will be further elaborated in each chapter.

C-1 An analysis of the requirements and definitions of seamless operation in microgrid.

C-2 A methodology to analyze and isolate the microgrid from the upstream disturbance.
- Evaluation of existing fast method for upstream disturbance detection
- Proposition of a novel detection method

C-3 A development of energy storage's inverter controls to reduce the microgrid restoration time to only few milliseconds.

C-4 An advanced microgrid control sequence operation method that ensure load uptime while respecting low voltage ride through requirements from grid codes.

C-5 The validation of the proposed concept using power hardware in the loop and small-scale mockup

C-6 A modeling framework for hardware in the loop in order to facilitate the power electronics integration within microgrid ecosystems.

Please note that this research is an industrial PhD conducted in collaboration between Schneider Electric, the University of Grenoble Alpes, and the laboratory G2Elab under CIFRE 2020/1494. As such, a significant portion of the work presented in this manuscript is aligned with the objectives set forth by Schneider Electric. It is important to highlight that there are no known competing monetary interests or personal relationships that could have potentially influenced the results reported in this thesis. The research is conducted with integrity and impartiality to ensure the credibility and reliability of the findings.

1.7 Publication and Patent

The described contributions have led to four conference publications and submitted patents, listed below: Conference proceedings:

- *S. Kamajaya*, J. Buire, R. Caire, S. Bacha, and J. Wild, "Microgrid Control Strategy to Achieve Seamless Transition from Grid Connected to Islanded Mode," in 27th International Conference on Electricity Distribution CIRED 2023, 2023. [53]
- *S. Kamajaya*, J. Buire, R. Caire, S. Bacha, and J. Wild, "P-HIL Validation for Double Loop Proportional Resonant Control in ABC Stationary Frame for Grid Forming Inverter," in 2023 IEEE PES Innovative Smart Grid Technologies Conference Europe (ISGT-Europe), 2023. [54]
- *S. Kamajaya*, A. Moulichon, F. Aubert, and J. Wild, "Ensuring Reliable Microgrid Solutions: Hardware-in-the-Loop (HIL) Modeling and Validation Processes for Testing and Commissioning," in 2023 IEEE PES Innovative Smart Grid Technologies Conference Europe (ISGT-Europe), 2023. [55]
- J. Wild, *S. Kamajaya*, F. Cazals, and A. Moulichon, "Power Hardware in The Loop and Standardization for The Growing Microgrid Industry," in 2023 IEEE PES Innovative Smart Grid Technologies Conference Europe (ISGT-Europe), 2023. [56]

Patents:

- *S. Kamajaya*, J. Buire, R. Caire, S. Bacha, and J. Wild, "Method for protecting a microgrid from a voltage drop or sag occurring in a main grid connected to said microgrid". EP 23306594.5, Filing date: 25.09.2023
- *S. Kamajaya*, J. Buire, R. Caire, S. Bacha, and J. Wild. "Method for controlling a microgrid" EP 23306592.9, Filing date: 25.09.2023

1.8 Organization of the Thesis

This thesis is organized into five chapters.

This chapter provides a comprehensive literature review to establish a broader context for this thesis. This chapter focuses on the characteristics of low voltage microgrids. It delves into the various types of DERs, loads, and conventional power outage solutions.

Chapter 2 presents a strategy for islanding in response to grid disturbances , which will be employed throughout the remainder of this manuscript. This strategy requires rapid detection of grid loss to effectively isolate local loads from grid loss or disturbances.

Chapter 3 deals with the design of the control of inverters in grid following and grid forming modes. Two seamless transfer strategies are also presented, taking into account the performance and technical limits of the microgrids.

Chapter 4 provides the experimental results of the proposed methodology. It includes the development and validation of a prototype for a fast grid loss detection strategy, followed by a full system test performance during unplanned islanding scenarios.

Chapter 5 offers conclusions and perspectives, summarizing the findings and suggesting avenues for future research.

1.9 Conclusion

This chapter discusses the role of microgrids as catalysts for integrating renewable energy into the transition to sustainable energy. The use of DER in buildings, particularly for self-consumption purposes, requires the incorporation of energy storage systems. Energy storage systems enable buildings to optimize their energy usage, balance supply and demand. Additionally, this energy storage can be used to enhancing the resilience of the building's electricity supply. By storing excess energy generated by DER, it can ensure a continuous and reliable power supply, even during times of grid outages.

The current state-of-the-art DER technology helps us identify areas that can be improved. Furthermore, knowing the electrical load characteristics within buildings helps us design and enhance microgrid operation. The microgrid controller ensures that DER works in harmony while prioritizing the safety of the power supply. By optimally integrating these components, we can create a robust microgrid system that maximizes DER benefits and ensures a stable and secure power supply.

Trends in distributed energy storages offers a horizon of research, particularly improving

the availability of power supply. The main limitation of the previous studies is the lack of strategies for microgrid resiliency using local DER and they are not discussed from the viewpoint of whole microgrid systems. This manuscript aims to address these gaps by emphasizing the extended usage of battery energy storage as an uninterrupted power supply solution.

In Chapter 2, a strategy for islanding in response to grid disturbances is presented, which will be employed throughout the remainder of this manuscript. This strategy necessitates fast grid disturbance detection to effectively isolate local loads from grid disturbances. Finally, a prototype implementing this strategy is evaluated through laboratory experiments.

Chapter 2

Islanding Decision on Grid Disturbance

Contents

2.1 Introduction

The stability and reliability of power systems are critical aspect in modern electrical infrastructure, impacting everything from commercial and industrial applications to residential power usage. This chapter presents an in-depth exploration of microgrid islanding decision-making in the context of grid disturbances, with a particular focus on the development and implementation of a novel method for fast grid outage detection.

The discussion is focused on several key elements: the impact of power supply on loads, the variety of power issues encountered, the concept and requirements of microgrid seamless transition, the current state of grid outage detection technology, and the detail of our proposed loss of main detection method.

At the forefront of this discussion is the impact of power supply on various loads. Power supply problem encompass a wide range of disturbances, from voltage fluctuations to frequency instabilities, which can lead to malfunctions or stop of electrical equipment. Poor power quality not only leads to equipment inefficiency and damage but also contributes to financial losses and safety hazards. This aspect is crucial in the context of grid disturbances, as it sets the stage for understanding the necessity and urgency of effective islanding decisions. The variety of power quality issues encompasses a wide range of phenomena, including voltage sags, interruptions, harmonics, frequency variations, and transients.

The concept of microgrid seamless transition is central to this discussion. It refers to the ability of a microgrid to detect grid disturbances and autonomously transition from grid-connected to islanded mode without impacting too much the supply of the connected loads or at least their proper functioning. This transition is critical for maintaining power stability and reliability, especially in critical applications. The seamless transition requires advanced detection mechanisms, fast decision-making processes, and robust control systems to ensure minimal impact on the load during grid disturbances.

Current approaches to grid outage detection involves various methodologies and technologies such as conventional under voltage relays [57], advanced algorithms employing artificial intelligence, and machine learning [58]. However, there remain limitations in terms of detection speed, accuracy, and the ability to effectively distinguish between different types of disturbances, which are crucial for effective microgrid islanding.

Addressing these challenges, this chapter introduces a novel method for fast grid outage detection, specifically tailored to facilitate microgrid seamless transition. This method leverages signal processing techniques offering a significant improvement in terms of speed and reliability. This method is designed to quickly and accurately identify grid disturbances, enabling timely and precise islanding decisions, and thus enhancing the overall resilience and efficiency of power systems.

2.2 Power quality problems

Today's electronic equipment requires a power supply that is free of interruption or disturbance. This is particularly relevant in the context of modern industrial and information technology infrastructures, where the reliability and stability of the power supply is vital.

Ideally, power supply should produce a sine wave oscillating at frequencies of either 50 or 60 Hz. Power quality disturbances are defined as any alterations in power attributes, including voltage, current, or frequency, that negatively impact the normal operation of electrical equipment. Such disturbances, for example, voltage sags and brief interruptions, can significantly and adversely affect sensitive electronic devices. Many power issues occur within the commercial power grid, which is vulnerable to both external factors, including weather conditions (hurricanes, lightning, snow, ice, and floods), construction activities (digging), and tree interference, as well as internal factors like equipment malfunctions, inrush current, and switching.

The power quality impacts are strongly interconnected with electromagnetic phenomena[59]. To address this, standards such as IEEE 1159[1] and IEC TR 61000-2-5[2] have provided classification for them. The purpose behind categorizing electromagnetic phenomena is to identify the appropriate solutions for specific power quality issues, depending on the nature and magnitude of the variation. In this thesis, we will adopt a similar classification approach as presented in [60], categorizing the phenomena into two main groups based on their occurrence:

Steady-state Variations refer to the small deviations in voltage or current characteristics from their nominal or ideal values. These variations are disturbances that can be measured at any given moment. All of these characteristics can be quantified, and limits for the variations can be developed. The following phenomena fall under this category:

1. Waveform distortion
2. Unbalanced

Events refer to larger deviations that occur occasionally, at random intervals often caused by aforementioned factors such as weather conditions. These disturbances are characterized by a distinct start and end, usually indicated by a threshold crossing. The following phenomena fall under this category:

3. Transient
4. Sag
5. Interruption
6. Voltage swell

The characteristic of each disturbance, their causes, and their implication on various types of electronic equipment is provided in Appendix B. Table 2.1 summarize the power quality issue characteristics and their possible solution.

Variations based power quality problem always exist in the commercial power grid supply.

[1]IEEE Recommended Practice for Monitoring Electric Power Quality

[2]Electromagnetic compatibility (EMC) – Part 2-5: Environment – Description and classification of electromagnetic environments

Table 2.1: Summary of power quality issues and their solution [59], [61]

Disturbance Category			Typical Magnitude	Typical Duration	Possible Solution
Event based	1	Transient		0.1 – 100 µs	TVSS
	2	Voltage dip	0.1 – 0.8 pu	0.5 cycles – 3 s	- power conditioner - UPS - this thesis
	3	Interruption	<0.1 pu	> 0.5 cycles	- power conditioner - UPS - this thesis
	4	Voltage swell	1.1 – 1.4 pu	0.5 cycles – 3 s	- power conditioner - UPS
Steady state variations	5	waveform distortion		steady state	mostly mitigated at design stage to comply with the standards
		- dc offset	0 – 0.1%		
		- harmonics	0 – 20 %		
		- voltage fluctuation	0.1 – 7%		
	6	Imbalance	0.03 pu	steady state	

This mostly mitigated at design stage and is covered by the public distribution standards such as EN 50160[3]. Meanwhile, electrical loads are mostly compliance to the (Electro-Magnetic Compatibility) EMC standards, thus limiting the variations. Some standards define the limits for public power supply network, as summarized in Table 2.2. Therefore, in this thesis we will not seek a solution for this issue, but rather considered it as a constraint. Our focus is on extending the use case of BESS to provide an alternative solution for voltage sag and interruptions.

Table 2.2: Low Voltage Network Supply Characteristics [62]–[64]

Parameter	**Standards**				
	IEC 61000-2-4[a]			**IEC 61000-2-2**[b]	**EN50160**[c]
	class 1	**class 2**	**class 3**		
Voltage Deviation	8%	10%	5.00%	-	10%
Frequency					
grid connected	± 1 Hz	± 1 Hz	± 1 Hz	± 1 Hz	± 1 Hz
isolated network	± 2 Hz	± 2 Hz	± 2 Hz	-	± 4Hz
temporary deviation	to be agreed			-	-
Voltage Unbalance (U^-/U^+)	2%	2%	3%	2%	2%
THD	5%	8%	10%	8%	8%
Harmonics (%)					
odd					
5	3	6	8	6	6
7	3	5	7	5	5

[3]Voltage characteristics of electricity supplied by public electricity networks

11	3	3.5	5	3.5	3.5
13	3	3	4.5	3	3
17	2	2	4	2	2
$17 < h \leq 49$	A[e]	A[e]	B[e]	A[e]	1.5[f]
multiple of 3					
3	3	5	6	5	5
9	1.5	1.5	2.5	1.5	1.5
15	0.3	0.4	2	0.4	0.5
21	2	0.3	1.75	0.3	0.5
$21 < h \leq 45$	0.2	0.2	1	0.2	
even					
2	2	2	3	2	2
4	1	1	1.5	1	1
6	0.5	0.5	1	0.5	0.5
8	0.5	0.5	1	0.5	0.5
10	0.5	0.5	1	0.5	0.5
$10 < h \leq 50$	C[e]	C[e]	1	D[e]	0.5[f]

[a] Compatibility levels in industrial plants for low frequency conducted disturbances

[b] Compatibility levels for low frequency conducted disturbances and signaling in public low-voltage power supply system

[c] Voltage characteristics of electricity supplied by public electricity networks

[d] +10% to -15% deviation is allowed for no more than 60 seconds

[e] limits is calculated by A:$2.27 \times (17/h) - 0.27$; B: $4.5 \times (17/h) - 0.5$; C: $0.52 \times (10/h) + 0.25$; D: $0.25 \times (10/h) + 0.25$

[f] no values are given for harmonics higher than 25

2.2.1 Voltage Dip and Interruption

Voltage dip, also known as voltage sag, is sudden drop in the rated voltage. It is characterized by its duration and magnitude. The magnitude is measured by its rms value, calculated in

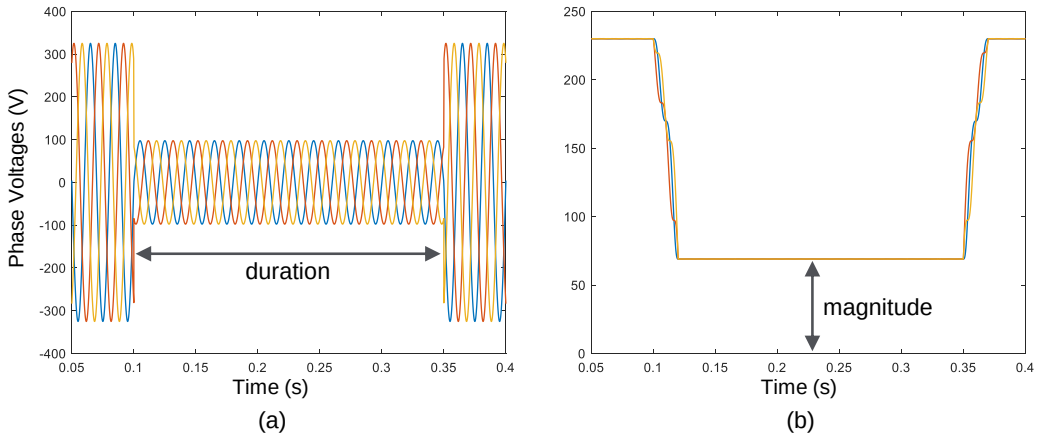

Figure 2.1: Illustration of (a) three phase voltage dip and (b) its computed rms value

moving window of one cycle duration or half cycle duration.

IEEE Standard 1159 classify the voltage dip and interruption by its magnitude as shown in Table 2.3. Normally voltage dip magnitudes are expressed as residual voltage during the disturbance in per unit.

Table 2.3: Voltage dip and interruption classification [59]

Events	RMS Voltage	Duration
Interruptions		
Momentary interruptions	<0.1 pu	0.5 cycles–3 s
Temporary interruptions	<0.1 pu	3 s–1 min
Sustained interruptions	<0.1 pu	>1 min
Voltage Dips		
Instantaneous voltage sags	0.1 pu–0.9 pu	0.5–30 cycles
Momentary voltage sags	0.1 pu–0.9 pu	30 cycles–3 s
Temporary voltage sags	0.1 pu–0.9 pu	3 s–1 min

Magnitude and Phase Angle

Voltage sags occur due to various reasons such as faults, starting of large motors, or transformers energizing. Minor voltage sags can occur because of starting large motors and energizing transformers. However, most severe voltage sags are the result of electrical faults on power systems[65], [66]. Voltage dip due to short circuit and earth faults are the cause of the vast majority of equipment problems [60]. The voltage dip magnitude is defined by the residual voltage during the dip occurs. The magnitude of voltage dip can be calculated using simple voltage divider circuit.

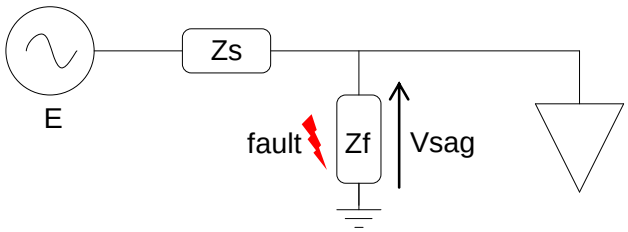

Figure 2.2: Simplified radial network voltage divider

Figure 2.2 shows radial network with faulted feeders. The voltage dip at PCC, while being able to neglect the load current, can be calculated using Equation 2.1 where E, Zs, Zf are magnitude of the voltage source, source impedance, and impedance of faulted branch respectively.

$$\overline{V}_{sag} = \frac{\overline{Z}_f}{\overline{Z}_s + \overline{Z}_f} \tag{2.1}$$

Moreover, the faulted path can create phase angle jump due to the sudden change of impedance. Supposed $Zf = Rf + jXf$ and $Zs = Rs + jXs$, the phase angle jump in the voltage can be calculated from:

$$\Delta\phi = \arg\left(V_{sag}\right) = \arctan\left(\frac{X_f}{R_f}\right) - \arctan\left(\frac{X_f + Xs}{R_f + R_s}\right) \tag{2.2}$$

Duration

The duration of a voltage dip is typically measured from the point at which the voltage drops below the threshold to the point at which it returns to a normal level. The threshold is often defined as a percentage of the nominal voltage value, using the same previously mentioned definition is 90%.

The duration of a voltage dip can vary depending on the cause of the event. It can range from a few milliseconds to several seconds or even minutes. Voltage dip caused by faults near to the load can be cleared with miniature circuit breaker (MCB) in less than 20ms. Faults in the transmission system is typically cleared within two to three cycles, while on the sub-transmission system, faults are cleared within three to six cycles. Some protective relay schemes can take as long as 20 cycles to clear the fault. Voltage dips caused by starting large motor typically last from a fraction of a second to a few seconds. The same also applies to the inrush of transformers.

Voltage Dip Type

For three phase system, there are several various types of voltage dip that can occurs depending on which phase that is affected. To classify voltage dip, ABC classification is the oldest classification and the one most commonly used [67], [68]. It categorized the voltage dip into seven types from A to G. However, in this thesis we would like to use the classification from IEEE 1668 Standard[4][65] as it is simpler to understand. This standard adopts CIGRE voltage dip immunity working group[69] classify the three general types of voltage dip that may occur at the terminals of load:

Type I drop voltage that takes place mainly in one of the phase-to-ground voltages. However, due to propagation the other two phase can be slightly affected

Type II drop voltage magnitude in one of the phase-to-phase voltages

Type III drop voltage magnitude that is equal for three voltages.

The characteristic of voltage dip change through propagation of the networks i.e., transformers windings connections. A single line-to-ground fault on the primary side of a distribution

[4]Recommended Practice for Voltage Sag and Short Interruption Ride Through Testing for End-Use Electrical Equipment Rated Less than 1000 V [65]

Table 2.4: Different voltage dip type and its characteristics. author reproduction from [69]

Dip Type	Vector Diagram	Waveform
Type I	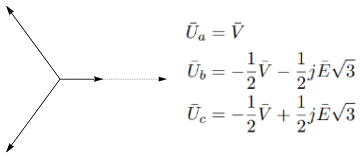 $\bar{U}_a = \bar{V}$ $\bar{U}_b = -\frac{1}{2}\bar{V} - \frac{1}{2}j\bar{E}\sqrt{3}$ $\bar{U}_c = -\frac{1}{2}\bar{V} + \frac{1}{2}j\bar{E}\sqrt{3}$	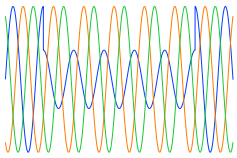
Type II	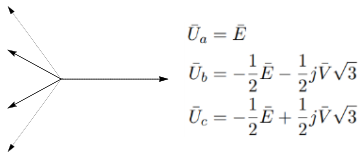 $\bar{U}_a = \bar{E}$ $\bar{U}_b = -\frac{1}{2}\bar{E} - \frac{1}{2}j\bar{V}\sqrt{3}$ $\bar{U}_c = -\frac{1}{2}\bar{E} + \frac{1}{2}j\bar{V}\sqrt{3}$	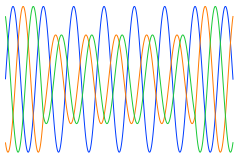
Type III	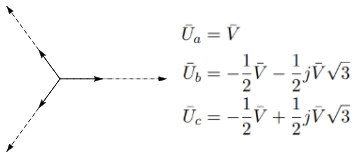 $\bar{U}_a = \bar{V}$ $\bar{U}_b = -\frac{1}{2}\bar{V} - \frac{1}{2}j\bar{V}\sqrt{3}$ $\bar{U}_c = -\frac{1}{2}\bar{V} + \frac{1}{2}j\bar{V}\sqrt{3}$	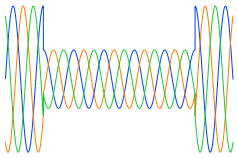

V = Residual voltage. E = Pre-event voltage. Ua,Ub,Uc = Phase to neutral voltages

transformer will result in a voltage dip to no lower than 33% of normal voltage on any phase on the secondary side if the zero-sequence current is not propagating [66].

Furthermore, precedent study [69] gather voltage dip data for all around the world. Just counting the number of events, without any percentile classification, an overall view of type I, II and III dips is obtained, as shown in Table 2.5. It shows on the LV network, almost two thirds of dip occurrence are single phase dip.

Table 2.5: Overall distribution on voltage dip type [69]

Networks	Type		
	I	II	III
MV & HV	27%	53%	20%
LV	64%	25%	11%

2.3 Defining a *seamless* transition

Microgrid seamless transition is a vague term to express the microgrid islanding transition as fast as possible. However, there is no clear performance indicator on how fast it should be, neither the characteristic on the voltage. This definition, currently only appear at IEEE

2030.7[5] and IEEE 2030.8[6] standards. As per this standard, the seamless transition is defined as "The connection and disconnection of a microgrid to and from the larger grid accomplished without voltage and frequency transients that exceed the specifications of the microgrid design and the interconnection requirements."[45], [70] Now the question is: what should be the microgrid specifications for this voltage and frequency transient?

Before addressing that question, it is unfortunate that many microgrid practitioner interpret this term as ensuring the uninterrupted transfer of power during the transition, meaning ensuring the continuity of operation for electrical equipment. If the objective is to provide the continuity of power for the site, the microgrid shall islanded as soon as possible during grid disturbance. However, this approach leads to several issues:

- DER must stay connected during short time, known as ride-through requirements.
- Electrical appliance will probably stop during this ride through duration. Thus, how long the electrical loads can sustain a voltage dip or interruptions?
- How to distinguish the disturbance from the upstream (grid side) or downstream (load side)? If false islanding occurs due to downstream disturbance, the inverter-based generator will not be able to provide sufficient short circuit current for the breaker to trip, potentially leading to a blackout of the site.

In this section we will delve to those question to define the specification of seamless transition.

2.3.1 How long electrical load can sustain voltage dip or interruption ?

In general, a voltage drop cause a reduction of power transfer to the electrical loads. Different types of equipment handle these drops differently. For example, some electronic devices are very sensitive to changes in voltage magnitude. Even a short interruption can cause them problems. On the other hand, things like heaters and incandescent lights are more tolerant of voltage changes. They can keep working even when the voltage drops briefly. This ability to keep working during voltage drops is known as *ride-through* capability.

The severity of voltage dips and short interruptions depends not only on the direct impact they have on the equipment, but also on how critical the function of the equipment is. For instance, manufacturing processes rely on the integrated operation of multiple devices. A single device's malfunction or disconnection, triggered by a voltage dip or short interruption, can necessitate halting the entire production process [69]. This interruption can lead to significant product loss and potential damage of the equipment, representing one of the most severe and costly consequences of voltage fluctuations.

[5]IEEE Standard for the Specification of Microgrid Controllers
[6]IEEE Standard for the Testing of Microgrid Controllers

In this section, we synthesize equipment responses to short interruption, drawing from existing literature. We remove the magnitude variable of the voltage dip because at worst case scenario during the transition, there will be no residual voltage. Therefore, we would like to know the maximum time of seamless transition which loads tolerates. The discussion encompasses a variety of equipment including computers, lightning, adjustable speed drives (ASD), contactors, and programmable logic controllers (PLC), It is important to note that responses vary among manufacturers, influenced by differing technologies and algorithms. Therefore, the discussion is maintained at a generic level. To close, we examine existing standards concerning equipment ride-through capabilities in the context of voltage sags and interruptions.

2.3.1.1 Literature review

- **Computers**
  Computers typically has dc power supply integrated to provides power to computer systems such as motherboards, central processing unit (CPU), memory, and hard disk. The immunity of computers is significant for the power supply modules. Losing power causes loss of data and process, which means it requires time to restart the computer to a previous state. The Information Technology Industry Council (ITIC) curve, previously

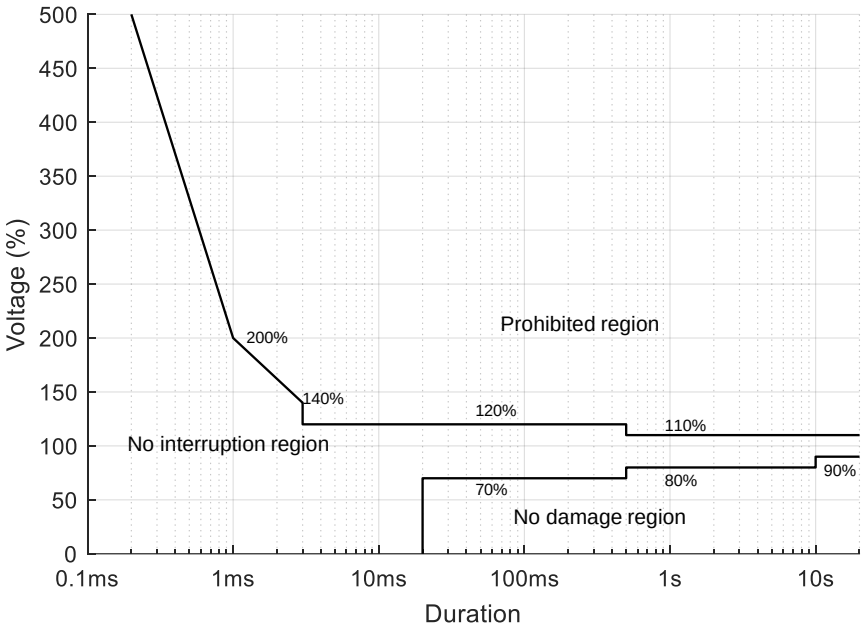

Figure 2.3: ITIC Curve [71]

known as the Computer & Business Equipment Manufacturer's Association (CBEMA) curve before 2000, establishes the minimum voltage immunity widely adopted for IT

applications. However, it is important to note that the ITIC curve specifically applies to IT equipment operating at 120V and 60Hz. As reported in [72], most computers satisfied the ITIC recommendation, some of them are capable to ride through 200 ms interruption.

- **Programmable Logic Controllers (PLCs)**
  Programmable logic controllers (PLCs) are used for automation and control process. In building application, for example it is used for building management systems such as HVAC. Typically, PLC consists of central processing unit (CPU) and input/output modules. Unlike computers, a dedicated power supply is used to supply the PLC system. Table 2.6 shows short interruption duration immunity for some industrial power supply reference. In practice, the power supply can be coupled with a battery module to solve this problem.

Table 2.6: Industrial Power Supply Immunity on Short Interruption

Reference	Application	Rated Power	Short Interruption Immunity
ABL7RM	commercial, residential	30 W	>10 ms
ABL7RP	industrial, commercial	60 - 240 W	>20 ms
ABL7UES	industrial	120 to 960 W	8 - 13 ms

- **Lightning**
  LED and fluorescent lamps are widely used to its efficiency. Fluorescent is one of gas-discharge lamps technology which are very sensitive to voltage dip. Gas-discharge lamps, immune to 0.5 to 1 cycle interruption [72]. When the light is extinguished, the ballast requires more time to restrike, which often mistaken as a longer outage [66]. Low-wattage LED lamps have been found to be capable of withstanding 2 – 6 cycles of interruption [73]. However, another test for high-wattage LED lamps used for street lighting reported in [74] revealed that approximately one-third of samples experienced complete shutdown when subjected to a 0.5 cycle interruption. These lamps required more than one second to restart. It is worth noting that the remaining two-thirds of the samples did not show any adverse effects even when subjected to a single cycle interruption.

- **Adjustable Speed Drives (ASD)**
  An Adjustable Speed Drive (ASD), also known as a variable speed drive, is a device that regulates the speed of a motor. It consists of two main components: a rectifier and inverters. The rectifier charges the DC bus capacitor, which acts as an energy buffer and filters out ripples in the power supply. The inverters convert the DC voltage into controllable AC voltage and frequency that are suitable for the motor's operation. The ability of an ASD to withstand voltage dips or interruptions depends on the DC capacitor size, type of voltage dip and the rated load of the drive [69] [75]. In the worst-

case scenario of a three-phase balanced voltage interruption, some ASDs may trip after only 5ms, while others remain immune for up to 20ms, as reported in [76].

- **Contactors**
  Contactors and relays are used to power and control loads. After a supply interruption, a motor contactor may also act as a safety device, to prevent the uncontrolled restarting of the motor. The contactors work by applying voltage on coil to close the contacts. In certain voltage drop, the magnetic force on the coil is not sufficient to maintain the contact, being a weak point on the systems [72]

  The voltage operating limit of contactors is 85% to 100% of rated voltage as defined in IEC 60947-4-1[77]. However, there is no specified time duration to determine when this limit should apply. The test carried out by [72] reveals that most contactors trips when exposed to a 50% dip lasting only one cycle. Furthermore, the sensitivity of ac contactors is different for point of wave of the voltage dip or short interruption [78]. The experiment conducted in [69] test multiple contactors for different manufacturers. The results shows that the most sensitive contactors withstand only 10 ms interruption where the least sensitive contactors can withstand up to 80 ms interruption.

Table 2.7 summarize the immunity of different equipment that has been reported in literature. At this stage, we cannot draw the conclusion yet on the maximum immunity time.

Table 2.7: Industrial Power Supply Immunity on Short Interruption

Equipment	**Immunity duration**	
	most sensitive	**least sensitive**
Personal Computer	10 ms	200 ms
Adjustable Speed Drive	5 ms[a]	20 ms
Lightning (HID)	10 ms	20 ms
Lightning (LED)	0 ms[b]	120 ms
PLC	8 ms	20 ms [c]
Contactor	10 ms	80 ms

[a] Three phase balanced interruption
[b] Fail on 0.5 cycle interruption test
[c] Industrial power supply without battery

2.3.1.2 Standards on short interruption immunity

Standards organization have produced some standards regarding testing and requirement for voltage dip or short interruption ride through. IEC 61000-4-11 and IEC 61000-4-34 specify testing methods for voltage dips and interruptions in equipment. The primary difference between these standards lies in their coverage of equipment based on input current levels. IEC 61000-4-11 applies to equipment with input currents up to 16A, while IEC 61000-4-34 applies to equipment with input currents exceeding 16A. These standards are part of

the electromagnetic compatibility series, which categorizes electromagnetic environments into different classes, as described below:

- **Class 1**: This class defines the most stringent compatibility requirements, primarily intended for equipment that is highly sensitive to disturbances. Typically, this class is secured by Uninterruptible Power Supplies (UPS).
- **Class 2**: The compatibility levels in this class are generally aligned with those of public networks.
- **Class 3**: This class represents a more relaxed compatibility standard, typically applicable to in-plant points of coupling within industrial environments.

Thus, the immunity requirements vary on each equipment depending on where this equipment will be installed. Additionally, the pass/fail criteria are determined by another related standards, which typically specific to the type of equipment.

Table 2.8: Related standards on LV equipment interruption immunity

Standards	Equipment / application	Immunity test requirements
IEC EN 61000-6-1	Residential, commercial, light-industrial	1 cycle
IEC EN 61000-6-2	Industrial	1 cycle[a]
IEC EN 61000-6-5	Power station and substations	50 cycles and 5 cycles
IEC EN 61000-6-7	Industrial safety related systems	2 seconds
CISPR 35 / EN 55020	Multimedia equipment	0.5 cycle
CISPR 24 / EN 55024	Information technology equipment	0.5 cycle

[a] loss of function are acceptable for some electronic power converter

The Table 2.8 summarizes the duration of short interruption immunity for each standard. The immunity requirements shown in this table are for performance criterion B or higher, indicating that the equipment is capable of withstanding interruptions without changing its operating state. However, some degradation of performance is allowed during the test.

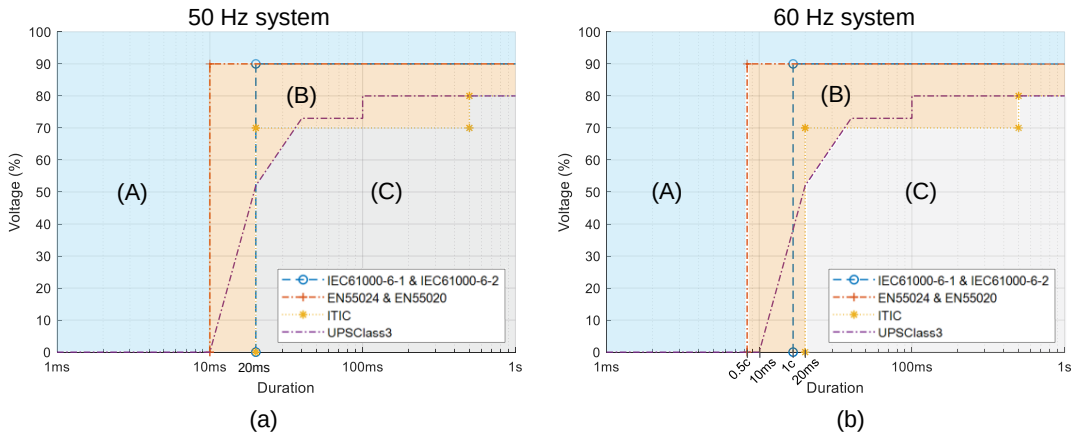

Figure 2.4: Different voltage curve immunity for (a) 50 Hz and (b) 60 Hz systems

Figure 2.4 illustrates the overlay of immunity requirements, as specified by European standards, alongside the well-known ITIC and UPS class 3 performance curve. This figure consists of three distinct regions: region (A) represents the area where equipment immunity is guaranteed by all standards or voltage curves; region (C) indicates the area where equipment immunity is not assured by all standards; region (B), the immunity of equipment is subject to debate, as it is not covered by the harmonized standards. In this perspective, the 20ms immunity duration from ITIC is deemed insufficient to meet the necessary requirements.

2.3.2 Proposed seamless performance

Based on the information provided in the previous subsections, we can conclude that it is necessary to consider a maximum interruption time of 0.5 cycles. This duration will help ensure the security of most critical equipment during the transition.

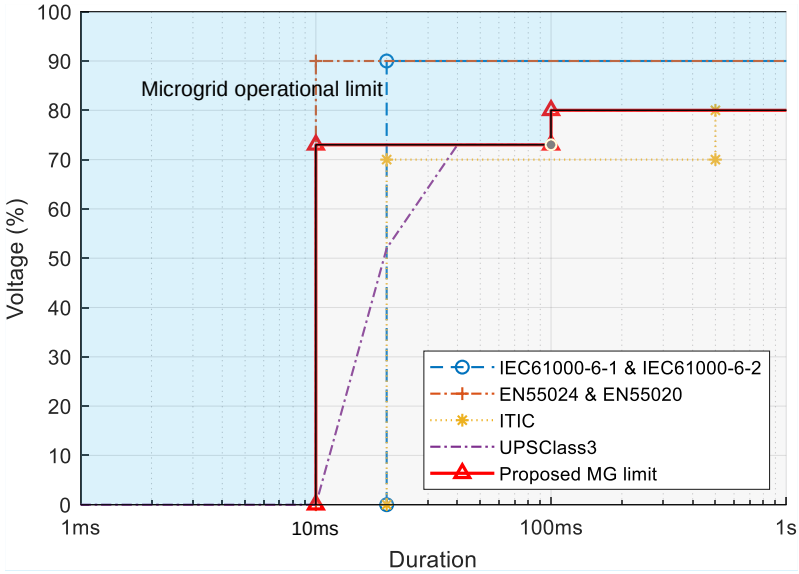

Figure 2.5: Microgrid's critical load operational limit

This requirement present a significant challenge. It means to perform seamless transition due to grid disturbance or grid loss, all three transition steps: detection, disconnection, and voltage restoration be completed within 0.5 cycles or 10ms in 50 Hz systems as illustrated in Figure 2.6. For simplicity, we will consider only 50 Hz ac systems throughout this thesis.

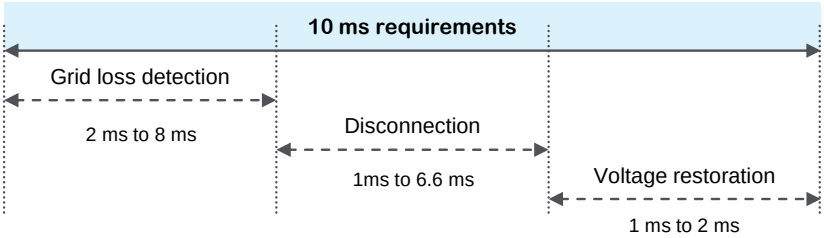

Figure 2.6: Microgrid seamless transition phase

Voltage restoration

Following the disconnection, the DERs change its mode from grid following to grid forming to restore the microgrid voltage. The recovery speed of this voltage is related to the voltage control bandwidth of the inverter. As many PCS manufacturer use 20kHz switching frequency, a 1 ms to 2 ms of voltage control loop bandwidth is theoretically achievable. However, the inverters need also to maintain the control stability while respecting some constraints. Chapter 3 details the inverter control design to achieve the maximum voltage restoration performance.

Disconnection

The disconnection time, however, varies with switch technology, as shown in Table 2.9.

Table 2.9: Low voltage interruption switch technology

Type	Interruption time (min – max)	Maturity level
Mechanical circuit breaker	20 ms - 50 ms	Industrialized
Thyrisytor based static switch	4 ms - 10 ms	Industrialized
IGBT based static switch	7 us - 0.1 ms	Project based
Hybrid circuit breaker	0.1 ms - 2 ms	Research

[a] loss of function are acceptable for electronic power converter

Electromechanical breakers typically take about 50 ms to open. For shorter interruption time, solid-state switch technology is used. The most common technology for this application is thyristor based[79]–[81]. Thyristor only able to turn off the circuit only when the current commutates to zero, leading to a maximum natural disconnection time of 6.6 ms in a three-phase system without a neutral connection. Indeed, because the last phase will naturally open after the two other phases are disconnected. Another technology is IGBT-based static switch that has the capability to interrupt in few microseconds [82]. However, IGBT is costly, have inferior performance in withstanding overload currents and have higher conducting losses. Thus, hybrid switch technology is developed, it is able to interrupt the current in less few milliseconds and have much lower conducting losses [82]–[84]. Despite these advancements, hybrid and IGBT based switches are not yet widely industrialized for LV AC application, making thyristor-based static switches the most feasible option currently. It is worth noting, however, that the hybrid switches are been used for HV/MV DC application.

Loss of main detection

Therefore, considering the maximum opening time of the static switch, the time required to decide on islanding is approximately 2 to 3 ms. Figure 2.7 synthesis in purple the detection area requirement and the voltage boundaries for microgrid to ensure the critical loads operation.

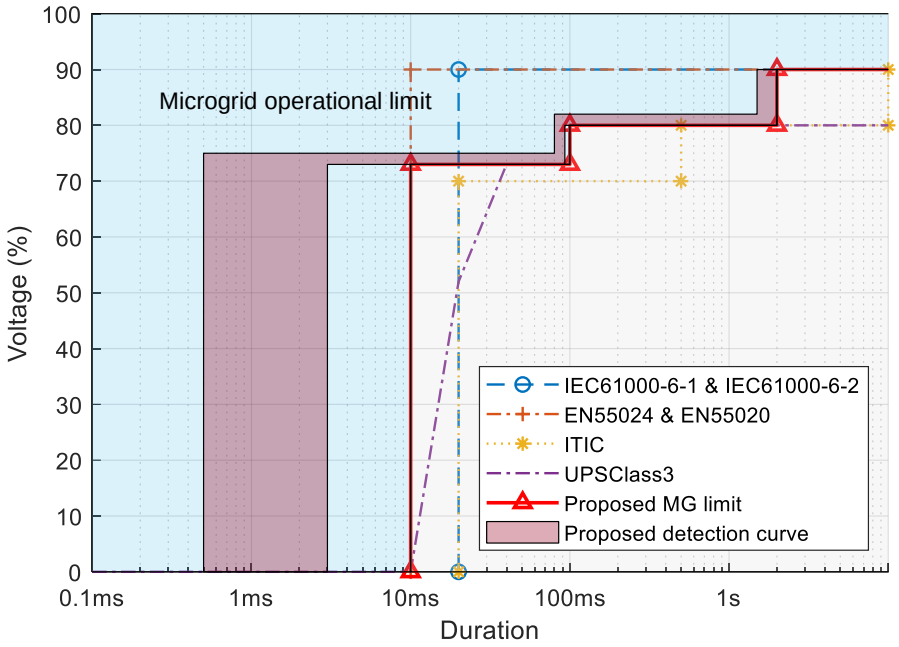

Figure 2.7: Microgrid voltage tolerance and proposed detection curve

2.4 Complying with ride through requirements

2.4.1 DER ride through requirements

Generators that connected to the grid, including inverter-based generator, are required to meet the fault ride through (FRT) requirements as defined by the grid code. FRT is required so that

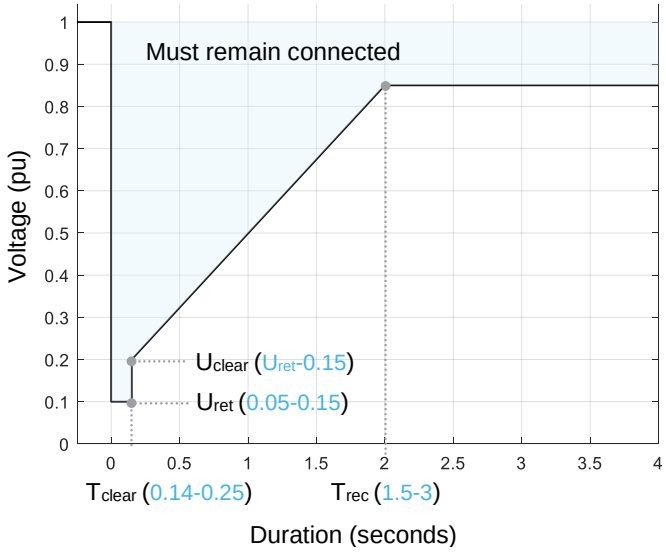

Figure 2.8: Fault Ride Through Requirement Capability (EU)2016/631

after the fault are cleared, not all generators are disconnected from the grid, leaving the grid with important unbalanced between consumption and production. For example, Figure 2.8 shows Fault Ride-Through (FRT) curve in accordance with European Union Regulation (EU) 2016/631 [49]. The values indicated inside the bracket are the minimum and maximum value of the settings respectively.

Although currently this requirement is not mandatory for PV generation under 1 MW, there is no technical reason to exclude smaller DER in the near future. This is particularly relevant as more small-scale PV rooftop system are connected to the distribution grid. For instance, in US, the FRT is mandated for small systems by Rule 21.

2.4.2 Proposed microgrid seamless architecture

Unfortunately, the DER ride through requirement is not compatible with the 10 ms seamless requirements that we proposed. In one hand, the DERs within the microgrid must ride through during the fault, supporting the grid for at least 140 ms. In the other hand, the critical loads must be isolated from the fault in less than 10 ms. Practically, the ride-through requirement can be waived by the utility company if some conditions are met (for example not exporting more than 10% of the subscribed power). This allow the microgrid to perform seamless transition. The traditional microgrid electrical topology must then be modified to

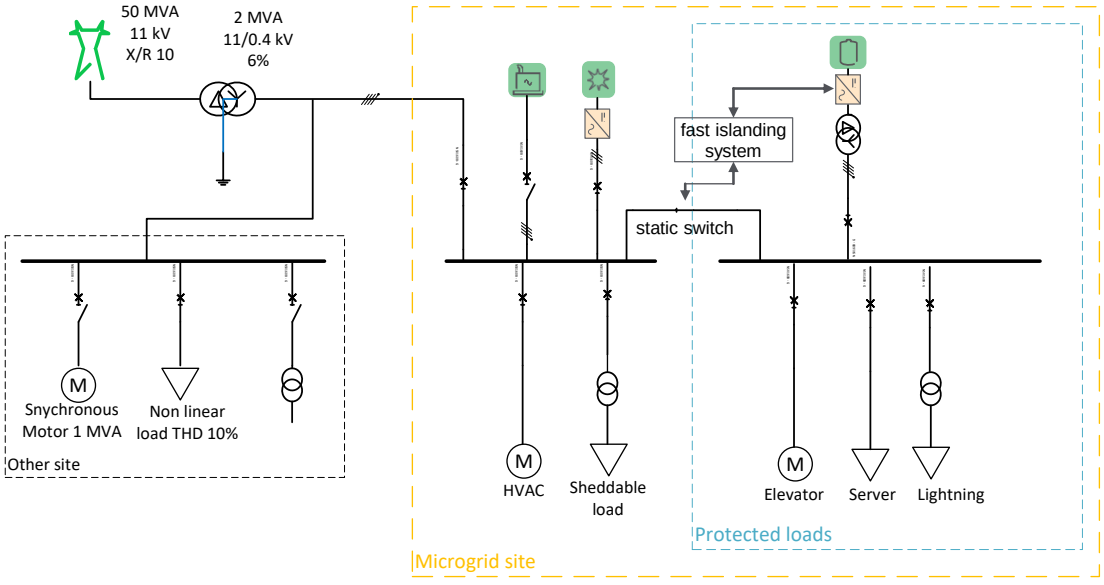

Figure 2.9: Microgrid electrical architecture to achieve seamless performances

implement the seamless feature. The idea is to make possible the critical loads to perform fast islanding within the microgrid, allowing the rest of DERs and loads keep connected during the

FRT requirements. For example, in this case, we split the main busbar inside the main distribution board (MDB) into two: a main busbar and a critical busbar as shown in Figure 2.9. The static switch is used as a bus tie from critical busbar to the main busbar to provide fast isolation in case of grid disturbance. The critical loads and BESS are connected to the critical busbar, while the PV, genset, and non-critical loads are still connected to the main busbar. In this configuration, the critical busbar can perform seamless transition to protect the critical loads, and the PV and other DERs can perform the ride-through requirement. This configuration is also effective with multiple BESS and critical bus, as they can be disconnected and synchronized independently to the main busbar. In summary, this configuration provides flexibility for BESS to island locally within microgrid to protect the load by performing seamless transition in case of grid disturbance.

2.4.3 Microgrid transition summary

Up to this point, the discussion in this manuscript has centered on the microgrid transition between grid-connected and islanded modes. We have introduced the concept of *seamless transition*. Additionally, transitions in microgrids are often characterized by the transfer time required between sources, which can also apply to transitions between local sources in islanded mode, such as between BESS and Genset. In this manuscript, we categorize transitions into four types: open, close, fast, and seamless. An open transition involves a phase of blackout and is usually restored within less than 10 seconds. A close transition, on the other hand, maintains nominal voltage throughout the transition phase and is can only be achieved when the transition does not result from a disturbance, such as transitioning from islanded to grid-connected mode. A fast transition, achieved within 200 to 300 milliseconds, is imperceptible to the naked eye and can be achieved by conventional protection relays and mechanical breakers. Table 2.10 summarizes the characteristics of each transition type.

Table 2.10: Microgrid transition performances summary

Transition type	Maximum duration	Note
Open	10 s	Mostly the requirement standard for emergency backup
Close	0 ms	Not feasible on unplanned transition
Fast	200 ms - 300 ms	Depend on DER ride through grid code
Seamless	10 ms	For class 2 and class 3 equipment protection

2.5 Review on existing fast loss of main detection

This loss of main detection can benefit from voltage dip detection method developed for Dynamic Voltage Restoration (DVR) application. In microgrid application, the detection time

and dip threshold should be configurable depending on the microgrid site. Furthermore, the reliability and accuracy of the voltage dip detection method should be immune to harmonic distortion, frequency change and phase jump that is expected occurs in public electricity networks.

In the literature, several methods have been reported for detecting voltage dips [85]–[87], including peak value monitoring [88], [89], root-mean-square (RMS) [90], [91], instantaneous value [89], [91], DQ transformation [87], [88], [92]–[95], wavelet transform, Fourier transform [89], Discrete Fourier Transform [96], [97] and Kalman filtering[98], [99]. These methods utilize Digital Signal Processing (DSP) techniques, where the analog voltage and current measurements are sampled using an analog-to-digital converter (ADC). As a result, the computation process is carried out in the discrete time domain. Below is a brief overview of existing voltage dip detection methods capable of detecting dips in less than half a line cycle.

- **Root mean square (RMS)**

  Rms calculation is the most common method for the voltage measurement in power system. The RMS value calculation using sliding window is used to determine voltage disturbance [100]. Despite its simplicity, the performance of this method depends on window length and residual voltage.

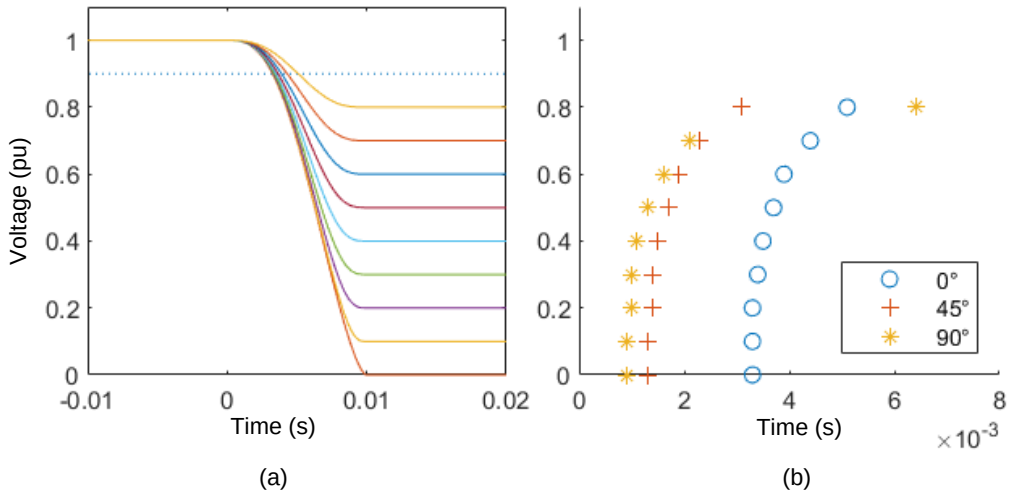

Figure 2.10: (a) the rms value computation for a different residual voltage. (b) the detection time with different dip angle and residual voltage.

To detect faster, the sliding window of half electrical cycle is used. Fig 3a shows the rms for different voltage dip magnitude are compared to a fixed lower limit. The time to detect voltage dip varies from 1ms to up to 7ms for the worst case as shown in Fig 3b. If the Threshold is lowered, then the detection time will be higher.

- **Phasor**

  Phasor is be used to determine the magnitude, frequency, and phase angle of the time-varying quantities during a specific time interval. A sinusoidal signal is described by its frequency f, amplitude X_m and angular position ϕ.

$$x(t) = X_m cos(2\pi ft + \phi) \tag{2.3}$$

  The complex phasor representation X of Equation 2.3 is given by

$$\bar{X} = \left(X_m/\sqrt{2}\right)\varepsilon^{j\phi} \tag{2.4}$$

  Nowadays, most protective relays effectively operate on phasor-based principles[96], [101]. One common approach to phasor estimation is the Discrete Fourier Transform (DFT) [96], [97]. Since it is impossible for DSP to process infinite samples, a discrete windowing function is used to extract a portion of the signals. As we are interested in the fundamental component, the samples extracted should contain N samples of a full cycle of the signal. Some practical microprocessor-based relays today use a half-cycle data window with a tradeoff of higher transient error[101]. Smaller window for instance 1/4 cycles is very sensitive to noise and will give significant error on the magnitude and angle estimation [102], [103].

- **DQ transformation**

  Using the Direct Quadrature (DQ) transformation, a three-phase alternating signal is transformed into two DC signals in the direct and quadrature frames, thereby simplifying the analysis of three-phase systems. The voltage dip detection based on DQ transformation has been proposed in several literature [86], [88], [93]–[95]. While effective for three phase balanced sags in ideal sinusoidal voltages, this method struggles with practical condition of harmonically distorted grid as well as to face DC component in case of a short circuit in the area.. These harmonics components appear as alternating signal in DQ frame. Although low-pass filters can mitigate this, it introduces delays thus increasing detection time. Furthermore, this method is not effective at detecting single-phase sags, which is majority of grid voltage sags [69]. The influence of unbalanced voltage on dq components is characterized by the appearance of a sinusoidal component, which oscillates at twice the nominal frequency. To counteract this effect, low pass filter [95] or differentiator [92] can be used. However, these methods, which are based on three-phase measurements, has a notable limitation: a 30% drop in single-phase voltage has an equivalent impact to a 10% drop in three-phase balanced voltage. Consequently, despite their efficiency, DQ transform approaches demonstrate practical shortcomings in scenarios where single-phase voltage sags are less than 30% in depth

- **Kalman filter**

  Kalman filter is an estimator that use model of the voltage signals. To estimate the

voltage amplitude, the model can consider multiple harmonics components, resulting higher model order. However, it is shown that Kalman filter with only fundamental frequency with a low pass filter has overall better performance [104]. Furthermore, the speed of detection varies up to a quarter cycle depending on the voltage magnitude and the point on the wave where the voltage dip start. A study in [98] used an Extended Kalman Filter (EKF) to improve the estimation of nonlinear processes in voltage event detection, achieving detection times between 1.7 ms and 6.8 ms. However, the detection performance of EKF is generally slightly slower compared to linear Kalman Filters [105]. Additionally, A hybrid method combining Kalman Filter with RMS calculations is proposed to reduced detection times. Nonetheless, in about 10% of cases, this method resulted in detection times exceeding a quarter cycle [99].

- **Discussion on other voltage detection method**

  Wavelet transform has been used to analyze transient and power quality [106], [107]. Further, the usages are extended for voltage sag detection [58], [108]. Wavelet techniques decompose signals that can be analyzed in both the time and frequency domains. Notably, by examining signals in the higher frequency band, voltage dips can be detected more swiftly. However, this approach requires an auxiliary method to distinguish voltage events from other high-frequency disturbances [109]. Furthermore, wavelet output is combined with artificial neural network model for power quality classification[110] and fault detection [58]. Another method is to measure the voltage peak value as discussed in [87], [88] which will takes half fundamental cycles to determine the voltage dip. Sadigh et al. [87] used mathematical transformations to compute the equivalent DC value for each phase, resulting in the best and worst detection times of 1ms and 8.8ms, respectively. Bae et al [91] compare the instantaneous voltage of a single phase with a reference. this comparison triggers the advanced rms calculation to ensure the voltage sag detection in less than 1.6ms

From the literature, analyzing instantaneous voltage measurement directly provides detection time faster. Thus, we propose a fast detection method by comparing instantaneous measurement value with reference value given by Phase Locked Loop (PLL).

2.6 Proposed fast grid loss detection

Let's recall the typical microgrid single line diagram in Figure 2.11. Some possible fault location can result in a voltage dip or even interruption. This includes some faults which originate from microgrid site which is pointed in location 3. For fault located in location 1 and 2, upstream of the microgrid must island to protect its load. On the contrary, microgrid must be kept connected when the fault located in the microgrid site (downstream fault). This

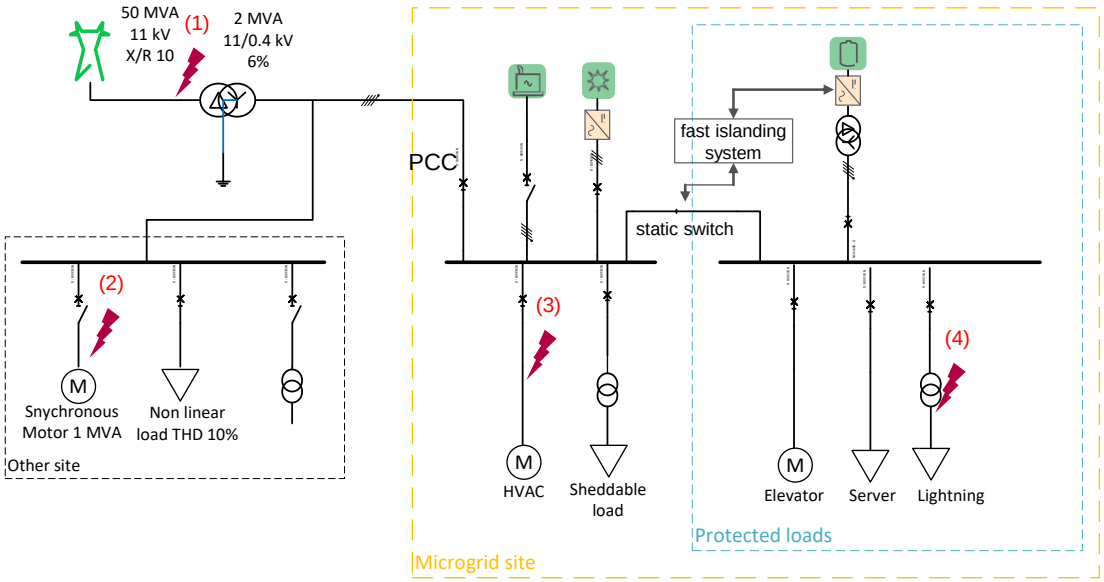

Figure 2.11: Possible fault location in microgrid

allows the protection selectivity works and able to clear the fault at precise location.

As explained in subsection 2.3.2, the decision of islanding must be made within 3ms. As a result, we propose a novel method that employs two key components: a counter with linear increment and an instantaneous sinusoidal reference threshold. This method involves creating a reference voltage, which is derived from the phase angle as estimated by the Phase Locked Loop (PLL). Consequently, a PLL which can track the grid voltage angle in various conditions is needed. Firstly, we will look into different PLL structure and choose the one that fits our criteria: high tracking bandwidth yet immune to disturbance. Then, we present the algorithm to decide *"loss of main"* based on counter.

2.6.1 Choices of PLL structure

Phase locked loop (PLL) is widely used for grid synchronization of inverters. The conventional Synchronous Reference Frame (SRF-PLL) method has been pioneered to track the voltage angle of three phase systems [111]. However, grid voltage distortions, such as harmonics and imbalances, degrade the dynamic performance. To address these challenges, advanced PLL designs have been developed. In this section, we will compare the performance of advanced PLL structures. These include the Adaptive Gain Moving Average Filter SRF-PLL, the Decoupled Double SRF (DDSRF), and the Cascaded Delayed Signal Cancellation (CDSC).

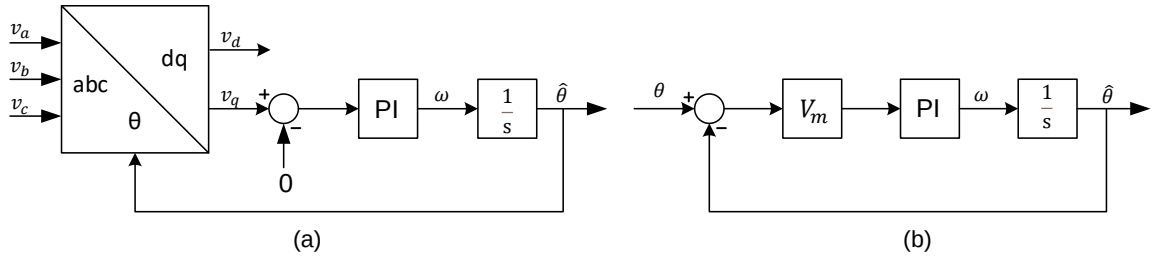

Figure 2.12: Block diagram of (a) SRF PLL and (b) its linearized model.

Synchronous Reference Frame PLL (SRF-PLL)

SRF system consists of two major parts, the phase detecting devices and loop filter. The phase detecting can be readily implemented by using the dq-transform in the three phases system.

Assuming that the real and estimated phase difference is small, the relation of ν_q and grid angle θ can be linearized as

$$\nu_q \cong V_m \left(\hat{\theta} - \theta\right) \tag{2.5}$$

The Proportional-Integral (PI) filter type for second order loop can be used to avoid steady state error. Its gain can be written as

$$k_p = \frac{2\omega_m \zeta}{V_m}, k_i = \frac{{\omega_m}^2}{V_m} \tag{2.6}$$

The loop filter bandwidth is a compromise between the filtering performance and fast response. The higher bandwidth result in faster dynamic response however the tracking error is increased under the distorted utility conditions such as harmonics and unbalanced [111].

The dq transforms is rotating in the same direction as positive sequence. Thus, negative sequence will appear as sine wave disturbance with twice of fundamental frequency in the dq axis[112]. Simillarly, harmonics will appear as another sine wave disturbance with multiple of fundamental frequency, resulting the tracking error of the loop filter. Advances PLL structures deals with filtering these disturbance or enhancing the performance of loop filter.

Moving Average Filter PLL (MAF-PLL)

The common techniques to solve with the aforementioned problem is to use moving average filter as it easy to implement [113], [114]. MAF can be incorporated to PLL structure as shown in the Figure 2.13. The window of a fundamental period is used as the focus is to track the fundamental voltage. As grid frequency can slightly change, adaptive window can used based on the grid frequency information computed by the PLL. In addition, the input amplitude of the loop filter is normalized using the positive sequence voltage. In this case, PID type loop filter can provide higher bandwidth compared to PI type loop filter [113].

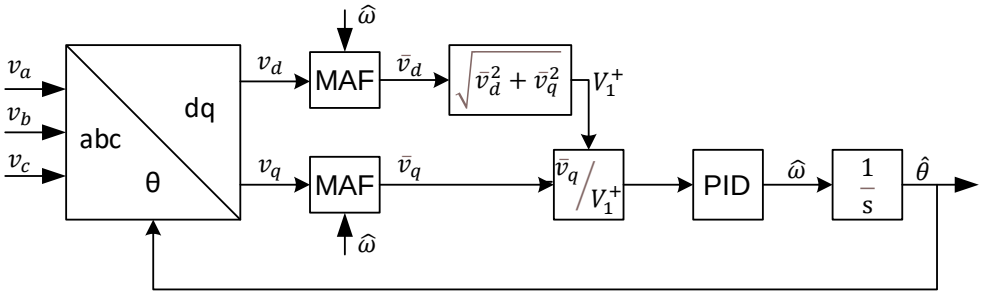

Figure 2.13: Block diagram of MAF PLL with adaptive gain and frequency

Cascaded Delayed Signal Cancellation PLL (CDSC-PLL)

The cascaded delayed signal cancellation (CDSC) PLL is using the delayed signal techniques to filter the input signal[115]–[117]. The delayed signal cancellation (DSC) operator delays a voltage signal by T/n where T represent the fundamental period and n is DSC order. This block is further cascaded to reject all undesired harmonics. Then the conditioned voltage signal can be used for PLL without suffering the steady state errors because of harmonics. CDSC blocks is often applied outside of the loop thus design of PLL loop parameters is not affected by the DSC delay.

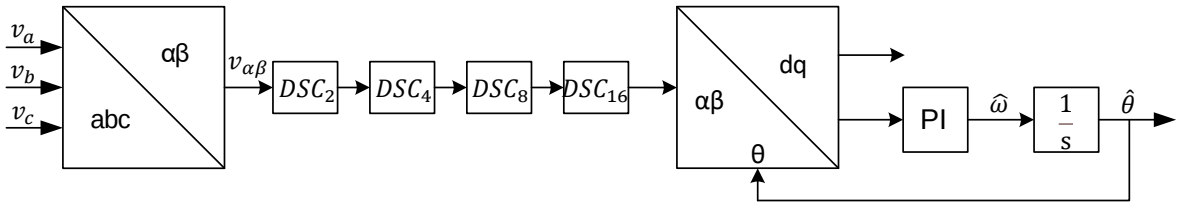

Figure 2.14: Block diagram of CDSC-PLL

Decoupled Double SRF PLL(DDSRF-PLL)

DDSRF-PLL uses positive sequence detector, which completely eliminates the detection errors of conventional SRF-PLL [118]. The PLL use two synchronous reference frame, denoted as dq^n and dq^m that rotates with $n\omega$ and $m\omega$ frequencies respectively as shown in Figure 2.15a. For the extraction and separation of positive and negative sequence, the values of n and m are set to 1 and -1, respectively, utilizing decoupling cell depicted in Figure 2.15b.

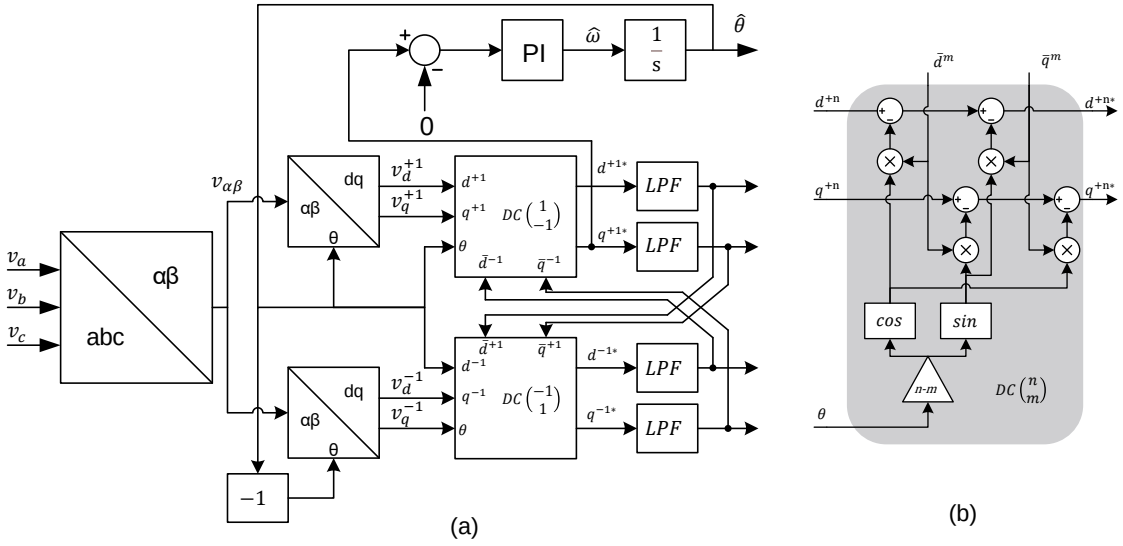

Figure 2.15: Block diagram of (a) DDSRF PLL and (b) decoupling cell

PLL performance

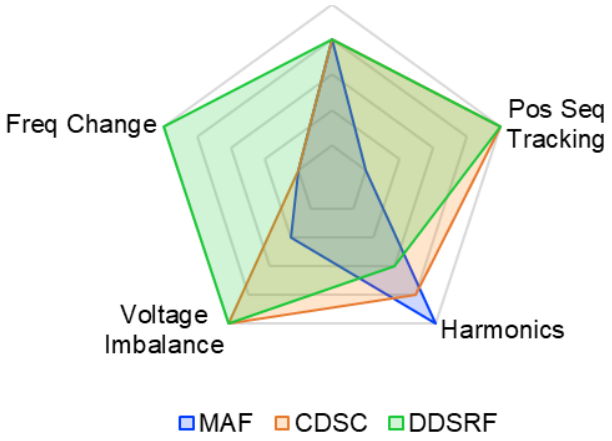

Figure 2.16: Performance difference of MAF-PLL, CDSC-PLL, DDSRF-PLL

All of the presented advanced PLL structures had been implemented within Simulink in discrete simulation, facilitating later implementation for prototyping. We tested their performance based on their phase estimation response on various grid disturbance. Over 20 test cases including balanced and unbalanced voltage sag, harmonics, phase jump, frequency drift are applied. We evaluate their phase estimation error and its response time for each disturbance. Each type of PLL have strong or weak points to several disturbance type. However, DDSRF comes as the best overall as shown in Figure 2.16.

2.6.2 Loss of grid detection algorithm

We investigate the possibility on detecting voltage dip or interruption by analyzing only the voltage at the Point of Common Coupling (PCC). The current measurement though is relevant to determine the fault origin. If the location in downstream, a very high current will flow from the grid. In contrary, if fault originate from upstream, the short circuit current contribution from DER is far less significant. Figure 2.17 illustrates instantaneous detection

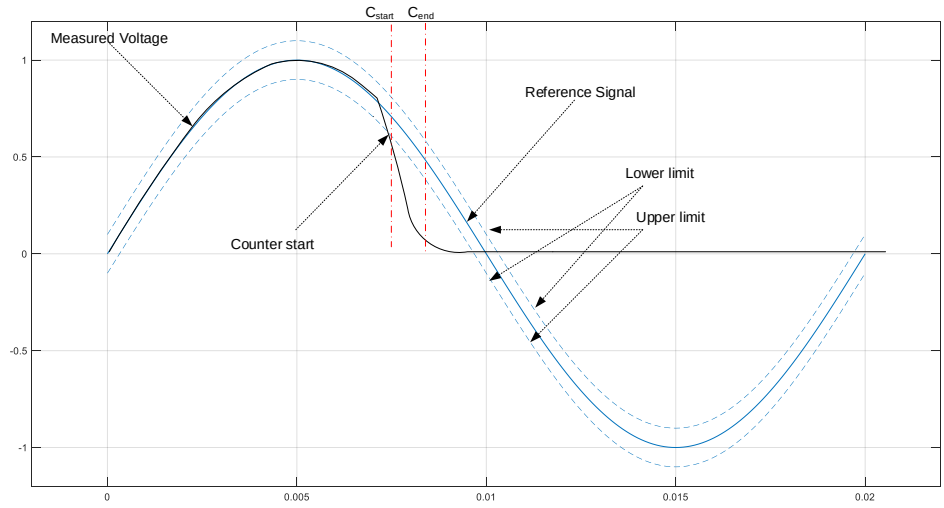

Figure 2.17: Illustration of instantaneous fast detection

principles for one channel. The measurement of three-phase voltage is divided into six channels, comprising three phase-to-phase voltages and three phase-to-neutral voltages. All these channels are monitored following the same principles. A threshold limit (dashed-blue) from reference signal (blue) is generated thanks to the PLL. This limit has fixed part and linear to deal for calculation near zero crossing. The linear part is defined by a threshold percentage of nominal voltages.

When the measured signal (black) is exceeding the threshold, a counter is started. The counter increments linearly with delta difference between the measured voltage and the limit. If the counter passed the counter threshold, a loss of main is detected. Figure 2.18 provides algorithm flowchart of the proposed detection method.

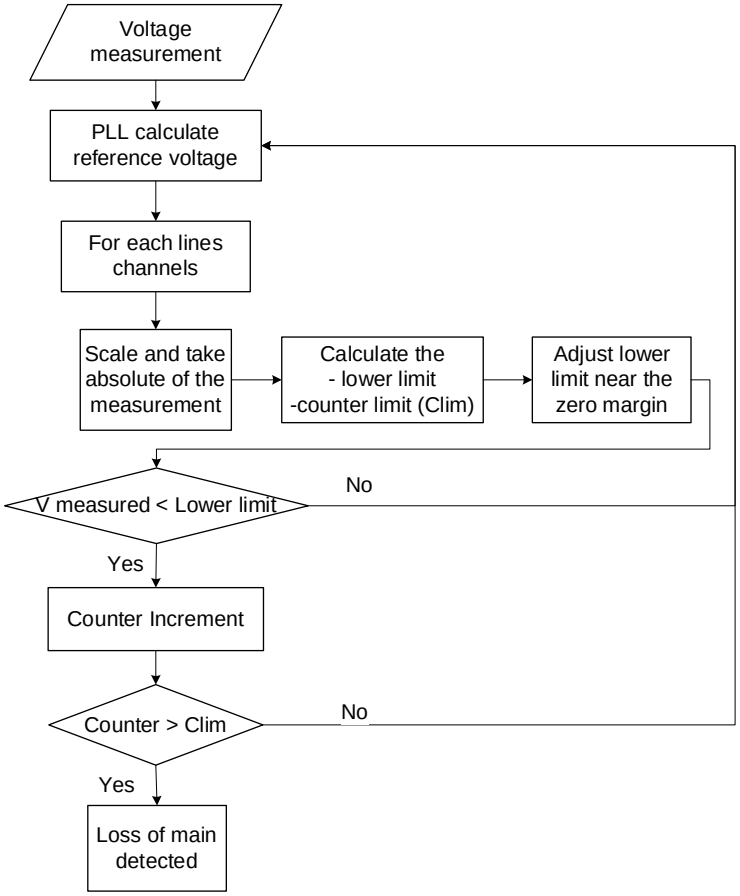

Figure 2.18: Loss of main detection algorithm based on instantaneous voltage

2.6.3 Detection performance

The proposed algorithm is modeled and verified using MATLAB Simulink. The model is implemented in discrete with time step of 10 μs and optimized for the implementation on DSP. The detection performance is verified with different voltage dip level and type as previously described in Table 2.4. To validate the algorithm thoroughly, nine scenarios were developed, combining three types of voltage dips (Type I, II, and III) with THD levels of 0%, 8%, and 10%. For each scenario, 598 test cases were conducted, varying the voltage dip magnitude from 0 to 0.9 per unit and the point of wave where the dip occurs from 0 to $\pi/2$.

Figure 2.19 displays the results of the test set, wherein the detection time target was set at 2 ms and the voltage threshold at 0.73 pu. Each curve point indicates the detection time corresponding to specific dip magnitudes and angles, with the red area denoting the detection zone. The results reveal that, for Type I voltage dips, the algorithm did not detect certain events within the specified range of 0.5 to 0.73 pu, accounting for 15% of the total tests. However, these detection failures predominantly occurred when the dips angle were close to

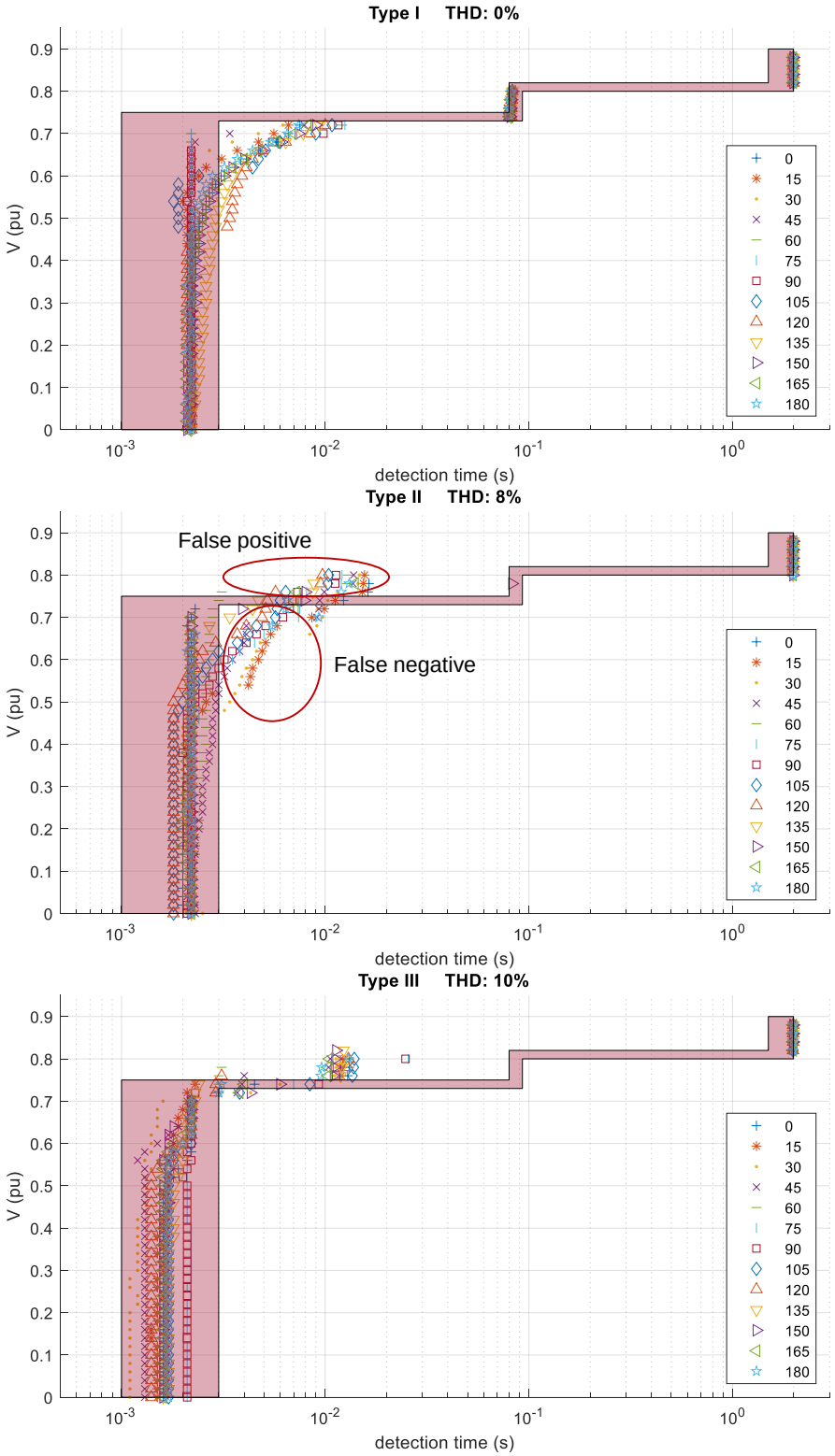

Figure 2.19: Fast lost of main detection time performance for various voltage sag value and types

zero. Additionally, in the Type II test, some false positives were observed, constituting only 2% of the cases. Finally, Figure 2.20 presents the statistics of detection performance, which includes tests cases conducted in a polluted environment, indicated by a THD of 8% and 10%. Appendix C presents the complete test results.

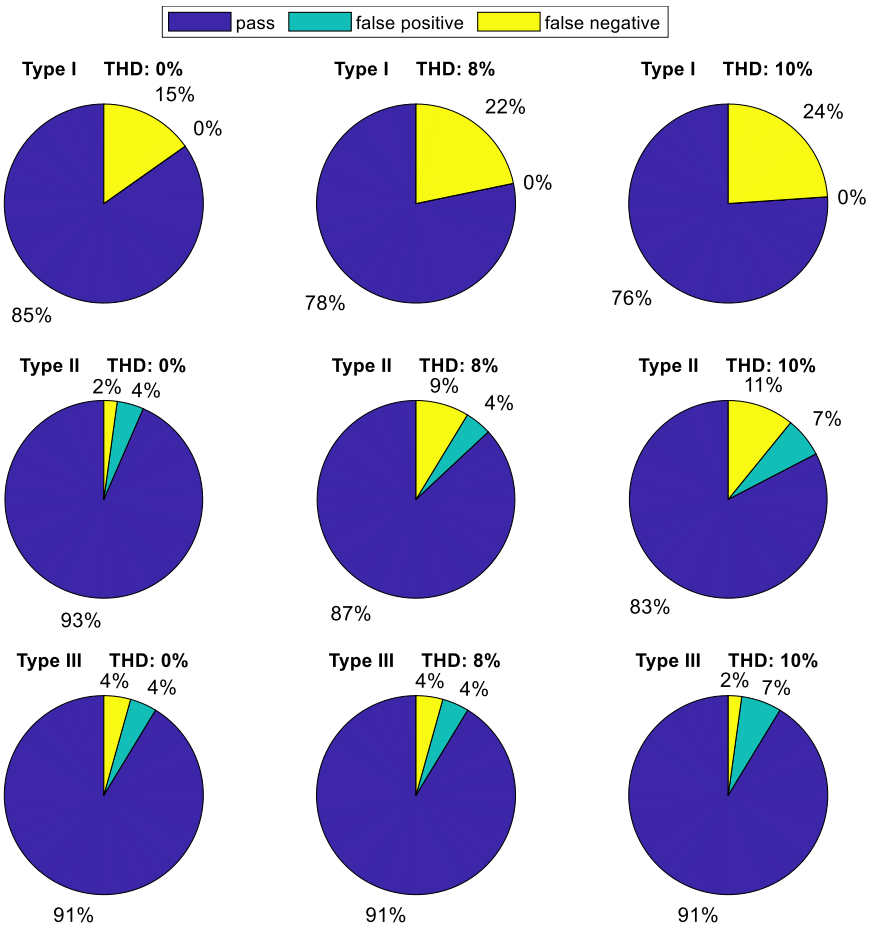

Figure 2.20: Fast detection performance statistics

2.7 Conclusion

This chapter explained the grid condition under which a microgrids needs to island. Considering the susceptibility of critical loads to grid disturbances, our analysis of literature and relevant standards has led us to establish performance requirements for seamless operations of 10 milliseconds to reach 73% of the nominal voltage. Furthermore, we presented the challenges on fast detection of loss of main, along with our novel approach on the fast detection of loss of main. This chapter is part of thesis 's contribution C1 and C2.

Our method, analyze the instantaneous values of the measured voltage and compare it to

a reference signal which tracks the positive sequence. The proposed method is validated in simulation and prototype, the result of prototype is presented in chapter 4. Table 2.11 the difference method of fast voltage dip detection.

Table 2.11: Difference of the proposed method and the literature

Ref	**Method**	**Phase**		**Harmonics**	**Unbalanced**	**Speed**	**Configurables**
		1	3				
this thesis	instantaneous	yes	yes	good	good	2 ms	yes
[88][79]	DQ transformation	yes	no	no	0.8 - 7 ms	no	
[98]	Kalman filter		yes			1.7-6.8ms	no
[91]	Instantaneous voltage comparison		yes	fair	no	2 ms	no
[87]	Vdq without PLL		yes	good	-	1-8 ms	no

Chapter 3

Seamless Power Converter Control

Contents

3.1 Introduction

In microgrid systems, inverters serve the critical function of converting DC power to AC power and vice versa, enabling the power transfer from the majority of Distributed Energy Resources (DERs). Inverters are capable of operating in various modes, adapting to the operational state of the microgrid.

When the microgrid is interconnected with the utility grid, inverters function in a grid-following mode, where they either inject or absorb specified quantities of active and reactive power. This operation can be for purposes such as cost optimization, providing flexibility, or ancillary services to the utility grid. Conversely, in scenario of grid outages, the microgrid

may operate in an islanded mode. During such instances, inverters, especially those used in BESS, transition to a grid-forming mode. In this mode, they are responsible for maintaining the voltage and frequency stability of the microgrid to supply power to the local load.

The transition of inverters from grid-following to grid-forming mode and vice versa has been extensively explored in several academic articles [51], [52], [119]–[121], mostly developed for single-phase line interactive UPS application [119], [122]–[124]. During transition, the inverter must maintain its control stability while respecting the technical constrains such as overcurrent and overvoltage. Additionally, if there is no disturbance prior to the transition, the transition can be achieved smoothly. However, within microgrid systems, various challenges are recognized in achieving a seamless transition following grid loss, including:

- The technology for static switch predominantly relies on thyristors, necessitating a wait for the zero-crossing current to turn off the circuit. As a result, the disconnection time may extend up to 10 ms
- Time delay caused by islanding detection may bring voltage stability problems[125].
- Considering practical implementation, the distance between static switch and BESS may be a problem for current measurement
- Three phase transformers usually used to connect BESS and microgrid, which complicates the control

This chapter begins by introducing the fundamental concepts of inverter control in section 3.2. Following this, section 3.3 elaborates in detail on the control design of the inverter. Subsequently, section 3.4. outlines the strategy for seamless transition between grid-connected and grid-forming in case of a grid loss. Finally, section 3.5. demonstrates the full microgrid sequence of operation, ensuring not only the uninterrupted operation of critical loads but also other DERs, all the while maintaining compliance with grid code requirements.

3.2 Inverter Control Structure

In this chapter, the term *inverter* will be used to specifically refer to a bidirectional AC-DC power converter. The control of converter can be mainly classified into two: grid-forming and grid-following control. The primary distinction lies in their control objectives. In grid-following control, the aim is to regulate the current, typically derived by the power reference. Whereas in grid-forming, the focus is on regulating both voltage and frequency. This section briefly explains the converter control structure that allows inverters achieve those objectives.

3.2.1 System description and modeling

In this thesis, we consider the most common topology for BESS connected to microgrid as presented in Figure 3.1. The BESS comprises a two-level voltage source converter (VSC), which is connected to a battery pack on the left side and an LC filter on the right side. The BESS interfaces with the microgrid through Delta-Y (D-Y) transformers. A static switch is used to connect the microgrid to the main grid.

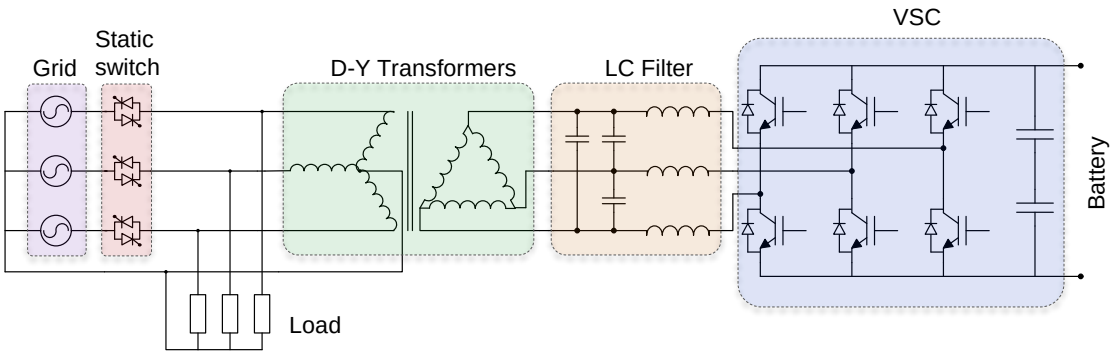

Figure 3.1: Representation of BESS connection in microgrid system

Figure 3.2 shows of the simplified schematic of the systems. The Delta-Y transformers are represented by their equivalent inductance, denoted as L_{xtf}. Additionally, the terms L_f, C_f, Z, and ss represent filter inductance, filter capacitance, load impedance, and static switch, respectively.

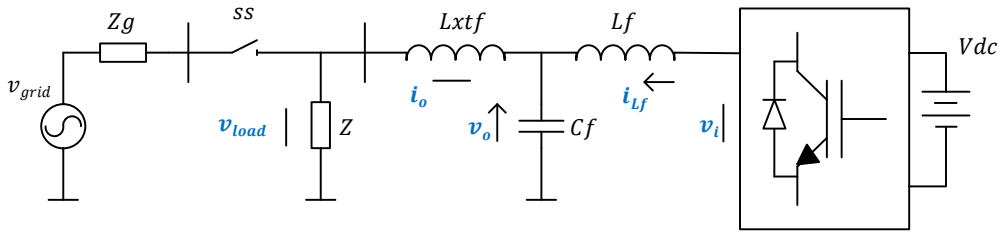

Figure 3.2: Simplified schema of microgrid system

The voltage $v_i = [v_{i_a}, v_{i_b}, v_{i_c}]^T$ are produced by the modulation of the DC voltage through the switching stage. It is assumed that the switching time is small enough to consider vi as equivalent to its average value. In this systems, the state variables are defined as follows: the current in the inductance L_f is denoted $i_{Lf} = [i_{Lf_a}, i_{Lf_b}, i_{Lf_c}]^T$; the voltage of the capacitor C_f is denoted $v_o = [v_{o_a}, v_{o_b}, v_{o_c}]^T$; and the current which enters in the transformer (D side) is denoted $i_o = [i_{o_a} i_{o_b} i_{o_c}]^T$. A balanced grid is modeled by a Thevenin equivalent AC source (V_{grid}) in series with its equivalent grid impedance (Z_g). The mathematical model of the

system is expressed below.

$$v_i - v_o = L_f \frac{di_{Lf}}{dt} + R_f i_{Lf} \tag{3.1}$$

$$i_{Lf} - i_o = C_f \frac{dv_o}{dt} \tag{3.2}$$

$$v_o - v_{pcc} = L_{xtf} \frac{di_o}{dt} + R_{xltf} i_o \tag{3.3}$$

Throughout this chapter, we will use typical parameter values for the system as listed in Table 3.1. To facilitate the implementation on the experimental setup, the 50 Hz 110 V systems was selected. The LCL filter is designed using typical values found in the literature [126]–[128].

Table 3.1: Typical system parameter

Parameter	**Value**
Nominal Frequency	50 Hz
Nominal Power	4 kW
Nominal phase-neutral voltage	110 V
Switching frequency	10 kHz
Filter inductance - Lf	3 mH
Filter resistance - Rf	0.04 ohm
Filter capacitance - Cf	6.5 µF
Filter damping - R_{cf}	4 ohm
Transformers winding connection	110/110V D/Y
Transformers eq inductance - L_{xtf}	1.4 mH
Transformers eq resistance - R_{xtf}	0.4 ohm

3.2.2 Converter Control Structure

The control of converter is achieved by feeding back the state variables shown in Figure 3.2 into a closed-loop control. If only one variable is measured and regulated, the system is known as a single-loop control structure. When two state variables are controlled, two controllers are cascaded, creating a double-loop control structure. The later allows more control flexibility which often results in better performance. On the other hand, single-loop control is often used when dual-loop is infeasible. For example, in situations where the ratio of switching frequency to fundamental frequency is low, as seen in 400 Hz system for airplane application [129], [130].

Dual loop control structure can be configured differently depending which states are fed back to the inner loop and the outer loop. Additionally, the variables can be used for feed-forward to improve the performance. Among numerous control schemes for three phase VSC reported in the literature, as referenced in [131]–[139] and from the comprehensive overview

provided in [140], [141] we choose to use dual loop control structure configuration as shown in Figure 3.3.

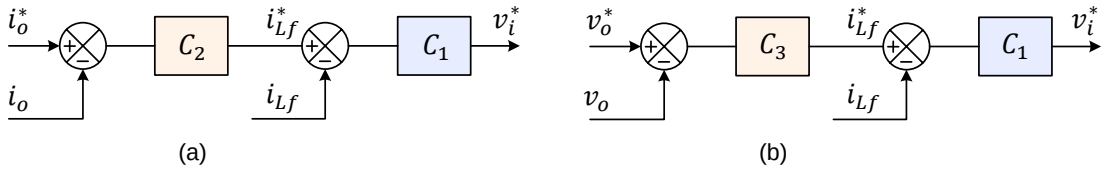

Figure 3.3: Dual loop control structure of (a) grid-following, (b) grid-forming. C_1 is the inner loop, C_2 and C_3 are the outer loop regulator.

The inner loop controller C_1 is used to regulate the current i_{Lf}, which gives voltages reference for modulation v_i^*. In grid following control, the outer loop controller C_2 is used to regulate inverter output i_o, while in grid-forming, the outer loop controller C_3 is used to regulate capacitor voltage control v_o The control structure can be implemented in difference reference control frame: rotating reference frame (dq frame), stationary reference frame ($\alpha\beta$ frame) and natural stationary reference frame (abc frame). Proportional-integral (PI) regulator is typically used in dq frame. Whereas the proportional-resonant (PR) regulator is typically used in stationary frame.

3.2.2.1 Grid forming control structure

The grid forming control consist of current control loop and voltage control loop. Additional loop or external loop, such as droop can be added to the input of the voltage control. Furthermore, previous studies have explored the use of droop [127], [142]–[144], virtual synchronous generator [144], [145], and virtual oscillator [146] as external control to control the grid forming in parallel to the grid. However, these grid-forming controls can lead to stability issue when connected to the stiff grid [127], [147], [148]. In this thesis, the external control is not the focus; instead, attention is given the voltage control to enhance fast voltage recovery and disturbance rejections. Figure 3.4 show the implementaion of the grid forming structure in different control frame.

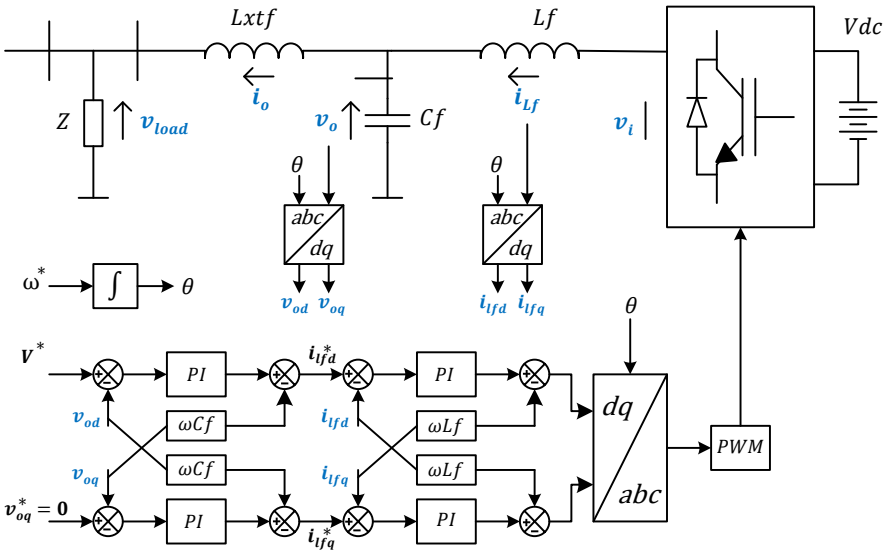

(a) Control in dq frame

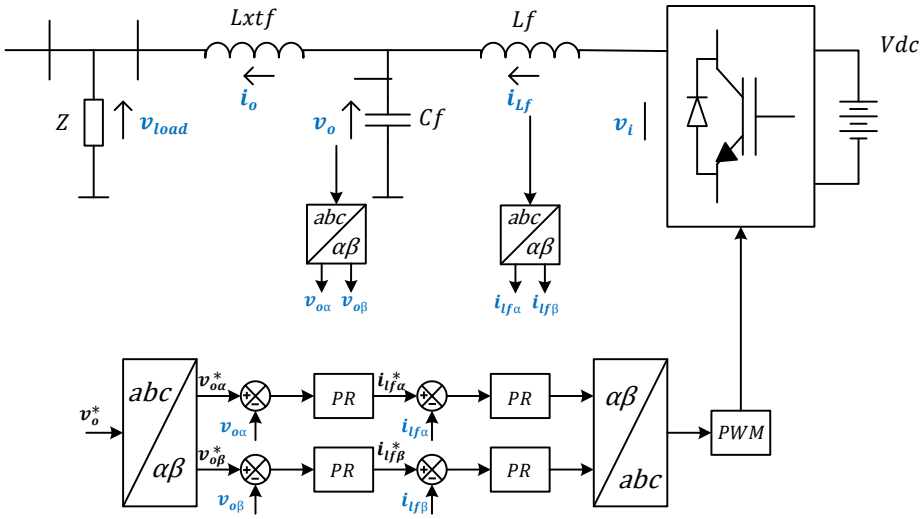

(b) Control in αβ frame

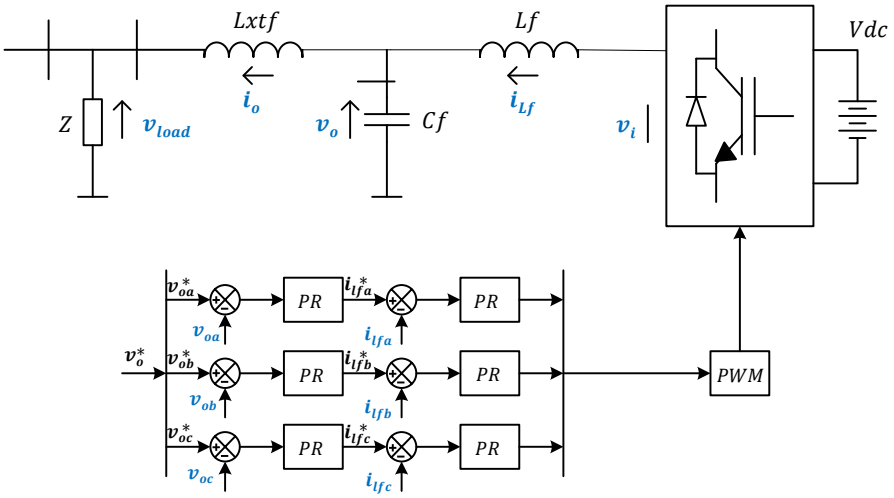

(c) Control in abc frame

Figure 3.4: Grid forming control structure

In microgrid application, the converters need to supply significant unbalanced power. As the dq frames use rotating transformation that rotates in the same direction as voltage, additional negative sequence rotating frames is then needed to control the unbalance condition. The negative sequence vector rotates in the opposite direction of the dq axes, and its d and q components will thus appear as a 2nd harmonic [112]. Figure 3.5 illustrate how to extract positive and negative sequence using two rotating frames that rotate in the opposite direction. A band stop filter is used to reject the 2nd harmonic that appears.

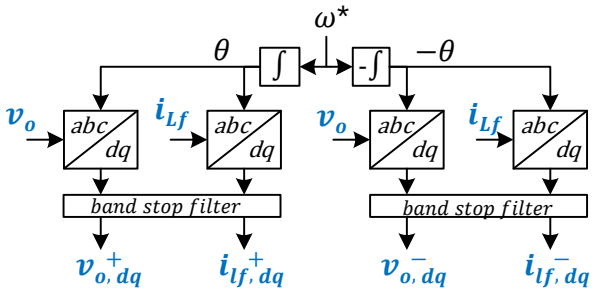

Figure 3.5: Positive and negative sequence extraction in dq frame control

By incorporating negative sequence to the control, the control presented in Figure 3.4(a) becomes to the one depicted in Figure 3.6.

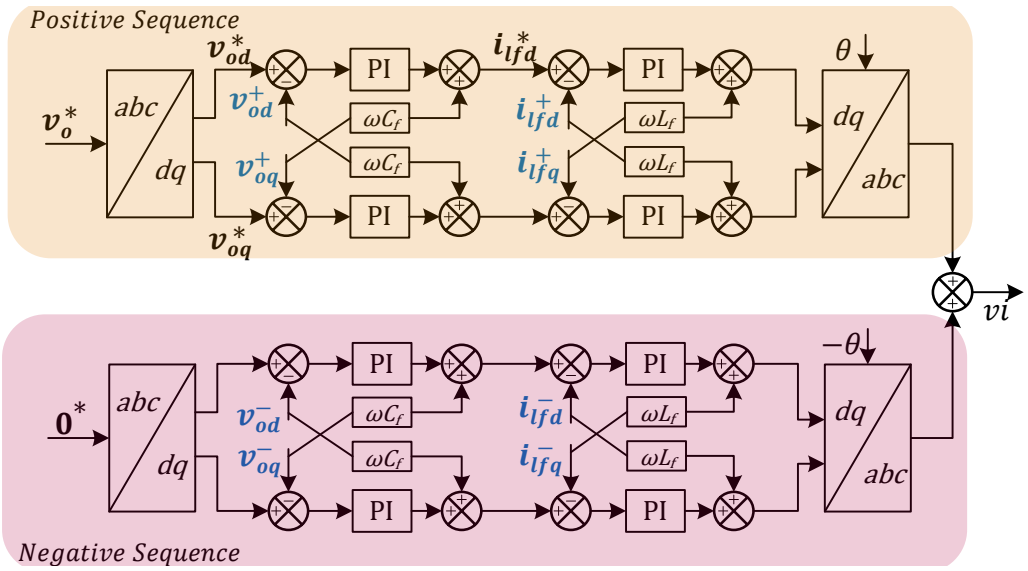

Figure 3.6: unbalanced control in *dq* frame

For this application, the use of dq frame control does not simplify the control, conversely, more controllers are needed to manages the control objective. Therefore, we choose to use control in stationary abc frame as depicted in Figure 3.4 (c).

3.2.2.2 Grid following control in abc frame

The grid following control is composed of an inner current loop and an power loop.The power loop control is directly related to the current control i_o. The active power at PCC can be expressed as

$$P = Real(\overline{V_{load}}.\bar{I_o}^*) = V_{load}.I_o.cos(\phi) \tag{3.4}$$

$$Q = Im(\overline{V_{load}}.\bar{I_o}^*) = V_{load}.I_o.sin(\phi) \tag{3.5}$$

In grid following control, the V_{load} is defined by the grid voltage and can be assumed as constant. Thus, the power control can be accomplished by means of controlling I_o and $cos\,(\phi)$. In dq frame, the $cos\,(\phi)$ is aligned to the direct axis and $sin\,(\phi)$is aligned to quadrature axis, simplifying the active and reactive control. Figure 3.7 shows grid following with closed loop control structure.

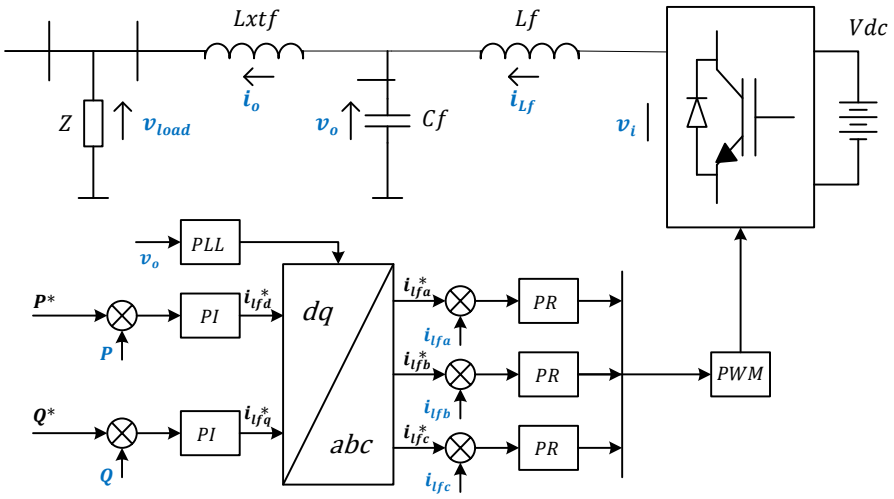

Figure 3.7: Grid following control structure

In this configuration, we use the same current controller structure for grid forming. However, the power loop control is implemented in dq rotating frame, facilitating the active and reactive power control.

3.3 Design of the Control Loop

3.3.1 Current control loop

The Proportional-Resonant (PR) is very popular for current control application [131], [149]. It's important to note that the PR control tuned at the fundamental frequency is essentially

equivalent to two PI controllers working in parallel in the positive and negative sequence rotating frame [150], [151]. Figure 3.8 presents the block diagram of the current controller for the LCL filter, where $G_{pr}(s)$ and kpwm represents proportional-resonant regulator and gain of the PWM respectively.

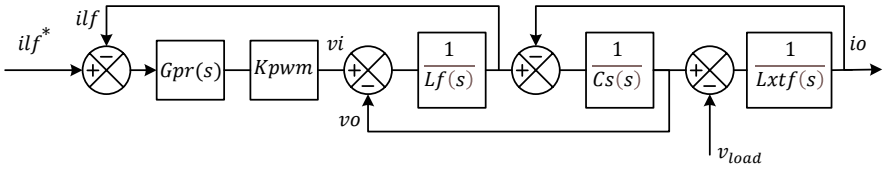

Figure 3.8: Block diagram of current controller

The transfer function of current controller can be expressed as

$$G_{pr}(s) = Kp + \sum_{h=1,5,7} \overbrace{\frac{Kis}{s^2 + h^2{\omega_1}^2}}^{R_h(s)} \tag{3.6}$$

where K_p is proportional gain, $\omega 1$ is the fundamental frequency and h is the harmonic order [132], [149], [152]–[154]. G_{pr} provides infinite open loop gain at the resonant frequency $h\omega_1$. Resonant terms $R_h(s)$ is set in parallel configuration to effectively address harmonics 1,5, and 7, as they represent the most significant harmonics in typical converter's current. Harmonics with multiples of 3 does not appear because the converter connected to transformers in delta configuration.

3.3.1.1 Tuning of current controller

Based on implementation best practices, the bandwidth of the current control is set to 10 times slower than the switching frequency. If we take into account inductor resistance and damping resistor in series with capacitor, the transfer function of LCL filter in Figure 3.8 can be express as

$$\begin{aligned}\frac{i_{lf}}{\nu_i} = \frac{C_f L_{xtf} s^2 + C_f(R_{cf} + R_{xtf})s + 1}{C_f L_f L_{xtf} s^3 + C_f(L_f(R_{cf} + R_{xtf}) + L_{xtf}(R_{cf} + Rf))s^2 + \\ (L_f + L_{xtf} + C_f(R_{cf}(Rf + R_{xtf}) + Rf R_{xtf}))s + Rf + R_{xtf}\end{aligned} \tag{3.7}$$

This transfer function can be approached with only an L filter (see Figure 3.9) provided one of the following conditions is respected:

- The LCL resonant frequency is far higher than the current control loop bandwidth. Which is typically the case for VSC, the LCL resonance is designed in between 1/4 to 1/2 of the switching frequency ensuring the effective harmonic attenuation and good dynamic system. [155]

- The LCL resonant is attenuated (i.e. using passive damping) [126]

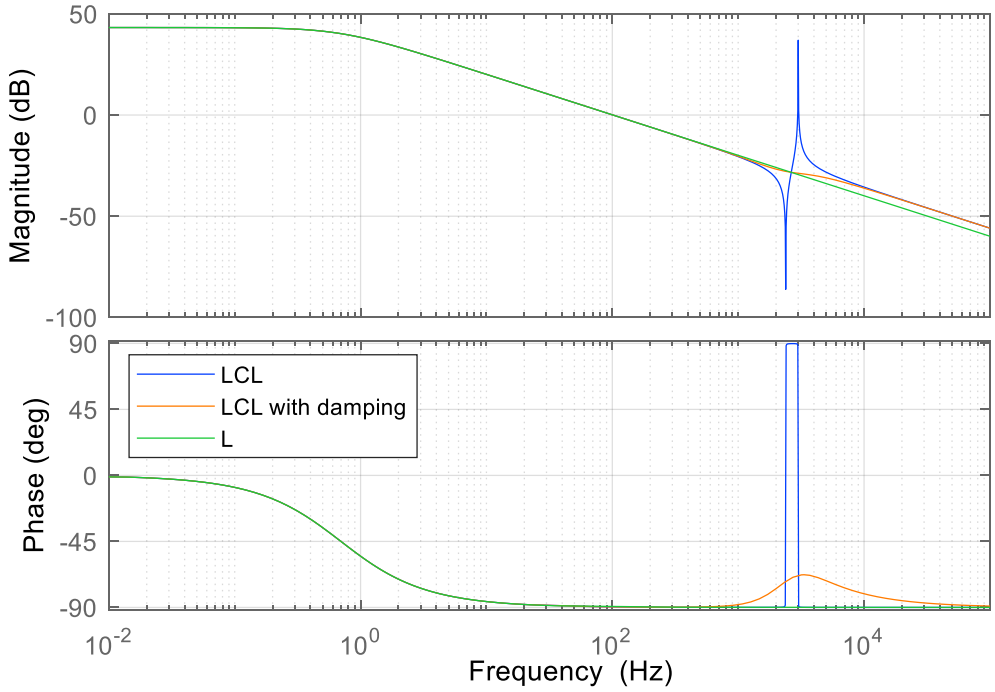

Figure 3.9: Bode plot of different modeling approach for LCL filter

Moreover, the Bode diagram approach is frequently utilized for tuning Proportional-Resonant parameters [132], [138], [149], [152], [156]–[162]. Given that the plant can be modeled as an L filter, the following are the characteristics of PR controllers that can be generalized from literature.

- The proportional gain Kp determines the controller bandwidth fc, at which the open loop gain is 0 dB[151], [152], [158].
- The resonant gain Ki only affect around the harmonics frequency, which has insignificant influence to the controller bandwidth [158].
- The resonance width around $h\omega_1$ is defined by the gain Ki. As Ki increase, the resonant more tolerant to frequency deviations, and the transient response at $h\omega_1$ increase [149], [151].
- Increasing the gain Ki results in a decrease in the phase margin. In real implementation, the transfer function is affected by additional delay, further limiting the feasible range of gain Ki to maintain a reasonable phase margin [158].
- To ensure the stability, the highest resonant harmonics must be lower than fc [138], [151], [159] additional security bandwidth of 1000 radians can be added to keep the influence of the highest harmonics [159].

- Tuning PR controllers with identical Ki gains for all harmonics is a commonly practiced approach [138], [149], [163].

Based on the points above, the value of Kp can be calculated as a function of controller open loop bandwidth fc as

$$Kp = \sqrt{2\pi fc\,(L_f + L_{xtf})^2 + (R_f + R_{xtf})^2} \tag{3.8}$$

The Ki gain can be calculated to minimize its influence on the phase margin. Considering identical values Ki for all harmonics order, the Ki can be calculated as a functions of phase addition $\Delta\Phi$ at the cutoff frequency fc [159] as given in Equation 3.9, where $\omega_{OL} = 2\pi fc$.

$$Ki = \frac{-2 * Kp\ \omega_{OL} \prod_{y=1}^{N} (y\omega_1^2 - \omega_{OL}^2)}{\tan(\Delta\Phi - 90)(\prod_{y=1}^{N} (y\omega_1^2 - \omega_{OL}^2) - 2\omega_1^2 \sum_{n=1}^{N} \prod_{\substack{y=1 \\ y\neq n}}^{N} (y\omega_1^2 - \omega_{OL}^2))} \tag{3.9}$$

The controller parameters are calculated based on system parameter listed in Table 3.1. Based on equations Equation 3.8 and Equation 3.9, the values of $Kp = 27$ and $Ki = 200$ have been obtained to achieve 1kHz bandwidth and phase addition $\Delta\Phi$ of less than one degree. Figure 3.10 depicts the open-loop frequency response after the tuning. The plant model in Equation 3.7 and PR controller in Equation 3.6 are discretized using zero order hold with $10kHz$ frequency, and a unit delay is added to reflect the computation. The system has a satisfactory phase margin of 43°, ensuring the stability.

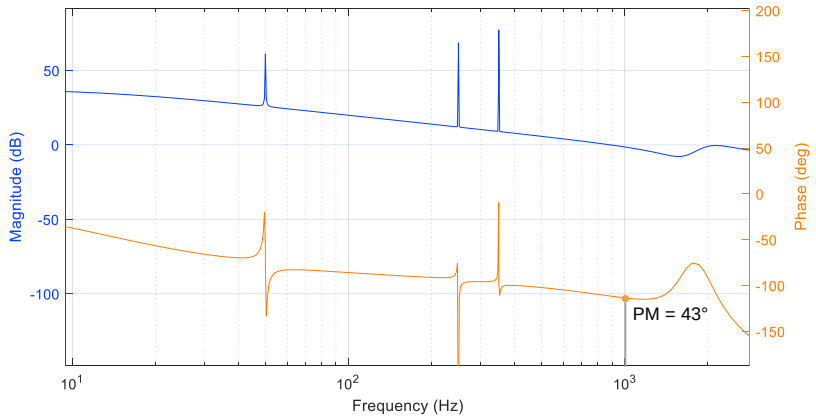

Figure 3.10: open loop Bode of current controller $G_{pr}(z)$ $G_{lcl}(z)$.

3.3.1.2 Validation of current controller

To validate the designed current control, the designed current controller performances are verified through time domain simulations using Matlab Simulink SimPowerSystem toolbox. The microgrid systems described in subsection 3.2.1 is used for the test case. Figure 3.11 shows the inverter's control loop response.

- $t = 0s$, inverter is turned on, sinusoidal current reference with amplitude of 1 A is applied
- $t = 0.105s$, Iref step to 2 A is applied.

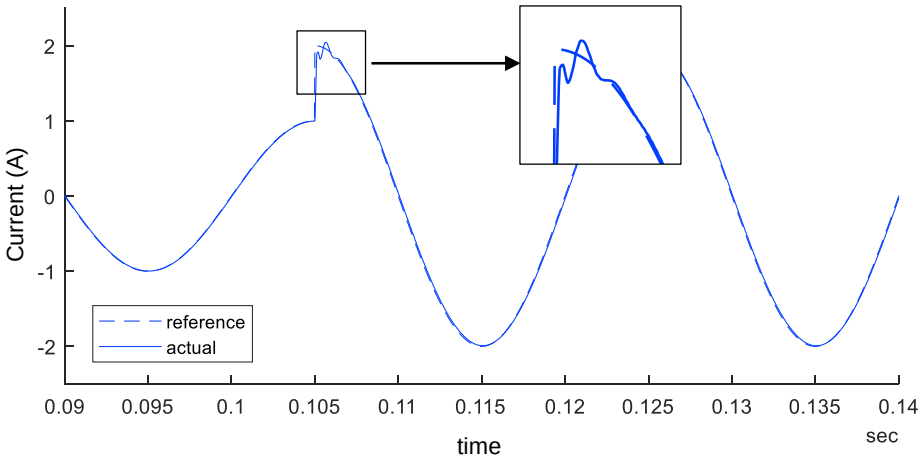

Figure 3.11: Current loop response at step of reference current amplitude

3.3.2 Grid forming outer voltage control loop

To have high response, PR controller is also used to regulate the capacitor voltage. Figure 3.12 shows block diagram of the voltage control. The voltage loop is tuned five times slower than the current loop. Thus, the inner loop current control can be simplified by a first order transfer function with its cutoff bandwidth.

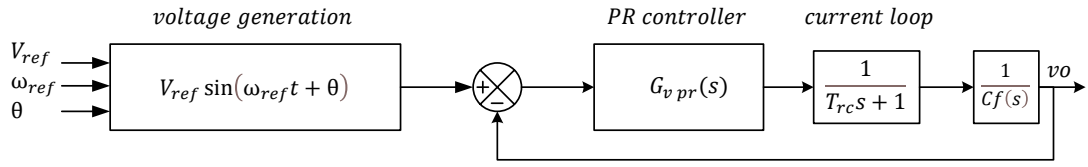

Figure 3.12: Block diagram of outer loop voltage control in grid forming mode

Transfer function of voltage controller can be expressed as

$$G_{v\ pr}(s) = Kp_v + \sum_{h=1} \frac{Ki_v\ s}{s^2 + h^2\omega_1^2} \tag{3.10}$$

The tuning procedure is similar with the one used in current control. However, only fundamental harmonics is considered due to the limit of voltage control bandwidth which around

200 Hz. Incorporating the fifth harmonics will result instability. The controller gains that were designed are $Kp_v = 0.06$, $Ki_v = 50$. Figure 3.13 shows sensitivity transfer function $v_o(s)/v_o ref(s)$.

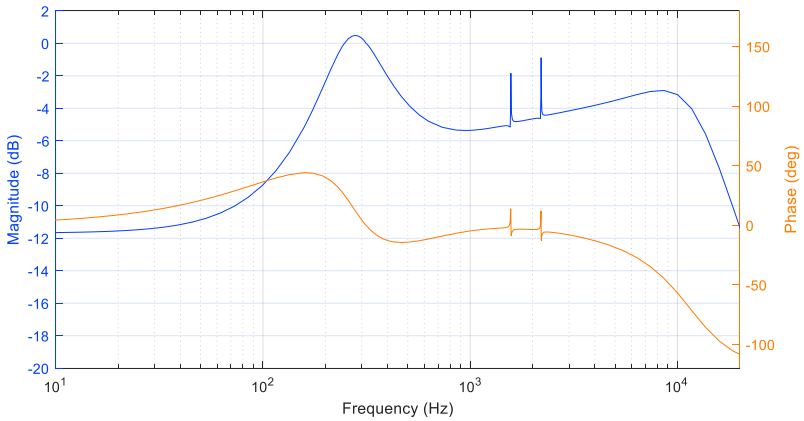

Figure 3.13: Bode plot of closed loop voltage control $(vo(s)/vo_{ref}(s))$. $Kp_v = 0.06$, $Ki_v = 50$

The voltage controller performances are verified through time domain simulations illustrated in Figure 3.14 and Figure 3.15. The load is assumed to be purely resistive. Voltage reference step and unbalanced load step are tested to assess the performance of the system.

- $t = 0.05\ s$, the inverter is turned on, voltage reference is set to 155 V peak.
- $t = 0.205\ s$, voltage reference is set to 186 V peak.

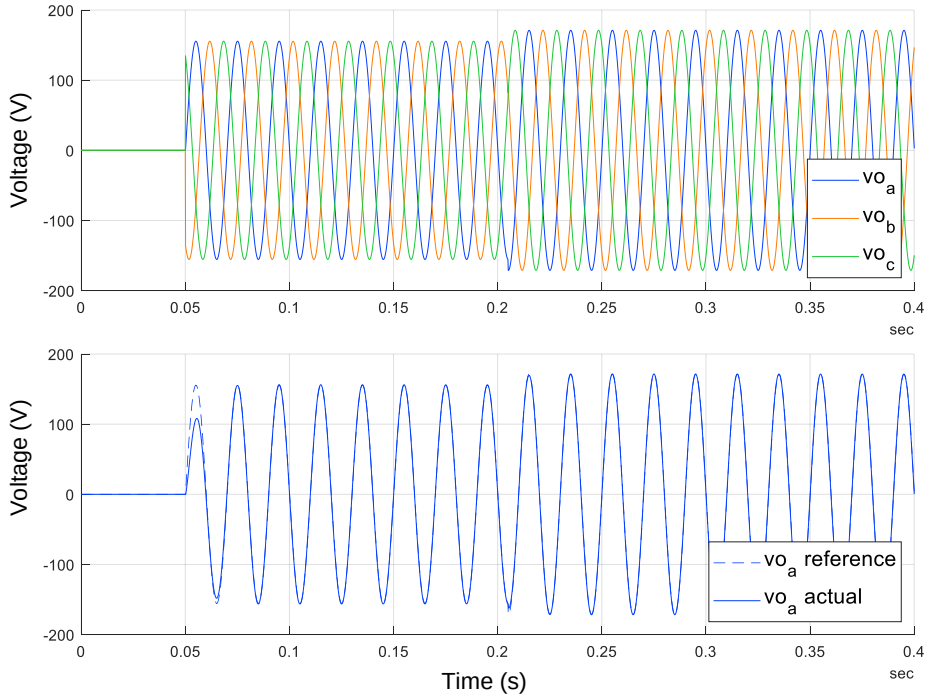

Figure 3.14: Grid forming control response on voltage reference step

During the starting, the step function is applied to the reference voltage Vref. The inverter's output voltage reached the steady state in less than one fundamental cycle. In practice, a ramp function can also be used to facilitate soft start of the inverter.

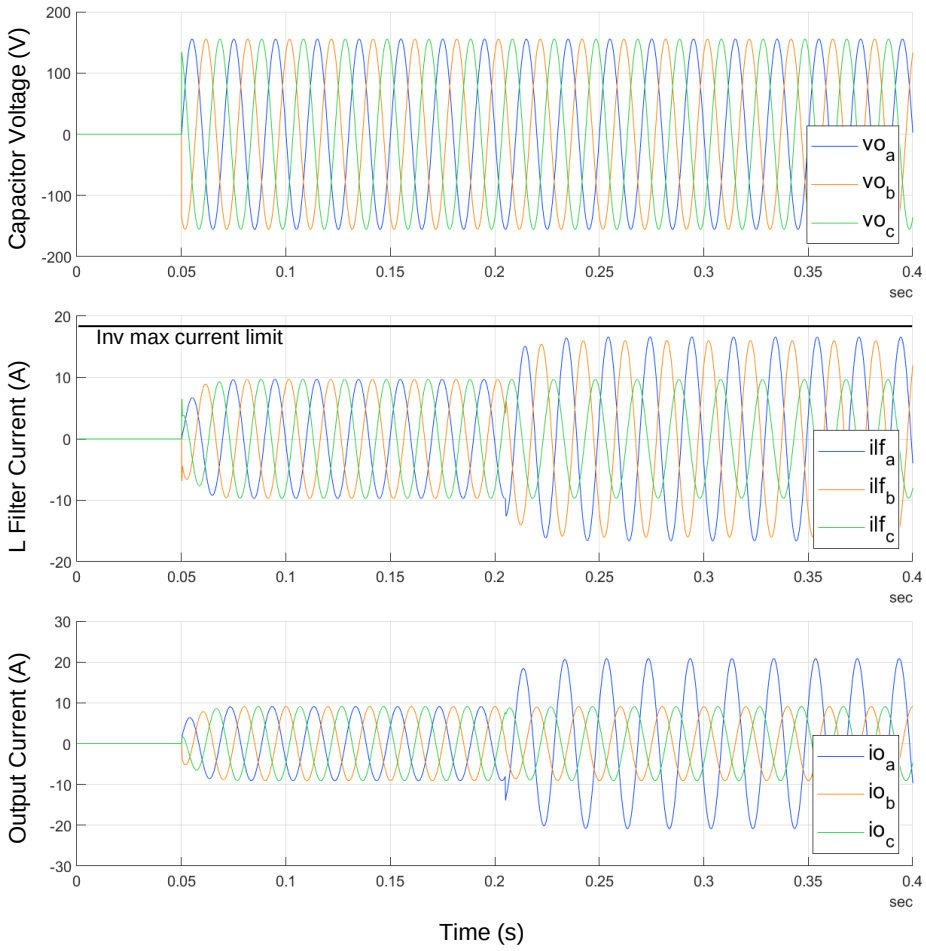

Figure 3.15: Grid forming control response to unbalance step load.

- $t = 0.05\ s$, the inverter is turned on, three phase balanced load at 50% rated power is already connected.
- $t = 0.205\ s$, single phase load of 75% rated of single-phase power is connected to the system.

The grid forming control able to maintain perfectly balance voltage despite extensive unbalance load. The single-phase load current is split into two phases by Delta-Y transformers, enabling the inverter to deliver higher current up to its single-phase maximum limit.

3.3.3 Grid following outer power loop control

The instantaneous active and reactive power can be calculated in dq frame with following equations:

$$p\,(t) = v_{load\ d}\,(t)\,i_{o\ d}\,(t) + v_{load\ q}\,(t)\,i_{o\ q}\,(t) \tag{3.11}$$

$$q\,(t) = -v_{load\ d}\,(t)\,i_{o\ q}\,(t) + \ v_{load\ q}\,(t)\,i_{o\ d}\,(t) \tag{3.12}$$

Since, the PLL ensure the direct axis to align with grid voltage, $v_{load\ q}$ can be assumed to be zero. Thus, as shown in Equation 3.11 and Equation 3.12, the active and reactive power can be controlled independently by changing i_d and i_q respectively A low-pass filter is applied to extract the average values of the active and reactive powers, allowing time scale separation between the power and current loops [164].

$$P = \frac{\omega_c}{s + \omega_c} p \tag{3.13}$$

$$Q = \frac{\omega_c}{s + \omega_c} q \tag{3.14}$$

Where ω_c is a low pass filter cutoff frequency. This cutoff frequency is set to 30 rad/s, equivalent to 100 ms time response to ensure stable operation [164], [165].

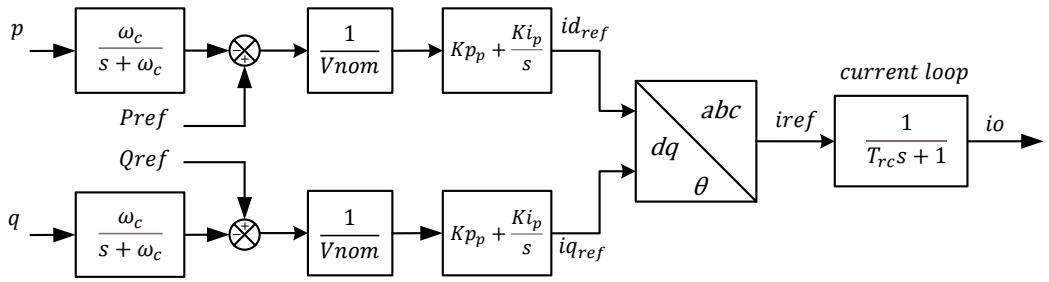

Figure 3.16: Block diagram of outer loop power control cascaded with simplified current loop

PI controller is used to track the power reference without steady state error. With a current control time response of 1 ms and a low-pass cutoff frequency of $30rad/s$, the controller gains were designed as follows to achieve a closed-loop time response of $20ms$: $Kp_p = 3.323$ and $Ki_p = 109$ Furthermore, to prevent current overload, the id_{ref} control is saturated to i_{max}, and the iq_{ref} control is saturated to $\sqrt{i_{max}^2 - id_{ref}^2}$, giving priority to active power control. Additionally, extra control loops can be integrated for the regulation of Pref and Qref. This integration facilitates rapid ancillary grid services, including frequency-active power droop and voltage-reactive power droop.

The power controller performances are verified through time domain simulations illustrated in Fig 56.

– $t = 0.08s$, inverter is turned on, active and reactive setpoint are set to 0,

– $t = 0.2s$, Pref step to 2000 W (50% of inverter capacity) is applied.
– $t = 0.4s$, Pref step to -2000 W is applied.
– $t = 0.6s$, Qref step to 2000 Var is applied
– $t = 0.8s$, Qref step to -2000 Var is applied

The power loop control attains its reference within 40 ms without any overshoot. Nonetheless, the actual response even shorter than indicated, as the measured signal depicted in the figure is subject to a delay caused by the low-pass filter.

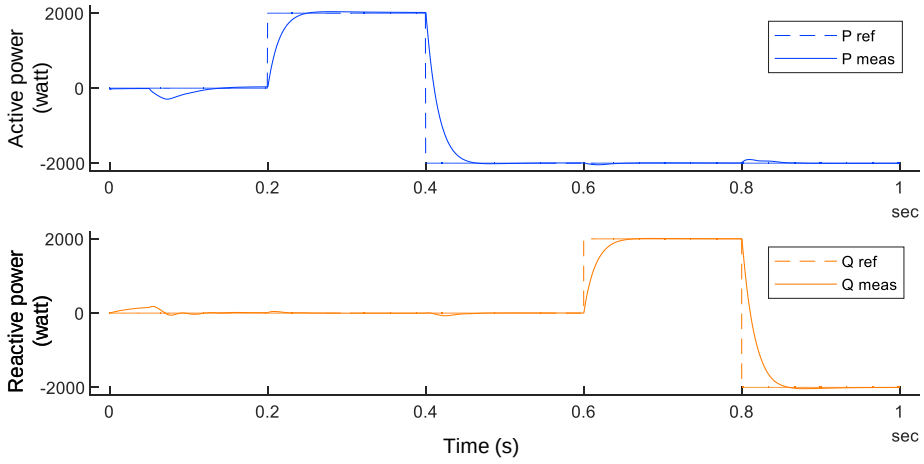

Figure 3.17: Grid following control response on power reference step

Following the design and time domain simulation validation of each control loop, Table 3.2 summarize the control parameters for the current, voltage, and power loops.

Table 3.2: Controller Parameter

Current Loop		**Voltage Loop**		**Power Loop**	
kp_c	27	kp_v	0.06	kp_p	3.323
kr_{c1}	200	kr_v1	50	ki_p	109
kr_{c5}	200			ωc_p	30 rad/s
kr_{c7}	200				

3.4 Seamless Mode Operation Transfer for Grid Loss

Let's recall the microgrid electrical topology as shown in Figure 3.18. To perform seamless transitions, BESS and fast islanding system must work in harmony. If fast-islanding system decide to island, opening the static switch, the BESS must change its control mode to the grid forming. Same applies when fast-islanding system decide to connect the critical bus to the main bus, the BESS must change its mode to grid following. The technology of static switch

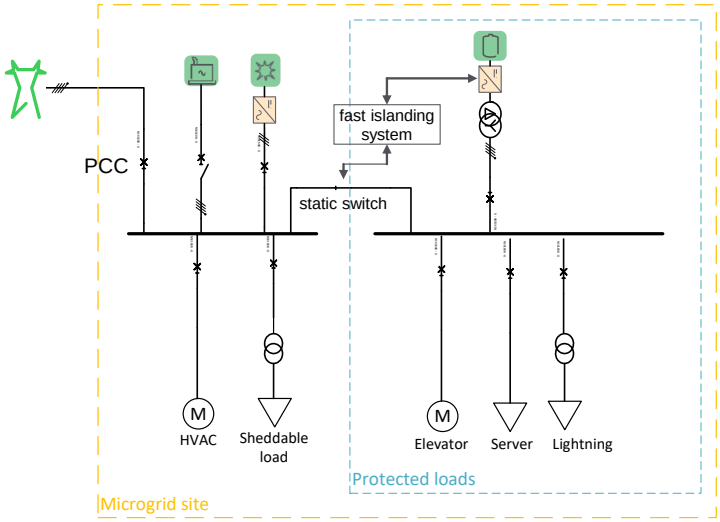

Figure 3.18: Microgrid electrical architecture to achieve seamless operation

itself plays a significant role on the transition, the slower switch open, the longer disturbance experienced by the system. Consider, for instance, a fault occurs on the "other site" of the system in Figure 3.18. Should the switch remain closed, the maximum current provided by the BESS would be insufficient to restore the voltage to its nominal value. We need also to recall that we only consider thyristor-based static switch in this thesis for the reason explained in subsection 2.3.2. Furthermore, BESS must be sized properly to at least capable to supply all critical loads.

In practical implementation, there can be a significant distance between the BESS and static switch. The main distribution board is most probably placed in electrical room, where the static switch is also installed. The BESS itself usually installed in outdoor, such as building roof to reduce the fire risk. Consequently, the fast-islanding system cannot be installed in the BESS's cabinet but rather should be installed in or near the main electrical cabinet. In this way, the fast-islanding system can be integrated into the static switch module. The status of open or close is relayed to BESS system through a robust hardwired signal allowing the BESS to change its mode. Up to this point, we have designed grid forming control and grid following control independently. Since both controls are using the same current control block, they can be combined using a switch to change its mode, as shown in Figure 3.19.

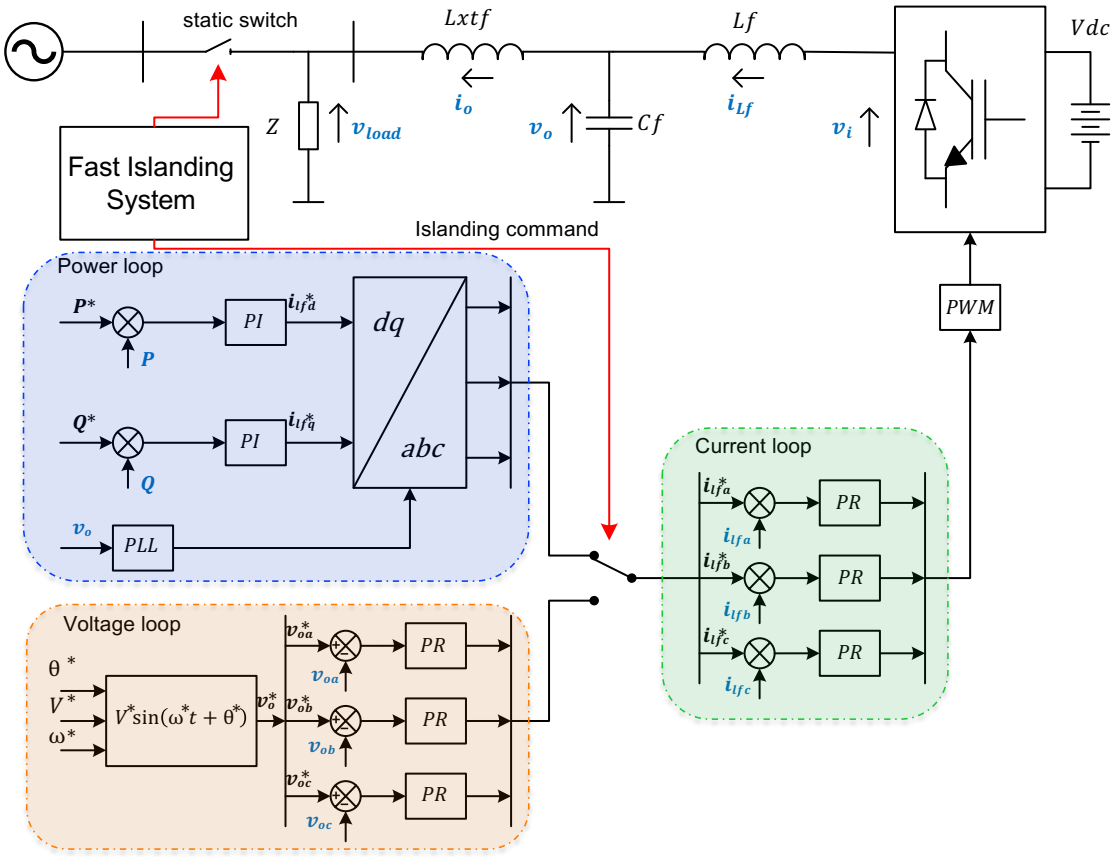

Figure 3.19: Seamless inverter control

3.4.1 Transfer strategy grid following to grid forming

The objective is to achieve fastest voltage recovery possible after the islanding signal received. We explore two transfer mode strategy: direct voltage control activation, and momentary cessation.

Direct voltage control activation (Strategy A)

In this strategy, the voltage control loop is immediately activated when islanding signal received. The voltage control loop immediately taking relay to provide current reference for the current loop. For smooth transfer, the voltage reference must start from the previous grid positive sequence angle.

Momentary cessation before islanding (Strategy B)

In this strategy, the inverter stops for certain delay before restarting its operation in grid forming mode. We assume that the critical loads are mostly power electronics-based load with constant power, therefore the load will not contribute to the short circuit during

the transition. Thus, stopping the BESS for short amount of time will leads to faster opening of the static switch.

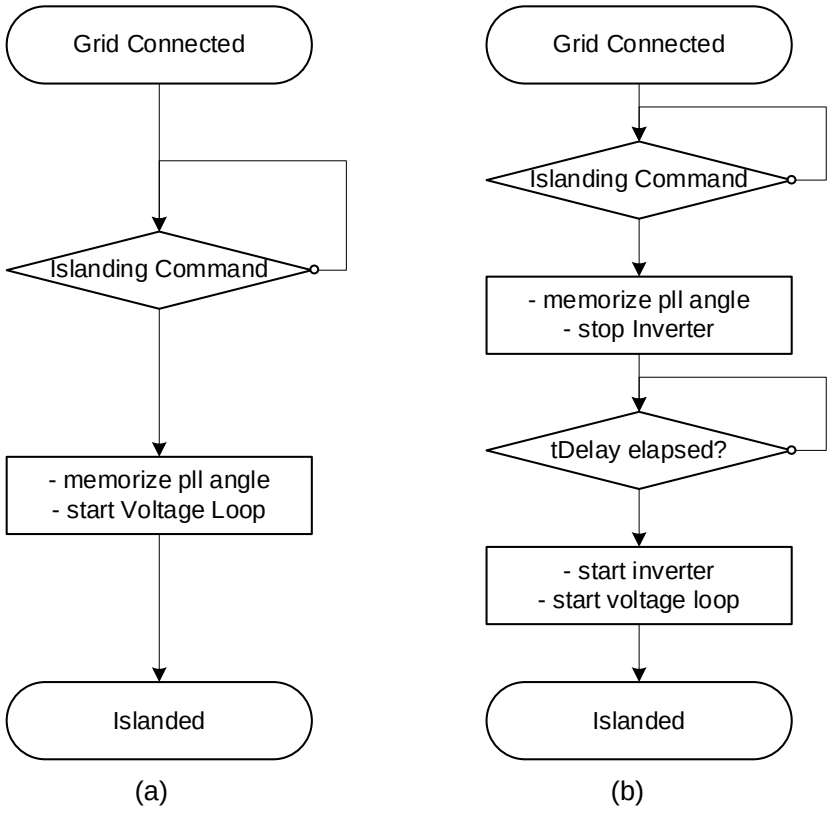

Figure 3.20: Flowchart of transfer strategy: (a) Direct voltage control activation. (b) Momentary cessation before islanding

3.4.1.1 Intentional islanding

Firstly, both control strategies are verified by performing intentional islanding, where no disturbance occurs on the grid. For this, three scenarios with different initial condition have been considered: P_{bess} and P_{load} are equal, BESS is at full charging, BESS is at full discharging. Figure 3.21 and Figure 3.22 shows simulation result for the three mentioned scenario.

- $t < 0.5s$, inverter power reference is set as per scenario
- $t = 0.5s$, islanding command followed by the opening of static switch

Simulation results of the three scenarios where initial conditions of BESS power varies is shown in left, center, and right column, respectively. The first row represents the load voltage, the middle row represents the load voltage rms, and the last row represent the inverter current. All the measurements are in per unit.

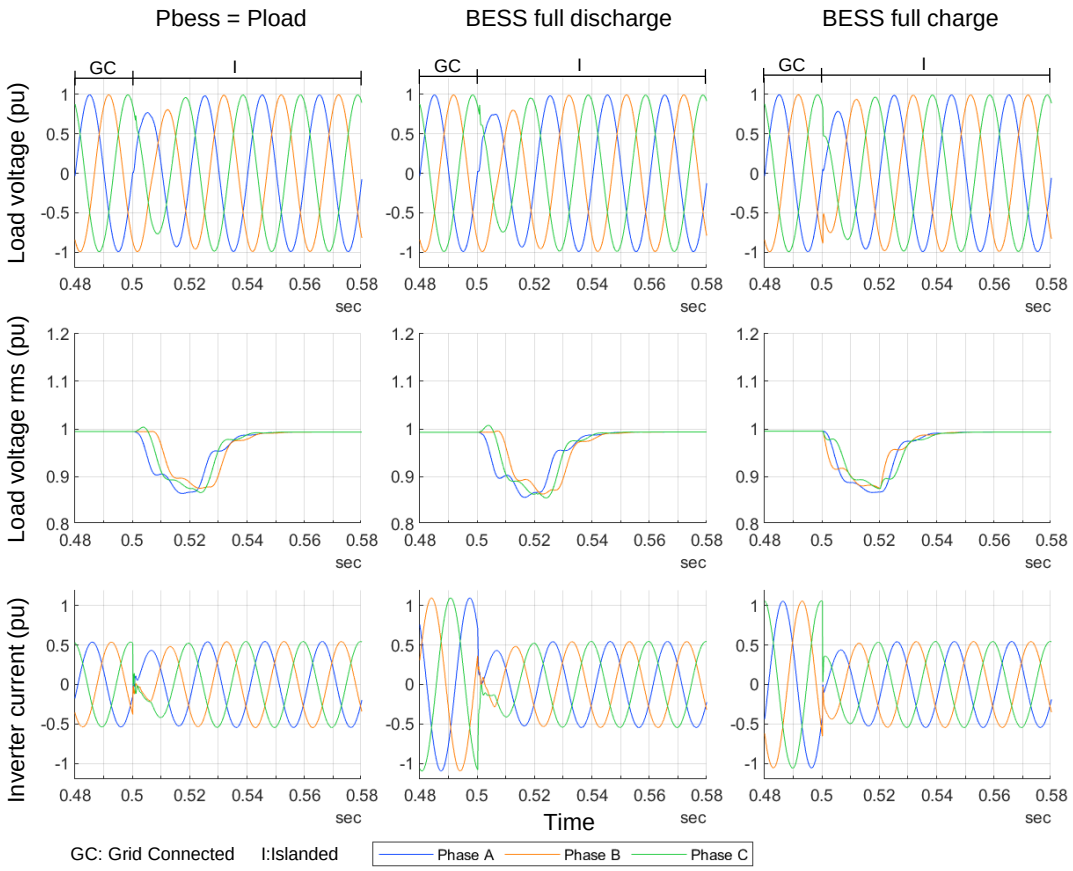

Figure 3.21: Intentional islanding simulation with transfer strategy A

For all scenarios, the transfer strategy A capable to resume grid supply with only a minor voltage drop (less than 15%) within a fundamental cycle. Furthermore, from this test, we can conclude that the inverter control respond is very fast, thus the delta power (before and after) disturbance doesn't have impacts on the load's voltage.

In contrast, the transfer strategy B have a deeper voltage decrease to almost 20%. However, from this result we can analyze that the instantaneous load voltages recovered to 70% of the voltage nominal just after the restarting.

Even though, minor disruption can be observed at load voltage for both strategy, this should not impact to the operation of critical loads as the rms voltage stay within the nominal values.

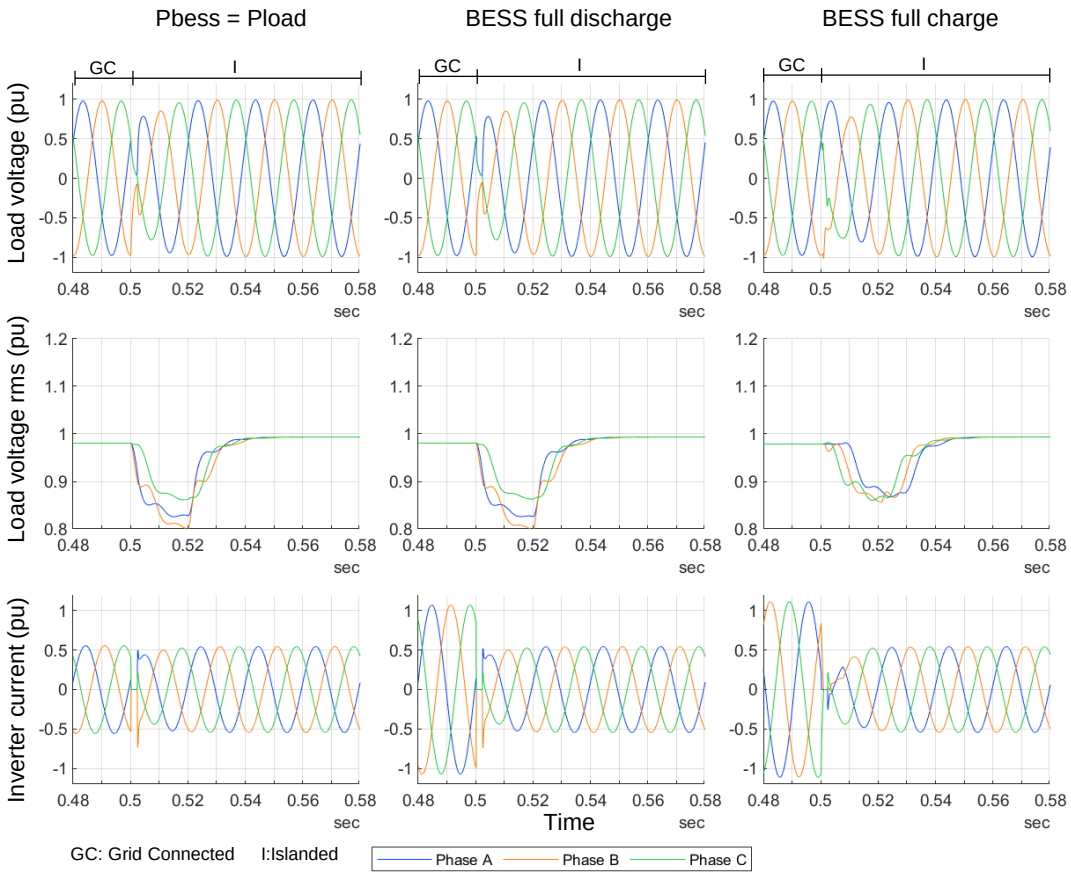

Figure 3.22: Intentional islanding simulation with transfer strategy B

3.4.2 Seamless islanding due to grid loss with strategy A

To assess the seamless performance when islanding, two simulation sets denoted as ShortSet and ComplexSet are used. These simulation sets define combinations of different initial operating conditions of the system defined as

$$\begin{aligned} \text{ShortSet} = &\{P_{load} \in 0.1, 0.5, 1, \quad \text{ComplexSet} = P_{load} \in \{0.1, 0.3, 0.5, 0.7, 1\}, \\ &P_{inv} = 0.5, \qquad\qquad\qquad P_{inv} \in \{-1, -0.5, 0, 0.5, 1\}, \\ &PoW = 0\} \qquad\qquad\qquad PoW \in \{0, \pi/5, 2\pi/5, 3\pi/5, 4\pi/5, \pi\} \end{aligned}$$

Where P_{load} is the critical load power, P_{inv} is the inverter power, and PoW is point of wave of the voltage when the grid loss occurs. ShortSet consist only three simulations to give idea of the performance of seamless transition. It consists of a typical situation with different P_{load} installed on the microgrid. ComplexSet consist of 150 simulations that cover all operating conditions in microgrid.

Figure 3.23 shows three different unplanned islanding simulation result using transfer strat-

egy A. In this test, ShortSet is used where the power of the load varies to 0.1 pu, 0.5 pu, and 1 pu for left, middle, and right column respectively. To simplify the analysis, the t=0 is aligned at the moment of grid loss. The fast-islanding system detect the grid loss at t=1ms, thus commanding the BESS directly to change its mode to grid forming.

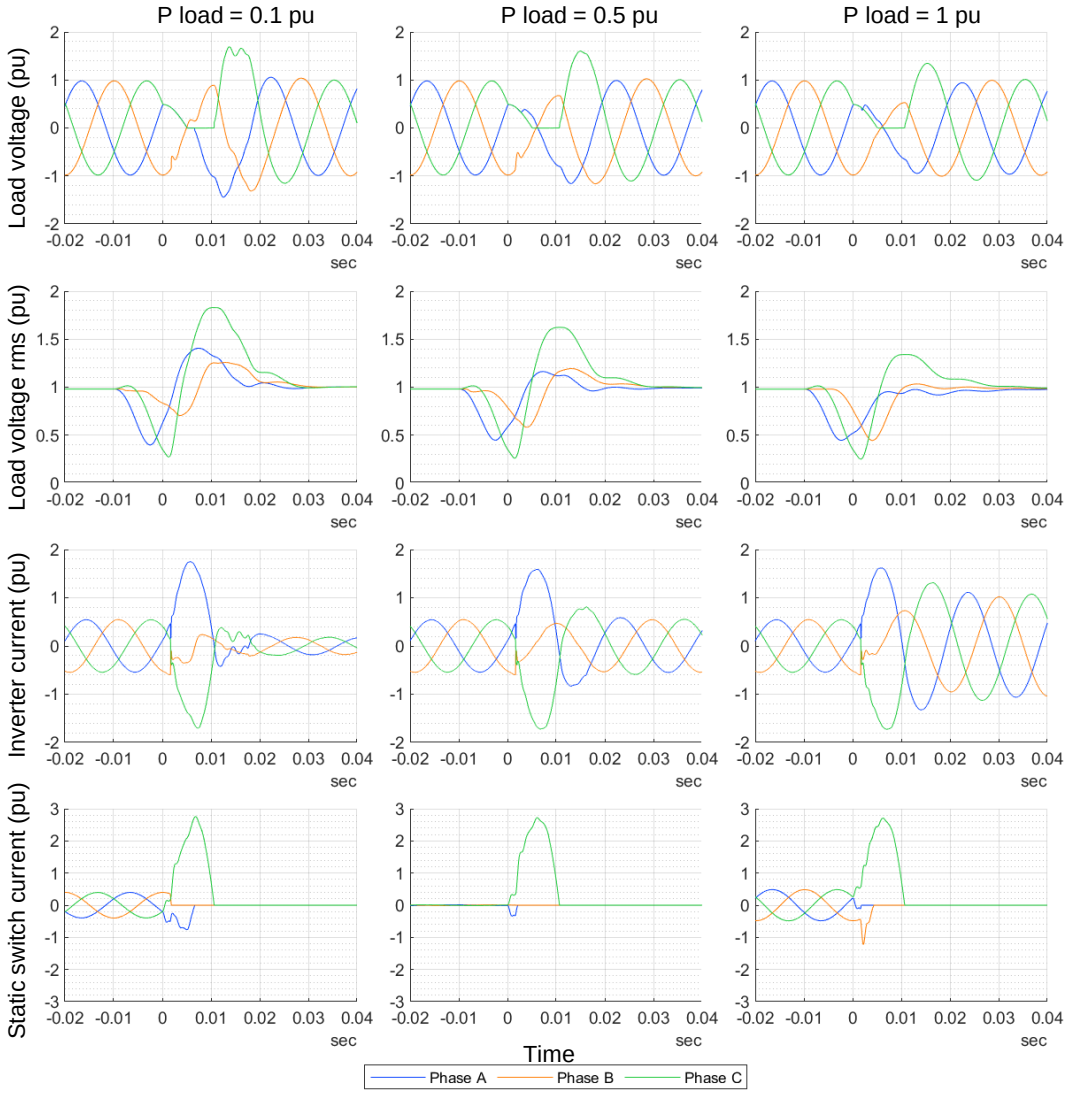

Figure 3.23: Islanding due to grid loss with strategy A for different load size scenario. $P_{ref} = 0.5pu$

For a short time before the grid loss is detected, there was no voltage source supporting the microgrid, thus the voltage will decrease to 0. The remaining voltage on the microgrid will flow to the grid, preventing the static switch to open as shown in the last row of Figure 3.23.

After the grid loss is detected, the BESS was trying to build up the voltage while the

static switch circuit has not turned off yet, in which worsening the transient condition. This condition can be mitigated in a single phase-system. Lo et al propose a static switch current compensation control which is used before going into grid forming mode [51]. The idea is to control the static switch current to 0, thus forcing the opening of the circuit. However, in our system, the transformers coupling changes the current behavior felt by the inverter. Additionally, static switch current measurement feedback to the BESS will reduce the reliability of the whole microgrid system.

In all scenarios, the instantaneous voltages at the load are seems to be recovered in 12 ms to 15 ms, although high overvoltage is observed on some phases. The IEEE 1547 only allow the voltage to exceed 1.4 pu within the limit of 3 ms. This limit is violated when the P_{load} is low compared to the nominal of the inverters. In addition, the inverter current rise to almost 2 pu for about 10 ms, which is just on the limit of the current technology of IGBT. Based on this result, we can identify seamless performance indicators as follows:

- recovery time.
- maximum transient voltage.
- maximum transient current.

To determine the recovery time, the same method of RMS calculation from UPS standards [1]is applied. In this method, the RMS is calculated using 10 ms forward sample windows [166]. The recovery time is calculated from the moment grid fault occurs to the rms voltage recovers to certain threshold, usually tolerated nominal voltage or 0.9 pu. Using this calculation, for all scenario in Figure 4.17, their voltage has recovered to 90% in less than 10 ms. Moreover, it would be fairer to compare with the UPS dynamic output performance, for example, the class 3 performance requires that the voltage to be recovered to 0.73 pu in 40 ms, as shown previously in Figure 2.7.

It is shown also from the result that the overvoltage peak value decrease with the load increase. However, it's premature to conclude that the ratio of critical load to inverter nominal power directly impacts overvoltage. Several other factors, such as initial inverter power conditions, and the point in the waveform when the fault happens, could have an influence. Thus, simulations using ComplexSet is performed to study their impact on the seamless performance. Figure 3.24 shows the impact P_{load}, P_{inv} and POW on the voltage recovery time, overvoltage, and overcurrent.

Figure 3.24 also shows the correlation of different operating values (on the x axis) with the seamless performances (on the y axis). P_{load}, and P_{inv} indicate load power and inverter steady state power at initial condition both are in per unit values, where POW indicates point of wave when fault happens in radian. I max and V max are the maximum current and the maximum voltage, respectively which are measured occurred during the transition. T_{rec7} and T_{rec9} are

[1]Uninterruptible power systems (UPS) - Part 3 : method of specifying the performance and test requirements

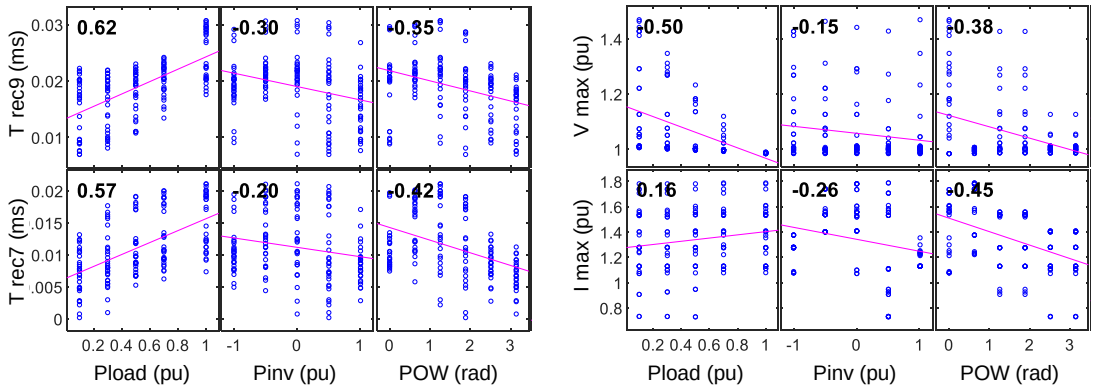

Figure 3.24: Impact of P_{load}, P_{inv}, and point of wave of fault on seamless performance using strategy A

the recovery time when rms voltage reaches 0.73 pu and 0.9 pu, respectively. Additionally, the pink line represents least square line for the data where the bold number values represent its gradient, which shows how the parameters are correlated.

From the result, the good side of this strategy is that the recovery time is quite fast, all cases shows that the voltages recover to 73% in less than 10 ms, further the voltage recovers to 90 % in less than 21 ms. However, the downside of this strategy is that 22% of the cases result in overvoltage more than 1.4 pu, some even reach 1.6 pu which can be considered as safety issues for the loads. It can be seen also that as the load increase, the voltage recover slower.

3.4.2.1 Reducing overvoltage using virtual impedance technique

From the previous simulation set, the overvoltage only occurs when current exceed 1.5 pu as depicted in Figure 3.25.

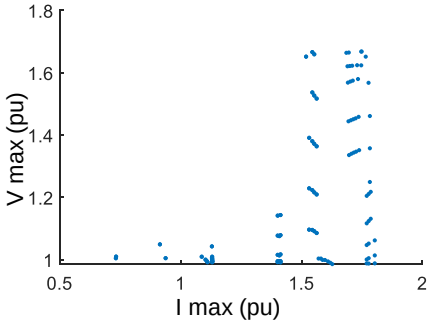

Figure 3.25: Impact of inverter current to inverter output voltage

Since there are no current limitation, the inverters back feed the grid when the static switch is not opened yet. When the static switch open, this current feeds only the critical loads, resulting high overvoltage.To resolve this issue, we use virtual impedance technique to limit the inverter current [139]. The idea is to reduce the voltage reference of the voltage loop thus limiting the inverter current as shown in Figure 3.26. If we consider a worst-case scenario of three-phase bolted fault at the output of the transformers, the virtual impedance can be designed to limit the inverter current for this condition.

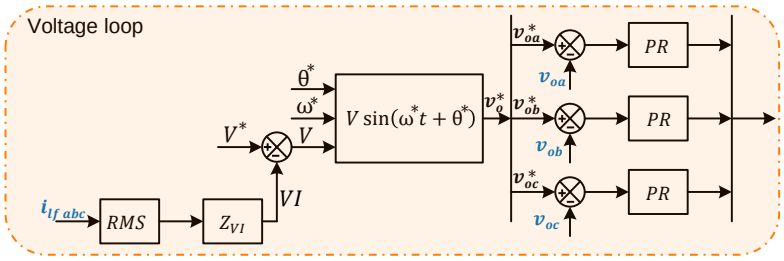

Figure 3.26: Voltage loop with virtual impedance

The virtual impedance Z_{vi} is only activated when inverter current exceeds a threshold I_{th} as

$$Z_{VI} = \begin{cases} Z\frac{I_{lf}-I_{th}}{I_{max}-I_{th}}, & \text{if } I_{lf} > I_{th} \\ 0, & \text{otherwise} \end{cases} \tag{3.15}$$

Where Imax is maximum overcurrent allowed for certain times, these values can be changed dynamically to provide a current injection without damaging the IGBT, for example 1.5 pu for 300 ms, then decrease to 1.2 pu for 2 seconds. before it decreases to continuous maximum allowable current. I_{th} is the threshold value, typically is maximum continuous allowable current. I_{lf} is the highest three phase rms current, calculated as Equation 3.16 with rms sliding window of half cycles.

$$I_{lf} = max\left(RMS\left(i_{lfa}\right), RMS\left(i_{lfc}\right), RMS\left(i_{lfb}\right)\right) \tag{3.16}$$

Thus, the virtual impedance voltage that will reduce the voltage magnitude reference can be simply calculated as

$$V_{VI} = Z_{VI} I_{lf} \tag{3.17}$$

Additionally, this virtual impedance can also be used for harmonic current sharing for parallel application in the future [167].

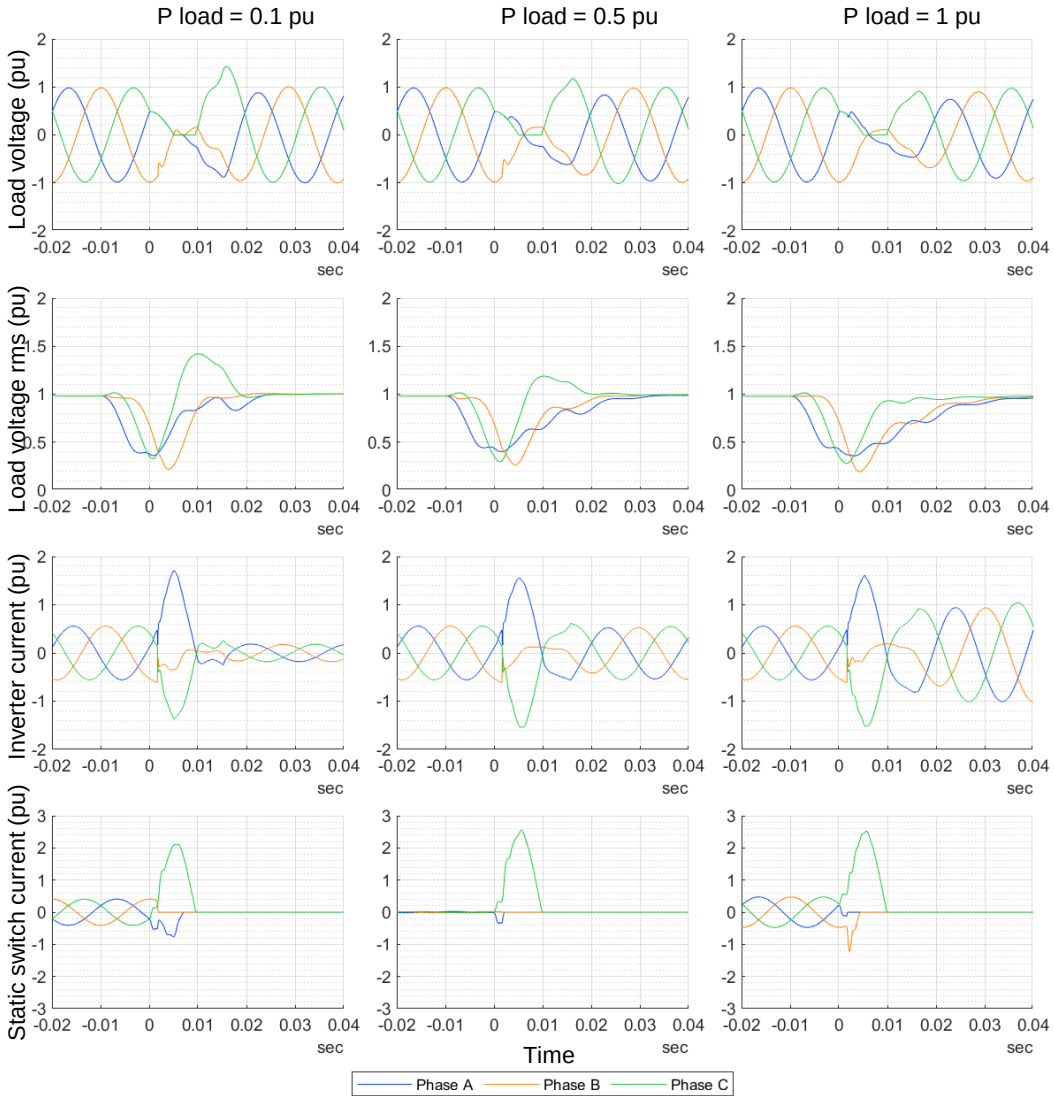

Figure 3.27: Islanding due to grid loss using strategy A with virtual impedance technique, $I_{max} = 1.3pu$, $Z_{vi} = 0.8pu$

Figure 3.27 shows the seamless transition with virtual impedance using ShortSet. At low load conditions, the transition still create overvoltage of 1.4 pu. However, this value is much lower compared to 1.7 pu from the previous strategy.

Generally, the recovery time of this strategy are slower compared to strategy A. At full load, the inverter needs more than 10 ms to recover voltage to 0.73 pu. Moreover, Figure 3.28 shows the seamless performance with different operating conditions using ComplexSet.

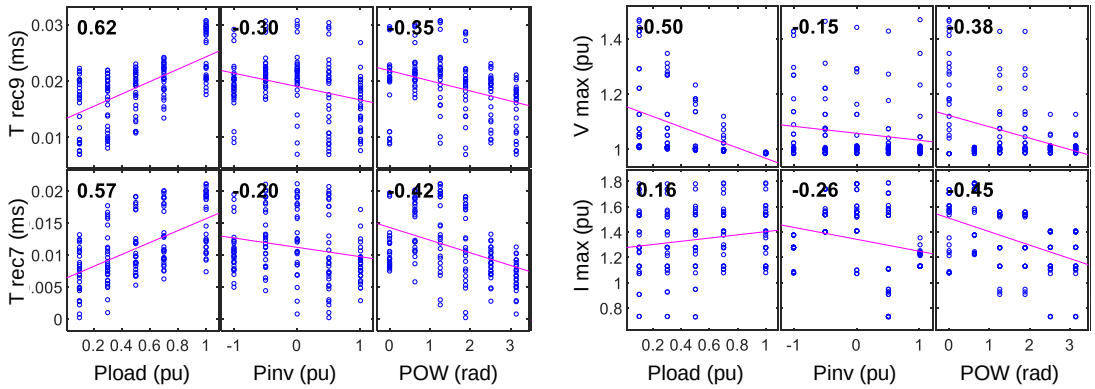

Figure 3.28: Seamless performance of strategy A with virtual impedance

3.4.3 Seamless islanding due to grid loss with strategy B

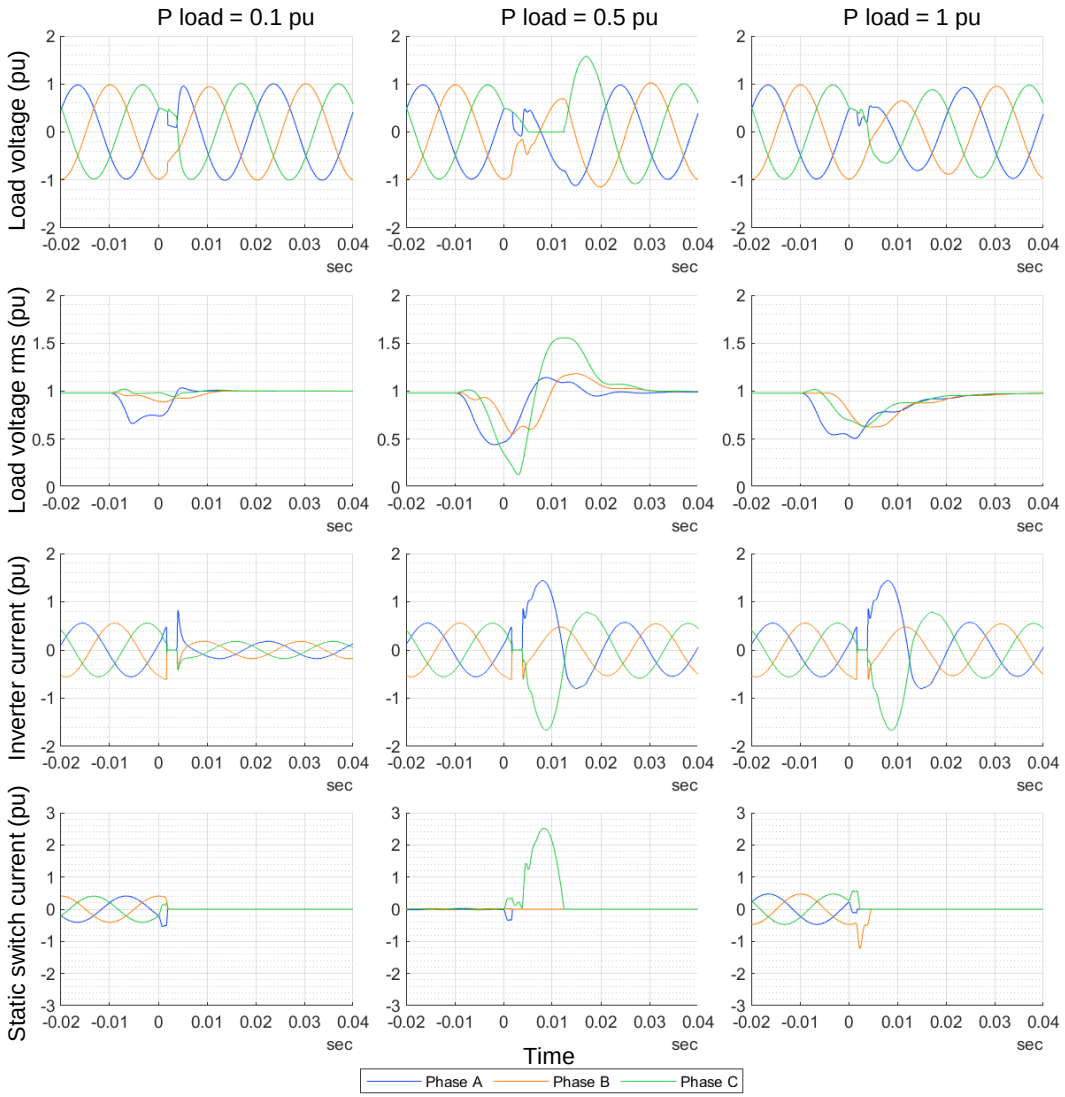

Figure 3.29: Islanding due to grid loss using strategy B

Figure 3.29 shows simulation result using transfer strategy B. In this test, ShortSet is used, the power of the load varies to 0.1 pu, 0.5 pu, and 1 pu for left, middle, and right column respectively.

With strategy B: momentary cessation before islanding, the inverter currents are "ceased" for 2 ms as shown in third row of Figure 3.29. This allows faster static switch turn off. Thus, the voltages are recovered faster. Unfortunately, this doesn't occur in every operating condition. To know more the impact of this strategy, Figure 3.30 shows the seamless performance with different operating conditions using ComplexSet.

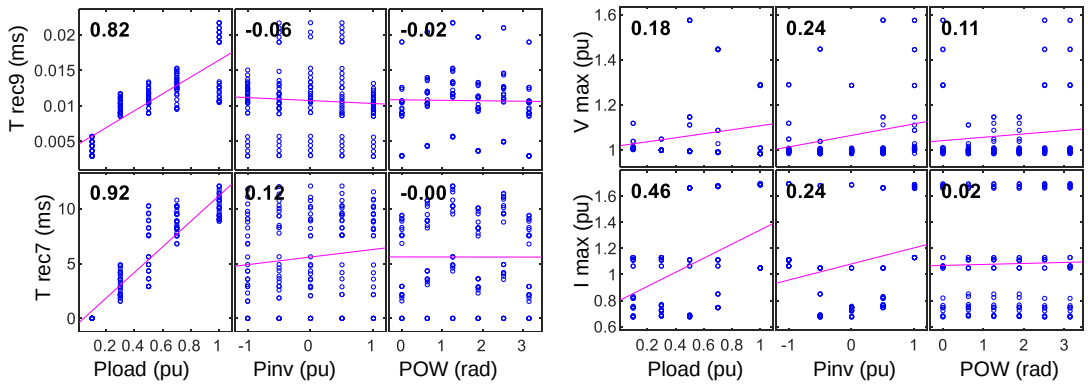

Figure 3.30: Seamless performance of strategy B

Strategy B results in fast recovery time compared with the previous strategy. However, 8% of the cases still experience overvoltage. The maximum overvoltage is 1.57 pu, that last less than 3 ms, which is still in the margin of overvoltage imposed by the standard.

3.4.4 Summary

Even though the seamless requirements that we proposed in previous chapter are challenging (10 ms recovery time to reach 73% of the nominal voltage), the simulation results shows that this can be achieved with the proposed transfer strategy for most of the cases. Figure 3.31 shows the percentages of recovery times for different strategy.

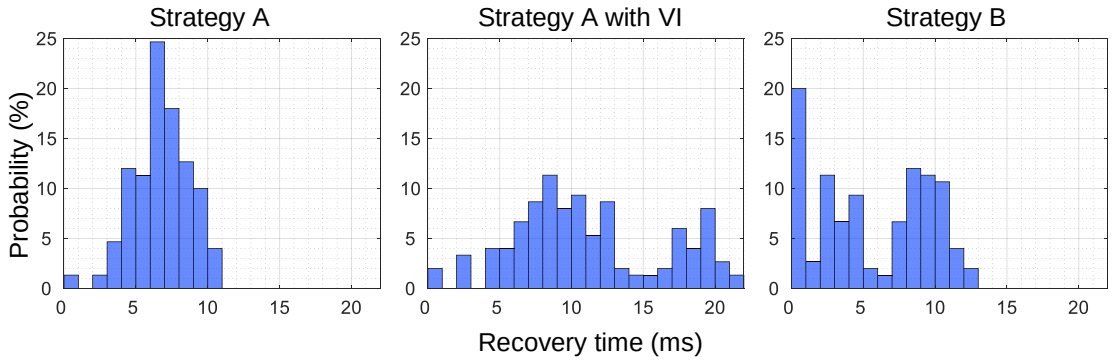

Figure 3.31: Recovery time probability occurrence for different strategy

With direct voltage control activation (strategy A), only 4% of the simulations which are exceeding the requirements by 0.9 ms. However, this strategy generates overvoltage at dangerous level which make this strategy not feasible for the implementation. The use of

virtual impedance technique can mitigate the overvoltage. However, this comes to a drawbacks of longer recovery time to almost twice longer. Only 48% cases comply with the requirements when using virtual impedance. In the worst case, the recovery time is 21 ms, which is still better than the required recovery time of 40 ms for UPS class 3 performance.

The last strategy: momentary cessation before islanding (strategy B), surprisingly has faster recovery time distribution Figure 3.31 compared to the other two. Nevertheless, overvoltage issue remains a drawback of this strategy, even though it does not exceed the limit imposed by the standard. Moreover, Table 14 shows summary of the performance of three presented transfer strategy.

Table 3.3: Comparison between different mode transfer algorithm

Strategy	**Recovery time (ms)**			**Maximum transient peak voltage (pu)**	
	Worst	Mean	Best	Worst	Mean
A	10.9	6.8	0.54	1.66	1.19
A With VI	21.1	11.2	0.19	1.46	1.05
B	12.1	5.6	0	1.57	1.06

3.5 Microgrid voltage back feed to ensure continuous operation of DERs

Up to this point, we have designed microgrid with seamless performance for the critical loads. As mentioned in previous chapter, we propose microgrid operation with the objective to ensure the critical loads operations while maintaining the support to the grid during disturbances. Figure 3.32 recalls a simplified microgrid architectures.

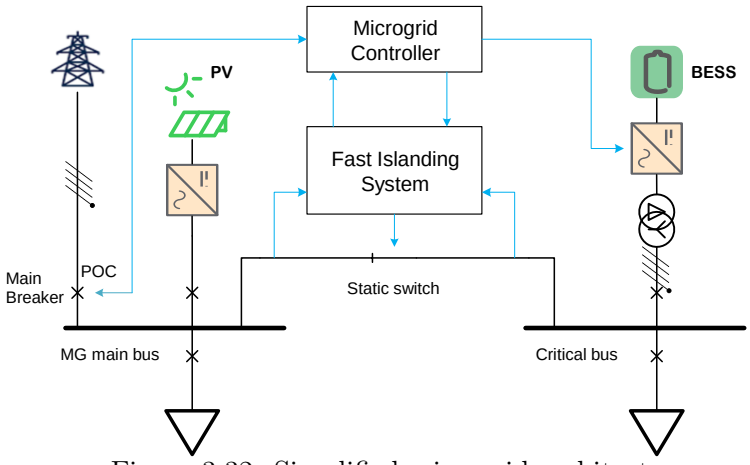

Figure 3.32: Simplified microgrid architecture

During the grid disturbances, such as voltage sag, the microgrid will be kept connected to the grid (main breaker close), while its critical busbar is protected by fast islanding system and BESS. After the FRT timer elapsed, DERs inverters will go into shutdown mode if the voltages are not recovered to certain level. To prevent this, the fast-islanding system coordinates with microgrid controllers and relay protection. The microgrid controller open the main breaker just after the FRT timer elapsed, the fast-islanding system is then closing the static switch so the voltage from the critical busbar can supply the rest of microgrid site. Of course, the microgrid controller need to calculate the power balance between the loads and productions beforehand and need to shed non-critical loads if necessary. For a comparison, Figure 3.33 shows FRT behavior of a PV inverter. In this scenario, PV inverter is connected to the grid and a three-phase fault occur at t=0.1. After the specified ride-through time of 250 ms, the PV inverter trips.

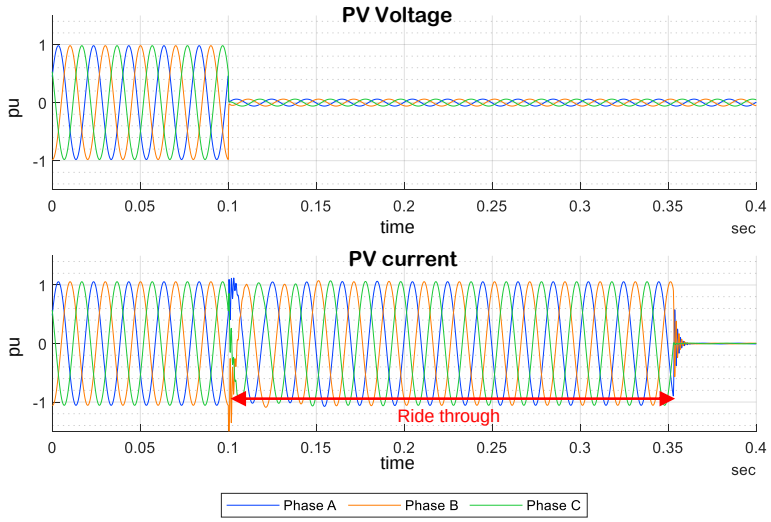

Figure 3.33: PV inverter behavior during FRT

The voltage back feed operations is verified through time domain simulations illustrated in Figure 3.34. For simplicity, following initial conditions are considered: the loads are assumed to be purely resistive and have the same nominal of 0.5 pu; the PV nominal and BESS nominal are equal. In this case, the fault ride through requirements is 180 milliseconds.

- $t = 0.1s$, grid loss occurs,
- $t = 0.11s$, voltage recovered in critical bus
- $t = 0.28$, main breaker open and voltage back feed operated,

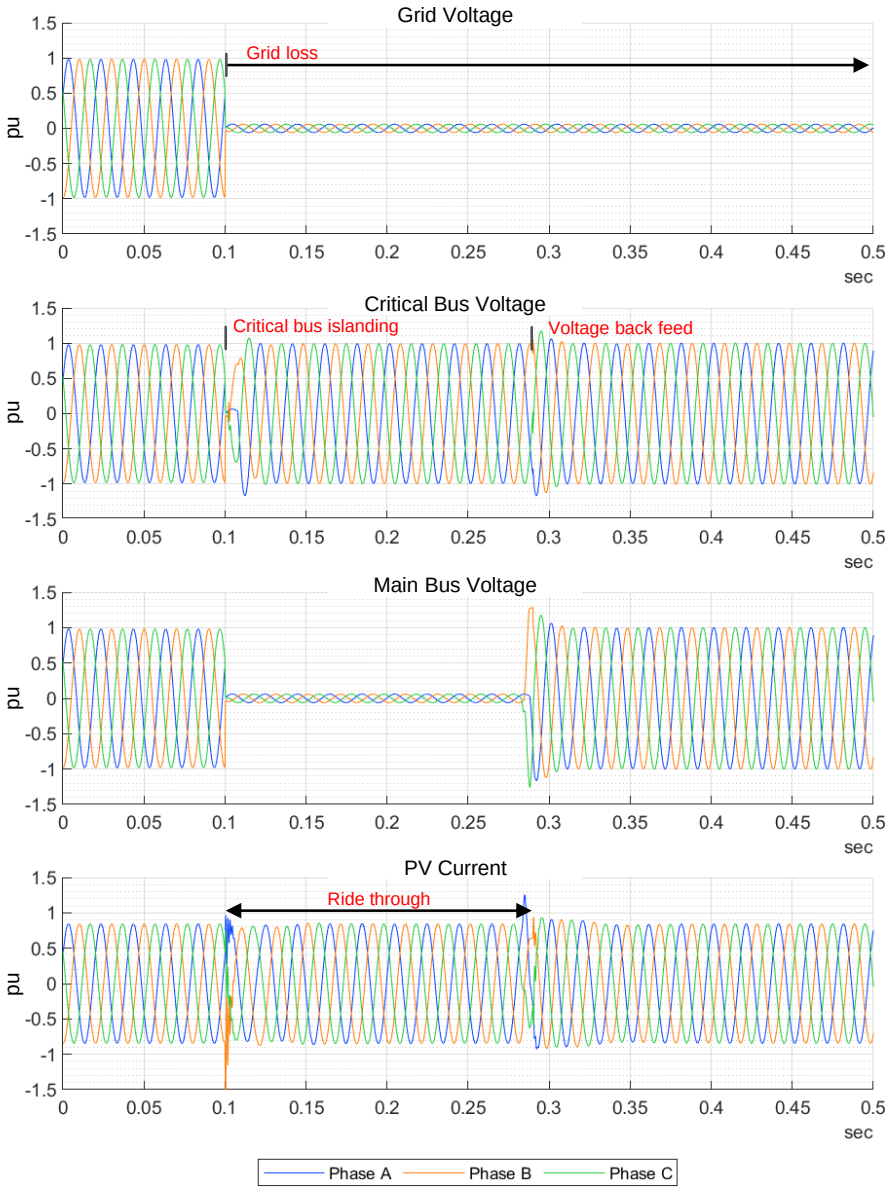

Figure 3.34: Microgrid voltages during grid loss with voltage back feed operation

Following a loss of main, the critical bus performed seamless islanding, while the main bus remained connected, allowing PV inverter to inject fault current into the grid to comply with the grid code. After 180 ms, the required duration for FRT had elapsed, the main bus was disconnected from the grid. Simultaneously, the critical bus was connected to the main bus, allowing a "voltage back feed" from the critical bus side. This operation, not only supply power to the loads on main bus but also prevented PV inverter from tripping.

3.6 Conclusion

This chapter starts with an explanation of the basis of inverter controls. The design of inverter control in grid following mode, grid forming mode and their transitions are presented. Special attention is given to grid forming control, designed to maximize voltage recovery while maintaining stability. Therefore, stiff grid forming based on PR control is utilized. While this type of controls performs very fast voltage regulation, unfortunately, it is not suitable to work parallel with the stiff grid.

It is outlined the demanding requirements for seamless transition, specifically a recovery time of 10 milliseconds to reach 73% of the standard voltage. Although this requirement is challenging, it achievable to some extent with the three strategy we have proposed. It's important to note that the performance measures used, while not the most stringent, are consistent with the usual standards in UPS technology.

Three strategies were analyzed for their performance in mitigating islanding transition due to grid loss. Strategy A, which uses direct voltage control activation, had 96% of cases comply with the requirement, but it generated dangerous overvoltage levels, making it unfeasible for implementation. Employing virtual impedance techniques within strategy A, mitigated overvoltage but had a longer recovery time, with only 48% of cases complying with requirements. Lastly, Strategy B, involving momentary cessation before islanding, surprisingly had a faster recovery time distribution compared to the other two strategies but still suffered from overvoltage issues within acceptable limits. Overall, none of the strategies were without drawbacks, but Strategy B showed promise in terms of recovery time while staying within acceptable overvoltage limits. Safer options can be chosen to implement Strategy A with virtual impedance, since the recovery times are still better than Class 3 UPS performance.

Simulations have confirmed that not only can a seamless transition be achieved within 10 ms, but also that microgrid systems can comply to the necessary grid codes. Furthermore, the operation of voltage back feed has also been demonstrated to be effective in preventing trip of DERs due to grid loss. The works in this chapter is part of thesis contribution C3 and C4. Taking practical considerations into account, Chapter 4 introduces a small-scale validation of the proposed systems.

Chapter 4

Experimental Validation of Microgrid Seamless Operation

Contents

4.1 Introduction

This chapter provides experimental validation of the various control algorithms developed in this thesis to demonstrate their effectiveness. The microgrid demonstrator was designed using Power Hardware in the Loop (P-HIL) technology and real equipment to closely replicate the behavior of a real microgrid building. The developed control algorithms were prototyped using model-based design approach. In this chapter, three main experiments are outlined:

- Prototyping of a fast-islanding system.
- Prototyping of a BESS inverter with seamless capability of 10 milliseconds.
- Full systems validation on microgrid seamless operation.

4.2 P-HIL test bench description

4.2.1 General description

During the experimental testing phase, certain equipment limitations were encountered, necessitating adaptations to the initial control strategy outlined in Section 3. This section will describe the details of experimental setup along with each component limitations. Figure 4.1 shows the overall microgrid test bench setup, which comprises the following components:

- Voltage source converter test bench (1)
- Fast islanding system prototype (4)
- Static switch (6)
- Transformers (5)
- Loads (7,11,12) and electronic appliance (9,10)
- Grid emulator, consist of real time simulator (14) and linear power amplifier (13)
- DC sources (8)
- PC development (2) and oscilloscope (3)

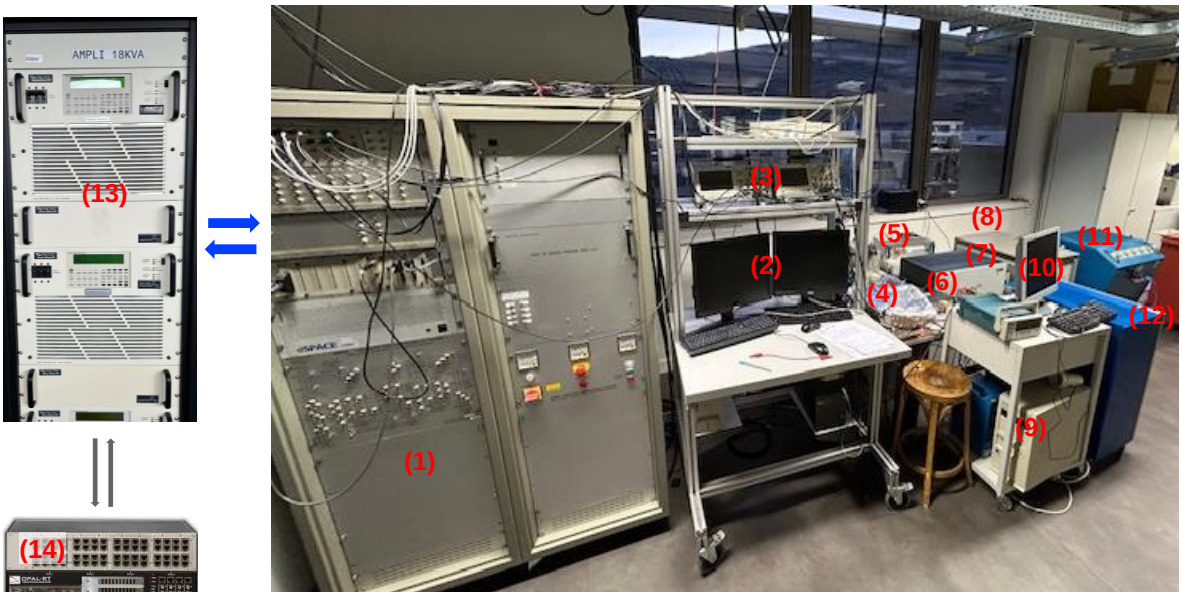

Figure 4.1: Microgrid demonstrator experimental setup

The functional schematic of the experimental setup is detailed in Figure 4.2. Unlike a simulation, the measurement point of the experimental setup is limited by the availability of voltage and current sensor. In this setup, $vo, io,$ and ilf are measured by the internal circuit of the VSC test bench. While mv_1, mv_2, mc_1 and mc_2 are measured using external isolated voltage sensor or current sensor. These external sensors are then feedback to the dSPACE to be sampled at 10 kHz. For each measurement point ($mv_1, mv_2, mc_1,$ and mc_2), three sensors are used to measure each phase.

In Figure 4.2, from left to right, the setup begins with the OPAL-RT 5600 real time simulator and Pacific AMX 360 linear power amplifier, which are used to emulate the grid and a grid loss event. Following this, the Fast-Islanding System (FIS) measures the grid voltage (mv_2) and the critical bus voltage (mv_1), and it controls static switch (c_1) to close or open. The same command is also sent to the converter as an islanding command.

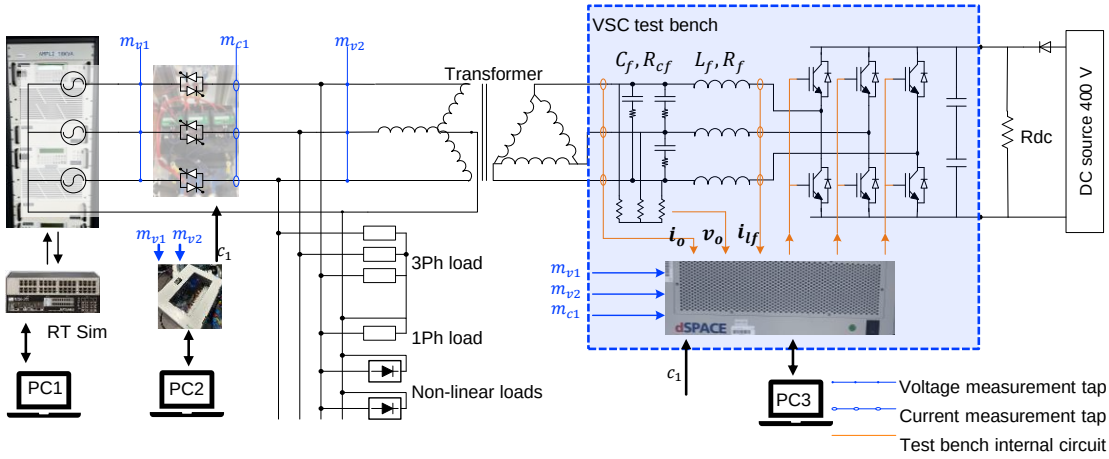

Figure 4.2: Functional schematic of seamless demonstrator

Behind the static switch is the critical bus where critical loads such as personal computer (PC) and monitors are connected. Single phase and three phase variable resistive load are also connected to this bus to test the system.This critical bus is connected to Y side of transformers which provide the neutral connection, where the Delta side of transformer is connected to the converter.

The voltage source converter test bench consist of two 2-level NPC VSC in back-to-back configuration, an internal LC filter, and DSPACE 1007 control board. This test bench setup has been successfully proven for flexible real-time control testing [168]–[171]. In this experiment, only one two-level VSC is used. The inverter control designed in chapter 3 is deployed to the DSPACE using Matlab code generation. This DSPACE boards are controlling the IGBT module. To emulate the battery, a unidirectional DC voltage source Xantrex XDC 600-20 is paralleled with dc load bank. This configuration allows the charging current from VSC to be discharged to the load bank.

Table 4.1: Nominal rating of the test bench equipment

Rating	Units	VSC	Linear Amplifier		Transformers	
			Inject	Absorb	Prim	Sec
Power	kVA	5	18	3.6	7.5	
$V_{\text{ac line-neutral}}$	V	231	135		246	231
Current	A	20	48	9.6	19	18
V_{dc}	V	800				

The rating of VSC, transformers and AC amplifier is detailed in Table 4.1. Due to the voltage limitation, the microgrid system is derated 110 V- 50 Hz ac system for the experiment. In our lab, the only available transformer has one to one winding ratio, which create $1 : \sqrt{3}$ voltage ratio with Delta-Y connection. As a result, the voltage of VSC is stepped down to 63 V line-to-neutral due to the transformer's voltage ratio, which consequently reduces its maximum power to 4 kVA. Moreover, Figure 4.3 shows transformers equivalent model and its parameter, which are derived from the open circuit and short circuit test. Transformers inductance equivalent is then use for inverter controls tuning.

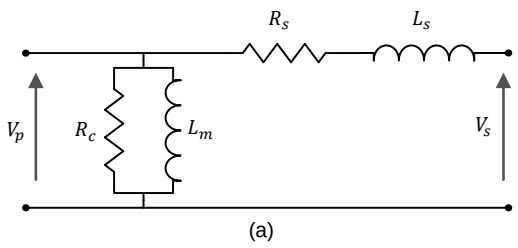

(a)

Parameter	Value
Nominal power	7 kVA
Nominal voltage	231/246 V
Windings ratio (n)	1:1.06
Inductance eqv (Ls)	3.5 mH
Resistance eqv (Rs)	0.36 Ohm
Magnetic inductance	4.1 H
Core resistance	5297 Ohm

(b)

Figure 4.3: Transformers equivalent model (a) and their parameters (b)

4.2.2 Supervisory control and data acquisition

The experimental setup, as illustrated in Figure 4.2, comprises three different development PCs and multiple measurement points. PC1 initializes the grid emulator through RT-LAB software, whereas PC2 controls and monitors the fast-islanding system. Supervisory control and data acquisition are developed on PC3 using Control Desk software, enabling the synchronized measurements of the systems. Measurement points are sampled by DSPACE at a 10 kHz sampling rate.

4.2.3 Fast islanding system prototype

Fast-islanding system (FIS) is intended to operate within microgrid as depicted in Figure 4.4, primarily to manages the static switch. By the authorization from the microgrid controller,

the FIS responsible of opening or closing the static switch. FIS encompasses three primary functionalities:

- Grid loss detection
- Passive synchronization with the grid
- Ensure voltage feedback operation

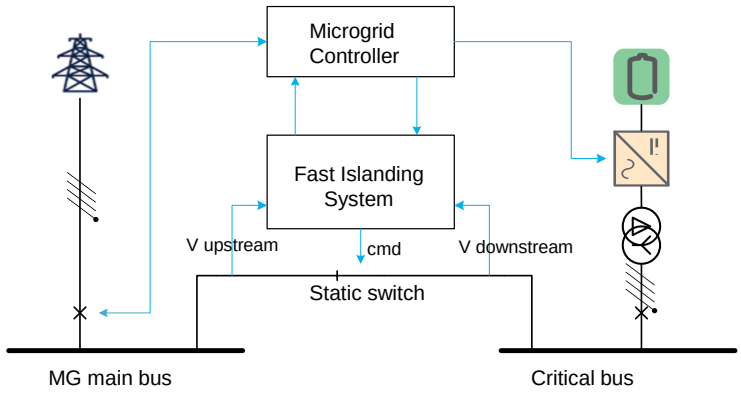

Figure 4.4: Fast islanding system functions within microgrid

The grid loss detection algorithm developed in Chapter 2 is implemented into the fast-islanding system. The fast-islanding system consists of voltage sensors, an analog amplifier for signal conditioning, a digital signal processing (DSP) board, an optocoupler to provide isolated output signal and a power supply as shown in Figure 4.5. Two 4-channel voltage sensor Isoblock V 700 are used. This voltage sensor provides 100 kHz bandwidth, isolated galvanically, and 0.15 V measurement error at to measure 110 V. The sensors yield a full range output of 10 Vac, which is processed through an analog amplifier for gain and offset adjustment, resulting in a voltage range of 0 to 3.3 V that can be sampled by the DSP. Following DSP processing, optocoupler is used to isolate the output and deliver higher current of 24 V to control the static switch.

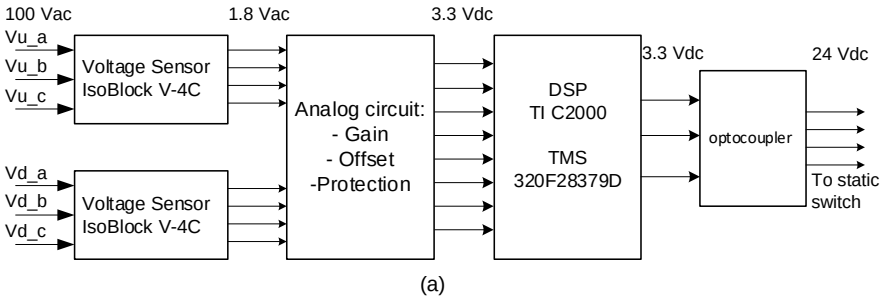

(a)

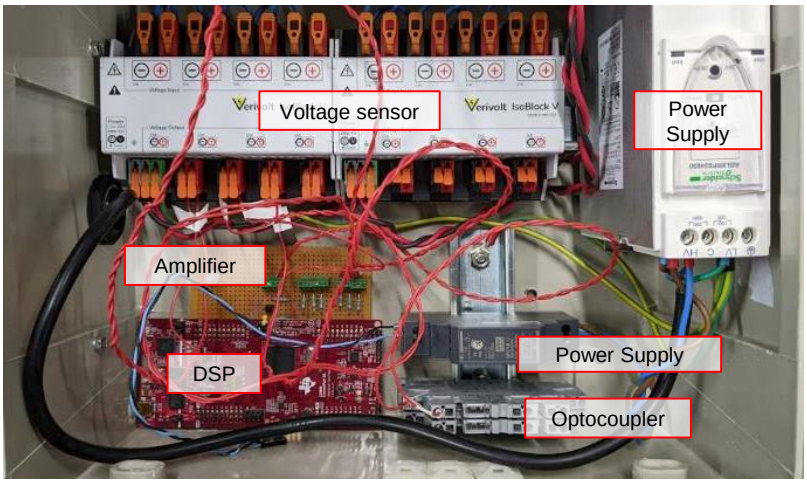

(b)

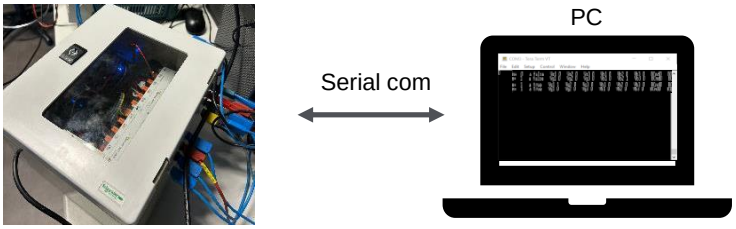

(c)

Figure 4.5: Fast islanding system. (a) schematic. (b) the prototype. (c) interface with the PC

For the operation, the system is interface with a PC via serial communication, enabling basic command and system monitoring. It operates in manual and auto mode: in manual mode, the static switch is controlled on closing command from the PC, while in auto mode, control follows the flowchart depicted in Figure 4.6. To prevent the closing of the two sources in out of phase, protection like sync check, dead upstream or dead downstream is used.

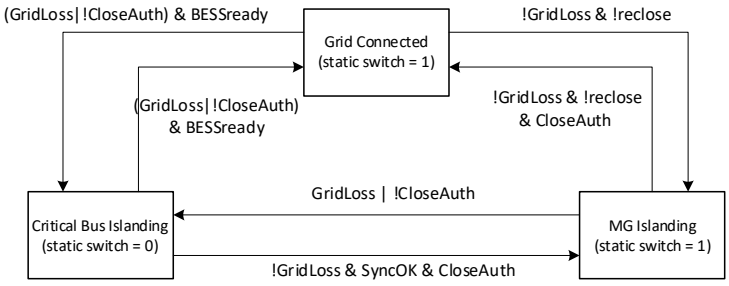

(a)

Signal Name	Origin
StaticSwitch	output
GridLoss	measurement
SyncOK	measurement
DeadUp	measurement
DeadDown	measurement
CloseAuth	input
BESSready	input
reclose	input

(b)

Figure 4.6: (a). Flowchart of fast islanding system's operation in auto mode. (b) signal descriptions

The fast loss of main detection algorithm is deployed to DSP using Simulink Embedded Coder. To sampling the voltage, 12-bit of 6 channels analog to digital converter (ADC) is used. Assuming linear gain from analog amplifier are not interfering with the accuracy, the total measurement error is estimated around 0.3 V. The signals measured from ADC is filtered with lowpass filter of 2 kHz. While ADC and filter are set to run at 20 kHz, the algorithm itself it's set to run at 10 kHz. Setting the algorithm to 20 kHz will overload the DSP. Moreover, serial communication block is developed to control and monitor the FIS.

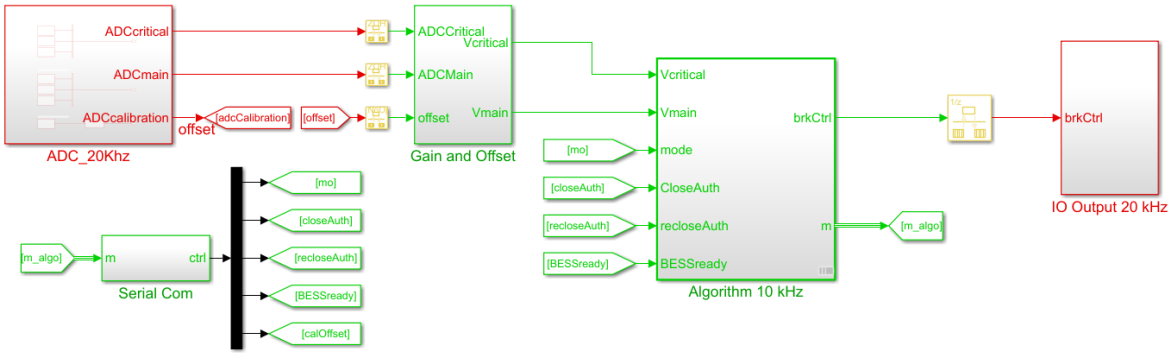

Figure 4.7: Algorithm deployment using Simulink Embedded Coder

4.3 Validation of fast detection of loss of main

4.3.1 Test setup

The prototype of the fast-islanding system is independently evaluated using a grid emulator. Figure 4.8 illustrates the test setup for validating the fast-islanding system. A grid emulator,

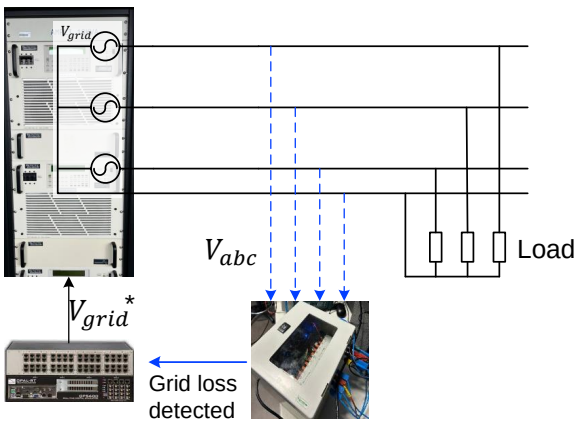

Figure 4.8: Test setup for fast islanding system validation

controlled by OPAL-RT is used in series with a three phase loads. The FIS measures the three-phase neutral voltage. When a grid fault is initiated by the OPAL-RT, the FIS is sending the

grid loss detected signal into the OPAL-RT this time delay is then measured as a detection time. In this setup, the OPAL-RT is running at 20 kHz sample rate, which results in a time measurement error of $\pm 5\mu s$.

4.3.2 Detection curve

Similar to the simulation test performed in chapter 2, the FIS is tested on different sag magnitude and point of wave. However, to reduce the testing time, the testing sets is reduced and only the most polluted public grid voltage conditions characterized by the THD of 10% is considered.

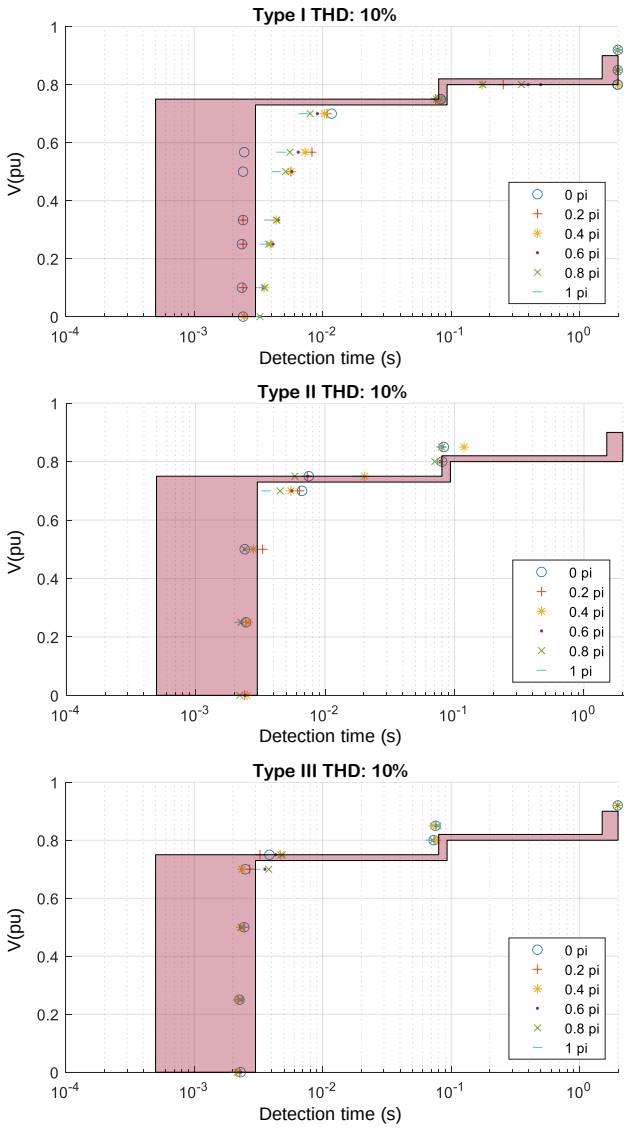

Figure 4.9: Detection curves of Fast Islanding Systems for different voltage sag types

Figure 4.9 shows the detection curve, indicating the time required to detect the loss of grid caused by voltage sags of various types and magnitudes, occurring at different points within the wave cycle. From Figure 4.9, it is apparent that some of test results do not meet the performance criteria indicated by the red area. Specifically, there are a few false negative results for tests involving sag types 2 and 3, whereas tests with sag type 1 yield several false positive results. Nevertheless, the majority of the results comply with the detection performance criteria.

4.4 Validation of grid forming and grid following control

4.4.1 Adjustment of control parameters

The constraints of certain components necessitated adjustments to the system parameters outlined in chapter 3, for two primary reasons: First, the experiment VSC test bench was designed with an LC filter rather than an LCL filter. Thus, the typical values considered in initial design are inaccurate. Second, the transformer available was found to be significantly large for the system's requirements. Consequently, the modified system parameters for the experimental setup are detailed in Table 4.2.

Table 4.2: Converter parameter for experimental setup

Converter Parameter	**Value**	**Control Parameter**	**Value**
Nominal Frequency	50 Hz	Current loop	
Nominal Power	3 kW	kp_c	40
Nominal phase-neutral voltage	63 V	kr_{c1}	200
Switching frequency	10 kHz	kr_{c5}	200
Filter inductance - L_f	3 mH	kr_{c7}	200
Filter resistance - R_f	0.04 Ohm	Voltage loop	
Filter capacitance - C_f	56 μF	kp_v	0.06
Filter damping - R_{cf}	10 Ohm	kr_{v1}	50
Transformers winding connection	63/110 V D/Y	Power loop	
Transformers eq inductance - L_{xtf}	3.5 mH	kp_p	0.02
Transformers eq resistance - R_{xtf}	0.36 Ohm	ki_p	100

4.4.2 Grid forming validation

4.4.2.1 Issues on unbalanced duty cycle due to sensor calibration error

When the inverter operates in grid forming, supplying power to a three-phase balanced load, it was observed that the duty cycle calculated by the control are not balanced, as shown in

Figure 4.10. Despite the output voltage and current generated by the inverters being perfectly balanced, the inverter's duty cycles diverged after the startup.

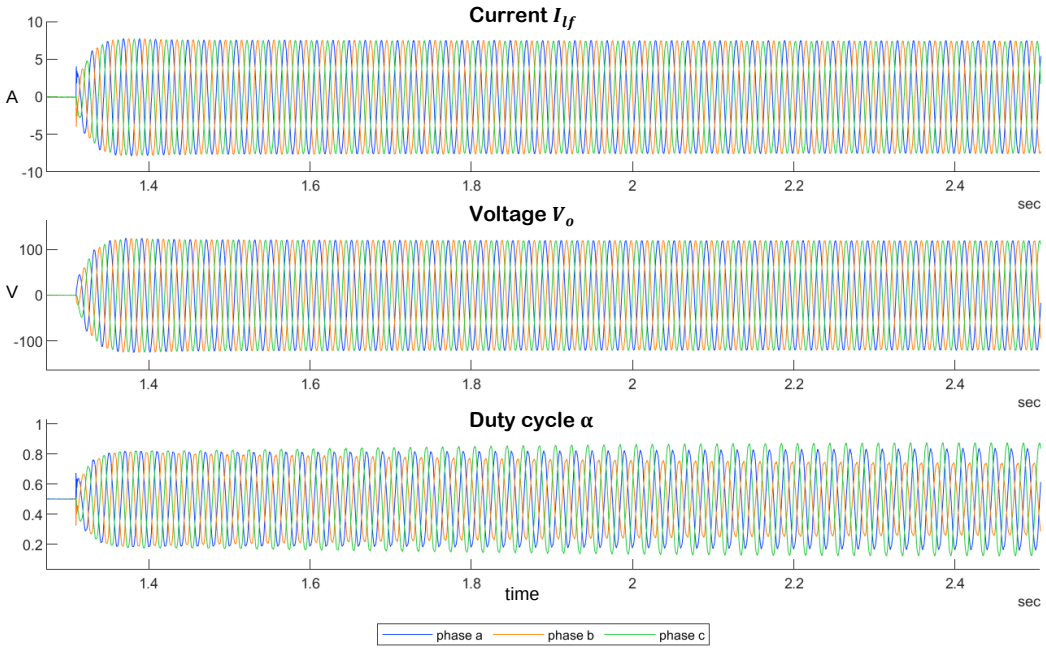

Figure 4.10: Unbalanced duty cycles due to measurement error.

It is worth noting that overmodulation is not employed in the control scheme. Therefore, this issue lies within the control of the voltage loop. It turns out that the issue is due to the error of voltage measurement. A minor error of the voltage measurement gain, as small as 0.3% leads to significant deviations in the control output, exceeding 25%. As shown in the Figure 4.2, the inverter is connected to Delta side of transformer. Thus, resistors are used to create an artificial neutral for the voltage measurement (V_o). When these resistors are not balanced, the control will see it as a disturbance, thus resulting the output deviation. The lesson learned from this issue is the necessity of implementing auto calibration of the measurement, taking into account the aging of the resistor, which may vary from one to the others.

4.4.2.2 Voltage step

Fig 10 shows dynamic response as a result of voltage setpoint change from 115V to 130V, equivalent to 13% voltage increase. The voltages reach steady state within 50 milliseconds. In this test, the inverter is loaded with 25% of its maximum power. The instantaneous value is displayed in left column and rms value is shown in right column.

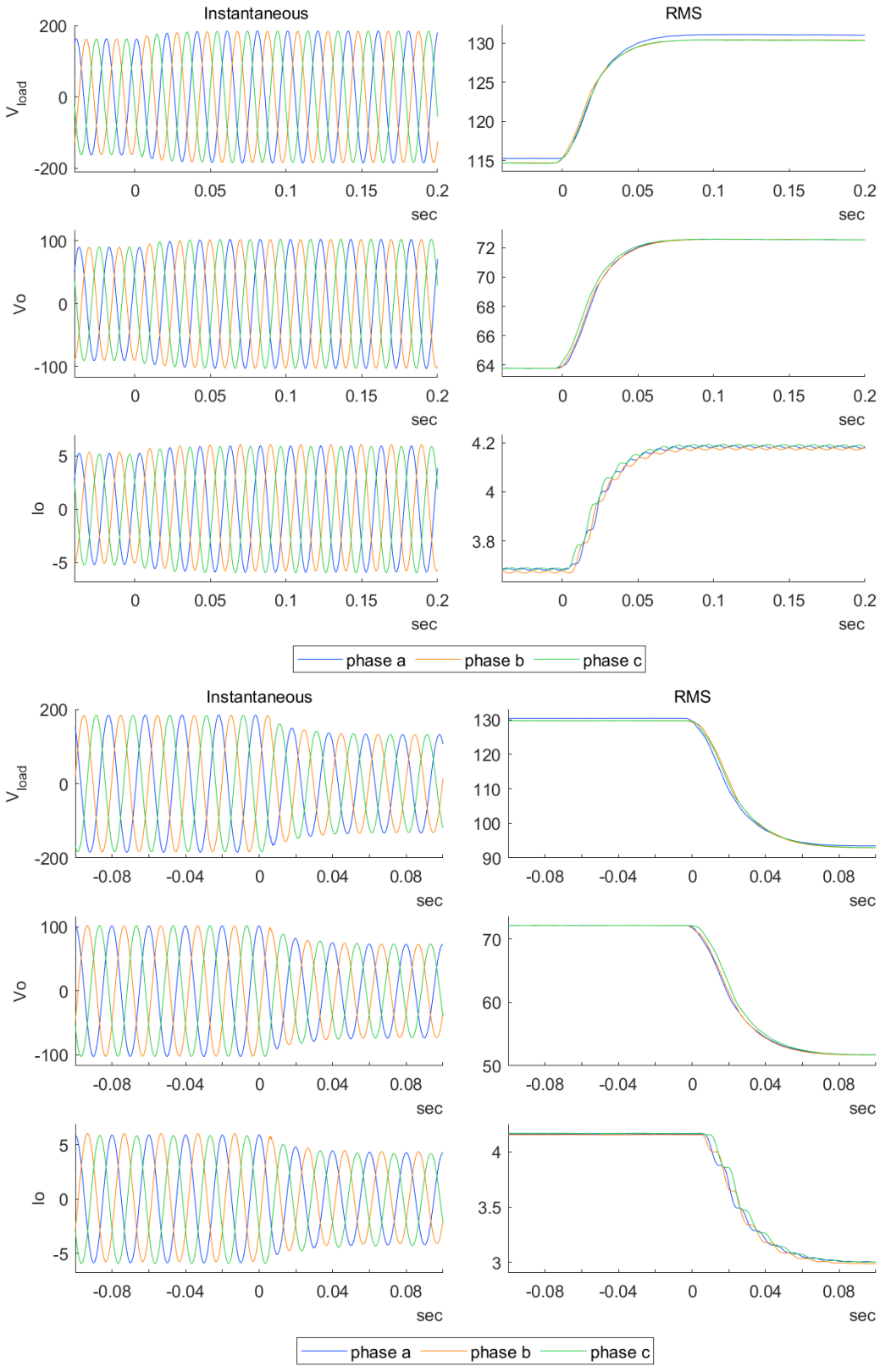

Figure 4.11: Grid forming control response on voltage reference step. (top)step up from 115V to 130V, (bottom) step down 130V to 93V.

4.4.2.3 Load step

In Figure 4.12 shows the grid forming control response to the unbalanced load and a load step.

- At initial conditions, the inverter is turned on, with a three-phase balanced load of 450W (15% of Prated) already connected. Additionally, a single-phase load of 760W (25% of Prated) is already connected to phase C of the inverter.
- $t = 0s$, 450W three phase load is connected to the system.

As can be observed from the results, a 10% voltage drop occurred during the load increase; however, the voltage recovered in less than 50ms. In addition, as we can see from the result that the inverter can provide unbalance current. Because of Delta-Y connection, the single-phase load's current is split into two phases on the inverter side. Even though that the unbalance current is still significant, the inverter is able to compensate the output current.

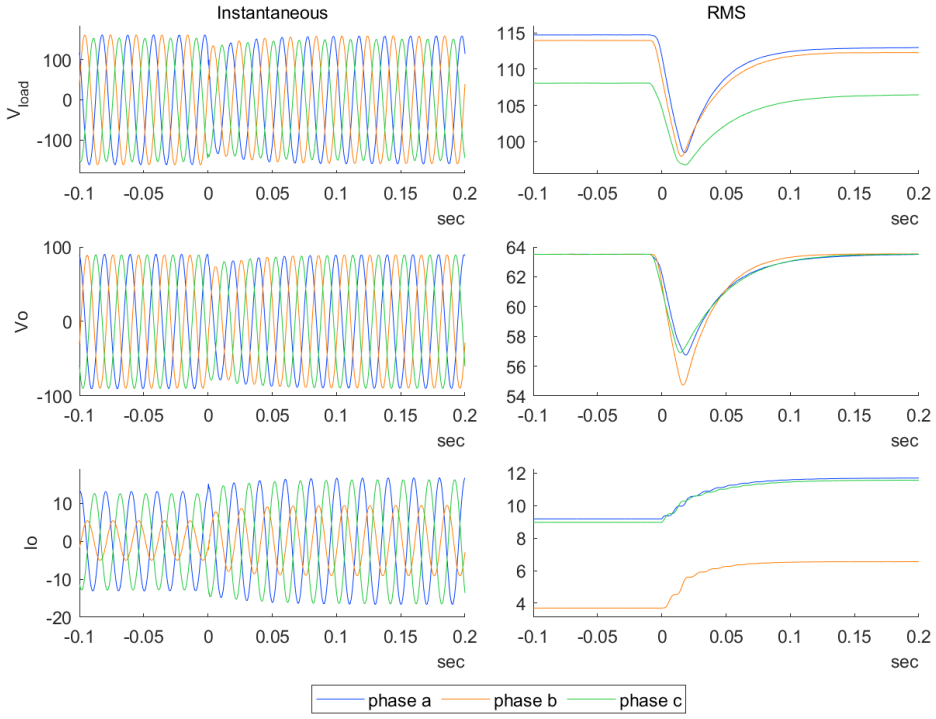

Figure 4.12: Grid forming control response to unbalance and step load.

Since the inverter only controls its terminal voltage i.e., capacitor voltage Vo, a per phase voltage drop due to the transformers and cables lead to unbalanced voltages on the load side.

4.4.3 Grid following control validation

With the static switch in closed position, the converter is connected to the grid emulator. The power controller performance is validated with a sequence of active and reactive power reference change as shown in Figure 4.13.

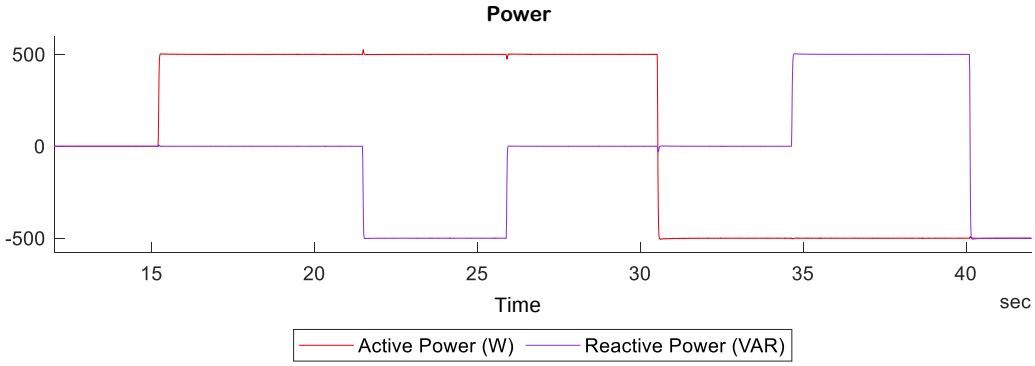

Figure 4.13: Inverter response on active and reactive power reference step

- $t = 0s$, the inverter is turned on, active and reactive reference are set to 0.
- $t = 15.2s$, active power reference is set to 500 W
- $t = 21.45s$, reactive power reference is set to –500 VAR
- $t = 25.9s$, reactive power reference is reset to 0.
- $t = 30.5s$, active power reference is set to –500 W
- $t = 34.5s$, reactive power reference is set to 500 VAR
- $t = 40s$, reactive power reference is set to -500 VAR

It has been observed from the results that the active and reactive power can be changed independently without affecting each other. Figure 4.14 and Figure 4.15 show the zoom around the reference change, to further analyze the impact to voltage and current evolution.

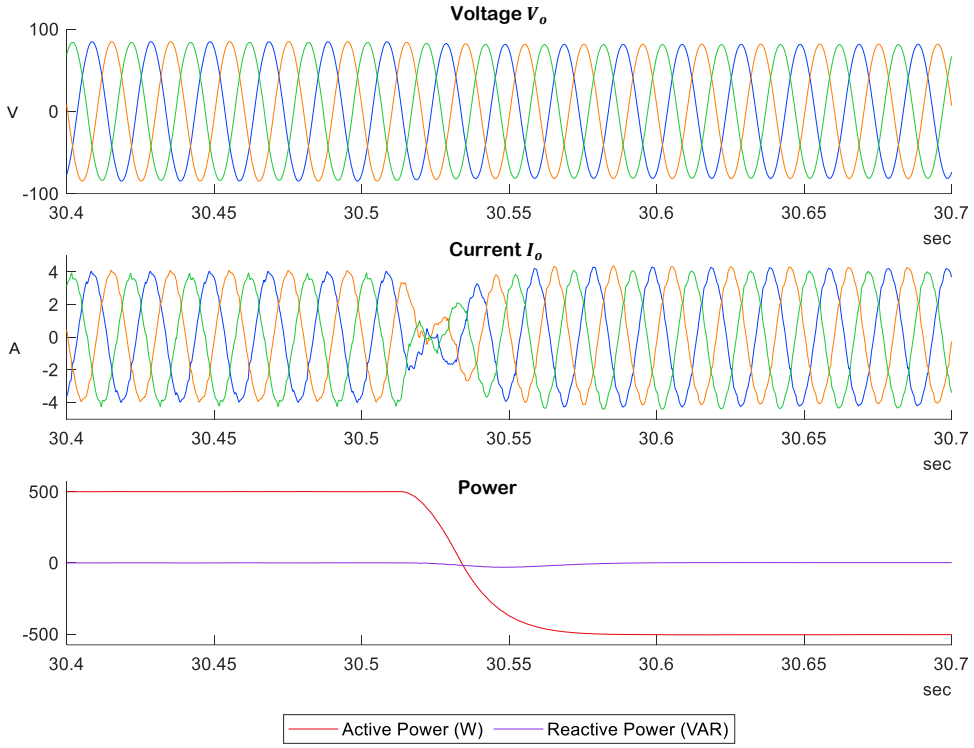

Figure 4.14: Zoom on grid following control response to active power reference setpoint change.

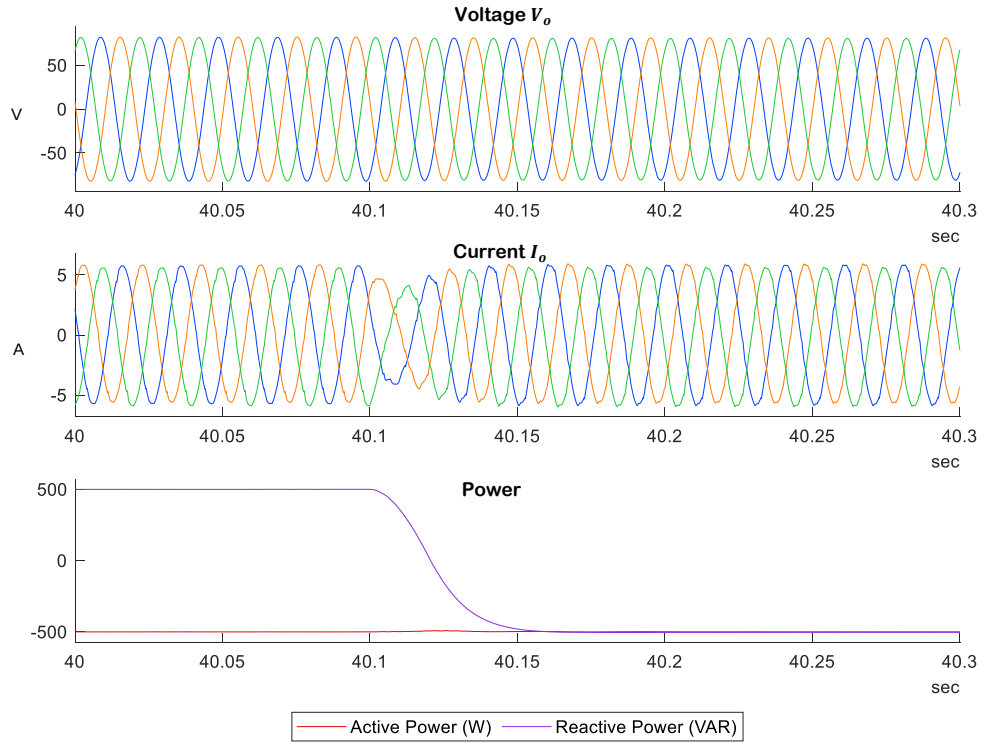

Figure 4.15: Zoom on grid following control response to reactive power reference setpoint change.

From these experimental results, we can conclude that in the grid following control, the active and reactive power can be controlled independently without influencing each other. Furthermore, the control responses of both active and reactive control are around 50 ms, which are no different than the one we tested previously by simulation means.

4.5 Validation of microgrid seamless operation

As the FIS and inverter control has been validated independently. Following this, the full system is tested in the scenario of grid loss. The direct voltage control activation strategy with virtual impedance is implemented in the inverter test bench. A real critical load i.e, PC and monitor are connected to the system. If the seamless operation is successful, followed by a grid loss, the PC will continue to run.

4.5.1 Test setup and procedure

The objective of the test is to see the microgrid seamless operation in response of the grid loss. Specifically, whether critical loads are protected during the disturbance. Thus, real critical loads i.e., PC and its monitor are connected to the system. Figure 4.16 recalls a simplified diagram of the microgrid demonstrator detailed in Sections 4.2.

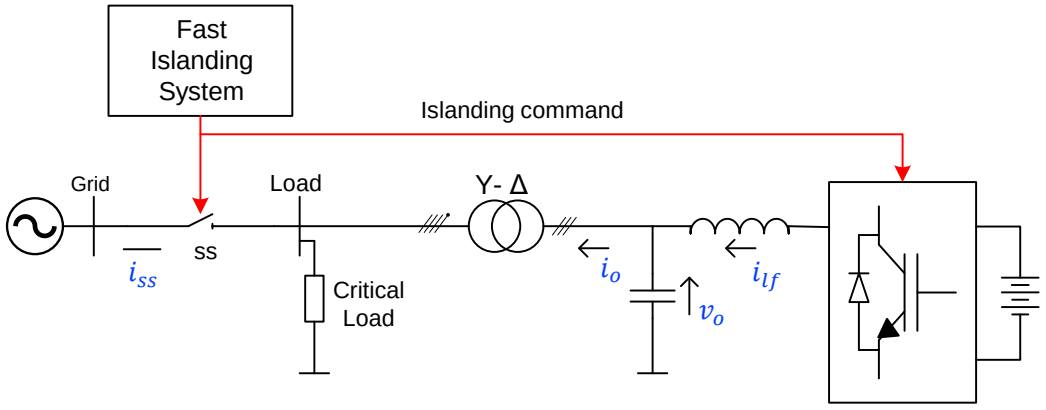

Figure 4.16: Simplified SLD of experimental setup

In this setup, fast islanding system ensure grid loss detection, this signal is sent to static switch (SS) to close or open and is sent to the inverter test bench for changing its mode of operation. Moreover, Table 4.3 shows the critical loads configuration connected to the systems. To simplify the test process, these loads are not changed in the test scenario. While the total loads used is 90% of the inverter rated power, however, due to the unbalanced, some inverter phases are already reaching the maximum current.

Table 4.3: Configuration of loads for microgrid seamless operation test

Load type	**Connection**	**Power (W)**	**% of rated power**
resistive load bank	three phases 2160	72	
resistive load bank	phase A	426	14.2
PC and monitor	phase A	140	4.7
Total			90.9

In this test, multiple grid loss disruptions are tested with different inverter's operating conditions. This grid loss is emulated by introducing a voltage sag on the grid, configured from the OPAL RT. For the starting up the system for the first time, the following steps are respected:

Step 1: Inverter off
Step 2: Static switch off
Step 3: Grid emulator on
Step 4: Static switch on
Step 5: Inverter on in grid following mode.
Step 6: Set Pref and Qref of inverter.

4.5.2 Seamless islanding due to grid loss

Figure 4.17 shows the system's measurement for seamless islanding test when inverter was idle. At initial conditions, the inverter is connected to the grid emulator while being idle i.e., injecting zero active and reactive power. At t=0 s, a 50 ms three phase voltage sag is applied to the systems. The FIS detect grid loss at t=2.2 ms. Although, the FIS has sent command to the static switch, the phase a and phase b static switch are not opened immediately. However, the instantaneous load voltage has fully recovered after 20 ms. Consistent with previous chapter, the method from UPS standards (IEC62040-3) is used for the RMS calculation. Based on this calculation, the voltage recovered to 0.73 pu within 9.4 ms indicating that the seamless performance is compliant with the requirement.

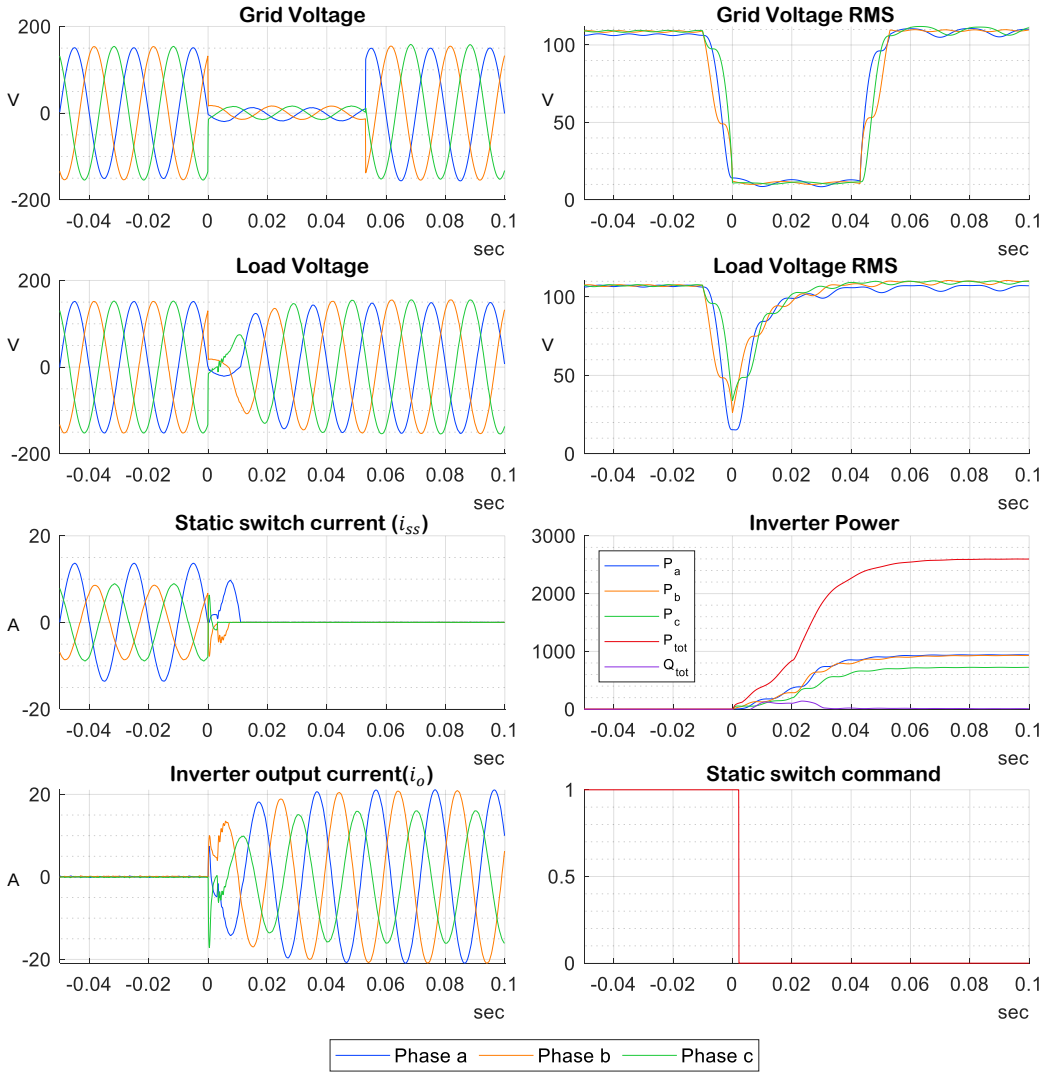

Figure 4.17: Seamless islanding due to three phase voltage sag. Pref = 0.

Figure 4.18 shows the system's measurement for seamless islanding test when inverter was at full charge. At initial conditions, the inverter is connected to the grid emulator while absorbing maximum active power. At $t = 0s$ a single-phase voltage sag is applied to the systems. Again, the FIS detect grid loss at $t = 2.2ms$.

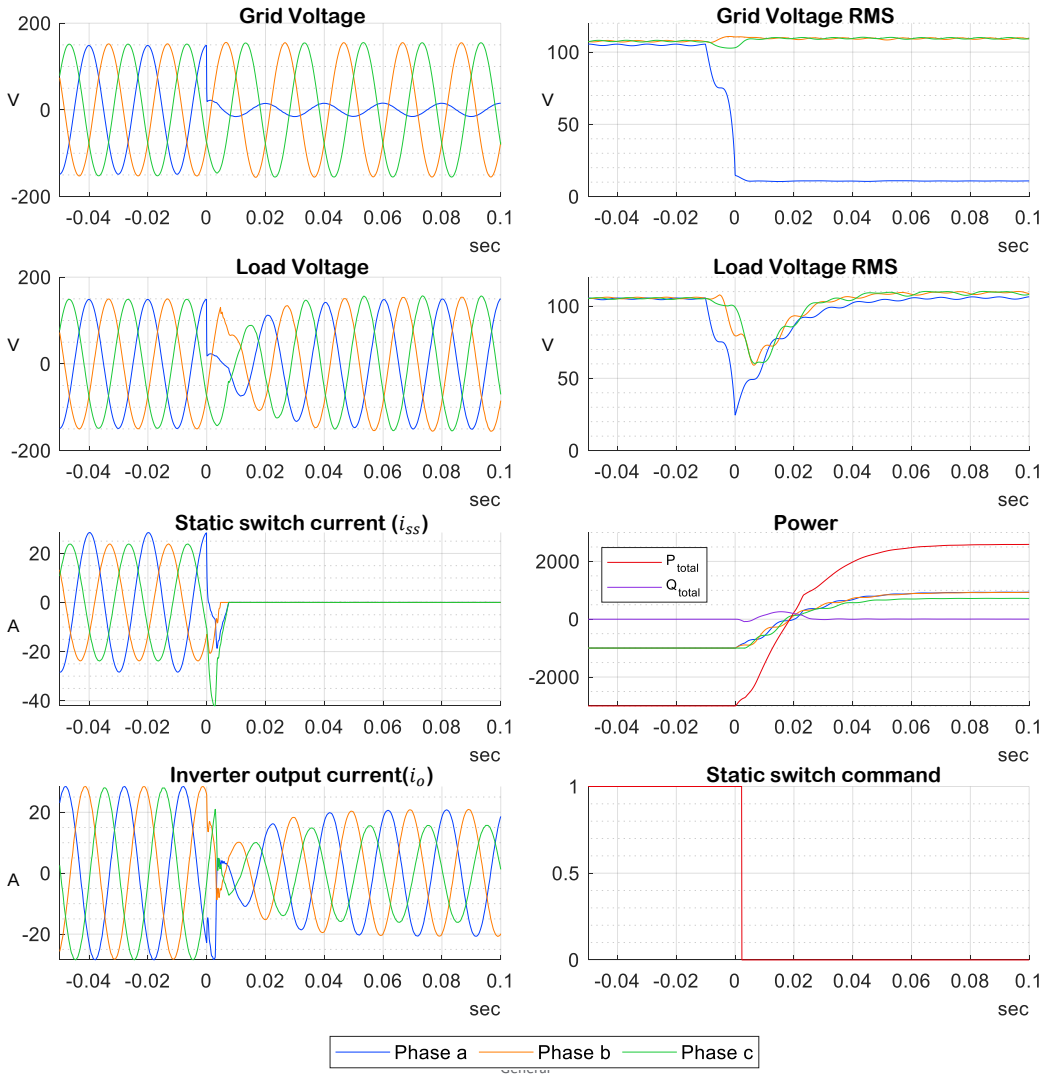

Figure 4.18: Seamless islanding due to single phase voltage sag. Pref = -3000 W (full charge).

The load voltage recovery time is slower than the previous scenario, this behavior is expected due to the inverter current control are changing from the full absorption to the full injection to supply the critical loads. Nevertheless, the inverter were able to provide a stable transition without violating the inverter output current limit nor the load voltage limit.

Figure 4.19 shows the system's measurement for seamless islanding test when inverter was at full discharge, which means the inverter were injecting maximum active power to the grid.

At $t = 0s$ a single-phase voltage sag is applied to the systems. Again, the FIS detect grid loss at $t = 2.1ms$.

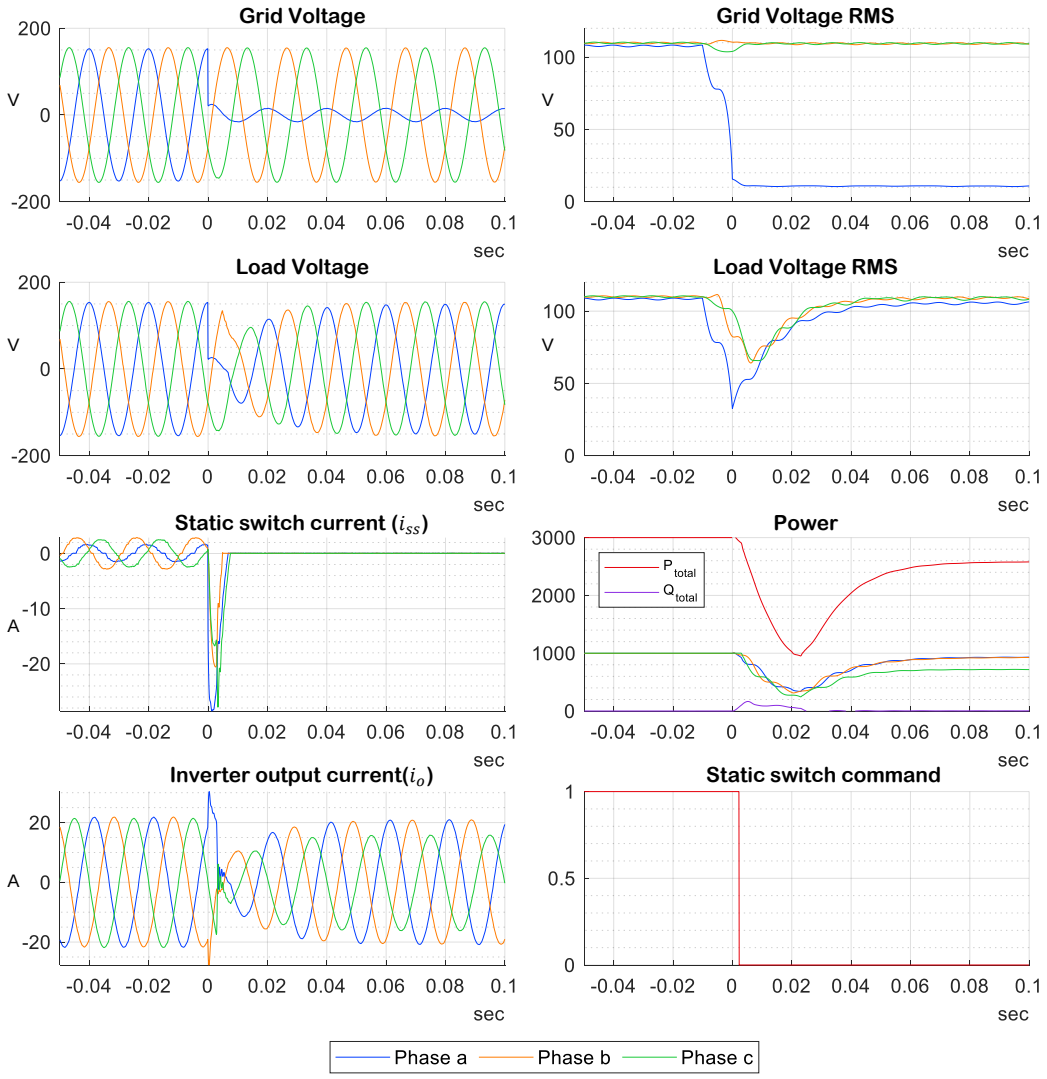

Figure 4.19: Seamless islanding due to single phase voltage sag. Pref = 3000 W (full discharge).

At the moment of fault occurs, a surge current flow to the grid side. The phase b is turned off firstly, at t=4.8 ms while the phase c is turned off at last at t=7.5 ms. Following the complete turned off of the static switch, the inverter able to recover the load voltage quickly. From the three presented scenario tests, where initial power inverters are idle, full charge and full discharge, the PC and monitor is still operating without any shutdown or reset. A deeper analysis and more tests are carried out to determine the voltage recovery time, which will be discussed in subsection 4.5.4.

4.5.3 Seamless reconnection to the grid

When the FIS detect that grid voltage is back into healthy state, it will close the static switch when grid voltage and load voltage are synchronized as shown in Figure 4.20. Once static switch closed, the grid provides the current to the critical loads. After that, the inverter power ramp up to the previous setpoint. When the inverter went into grid following mode, the power loop is control state is reset to zero. Because of this, during the transition, the inverter current went to zero before ramping up to achieve the given power setpoint. Nevertheless, as can be observed, the voltage of the critical load is not disturbed during this transition.

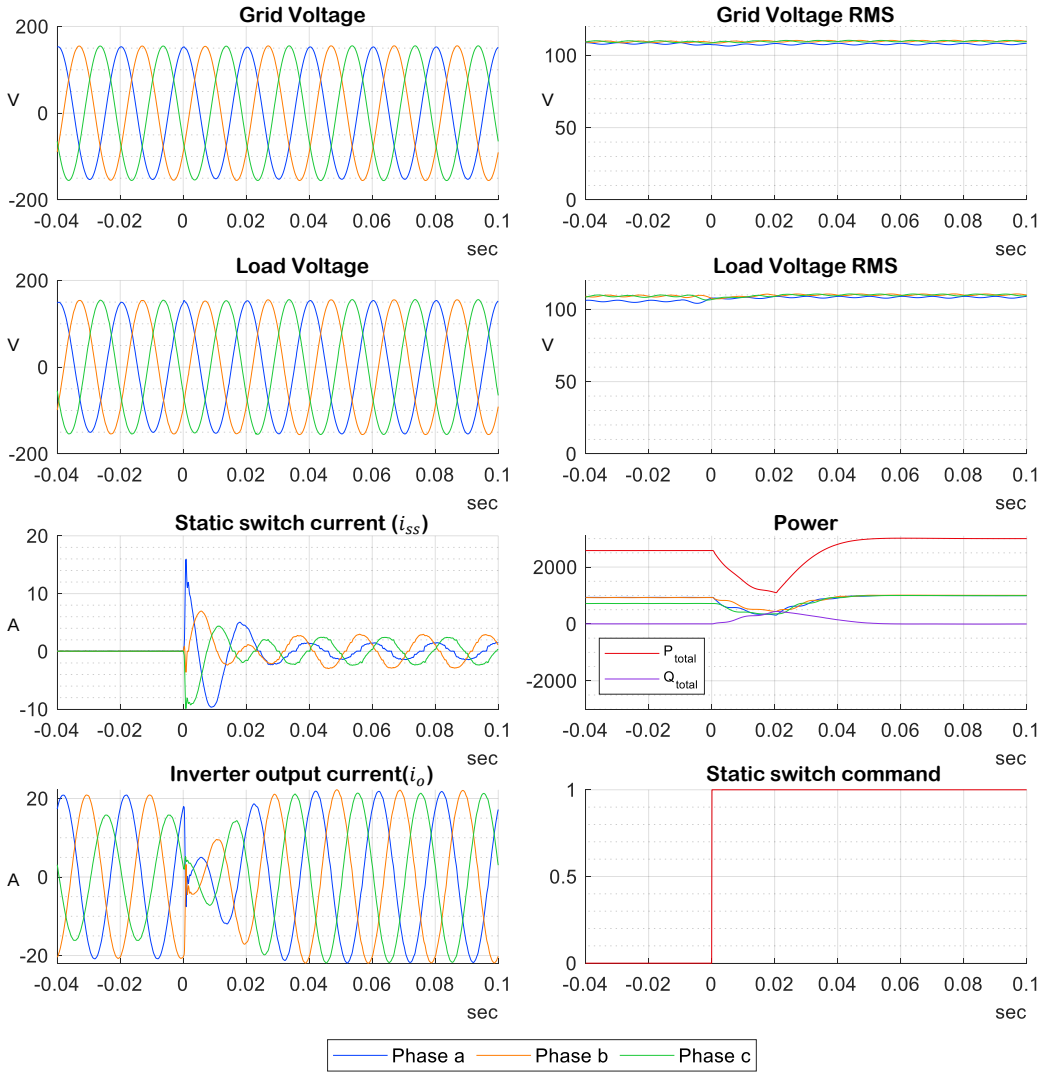

Figure 4.20: Seamless islanding due to three phase voltage sag. Pref = 0.

4.5.4 Analysis of the robustness and voltage restoration time

The performance of seamless microgrid operation both for islanding and grid reconnection are validated to be satisfied. Furthermore, a sequence of voltage sag, shown in Figure 4.21 is applied to the system to validate the robustness of the system. Also, with more islanding attempt, the voltage restoration time can be analyzed more thoroughly.

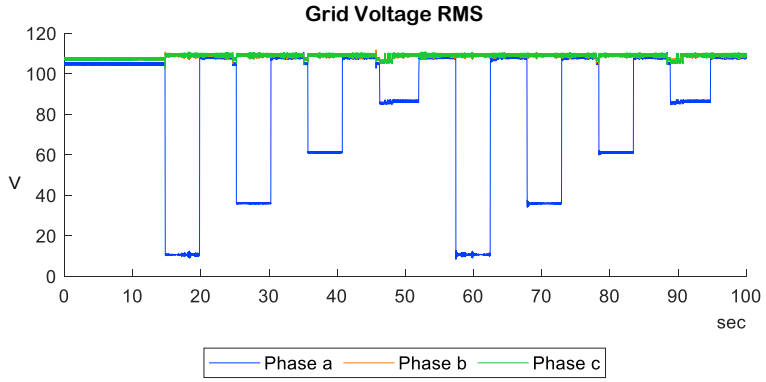

Figure 4.21: Grid voltage sag sequence test.

This voltage sag sequence test is repeated for different initial inverter power: zero, full charge, and full discharge. We observed that the inverter is consistently stable during the test. The critical loads are in operation without any disruption. Moreover, Figure 4.22 compile load voltage measurement recordings (blue curve) for each islanding during the test. The voltage measurements are normalized in per unit to simplify the analysis. For each measurement, x axis represents the time duration in seconds, where the t=0 is adjusted at the moment of voltage sag.

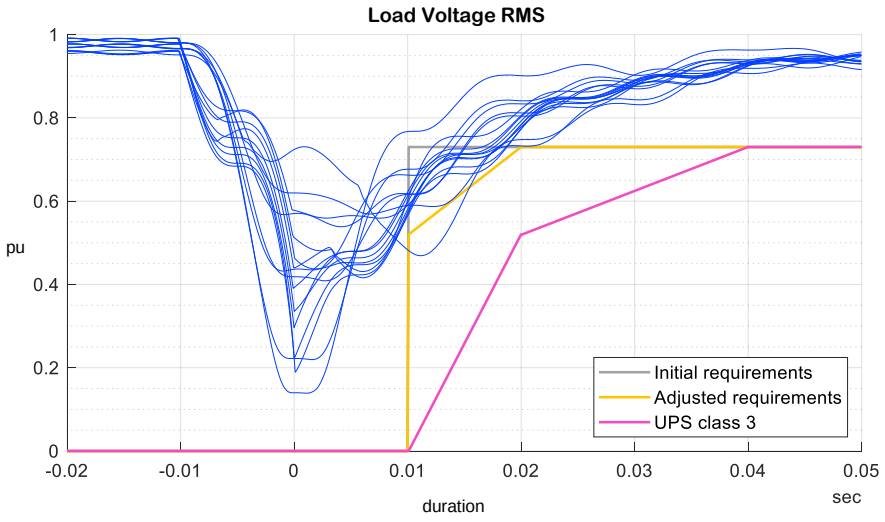

Figure 4.22: Load voltage evolution on multiples seamless islanding test sequence

The grey curve represents the initial microgrid performance requirement, proposed in chap-

ter 2. While the pink curve represents the UPS class 3 performance requirement. It can be concluded from these experimental results that the voltage recovery time to reach 0.73 pu are less than 20ms. while the recovery time to 0.52 pu are achieved in less than 10 ms. This is consistent with the simulation result carried on in chapter 3. The experimental results show that islanding performance are better than the UPS class 3. Moreover, the initial requirement can be adjusted to the one shown by yellow curve.

4.6 Conclusion

The thesis contribution C5 comprise the experimental validation to demonstrate the effectiveness of the research carried out in this thesis. A small-scale microgrid demonstrator was constructed to accurately represent a real microgrid building, incorporating real equipment such as critical load.

The loss of grid detection algorithm, proposed in chapter 2 has been prototyped as the Fast Islanding System (FIS). FIS has been validated to detect the grid loss within the performance criteria. Additionally, FIS is also designed to control the static switch and issue islanding command to the BESS.

Furthermore, BESS inverter control designed in the chapter 3 was implemented on 5 kW inverter test bench using DSPACE P-HIL. Both of grid following mode and grid following control mode have been validated. During islanding, it is observed that the unbalanced nature of the microgrid loads introduces voltage drops, resulting in unbalanced voltages on the load side. This issue could be resolved by implementing a secondary controller, such as a microgrid controller, which would send voltage setpoints for each phase. Thanks to the stationary abc control frame, the BESS would be capable of independently controlling the voltage of each phase, thereby easily following this command.

The ability of the microgrid to operate seamlessly was tested across multiple grid loss scenarios. It was observed that in all cases, following a grid loss, the voltage was recovered to 0.52 pu within 10 ms and to 0.73 pu within 20ms. The system demonstrated the capability to reconnect seamlessly once the grid voltage was restored. During these test sequences, critical equipment such as PCs and monitors continued to operate without any interruptions, indicating that the BESS effectively protects critical loads against grid disruptions.

Unfortunately, experimental validation of the microgrid voltage back feed to ensure continuous operation of DER could not be conducted due to PV inverter rating is not compatible with the system. Attempts were made to model the PV inverter within P-HIL setup for this purpose. However, the linear power amplifier limitation prevents the back feeding process. The work of PV inverter modeling on P-HIL have been presented at an international conference [55] and available on Appendix A. This work also provides real-time hardware in the loop framework as part of the thesis contribution C6.

Chapter 5

General Conclusions and Perspective

Energy transition from fossil fuels to cleaner energy sources involves integrating more DER. Under current policies trends and electricity prices, the expansion rate of small-scale PV is expected to outpace that of utility-scale installations. Moreover, energy storage systems have become essentials for energy balancing and maximizing the energy from solar PV system. Microgrid acts as catalyst for integrating these DER into buildings, enabling consumers to generate and manage their own electricity needs more efficiently. Furthermore, microgrids not only reduce reliance on traditional centralized power grids but also enhance resilience by providing backup power during grid loss. Within this context, this thesis aims to enhance the resilience of microgrid supply through seamless operation of local DER, effectively protecting critical loads in the face of grid disruptions. This PhD is a collaboration between G2Elab (Grenoble Electrical Engineering Laboratory) and Schneider Electric.

5.1 Conclusion

Low voltage microgrids for buildings are actually complex systems. They involve a variety of systems and aspects, including PV systems, BESS, control and protection mechanisms, and the regulatory frameworks. To improve the resilience of these microgrid, this thesis begins by explaining each component of the microgrid systems, laying the basis for understanding and improvements.

In the event of grid disturbance, microgrid is able to seamlessly transition from grid-connected to islanded mode without impacting too much the supply of the connected loads or at least their proper functioning. To guarantee this seamless operation, the contribution C1 of this thesis finds out the maximum disruption duration which is tolerated by the loads. Based on our analysis from literatures and relevant standards, we have determined performance requirements of seamless operations of **10 milliseconds** to reach 73% of the nominal voltage. This means, microgrid needs to **detect** the grid loss, **isolate**, and **restore** the voltage within this duration.

In order to accomplish this, we develop a fast grid loss detection algorithm based on

instantaneous voltage analysis. The grid loss itself is linked to the definition of the interruption and voltage sag. Our proposed algorithm is based on PLL which creates a voltage reference and a simple counter to determine the grid loss. The simulation demonstrates that this algorithm is generally accurate in determining grid loss, even in conditions of polluted voltage characterized by a THD of 10%. However, the algorithm has accuracy of 85%, 93% and 91% to determine voltage sag types I, II and III, respectively, under non-polluted conditions. In polluted conditions, these accuracies are slightly reduced to 76%, 83%, and 91%, respectively. Furthermore, the algorithm's detection time can be configured within the range of 2 to 10 milliseconds. This development represents contribution C2 of the thesis.

Dealing with grid code regulation, the microgrid electrical topology is modified by separating the critical busbar from the main busbar. A fast disconnection switch is used as a bus tie between these busbars to provide fast isolation for the seamless operation. The idea is to enable the critical loads to perform seamless islanding within the microgrid, while allowing the rest of DERs to stay connected, in compliance with the ride-through regulations. Furthermore, we propose voltage back feed from the critical bus to ensure the continuous operation of these DERs after the FRT time elapsed. This proposed solution constitutes contributions C4.

Upon disconnection, BESS's inverters ensures the voltage recovery. In order to accomplish this, we proposed inverter control tailored for the seamless operation. This control is based on dual loop control structure. For grid following mode, the outer power loop is based on PI regulator in *dq* frame. While in grid forming mode the outer voltage loop is based on PR regulator in *abc* frame. A single inner current control based on PR regulator in *abc* frame is used in both modes. We investigate three mode transfer strategies: direct voltage control activation (strategy A); momentary cessation before islanding (strategy B); and strategy A with virtual impedance technique. Strategy B performed faster recovery time compared to the others but introduce an overvoltage just within the limits of equipment. Safer option is opted in for strategy A with virtual impedance which solves the overvoltage issue, although has the longer recovery time. With this strategy, the seamless operation requirement is partially achieved. Nevertheless, the recovery times of this strategy are still better than class 3 UPS performance. This works represents contributions C3.

Finally, the effectiveness of the research presented in this thesis is demonstrated through experimental validation, which account for contribution C5. This includes both prototyping and Power Hardware-in-the-Loop simulations. The loss of grid detection algorithm has been prototyped as the Fast-Islanding System (FIS). FIS has been validated to detect the grid loss within the performance criteria with an additional task to control the static switch and issue islanding command to the BESS.

Furthermore, the proposed inverter was implemented on 5 kW inverter test bench using DSPACE P-HIL. The ability of the microgrid to operate seamlessly was tested across a se-

quence of multiple grid loss scenarios. In all cases, the voltage was recovered to 0.52 pu within 10 ms and to 0.73 pu within 20ms. The system also demonstrated the capability to reconnect seamlessly once the grid voltage was restored. During these test sequences, critical equipment such as PCs and monitors continued to operate without any interruptions, indicating that the BESS effectively protects critical loads against grid disruptions.

5.2 Perspective

This thesis opens up several avenues for future research. Firstly, in this thesis, we consider only the use of thyristor-based static switches for fast-disconnecting devices. Exploring alternative disconnecting switches, such as IGBT-based static switches or hybrid breakers, could significantly enhance transition times. This improvement could provide additional analysis time for grid loss, potentially increasing the accuracy of grid loss detection algorithms. Furthermore, with faster disconnecting switches, the strategy for mode transfer could be streamlined for simplicity.

In practical scenarios, microgrid might incorporate multiple BESS. An intriguing area of study would be the parallel control of these inverters, especially during transition phases. Implementing coordinated or unified voltage control could offer a novel approach to managing these dynamics.

The concept of unbalanced voltage drops compensation and power sharing merits further exploration. The voltage control developed in this thesis allows for independent control of each phase's voltage. Supervisory control could adjust per-phase setpoint to compensate unbalanced voltage drop. Future research could also explore how DERs can contribute to managing unbalanced power supply by utilizing a Volt-Var/Watt control for each phase.

This seamless operation provides a high level of resilience function of BESS, thereby increasing the value of BESS. This resilience function needs to be coupled with other well-used functions such as tariff management, peak shaving, and self-consumption. A novel Energy Management Systems and optimal DERs sizing can be investigated by considering the necessary margins to enhance resilience.

Finally, for some places, the grid loss can be considered as High Impact Low Probability (HILP) event. An approach on reinforcing local installation by installing BESS can be investigated and should be challenged versus more global approaches.

Appendix A

Earthing Systems for Low Voltage Microgrids

Earthing or commonly known as grounding in United States are important for the safety of electrical installations due several reasons. Primarily, it ensures safety by preventing electric shocks and reducing the risk of fire or equipment damage during electrical faults. Earthing system also establish a path for fault currents, facilitating the operation of protective devices and maintaining system reliability. Moreover, they play a vital role in surge protection, diverting excessive energy away from electrical equipment during lightning strikes. systems. Three earthing systems have been specified by international standard IEC-60364, shown in Figure A.1: TT, TN, and IT systems. The first letter denotes how the power system's live

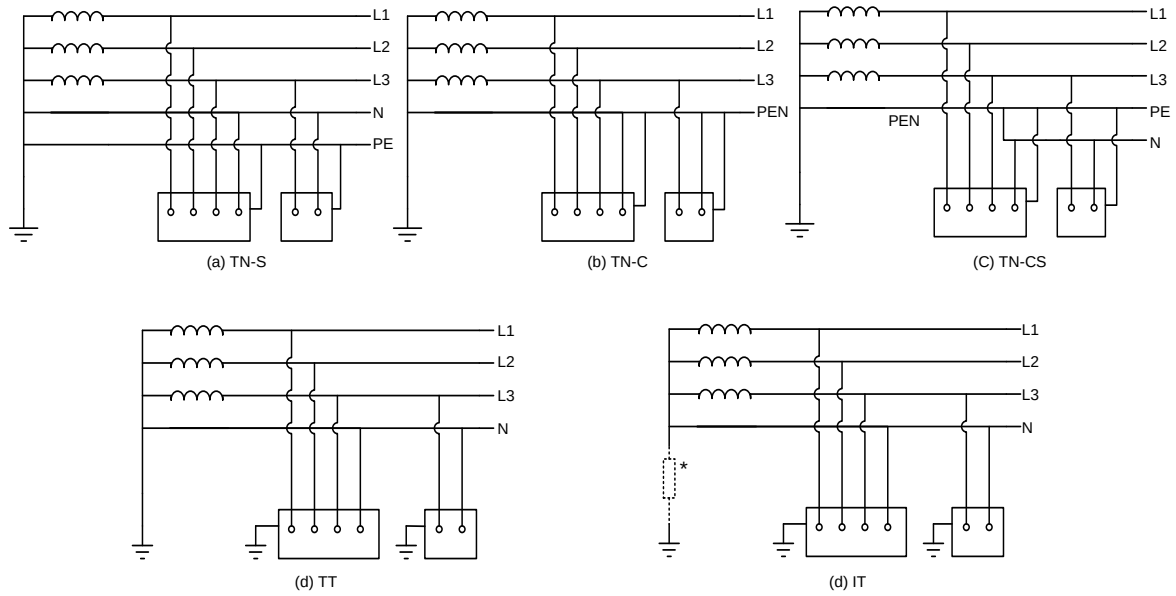

Figure A.1: Earthing Systems (a-c) TN systems. (d) TT system (e) IT system.

conductor is earthed and, if neutral or midpoint exist, it is connected to it. The second letter denotes how the exposed conductive parts at the installation site are connected.

TT system has only one point where the neutral (N) of the sources is directly connected to the earth. The exposed conductive parts of installation i.e., equipment frames are directly earthed independent from the supply system.

TN systems has only one point where the neutral (N) of the sources is directly connected to the earth. The equipment frames are connected to that point by protective conductors (PE). TN system is divided into three subsystems depending on the arrangement of neutral and protective conductors.

- **TN-S** neutral and protective conductor are separated throughout the system.
- **TN-C** neutral and protective conductor are combined in a single conductor (PEN) throughout the system.
- **TN-CS** neutral and protective conductor are combined in a single conductor (PEN) in part of the system.

IT system has the neutral (N) of the sources isolated from the earth or connected through high impedance. The equipment frames are earthed at one local points in installation.

In microgrid application, we need to consider this earthing systems during grid connected and islanding mode. As explained previously, only one neutral-grounding point allowed from multiple sources is permitted therefore this earthing connection may be changed from mode to another. In grid connection mode, the neutral earthing is typically established in the distribution transformer to support the TT and TN systems. However, when the site is islanded, this connection can be disconnected. As a result, the neutral must be locally earthed [172].

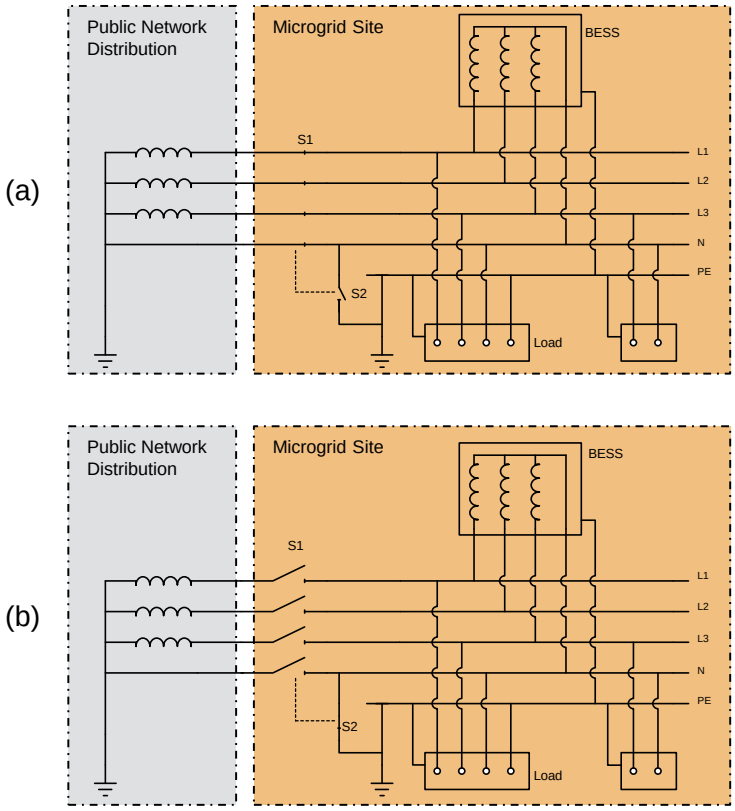

Figure A.2: (a) TT in grid connected mode. (b) TN-S in islanded mode.

Figure A.2 shows an illustration of TT system changed to TN-S system in islanded mode. In this configuration, the main switch (S1) and local neutral earthing switch (S2) are interlocked. In grid connected mode, the main switch (S1) is closed, and the switch S2 is opened. The neutral-earth connection point is established at the distribution transformers. When the site is islanding, the main switch (S1) is opened, causing all live conductors to float. Consequently, switch S2 must be closed to ensure that the neutral of the installation is no longer floating. Additionally, to ensure protection against a shock, a residual current device (RDC) can monitor this path an trip all DER in case a fault is detected.

Appendix B

Power Quality Issues Characteristics

B.1 Waveform distortion

Waveform distortion is commonly referred as harmonics distortion. A periodic waveform can be decomposed using Fourier series as summation of sinusoidal components. With f_0 is the fundamental frequency, A_h and ϕ_h are amplitude, and phase angle for harmonic order h respectively.

$$f(t) = \sum_{h=1}^{\infty} A_h \cos(2\pi h \ f_0 + \phi_h) \tag{B.1}$$

The fundamental component is indicated when $h = 1$, which represent the power system frequency which is 50 Hz or 60 Hz. Another frequency that appears in the waveforms is multiplication of this frequency and are called as harmonic components. For 50 Hz operating power systems, the 150 Hz, 250 Hz and 350 Hz components are called 3^{rd}, 5^{th}, and 7^{th} harmonics respectively.

The cause of this waveform distortion is the presence of non-linear loads. For example, on domestic and commercial loads: computers, LED lamp. For industrial, adjustable-speed drives, arc furnaces. Rotating machines are often regarded as sources of harmonics due to the non-sinusoidal distribution of windings in the slots, which leads to distortion in the magnetic field. However, it is generally accepted that the harmonics generated by rotating machines are considered negligible compared to those produced by other sources [173]. Additionally, it's a common misconception that capacitor banks are a source of harmonic distortion. In reality, while they do not generate harmonics, their resonance with transformers can amplify existing harmonic disturbances. The waveform distortion can be divides as follows:

Harmonics distortion is when the harmonics components are integer multiplication of the fundamental frequency. Harmonic distortion is a growing concern for many customers and for the overall power system due to increasing application of power electronics equipment. Harmonic distortion levels can be characterized by the complete harmonic spectrum with magnitudes and phase angles of each individual harmonic component. It is also common to use a single quantity, the total harmonic distortion (THD), as a measure of the magnitude of harmonic distortion

Interharmonic distortion is when the harmonics components are not integer multiplication of the fundamental frequency. The main sources of interharmonic waveform distortion are pulse-widge modulated inverters, static frequency converters, cycloconverters, induction furnaces, and arcing devices, especially those whose control is not synchronized with the power system frequency. The most noticeable effect of interharmonics is visual flickering of displays and incandescent lights, as well as causing possible heat and communication interference.

Voltage flicker or more accurately, voltage fluctuations leading to light flicker, are mathematically another special case of interharmonic distortion. The special interest in this type of disturbance is again due to the consequences. Even very small fluctuations in the r.m.s. voltage with frequencies between 1 and 15 Hz lead to light-intensity variation for which our eyes are very sensitive.

Dc offset can be seen as a special case of harmonic distortion but is often treated separately due to difference in measurement techniques and consequences. Direct current (DC) can be induced into an AC distribution system, often due to failure of rectifiers within the many AC to DC conversion technologies that have proliferated modern equipment. DC can traverse the ac power system and add unwanted current to devices already operating at their rated level.

Harmonics in power systems present significant challenges, including overheating in components like transformers and cables. This overheating is not only proportional to the root mean square (RMS) current, but also influenced by the nature of transformers, whose resistance increase with frequency. As a result, higher-order harmonics generate more heat per ampere compared to the fundamental frequency components, worsening the heating issue in these critical components.

Moreover, different types of equipment are affected differently by harmonics. For example, machines are primarily impacted by lower-order harmonics, leading to inefficiencies, while capacitor banks are more vulnerable to higher-order harmonics. Sensitive electronic loads are also adversely affected by high harmonic voltage. The third harmonic current is noteworthy for its potential to generate significant cumulative current in the neutral conductor, risking overheating in low-voltage installations, particularly in systems with numerous computers or energy-saving lighting.

Addressing harmonics involves understanding their effects and implementing solutions like harmonic filters, which attenuates higher frequencies, reducing their presence in the power system. Additionally, regulatory standards play a vital role in controlling harmonic levels, setting limits on allowable distortion levels.

B.2 Voltage imbalance

Voltage imbalance is often referred as voltage unbalance is a condition in three phase system where the magnitudes of the phases are not identical. It is defined as the percentage ratio between the magnitude of the negative sequence and the magnitude of the positive sequence. It applies to both voltage and current. Typically, the voltage imbalance in a three-phase service is below 5%. Equation B.2 can be used to mathematically represent the voltage imbalance.

$$\%V\ imbalance = \frac{|V^-|}{|V^+|} \times 100\% \tag{B.2}$$

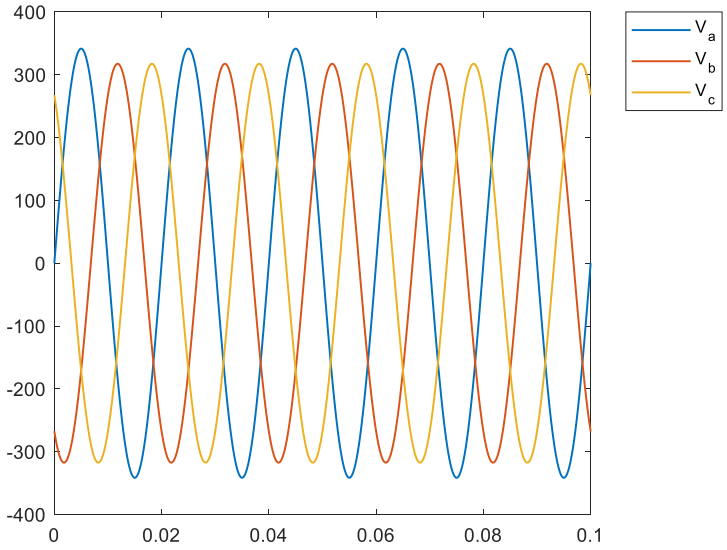

Figure B.1: Ilustration of 5% voltage imbalance

B.3 Transient

A transient represents a temporary deviation from a system's steady-state condition, characterized by its short duration relative to the relevant timescale. Transients are broadly categorized into two distinct types: impulse transients and oscillatory transients.

Impulse transient are sudden high-peak events that significantly elevate voltage and/or current levels, in either a positive or negative direction. These transients are primarily characterized by their peak value, as well as their rise and decay times, or duration. The rise time of these transients can be extremely brief, ranging from a few nanoseconds to several microseconds. The predominant sources of impulsive transients include lightning strikes and electrostatic discharges. Given the potential damage caused by excessive

transient voltages, it is common use to use surge protection at the input of installation. This surge protection is commercially available and commonly referred to as a lightning arrester or a transient voltage surge suppressor.

Oscillatory transient are characterized by rapid changes in polarity, typically multiple times, and usually decay within one fundamental cycle. This type of transient is commonly induced by switching actions in inductive or capacitive loads, such as the switching of capacitor banks in distribution substations. Oscillatory transients can lead to issues like the tripping of motor drives, a consequence of the transient energy elevating the DC bus voltage. To mitigate these effects, practical solutions often involve the installation of line reactors or isolation transformers for the impacted equipment.

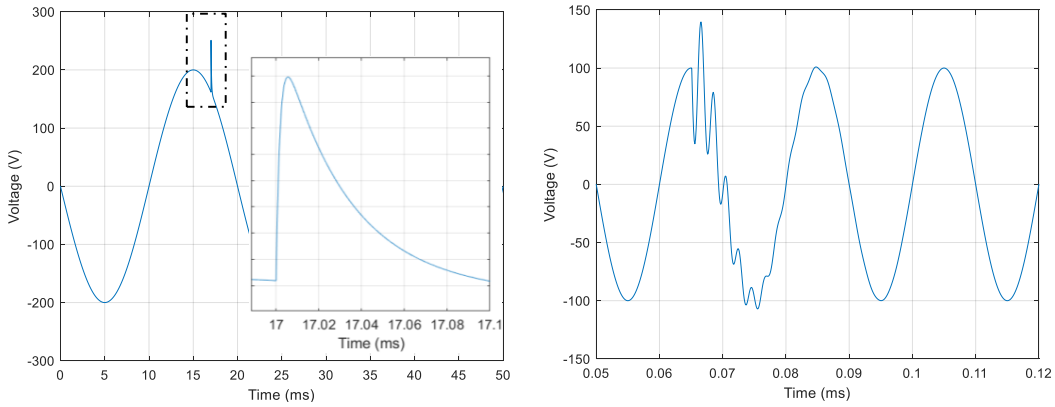

Figure B.2: typical transient voltage due to (a) lightning and (b) capacitor switching

B.4 Voltage Swell

A voltage swell is a temporary increase in the RMS (Root Mean Square) voltage level of an electrical power system, typically lasting from a few milliseconds to a few seconds. It is characterized by a voltage rise exceeding the normal levels, usually more than 110% of the nominal voltage, and can occur in one or more phases of a multi-phase system. Voltage swells are often caused by sudden reductions in load, switching off large loads, or by fault conditions in the network such as a short circuit in a parallel feeder. They can lead to detrimental effects on electrical equipment, including overvoltage stress, malfunction or damage to sensitive electronics, and operational disruptions. Voltage swell mitigation strategies include the use of voltage regulators, surge protectors, and power conditioning equipment. The monitoring and analysis of voltage swells are essential for maintaining the reliability and quality of power in electrical distribution systems.

Appendix C

Fast Grid Loss Detection Performance

Sag

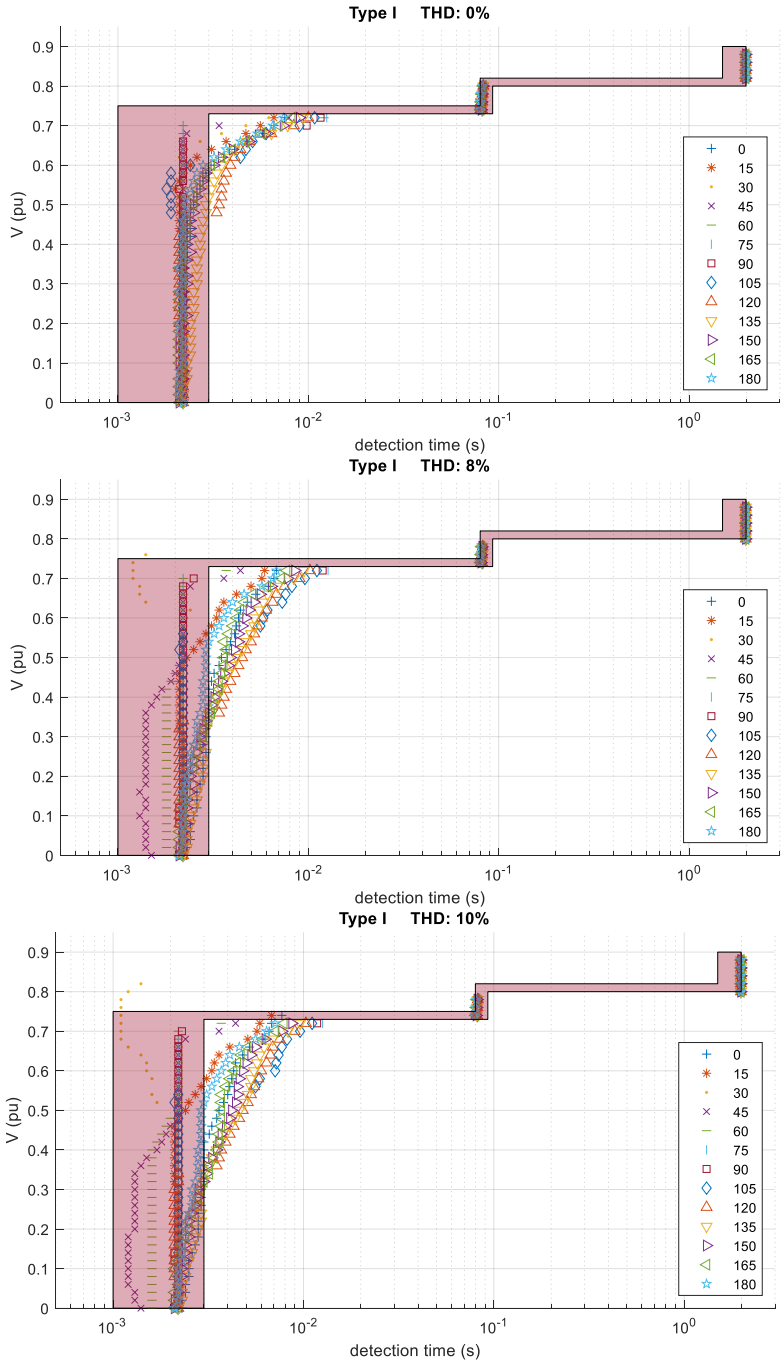

Figure C.1: Detection curves for voltage dips type I

Sag Type II

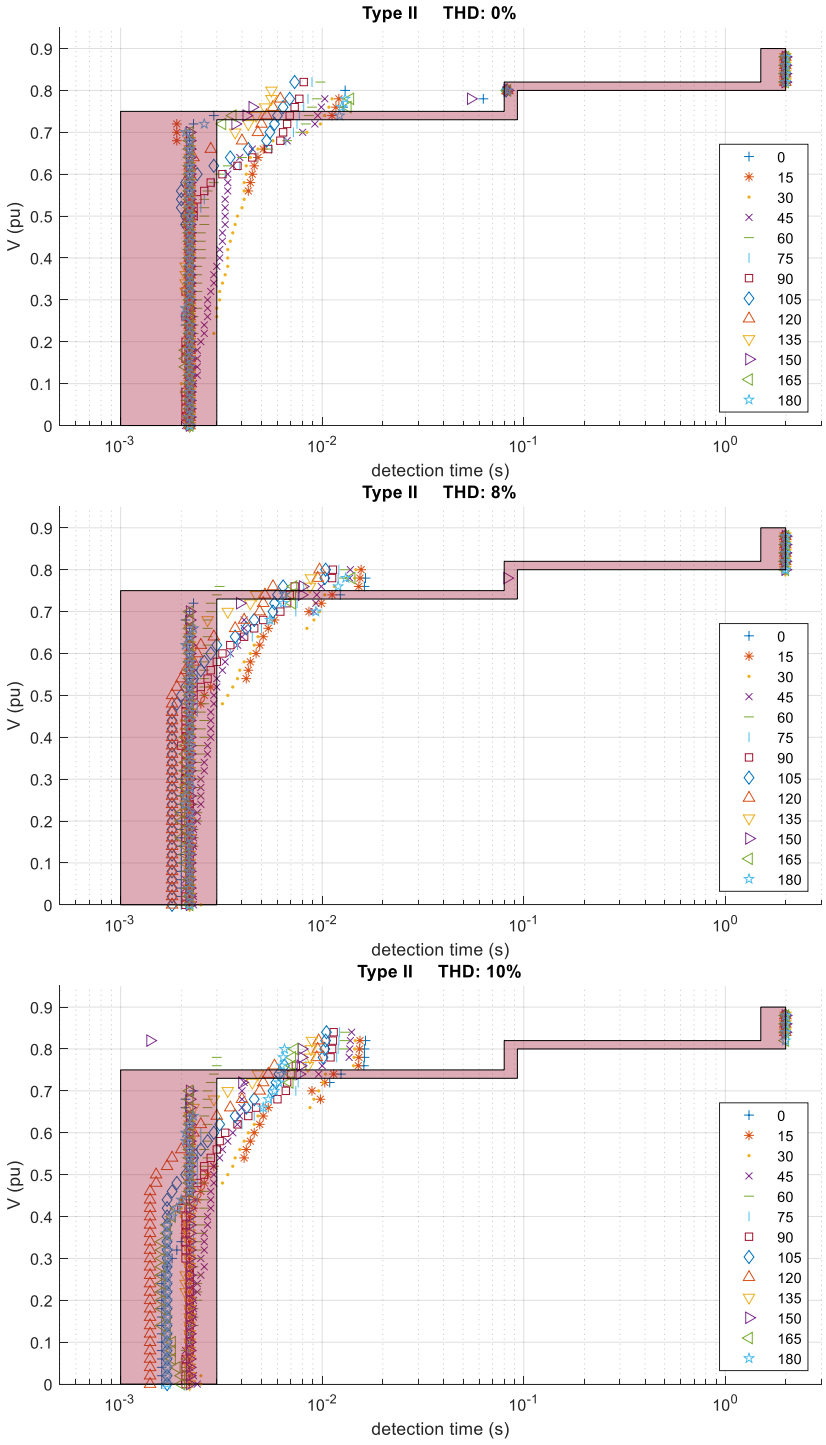

Figure C.2: Detection curves for voltage dips type II

Sag Type III

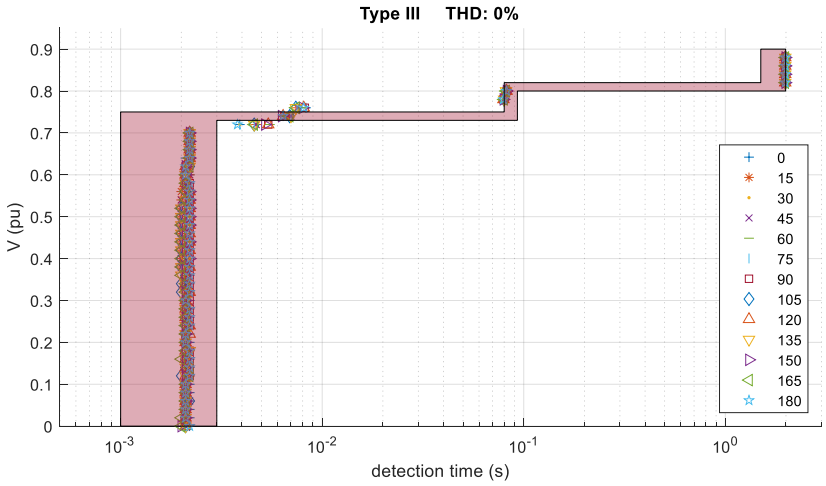

Figure C.3: Detection curves for voltage dips type III

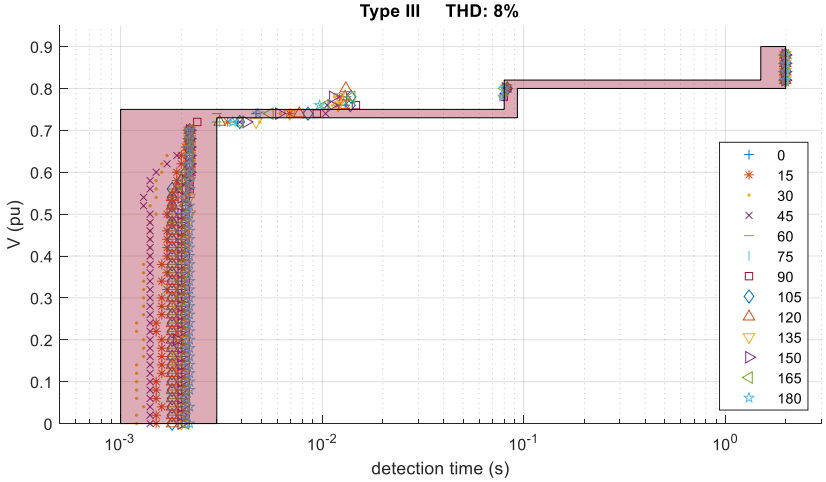

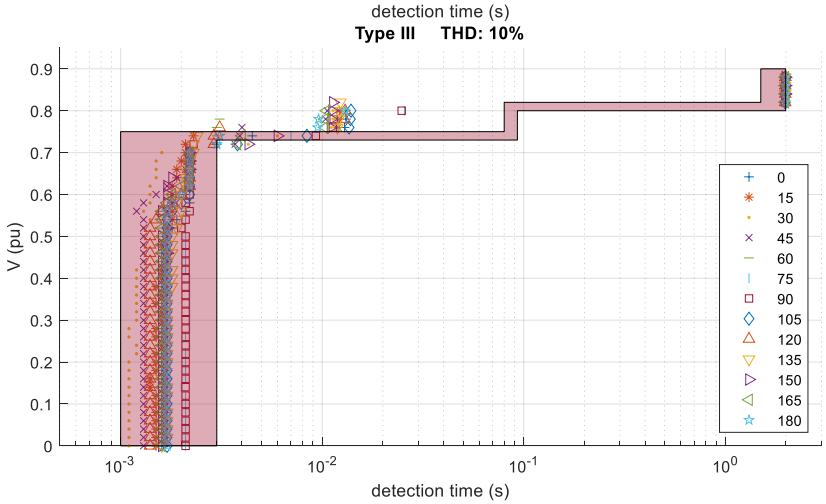

Appendix D

DERs modeling framework for microgrid systems

Microgrid system is comprised of multiple DERs system along with electrical distribution systems (relays, breakers, and power measurement), all coordinated by a microgrid controller. Microgrid controller leverages industrial communications, primarily using Modbus to control the DERs system. In practical, significant effort is required to integrate DERs into microgrid systems, leading to longer project execution times and increased microgrid cost.

Testing a microgrid system presents several challenges, including the absence of standardized interfaces and the diverse behavior of Distributed Energy Resources (DERs) products. Hardware in the Loop (HIL) testing emerges as the optimal choice for evaluating microgrid systems, allowing easier integration of DERs and development of control algorithm. This thesis has entailed the development of diverse DERs models for real-time testing, with the aim of assessing the work within complete microgrid systems.

D.1 Hierarchical modeling of DERs

Figure D.1 shows hierarchical modeling approach of DER. For illustration purposes, a PV inverter model is taken as an example. This modeling concept is also applicable for all type of DER. In this approach, we proposed three layered modelling described below:

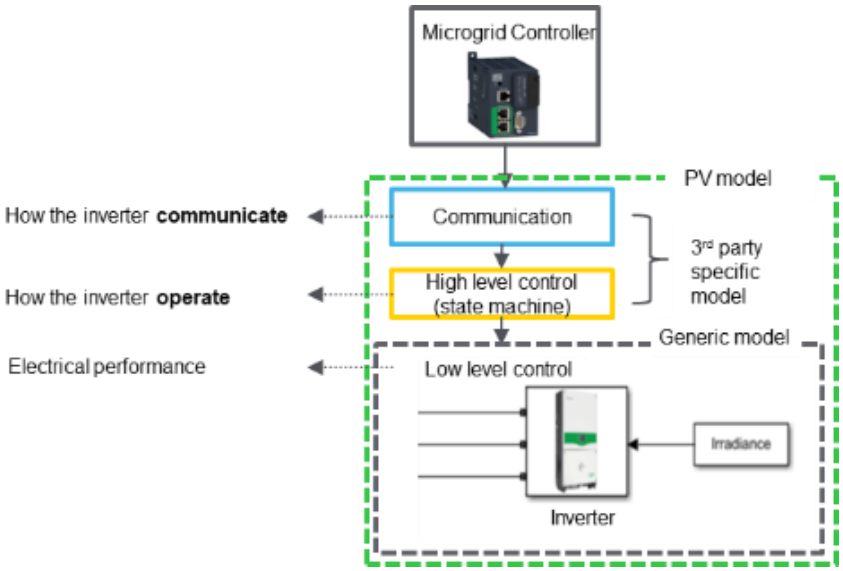

Figure D.1: Hierarchical modeling of DERs

D.1.1 Communication model

The communication models represent the interface between the DER and the microgrid controller. This model shall not only simulate the monitoring and control signal but also reflect the communication performance. This particularly important for Modbus communication. Modbus has limited bandwidth and can manage only 8 communication sockets at one time over ethernet. Thus, accurate mapping and control signal along with latency, function code, and exception response shall be modeled as highlighted in Figure D.2.

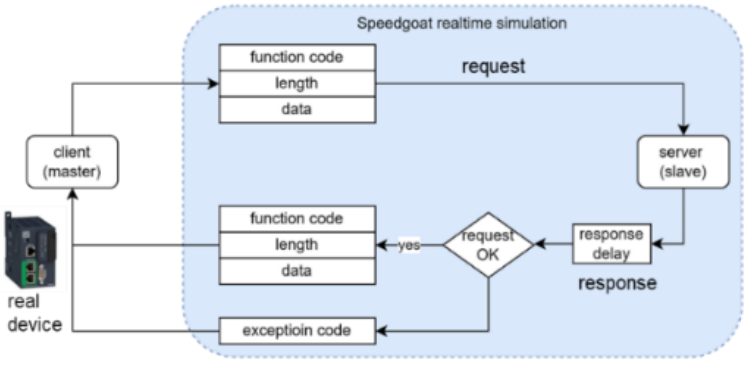

Figure D.2: Modbus communication modeling

D.1.2 State machine model

The developed models included a state machine that translates how DERs works. For example, starting sequence, stopping sequence, changing mode sequence. In practice, the microgrid controller need to send multiple command following a sequence of operation to change the DERs operation mode. Considering the operation flow chart of DERs systems allow the microgrid system testing reflect the reality

D.1.3 Electrical model

Dynamic power system simulation can be classified in two categories: RMS (Root Mean Square) simulation and Electro-magnetic Transient simulation (EMT).

- **RMS Simulation**
  In RMS electrical transient study, the electrical values are represented with a phasor, split in three different network sequences: positive, negative and zero sequence. Usually, only positive sequence is studied except in some cases that involve unbalanced network and/or loads. Most of the time, in case of RMS simulation, the timestep is in order of milliseconds.

- **EMT Simulation**
  Another simulation method that is widely used is Electro-magnetic Transient study. The timestep of this study is in order of microseconds [174]. The different electrical network components are modeled with more detailed than RMS simulations. In consequence, this simulation takes more time to solve but is more precise.

To validate microgrid systems, rms simulation is sufficient. Furthermore, implementing EMT simulation in real time face challenges of computation time as the model get bigger.

D.2 Benchmark of HIL model and real inverter

In our case study, we model the PV solar edge inverter. The electrical model consists of power loop, control loop, and protection i.e., overcurrent and anti-islanding as shown in Figure D.3.

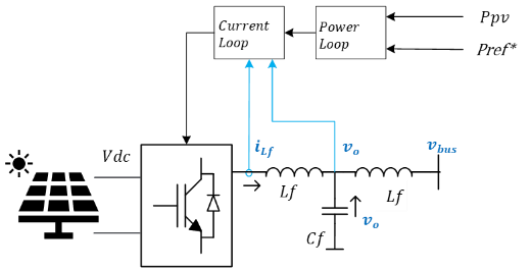

Figure D.3: PV inverter electrical model

Figure D.4 shows the comparison of the HIL model and measurement from real devices on power changes. Here, the same microgrid controller is used in both scenario. The PV is connected to the grid and the role of this microgrid controller in this test is to limit the PV export to the grid. Following an significant load reduction, the microgrid controller curtails the PV (Figure D.4a) few seconds later, the load is reconnected and microgrid controllers ramp up the PV power accordingly as shown in Figure D.4b.

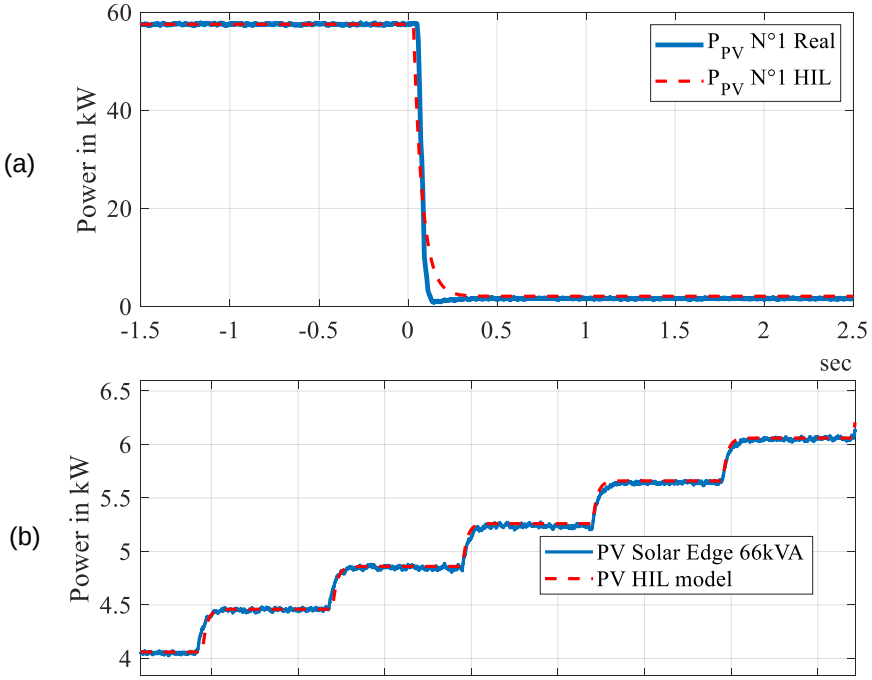

Figure D.4: benchmark of PV HIL model and real: (a) power curtailment applied (b) power curtailment removed

Bibliography

[1] IEA, "World energy outlook 2023," IEA, Paris, Tech. Rep., 2023, License: CC BY 4.0. [Online]. Available: https://www.iea.org/reports/world-energy-outlook-2023 (cit. on p. 2).

[2] IEA, "Renewable energy market update," IEA, Paris, Tech. Rep., Jun. 2023. [Online]. Available: https://www.iea.org/reports/renewable-energy-market-update-june-2023 (cit. on p. 2).

[3] D. T. Ton and M. A. Smith, "The u.s. department of energy's microgrid initiative," *The Electricity Journal*, vol. 25, no. 8, pp. 84–94, 2012. DOI: https://doi.org/10.1016/j.tej.2012.09.013. [Online]. Available: https://www.sciencedirect.com/science/article/pii/S1040619012002254 (cit. on p. 2).

[4] IEA, *The energy efficiency policy package: Key catalyst for building decarbonisation and climate action*, Online, Accessed: 2023-10-09, Paris, 2023. [Online]. Available: https://www.iea.org/commentaries/the-energy-efficiency-policy-package-key-catalyst-for-building-decarbonisation-and-climate-action,%20License:%20CC%20BY%204.0 (cit. on p. 3).

[5] E. Lightner, J. Leader, S. Berdahl, K. Cory, J. Morgenstein, and P. Schwabe, "Voices of experience: Microgrids for resiliency," Mar. 2021. [Online]. Available: https://www.osti.gov/biblio/1772428 (cit. on p. 4).

[6] E. CIAPESSONI, D. CIRIO, A. PITTO, M. PANTELI, M. V. HARTE, and C. MAK, "Defining power system resilience," *ELECTRA*, 2016 (cit. on p. 4).

[7] C. Kost, S. Shammugam, V. Fluri, D. Peper, A. D. Memar, and T. Schlegl, "Levelized cost of electricityrenewable energy technologies," Fraunhofer ISE, Tech. Rep., 2021 (cit. on p. 4).

[8] "Long-term strategy for mobilising investment in the renovation of the national stock of residential and commercial buildings, both public and private," *France Ministry of the Environment, Energy and the Sea - France Ministry of Housing and Sustainable Accommodation*, 2020. [Online]. Available: https://energy.ec.europa.eu/system/files/2017-10/fr_building_renov_2017_en_0_0.pdf (cit. on p. 5).

[9] S. Electric, *Et si intencity était le bâtiment le plus performant du monde ?* Accessed 10 Oct 2023, Feb. 2021. [Online]. Available: https://blog.se.com/fr/batiments/2021/02/04/et-si-intencity-etait-le-batiment-le-plus-performant-du-monde/ (cit. on p. 5).

[10] R. Gupta, F. Sossan, and M. Paolone, "Countrywide pv hosting capacity and energy storage requirements for distribution networks: The case of switzerland," *Applied Energy*, vol. 281, p. 116 010, 2021. DOI: https://doi.org/10.1016/j.apenergy.2020.116010. [Online]. Available: https://www.sciencedirect.com/science/article/pii/S0306261920314537 (cit. on p. 5).

[11] S. Hashemi and J. Østergaard, "Efficient control of energy storage for increasing the pv hosting capacity of lv grids," *IEEE Transactions on Smart Grid*, vol. 9, no. 3, pp. 2295–2303, May 2018. DOI: 10.1109/TSG.2016.2609892 (cit. on p. 5).

[12] G. F. Martin Nascimento, F. Wurtz, P. Kuo-Peng, B. Delinchant, N. Jhoe Batistela, and T. Laranjeira, "Green-er–electricity consumption data of a tertiary building," *Frontiers in Sustainable Cities*, vol. 5, 2023. DOI: 10.3389/frsc.2023.1043657. [Online]. Available: https://www.frontiersin.org/articles/10.3389/frsc.2023.1043657 (cit. on pp. 5, 17).

[13] ENEL-X, *University of queensland monetises bess with fcas*, accessed on 21. [Online]. Available: https://www.enelx.com/au/en/resources/university-of-queensland-vpp-participation-fcas (cit. on p. 6).

[14] V. Cavaliere, "Why some texas residents are ending up with $ 5,000 electric bills after the winter storms," *Business Insider [Online]*, 2021, Accessed Sept. 18, 2004. [Online]. Available: https://www.businessinsider.fr/us/why-texas-residents-hit-with-soaring-electric-bills-winter-storms-2021-2 (cit. on p. 6).

[15] J. J. Cook, C. Volpi, E. Nobler, and K. Flanegin, "Check the stack: An enablingframework for resilient microgrids," National Renewable Energy Laboratory, NREL/TP-6A20-71594, Nov. 2018, 2018 (cit. on p. 6).

[16] M. McGranaghan and B. Roettger, "Economic evaluation of power quality," *IEEE Power Engineering Review*, vol. 22, no. 2, pp. 8–12, 2002. DOI: 10.1109/MPER.2002.981339 (cit. on p. 6).

[17] "Cost of data center outages," *Ponemon Institute*, 2016 (cit. on pp. 6, 7).

[18] S. &C, "2021 state of commercial & industrial power reliability report," *S&C Electric Company*, 2021, Accessed 10 Nov 2023. [Online]. Available: https://www.sandc.com/globalassets/sac-electric/documents/public---documents/sales-manual-library---external-view/technical-paper-100-t131.pdf?dt=638094152703928519 (cit. on pp. 6, 7).

[19] M. J. Sullivan, J. Schellenberg, and M. Blundell, "Updated value of service reliability estimates for electric utility customers in the united states," *Berkeley National Laboratory*, 2015 (cit. on p. 7).

[20] "Ieee standard for interconnection and interoperability of distributed energy resources with associated electric power systems interfaces," *IEEE Std 1547-2018 (Revision of IEEE Std 1547-2003)*, pp. 1–138, Apr. 2018. DOI: 10.1109/IEEESTD.2018.8332112 (cit. on p. 8).

[21] G. Denis, T. Prevost, P. Panciatici, X. Kestelyn, F. Colas, and X. Guillaud, "Improving robustness against grid stiffness, with internal control of an ac voltage-controlled vsc," in *2016 IEEE Power and Energy Society General Meeting (PESGM)*, Jul. 2016, pp. 1–5. DOI: 10.1109/PESGM.2016.7741341 (cit. on p. 8).

[22] S. Kouro, J. I. Leon, D. Vinnikov, and L. G. Franquelo, "Grid-connected photovoltaic systems: An overview of recent research and emerging pv converter technology," *IEEE Industrial Electronics Magazine*, vol. 9, no. 1, pp. 47–61, 2015 (cit. on pp. 9, 10).

[23] W. Libo, Z. Zhengming, and L. Jianzheng, "A single-stage three-phase grid-connected photovoltaic system with modified mppt method and reactive power compensation," *IEEE Transactions on Energy Conversion*, vol. 22, no. 4, pp. 881–886, 2007. DOI: 10.1109/TEC.2007.895461 (cit. on p. 10).

[24] A. Saez-de-Ibarra, A. Milo, H. Gaztañaga, *et al.*, "Analysis and comparison of battery energy storage technologies for grid applications," in *2013 IEEE Grenoble Conference*, IEEE, 2013, pp. 1–6 (cit. on p. 10).

[25] M. Stecca, L. R. Elizondo, T. B. Soeiro, P. Bauer, and P. Palensky, "A comprehensive review of the integration of battery energy storage systems into distribution networks," *IEEE Open Journal of the Industrial Electronics Society*, vol. 1, pp. 46–65, 2020. DOI: 10.1109/OJIES.2020.2981832 (cit. on pp. 10, 12, 14).

[26] Z. Yang, J. Zhang, M. C. Kintner-Meyer, *et al.*, "Electrochemical energy storage for green grid," *Chemical reviews*, vol. 111, no. 5, pp. 3577–3613, 2011. DOI: https://doi.org/10.1021/cr100290v (cit. on p. 11).

[27] K. Mongird, V. Viswanathan, J. Alam, C. Vartanian, and V. Sprenkle, "2020 grid energy storagetechnology cost and performance assessment," Pacific Northwest National Laboratory, Tech. Rep., Dec. 2020 (cit. on p. 11).

[28] O. Krishan and S. Suhag, "An updated review of energy storage systems: Classification and applications in distributed generation power systems incorporating renewable energy resources," *International Journal of Energy Research*, vol. 43, no. 12, pp. 6171–6210, 2019 (cit. on p. 11).

[29] C. P. De Leon, A. Frías-Ferrer, J. González-García, D. Szánto, and F. C. Walsh, "Redox flow cells for energy conversion," *Journal of power sources*, vol. 160, no. 1, pp. 716–732, 2006 (cit. on p. 11).

[30] G. Zubi, R. Dufo-López, M. Carvalho, and G. Pasaoglu, "The lithium-ion battery: State of the art and future perspectives," *Renewable and Sustainable Energy Reviews*, vol. 89, pp. 292–308, 2018. DOI: https://doi.org/10.1016/j.rser.2018.03.002. [Online]. Available: https://www.sciencedirect.com/science/article/pii/S1364032118300728 (cit. on p. 11).

[31] F. Yang, D. Wang, Y. Zhao, K.-L. Tsui, and S. J. Bae, "A study of the relationship between coulombic efficiency and capacity degradation of commercial lithium-ion batteries," *Energy*, vol. 145, pp. 486–495, 2018. DOI: https://doi.org/10.1016/j.energy.2017.12.144. [Online]. Available: https://www.sciencedirect.com/science/article/pii/S0360544217321874 (cit. on p. 11).

[32] A. Grimaldi, F. D. Minuto, A. Perol, S. Casagrande, and A. Lanzini, "Ageing and energy performance analysis of a utility-scale lithium-ion battery for power grid applications through a data-driven empirical modelling approach," *Journal of Energy Storage*, vol. 65, 2023. DOI: https://doi.org/10.1016/j.est.2023.107232. [Online]. Available: https://www.sciencedirect.com/science/article/pii/S2352152X23006291 (cit. on p. 11).

[33] Simpliphi, "Phi 3.8-m™ battery specification sheet," *SIMPLIPHI POWER, INC.*, 2021 (cit. on p. 11).

[34] M. Brand, S. Gläser, J. Geder, *et al.*, "Electrical safety of commercial li-ion cells based on nmc and nca technology compared to lfp technology," in *2013 World Electric Vehicle Symposium and Exhibition (EVS27)*, Nov. 2013, pp. 1–9. DOI: 10.1109/EVS.2013.6914893 (cit. on p. 11).

[35] J. P. Rivera-Barrera, N. Muñoz-Galeano, and H. O. Sarmiento-Maldonado, "Soc estimation for lithium-ion batteries: Review and future challenges," *Electronics*, vol. 6, no. 4, 2017. DOI: 10.3390/electronics6040102. [Online]. Available: https://www.mdpi.com/2079-9292/6/4/102 (cit. on pp. 12, 13).

[36] F. Díaz-González, D. Heredero-Peris, M. Pagès-Giménez, E. Prieto-Araujo, and A. Sumper, "A comparison of power conversion systems for modular battery-based energy storage systems," *IEEE Access*, vol. 8, pp. 29 557–29 574, 2020. DOI: 10.1109/ACCESS.2020.2972412 (cit. on p. 12).

[37] A. Börger, J. Mertens, and H. Wenzl, "Thermal runaway and thermal runaway propagation in batteries: What do we talk about?" *Journal of Energy Storage*, vol. 24, p. 100 649, 2019 (cit. on p. 13).

[38] Mitsubishi, "Emergency operations," Mitsubishi Electric, Tech. Rep., Accessed 8 Nov 2023. [Online]. Available: https://www.mitsubishielectric.com/elevator/overview/elevators/e_operations01.html#e_ope01_04 (cit. on p. 17).

[39] schindler, "Automatic emergency lowering system," Schindler, Tech. Rep., Accessed 8 Aug 2023. [Online]. Available: https://www.schindler.com/content/dam/website/us/docs/modernization/automatic-emergency-lowering-system-brochure.pdf (cit. on p. 17).

[40] Z. Dalala, T. Alwahsh, and O. Saadeh, "Energy recovery control in elevators with automatic rescue application," *Journal of Energy Storage*, vol. 43, p. 103 168, 2021. DOI: https://doi.org/10.1016/j.est.2021.103168. [Online]. Available: https://www.sciencedirect.com/science/article/pii/S2352152X21008689 (cit. on p. 17).

[41] D. R. Danley, "Defining a microgrid usingieee 2030.7," NRECA, Tech. Rep., Nov. 2019, Acessed 10 Oct 2023. [Online]. Available: https://www.cooperative.com/programs-services/bts/documents/techsurveillance/surveillance-defining-microgrids-november-2019.pdf (cit. on p. 17).

[42] G. F. Reed, "Dc technologies," *IEEE Power & Energy Magazine*, pp. 10–17, 2012 (cit. on p. 19).

[43] "Dc building-scale microgrid platform," Accessed on 13 Nov 2023. [Online]. Available: https://cltc.ucdavis.edu/project/dc-building-scale-microgrid-platform (cit. on p. 19).

[44] T. Gabderakhmanova, J. Engelhardt, J. M. Zepter, *et al.*, "Demonstrations of dc microgrid and virtual power plant technologies on the danish island of bornholm," in *2020 55th International Universities Power Engineering Conference (UPEC)*, 2020, pp. 1–6. DOI: 10.1109/UPEC49904.2020.9209853 (cit. on p. 19).

[45] "Ieee standard for the specification of microgrid controllers," *IEEE Std 2030.7-2017*, pp. 1–43, 2018. DOI: 10.1109/IEEESTD.2018.8340204 (cit. on pp. 20, 39).

[46] J. Spitaels, L. Zhang, and P. Lin, "The different types of ups systems," *White Paper Schneider Electric*, 2021, accessed 10 Nov 2023. [Online]. Available: https://www.se.com/us/en/download/document/SPD_SADE-5TNM3Y_EN/ (cit. on pp. 22, 23).

[47] S. Rathmann and H. Warner, "New generation ups technology, the delta conversion principle," in *IAS '96. Conference Record of the 1996 IEEE Industry Applications Conference Thirty-First IAS Annual Meeting*, vol. 4, Oct. 1996, 2389–2395 vol.4. DOI: 10.1109/IAS.1996.563905 (cit. on p. 24).

[48] *Electric rule no. 21 generating facility interconnections. san francisco, california*, 2018 (cit. on p. 25).

[49] *Commission regulation (eu) 2016/631 of 14 april 2016 establishing a network code on requirements for grid connection of generators.* [Online]. Available: http://data.europa.eu/eli/reg/2016/631/oj (cit. on pp. 25, 47).

[50] H. Mokhtari, S. Dewan, and M. Iravani, "Analysis of a static transfer switch with respect to transfer time," *IEEE Transactions on Power Delivery*, vol. 17, no. 1, pp. 190–199, 2002. DOI: 10.1109/61.974207 (cit. on p. 26).

[51] K.-Y. Lo and Y.-M. Chen, "Design of a seamless grid-connected inverter for microgrid applications," *IEEE Transactions on Smart Grid*, vol. 11, no. 1, pp. 194–202, 2020. DOI: 10.1109/TSG.2019.2919905 (cit. on pp. 26, 62, 83).

[52] M. Ganjian-Aboukheili, M. Shahabi, Q. Shafiee, and J. M. Guerrero, "Seamless transition of microgrids operation from grid-connected to islanded mode," *IEEE Transactions on Smart Grid*, vol. 11, no. 3, pp. 2106–2114, May 2020. DOI: 10.1109/TSG.2019.2947651 (cit. on pp. 26, 62).

[53] S. Kamajaya, J. Buire, R. Caire, S. Bacha, and J. Wild, "Microgrid control strategy to achieve seamless transition from grid connected to islanded mode," in *27th International Conference on Electricity Distribution CIRED 2023*, 2023 (cit. on p. 27).

[54] S. Kamajaya, J. Buire, R. Caire, S. Bacha, and J. Wild, "P-hil validation for double loop proportional resonant control in abc stationary frame for grid forming inverter," in *2023 IEEE PES Innovative Smart Grid Technologies Europe (ISGT EUROPE)*, 2023, pp. 1–5. DOI: 10.1109/ISGTEUROPE56780.2023.10408366 (cit. on p. 27).

[55] S. Kamajaya, A. Moulichon, F. Aubert, and J. Wild, "Ensuring reliable microgrid solutions: Hardware-in-the-loop (hil) modeling and validation processes for testing and commissioning," in *2023 IEEE PES Innovative Smart Grid Technologies Europe (ISGT EUROPE)*, 2023, pp. 1–5. DOI: 10.1109/ISGTEUROPE56780.2023.10407245 (cit. on pp. 27, 115).

[56] J. Wild, S. Kamajaya, A. Moulichon, and F. Cazals, "Power-hardware in the loop and standardization for the growing microgrids industry," in *2023 IEEE PES Innovative Smart Grid Technologies Europe (ISGT EUROPE)*, 2023, pp. 1–5. DOI: 10.1109/ISGTEUROPE56780.2023.10408277 (cit. on p. 27).

[57] A. Vukojevic and S. Lukic, "Microgrid protection and control schemes for seamless transition to island and grid synchronization," *IEEE Transactions on Smart Grid*, vol. 11, no. 4, pp. 2845–2855, Jul. 2020. DOI: 10.1109/TSG.2020.2975850 (cit. on p. 32).

[58] Y.-Y. Hong and M. T. A. M. Cabatac, "Fault detection, classification, and location by static switch in microgrids using wavelet transform and taguchi-based artificial neural network," *IEEE Systems Journal*, vol. 14, no. 2, pp. 2725–2735, Jun. 2020. DOI: 10.1109/JSYST.2019.2925594 (cit. on pp. 32, 51).

[59] "Ieee recommended practice for monitoring electric power quality," *IEEE Std 1159-2019 (Revision of IEEE Std 1159-2009)*, pp. 1–98, 2019. DOI: 10.1109/IEEESTD.2019.8796486 (cit. on pp. 33, 34, 36).

[60] M. H. J. Bollen, "What is power quality?" *Electric Power Systems Research*, vol. 66, no. 1, pp. 5–14, 2003, Power Quality. DOI: https://doi.org/10.1016/S0378-7796(03)00067-1. [Online]. Available: https://www.sciencedirect.com/science/article/pii/S0378779603000671 (cit. on pp. 33, 36).

[61] J. Seymour, "The seven types of power problems," *Schneider Electric White Paper*, 2010, Accessed on 20 Nov 2023. [Online]. Available: https://www.se.com/us/en/download/document/SPD_VAVR-5WKLPK_EN/ (cit. on p. 34).

[62] "Electromagnetic compatibility (emc) - part 2-4: Environment - compatibility levels in industrial plants for low-frequency conducted disturbances," *IEC 61000-2-4:2002*, 2002 (cit. on p. 34).

[63] "Electromagnetic compatibility (emc) - environment - compatibility levels for low-frequency conducted disturbances and signalling in public low-voltage power supply systems," *IEC61000-2-2:2002+AMD2:2018*, 2018 (cit. on p. 34).

[64] "Voltage characteristics of electricity supplied by public electricity networks," *EN 50160*, 2011 (cit. on p. 34).

[65] "IEEE recommended practice for voltage sag and short interruption ride through testing for end-use electrical equipment rated less than 1000 v," *IEEE Std 1668-2017*, 2017 (cit. on pp. 36, 37).

[66] M. McGranaghan, D. Mueller, and M. Samotyj, "Voltage sags in industrial systems," *IEEE Transactions on Industry Applications*, vol. 29, no. 2, pp. 397–403, 1993. DOI: 10.1109/28.216550 (cit. on pp. 36, 38, 41).

[67] V. Ignatova, P. Granjon, S. Bacha, and F. Dumas, "Classification and characterization of three phase voltage dips by space vector methodology," in *2005 International Conference on Future Power Systems*, 2005, 6 pp.–6. DOI: 10.1109/FPS.2005.204283 (cit. on p. 37).

[68] V. Ignatova, "Méthodes d'analyse de la qualité de l'énergie électrique. application aux creux de tension et à la pollution harmonique.," Ph.D. dissertation, Grenoble, 2006. [Online]. Available: https://tel.archives-ouvertes.fr/tel-00170713 (cit. on p. 37).

[69] M. Bollen, M. S. S. Djokicand, K. Stockman, *et al.*, "Voltage dip immunity of equipment and installations," CIGRE/CIRED/UIE Joint Working Group C4.110, Tech. Rep., Apr. 2010 (cit. on pp. 37–39, 41, 42, 50).

[70] "Ieee standard for the testing of microgrid controllers," *IEEE Std 2030.8-2018*, 2018. DOI: 10.1109/IEEESTD.2018.8444947 (cit. on p. 39).

[71] "Iti (cbema) curve application note," Technology Ind Council (ITI), Tech. Rep., 2000 (cit. on p. 40).

[72] P. Pohjanheimo and M. Lehtonen, "Equipment sensitivity to voltage sags-test results for contactors, pcs and gas discharge lamps," in *10th International Conference on Harmonics and Quality of Power. Proceedings (Cat. No.02EX630)*, vol. 2, Oct. 2002, 559–564 vol.2. DOI: 10.1109/ICHQP.2002.1221496 (cit. on pp. 41, 42).

[73] S. Uddin, H. Shareef, and A. Mohamed, "Power quality performance of energy-efficient low-wattage led lamps," *Measurement*, vol. 46, no. 10, pp. 3783–3795, 2013. DOI: https://doi.org/10.1016/j.measurement.2013.07.022. [Online]. Available: https://www.sciencedirect.com/science/article/pii/S0263224113003217 (cit. on p. 41).

[74] S. Sakar, S. Rönnberg, and M. Bollen, "Light intensity immunity performance of led street lamps under power quality disturbances," in *CIRED 2019 Proceedinga*, AIM, 2019. DOI: 10.34890/282. [Online]. Available: https://urn.kb.se/resolve?urn=urn:nbn:se:ltu:diva-76485 (cit. on p. 41).

[75] K. Stockman, F. D'hulster, K. Verhaege, M. Didden, and R. Belmans, "Ride-through of adjustable speed drives during voltage dips," *Electric Power Systems Research*, vol. 66, no. 1, pp. 49–58, 2003, Power Quality. DOI: https://doi.org/10.1016/S0378-7796(03)00071-3. [Online]. Available: https://www.sciencedirect.com/science/article/pii/S0378779603000713 (cit. on p. 41).

[76] S. Djokic, K. Stockman, J. Milanovic, J. Desmet, and R. Belmans, "Sensitivity of ac adjustable speed drives to voltage sags and short interruptions," *IEEE Transactions on Power Delivery*, vol. 20, no. 1, pp. 494–505, Jan. 2005. DOI: 10.1109/TPWRD.2004.832353 (cit. on p. 42).

[77] "Low-voltage switchgear and controlgear –part 4-1: Contactors and motor-starters – electromechanical contactors andmotor-starters," *IEC60947-4-1:2018*, 2018 (cit. on p. 42).

[78] S. Djokic, J. Milanovic, and D. Kirschen, "Sensitivity of ac coil contactors to voltage sags, short interruptions, and undervoltage transients," *IEEE Transactions on Power Delivery*, vol. 19, no. 3, pp. 1299–1307, Jul. 2004. DOI: 10.1109/TPWRD.2004.824396 (cit. on p. 42).

[79] H. Mokhtari, S. Dewan, and M. Travani, "Performance evaluation of thyristor based static transfer switch," *IEEE Transactions on Power Delivery*, vol. 15, no. 3, pp. 960–966, Jul. 2000. DOI: 10.1109/61.871359 (cit. on pp. 45, 60).

[80] C. Meyer and R. De Doncker, "Solid-state circuit breaker based on active thyristor topologies," *IEEE Transactions on Power Electronics*, vol. 21, no. 2, pp. 450–458, Mar. 2006. DOI: 10.1109/TPEL.2005.869756 (cit. on p. 45).

[81] M. S. Mollik, M. A. Hannan, P. J. Ker, *et al.*, "Review on solid-state transfer switch configurations and control methods: Applications, operations, issues, and future directions," *IEEE Access*, vol. 8, pp. 182 490–182 505, 2020. DOI: 10.1109/ACCESS.2020.3028870 (cit. on p. 45).

[82] X. Zhang, Z. Yu, B. Zhao, *et al.*, "A novel mixture solid-state switch based on igct with high capacity and igbt with high turn-off ability for hybrid dc breakers," *IEEE Transactions on Industrial Electronics*, vol. 67, no. 6, pp. 4485–4495, Jun. 2020. DOI: 10.1109/TIE.2019.2928279 (cit. on p. 45).

[83] M. Al-Dweikat, J. Cui, S. Sun, M. Yang, G. Zhang, and Y. Geng, "A review on thomson coil actuators in fast mechanical switching," *Actuators*, vol. 11, no. 6, 2022. DOI: 10.3390/act11060154. [Online]. Available: https://www.mdpi.com/2076-0825/11/6/154 (cit. on p. 45).

[84] C. N. M. Ajmal, I. V. Raghavendra, S. Naik, A. Ray, and H. S. Krishnamoorthy, "A modified hybrid dc circuit breaker with reduced arc for low voltage dc grids," *IEEE Access*, vol. 9, pp. 132 267–132 277, 2021. DOI: 10.1109/ACCESS.2021.3115456 (cit. on p. 45).

[85] O.-y. Hua, B. Le-ping, and Y. Zhong-lin, "Voltage sag detection based on dq transform and mathematical morphology filter," *Procedia Engineering*, vol. 23, pp. 775–779, 2011, PEEA 2011. DOI: https://doi.org/10.1016/j.proeng.2011.11.2580. [Online]. Available: https://www.sciencedirect.com/science/article/pii/S1877705811054233 (cit. on p. 49).

[86] C. Ma, F. Gao, G. He, and G. Li, "A voltage detection method for the voltage ride-through operation of renewable energy generation systems under grid voltage distortion conditions," *IEEE Transactions on Sustainable Energy*, vol. 6, no. 3, pp. 1131–1139, Jul. 2015. DOI: 10.1109/TSTE.2014.2331684 (cit. on pp. 49, 50).

[87] A. K. Sadigh and K. Smedley, "Fast and precise voltage sag detection method for dynamic voltage restorer (DVR) application," *Electric Power Systems Research*, vol. 130, pp. 192–207, Jan. 2016. DOI: 10.1016/j.epsr.2015.08.002 (cit. on pp. 49, 51, 60).

[88] C. Fitzer, M. Barnes, and P. Green, "Voltage sag detection technique for a dynamic voltage restorer," *IEEE Transactions on Industry Applications*, vol. 40, no. 1, pp. 203–212, 2004. DOI: 10.1109/TIA.2003.821801 (cit. on pp. 49–51, 60).

[89] R. Naidoo and P. Pillay, "A new method of voltage sag and swell detection," *IEEE Transactions on Power Delivery*, vol. 22, no. 2, pp. 1056–1063, Apr. 2007. DOI: 10.1109/TPWRD.2007.893185 (cit. on p. 49).

[90] M. Moschakis and N. Hatziargyriou, "A detailed model for a thyristor-based static transfer switch," *IEEE Transactions on Power Delivery*, vol. 18, no. 4, pp. 1442–1449, Oct. 2003. DOI: 10.1109/TPWRD.2003.817790 (cit. on p. 49).

[91] B. Bae, J. Lee, J. Jeong, and B. Han, "Line-interactive single-phase dynamic voltage restorer with novel sag detection algorithm," *IEEE Transactions on Power Delivery*, vol. 25, no. 4, pp. 2702–2709, Oct. 2010. DOI: 10.1109/TPWRD.2010.2044194 (cit. on pp. 49, 51, 60).

[92] M. Tumay, M. Meral, and K. Bayindir, "Sequence reference frame-based new sag/swell detection method for static transfer switches," *Power Electronics, IET*, vol. 2, pp. 431–442, Aug. 2009. DOI: 10.1049/iet-pel.2007.1013 (cit. on pp. 49, 50).

[93] R. J. A. Frazao, "PMU based situation awareness for smart distribution grids," Theses, Université Grenoble Alpes, Oct. 2015. [Online]. Available: https://theses.hal.science/tel-01224221 (cit. on pp. 49, 50).

[94] Y. Sillapawicharn and Y. Kumsuwan, "An improvement of synchronously rotating reference frame based voltage sag detection for voltage sag compensation applications under distorted grid voltages," in *2011 IEEE Ninth International Conference on Power Electronics and Drive Systems*, 2011, pp. 100–103. DOI: 10.1109/PEDS.2011.6147231 (cit. on pp. 49, 50).

[95] O. Montero-Hernandez and P. Enjeti, "A fast detection algorithm suitable for mitigation of numerous power quality disturbances," *IEEE Transactions on Industry Applications*, vol. 41, no. 6, pp. 1684–1690, Nov. 2005. DOI: 10.1109/TIA.2005.857459 (cit. on pp. 49, 50).

[96] C. Ghafari, "Innovative numerical protection relaydesign on the basis of sampled measuredvalues for smart grids," Ph.D. dissertation, UNIVERSITÉ GRENOBLE ALPES, 2016 (cit. on pp. 49, 50).

[97] A. G. Phadke and B. Kasztenny, "Synchronized phasor and frequency measurement under transient conditions," *IEEE Transactions on Power Delivery*, vol. 24, no. 1, pp. 89–95, 2009. DOI: 10.1109/TPWRD.2008.2002665 (cit. on pp. 49, 50).

[98] E. Pérez and J. Barros, "An extended kalman filtering approach for detection and analysis of voltage dips in power systems," *Electric Power Systems Research*, vol. 78, no. 4, pp. 618–625, 2008. DOI: https://doi.org/10.1016/j.epsr.2007.05.006. [Online]. Available: https://www.sciencedirect.com/science/article/pii/S0378779607001101 (cit. on pp. 49, 51, 60).

[99] M. Gonzalez, V. Cardenas, and R. Alvarez, "Detection of sags, swells, and interruptions using the digital rms method and kalman filter with fast response," in *IECON 2006-32nd Annual Conference on IEEE Industrial Electronics*, IEEE, 2006, pp. 2249–2254 (cit. on pp. 49, 51).

[100] D. A. Pinto and J. Sepúlveda, "Design of a high-performance single-phase offline ups with reduced switching time," Jul. 2012. [Online]. Available: http://hdl.handle.net/1822/20972 (cit. on p. 49).

[101] E. O. Schweitzer, B. Kasztenny, A. Guzmán, V. Skendzic, and M. V. Mynam, "Speed of line protection - can we break free of phasor limitations?" In *2015 68th Annual Conference for Protective Relay Engineers*, Mar. 2015, pp. 448–461. DOI: 10.1109/CPRE.2015.7102184 (cit. on p. 50).

[102] J. A. de la O Serna, "Dynamic phasor estimates for power system oscillations," *IEEE Transactions on Instrumentation and Measurement*, vol. 56, no. 5, pp. 1648–1657, Oct. 2007. DOI: 10.1109/TIM.2007.904546 (cit. on p. 50).

[103] A. T. Munoz and J. A. de la O. Serna, "Shanks' method for dynamic phasor estimation," *IEEE Transactions on Instrumentation and Measurement*, vol. 57, no. 4, pp. 813–819, 2008. DOI: 10.1109/TIM.2007.913824 (cit. on p. 50).

[104] E. Styvaktakis, I. Gu, and M. Bollen, "Voltage dip detection and power system transients," in *2001 Power Engineering Society Summer Meeting. Conference Proceedings (Cat. No.01CH37262)*, vol. 1, 2001, 683–688 vol.1. DOI: 10.1109/PESS.2001.970124 (cit. on p. 51).

[105] V. A. Katić, A. M. Stanisavljević, R. L. Turović, B. P. Dumnić, and B. P. Popadić, "Extended kalman filter for voltage dips detection in grid with distributed energy resources," in *2018 IEEE PES Innovative Smart Grid Technologies Conference Europe (ISGT-Europe)*, Oct. 2018, pp. 1–6. DOI: 10.1109/ISGTEurope.2018.8571857 (cit. on p. 51).

[106] D. Robertson, O. Camps, J. Mayer, and W. Gish, "Wavelets and electromagnetic power system transients," *IEEE Transactions on Power Delivery*, vol. 11, no. 2, pp. 1050–1058, Apr. 1996. DOI: 10.1109/61.489367 (cit. on p. 51).

[107] S. Santoso, E. Powers, W. Grady, and P. Hofmann, "Power quality assessment via wavelet transform analysis," *IEEE Transactions on Power Delivery*, vol. 11, no. 2, pp. 924–930, Apr. 1996. DOI: 10.1109/61.489353 (cit. on p. 51).

[108] E. Perez and J. Barros, "A proposal for on-line detection and classification of voltage events in power systems," *IEEE Transactions on Power Delivery*, vol. 23, no. 4, pp. 2132–2138, Oct. 2008. DOI: 10.1109/TPWRD.2008.921121 (cit. on p. 51).

[109] E. Perez and J. Barros, "Voltage event detection and characterization methods: A comparative study," in *2006 IEEE/PES Transmission Distribution Conference and Exposition: Latin America*, 2006, pp. 1–6. DOI: 10.1109/TDCLA.2006.311552 (cit. on p. 51).

[110] A. K. Chandel, G. Guleria, and R. Chandel, "Classification of power quality problems using wavelet based artificial neural network," in *2008 IEEE/PES Transmission and Distribution Conference and Exposition*, 2008, pp. 1–5. DOI: 10.1109/TDC.2008.4517083 (cit. on p. 51).

[111] S.-K. Chung, "A phase tracking system for three phase utility interface inverters," *IEEE Transactions on Power Electronics*, vol. 15, no. 3, pp. 431–438, May 2000. DOI: 10.1109/63.844502 (cit. on pp. 52, 53).

[112] C. J. O'Rourke, M. M. Qasim, M. R. Overlin, and J. L. Kirtley, "A geometric interpretation of reference frames and transformations: Dq0, clarke, and park," *IEEE Transactions on Energy Conversion*, vol. 34, pp. 2070–2083, 4 2019 (cit. on pp. 53, 67).

[113] S. Golestan, M. Ramezani, J. M. Guerrero, F. D. Freijedo, and M. Monfared, "Moving average filter based phase-locked loops: Performance analysis and design guidelines," *IEEE Transactions on Power Electronics*, vol. 29, no. 6, pp. 2750–2763, Jun. 2014. DOI: 10.1109/TPEL.2013.2273461 (cit. on p. 53).

[114] Z. Ali, N. Christofides, L. Hadjidemetriou, E. Kyriakides, Y. Yang, and F. Blaabjerg, "Three-phase phase-locked loop synchronization algorithms for grid-connected renewable energy systems: A review," *Renewable and Sustainable Energy Reviews*, vol. 90, pp. 434–452, 2018. DOI: https://doi.org/10.1016/j.rser.2018.03.086. [Online]. Available: https://www.sciencedirect.com/science/article/pii/S1364032118301813 (cit. on p. 53).

[115] Y. F. Wang and Y. W. Li, "Grid synchronization pll based on cascaded delayed signal cancellation," *IEEE Transactions on Power Electronics*, vol. 26, no. 7, pp. 1987–1997, 7 2011. DOI: 10.1109/TPEL.2010.2099669 (cit. on p. 54).

[116] S. Golestan, M. Ramezani, J. M. Guerrero, and M. Monfared, "Dq-frame cascaded delayed signal cancellation-based pll: Analysis design and comparison with moving average filter-based pll," *IEEE Trans. Power Electron*, vol. 30, pp. 1618–1632, 3 2015 (cit. on p. 54).

[117] Q. Huang and K. Rajashekara, "An improved delayed signal cancellation pll for fast grid synchronization under distorted and unbalanced grid condition," *IEEE Transactions on Industry Applications*, vol. 53, pp. 4985–4997, 7 2017 (cit. on p. 54).

[118] P. Rodriguez, J. Pou, J. Bergas, J. I. Candela, R. P. Burgos, and D. Boroyevich, "Decoupled double synchronous reference frame pll for power converters control," *IEEE Transactions on Power Electronics*, vol. 22, pp. 584–592, 2 2007 (cit. on p. 54).

[119] J. M. Guerrero, J. C. Vasquez, J. Matas, M. Castilla, and L. Garcia de Vicuna, "Control strategy for flexible microgrid based on parallel line-interactive ups systems," *IEEE Transactions on Industrial Electronics*, vol. 56, no. 3, pp. 726–736, Mar. 2009. DOI: 10.1109/TIE.2008.2009274 (cit. on p. 62).

[120] Y. A.-R. I. Mohamed and A. A. Radwan, "Hierarchical control system for robust microgrid operation and seamless mode transfer in active distribution systems," *IEEE Transactions on Smart Grid*, vol. 2, no. 2, pp. 352–362, Jun. 2011. DOI: 10.1109/TSG.2011.2136362 (cit. on p. 62).

[121] D. S. Ochs, B. Mirafzal, and P. Sotoodeh, "A method of seamless transitions between grid-tied and stand-alone modes of operation for utility-interactive three-phase inverters," *IEEE Transactions on Industry Applications*, vol. 50, no. 3, pp. 1934–1941, 2014. DOI: 10.1109/TIA.2013.2282761 (cit. on p. 62).

[122] A. Micallef, M. Apap, C. Spiteri-Staines, and J. M. Guerrero, "Single-phase microgrid with seamless transition capabilities between modes of operation," *IEEE Transactions on Smart Grid*, vol. 6, no. 6, pp. 2736–2745, Nov. 2015. DOI: 10.1109/TSG.2015.2444912 (cit. on p. 62).

[123] M. A. Abusara and S. M. Sharkh, "Control of line interactive ups systems in a microgrid," in *2011 IEEE International Symposium on Industrial Electronics*, Jun. 2011, pp. 1433–1440. DOI: 10.1109/ISIE.2011.5984371 (cit. on p. 62).

[124] M. A. Abusara, J. M. Guerrero, and S. M. Sharkh, "Line-interactive ups for microgrids," *IEEE Transactions on Industrial Electronics*, vol. 61, no. 3, pp. 1292–1300, Mar. 2014. DOI: 10.1109/TIE.2013.2262763 (cit. on p. 62).

[125] X. Wang, J. Guerrero, F. Blaabjerg, and Z. Chen, "A review of power electronics based microgrids," English, *International Journal of Power Electronics*, vol. 12, no. 1, pp. 181–192, 2012 (cit. on p. 62).

[126] S. Jayalath and M. Hanif, "Generalized lcl-filter design algorithm for grid-connected voltage-source inverter," *IEEE Transactions on Industrial Electronics*, vol. 64, no. 3, pp. 1905–1915, Mar. 2017. DOI: 10.1109/TIE.2016.2619660 (cit. on pp. 64, 70).

[127] G. Denis, "From grid-following to grid-forming: The new strategy to build 100 % power-electronics interfaced transmission system with enhanced transient behavior.," Ph.D. dissertation, Nov. 2017 (cit. on pp. 64, 65).

[128] W. Du, Z. Chen, K. P. Schneider, *et al.*, "A comparative study of two widely used grid-forming droop controls on microgrid small-signal stability," *IEEE Journal of Emerging and Selected Topics in Power Electronics*, vol. 8, no. 2, pp. 963–975, Jun. 2020. DOI: 10.1109/JESTPE.2019.2942491 (cit. on p. 64).

[129] Z. Li, Y. Li, P. Wang, H. Zhu, C. Liu, and F. Gao, "Single-loop digital control of high-power 400-hz ground power unit for airplanes," *IEEE Transactions on Industrial Electronics*, vol. 57, no. 2, pp. 532–543, 2010. DOI: 10.1109/TIE.2009.2033490 (cit. on p. 64).

[130] X. Wang, P. C. Loh, and F. Blaabjerg, "Stability analysis and controller synthesis for single-loop voltage-controlled vsis," *IEEE Transactions on Power Electronics*, vol. 32, no. 9, pp. 7394–7404, Sep. 2017. DOI: 10.1109/TPEL.2016.2632065 (cit. on p. 64).

[131] F. Blaabjerg, R. Teodorescu, M. Liserre, and A. Timbus, "Overview of control and grid synchronization for distributed power generation systems," *IEEE Transactions on Industrial Electronics*, vol. 53, no. 5, pp. 1398–1409, Oct. 2006. DOI: 10.1109/TIE.2006.881997 (cit. on pp. 64, 68).

[132] A. Timbus, M. Ciobotaru, R. Teodorescu, and F. Blaabjerg, "Adaptive resonant controller for grid-connected converters in distributed power generation systems," in *Twenty-First Annual IEEE Applied Power Electronics Conference and Exposition, 2006. APEC '06.*, 2006, p. 6. DOI: 10.1109/APEC.2006.1620754 (cit. on pp. 64, 69, 70).

[133] A. Ovalle, G. Ramos, S. Bacha, A. Hably, and A. Rumeau, "Decentralized control of voltage source converters in microgrids based on the application of instantaneous power theory," *IEEE Transactions on Industrial Electronics*, vol. 62, no. 2, pp. 1152–1162, 2015. DOI: 10.1109/TIE.2014.2336638 (cit. on p. 64).

[134] T. Qoria, F. Gruson, F. Colas, X. Guillaud, M.-S. Debry, and T. Prevost, "Tuning of cascaded controllers for robust grid-forming voltage source converter," in *2018 Power Systems Computation Conference (PSCC)*, Jun. 2018, pp. 1–7. DOI: 10.23919/PSCC.2018.8443018 (cit. on p. 64).

[135] "Performance comparison of dc and ac controllers for a two-stage power converter in energy storage application," *Electric Power Systems Research*, vol. 164, pp. 47–60, 2018. DOI: https://doi.org/10.1016/j.epsr.2018.07.021. [Online]. Available: https://www.sciencedirect.com/science/article/pii/S0378779618302141 (cit. on p. 64).

[136] G. Liu, T. Caldognetto, P. Mattavelli, and P. Magnone, "Power-based droop control in dc microgrids enabling seamless disconnection from upstream grids," *IEEE Transactions on Power Electronics*, vol. 34, no. 3, pp. 2039–2051, Mar. 2019. DOI: 10.1109/TPEL.2018.2839667 (cit. on p. 64).

[137] N. Altin, S. Ozdemir, H. Komurcugil, and I. Sefa, "Sliding-mode control in natural frame with reduced number of sensors for three-phase grid-tied lcl-interfaced inverters," *IEEE Transactions on Industrial Electronics*, vol. 66, no. 4, pp. 2903–2913, Apr. 2019. DOI: 10.1109/TIE.2018.2847675 (cit. on p. 64).

[138] A. L. de Heredia, H. Gaztanaga, I. Etxeberria-Otadui, S. Bacha, and X. Guillaud, "Analysis of multi-resonant current control structures and tuning methods," in *IECON 2006 - 32nd Annual Conference on IEEE Industrial Electronics*, 2006, pp. 2156–2161. DOI: 10.1109/IECON.2006.347276 (cit. on pp. 64, 70, 71).

[139] N. Baeckeland, D. Venkatramanan, M. Kleemann, and S. Dhople, "Stationary-frame grid-forming inverter control architectures for unbalanced fault-current limiting," *IEEE Transactions on Energy Conversion*, vol. 37, no. 4, pp. 2813–2825, Dec. 2022. DOI: 10.1109/TEC.2022.3203656 (cit. on pp. 64, 85).

[140] Q. Liu, T. Caldognetto, and S. Buso, "Review and comparison of grid-tied inverter controllers in microgrids," *IEEE Transactions on Power Electronics*, vol. 35, no. 7, pp. 7624–7639, Jul. 2020. DOI: 10.1109/TPEL.2019.2957975 (cit. on p. 65).

[141] D. B. Rathnayake, M. Akrami, C. Phurailatpam, *et al.*, "Grid forming inverter modeling, control, and applications," *IEEE Access*, vol. 9, pp. 114 781–114 807, 2021. DOI: 10.1109/ACCESS.2021.3104617 (cit. on p. 65).

[142] A. Micallef, M. Apap, C. Spiteri-Staines, J. M. Guerrero, and J. C. Vasquez, "Reactive power sharing and voltage harmonic distortion compensation of droop controlled single phase islanded microgrids," *IEEE Transactions on Smart Grid*, vol. 5, no. 3, pp. 1149–1158, May 2014. DOI: 10.1109/TSG.2013.2291912 (cit. on p. 65).

[143] J. C. Vasquez, J. M. Guerrero, M. Savaghebi, J. Eloy-Garcia, and R. Teodorescu, "Modeling, analysis, and design of stationary-reference-frame droop-controlled parallel three-phase voltage source inverters," *IEEE Transactions on Industrial Electronics*, vol. 60, no. 4, pp. 1271–1280, Apr. 2013. DOI: 10.1109/TIE.2012.2194951 (cit. on p. 65).

[144] J. Liu, Y. Miura, and T. Ise, "Comparison of dynamic characteristics between virtual synchronous generator and droop control in inverter-based distributed generators," *IEEE Transactions on Power Electronics*, vol. 31, no. 5, pp. 3600–3611, May 2016. DOI: 10.1109/TPEL.2015.2465852 (cit. on p. 65).

[145] A. Moulichon, M. Alamir, V. Debusschere, *et al.*, "Observer-based current controller for virtual synchronous generator in presence of unknown and unpredictable loads," *IEEE Transactions on Power Electronics*, vol. 36, no. 2, pp. 1708–1716, Feb. 2021. DOI: 10.1109/TPEL.2020.3010085 (cit. on p. 65).

[146] S. Azizi Aghdam and M. Agamy, "Virtual oscillator-based methods for grid-forming inverter control: A review," *IET Renewable Power Generation*, vol. 16, no. 5, pp. 835–855, 2022 (cit. on p. 65).

[147] X. Wang, M. G. Taul, H. Wu, Y. Liao, F. Blaabjerg, and L. Harnefors, "Grid-synchronization stability of converter-based resources—an overview," *IEEE Open Journal of Industry Applications*, vol. 1, pp. 115–134, 2020. DOI: 10.1109/OJIA.2020.3020392 (cit. on p. 65).

[148] F. Zhao, X. Wang, and T. Zhu, "Power dynamic decoupling control of grid-forming converter in stiff grid," *IEEE Transactions on Power Electronics*, vol. 37, no. 8, pp. 9073–9088, 2022. DOI: 10.1109/TPEL.2022.3156991 (cit. on p. 65).

[149] X. Yuan, W. Merk, H. Stemmler, and J. Allmeling, "Stationary-frame generalized integrators for current control of active power filters with zero steady-state error for current harmonics of concern under unbalanced and distorted operating conditions," *IEEE Transactions on Industry Applications*, vol. 38, no. 2, pp. 523–532, 2002. DOI: 10.1109/28.993175 (cit. on pp. 68–71).

[150] I. Etxeberria-Otadui, "Sur les systèmes de l'électronique de puissance dédiés à la distribution électrique : Application à la qualité de l'énergie," Ph.D. dissertation, institut national polytechnique de grenoble, 2003 (cit. on p. 69).

[151] A. G. Yepes, "Digital resonant current controllers for voltage source converter," Ph.D. dissertation, university of vigo, 2011 (cit. on pp. 69, 70).

[152] D. Zmood and D. Holmes, "Stationary frame current regulation of pwm inverters with zero steady-state error," *IEEE Transactions on Power Electronics*, vol. 18, no. 3, pp. 814–822, May 2003. DOI: 10.1109/TPEL.2003.810852 (cit. on pp. 69, 70).

[153] L. R. Limongi, R. Bojoi, G. Griva, and A. Tenconi, "Digital current-control schemes," *IEEE industrial electronics magazine*, vol. 3, no. 1, pp. 20–31, 2009 (cit. on p. 69).

[154] A. G. Yepes, F. D. Freijedo, J. Doval-Gandoy, Ó. López, J. Malvar, and P. Fernandez-Comesaña, "Effects of discretization methods on the performance of resonant controllers," *IEEE Transactions on Power Electronics*, vol. 25, no. 7, pp. 1692–1712, Jul. 2010. DOI: 10.1109/TPEL.2010.2041256 (cit. on p. 69).

[155] C. Bao, X. Ruan, X. Wang, W. Li, D. Pan, and K. Weng, "Design of injected grid current regulator and capacitor-current-feedback active-damping for lcl-type grid-connected inverter," in *2012 IEEE Energy Conversion Congress and Exposition (ECCE)*, Sep. 2012, pp. 579–586. DOI: 10.1109/ECCE.2012.6342769 (cit. on p. 69).

[156] E. Twining and D. Holmes, "Grid current regulation of a three-phase voltage source inverter with an lcl input filter," *IEEE Transactions on Power Electronics*, vol. 18, no. 3, pp. 888–895, May 2003. DOI: 10.1109/TPEL.2003.810838 (cit. on p. 70).

[157] G. Shen, X. Zhu, J. Zhang, and D. Xu, "A new feedback method for pr current control of lcl-filter-based grid-connected inverter," *IEEE Transactions on Industrial Electronics*, vol. 57, no. 6, pp. 2033–2041, Jun. 2010. DOI: 10.1109/TIE.2010.2040552 (cit. on p. 70).

[158] S. Bacha, I. Munteanu, A. I. Bratcu, *et al.*, "Power electronic converters modeling and control," *Advanced textbooks in control and signal processing*, vol. 454, no. 454, 2014 (cit. on p. 70).

[159] I. Etxeberria-Otadui, A. Lopez De Heredia, H. Gaztanaga, S. Bacha, and M. Reyero, "A single synchronous frame hybrid (ssfh) multifrequency controller for power active filters," *IEEE Transactions on Industrial Electronics*, vol. 53, no. 5, pp. 1640–1648, Oct. 2006. DOI: 10.1109/TIE.2006.881994 (cit. on pp. 70, 71).

[160] F. Hans, W. Schumacher, S.-F. Chou, and X. Wang, "Design of multifrequency proportional–resonant current controllers for voltage-source converters," *IEEE Transactions on Power Electronics*, vol. 35, no. 12, pp. 13 573–13 589, Dec. 2020. DOI: 10.1109/TPEL.2020.2993163 (cit. on p. 70).

[161] N. Zhang, H. Tang, and C. Yao, "A systematic method for designing a pr controller and active damping of the lcl filter for single-phase grid-connected pv inverters," *Energies*, 2014 (cit. on p. 70).

[162] Z. Xin, X. Wang, P. C. Loh, and F. Blaabjerg, "Grid-current-feedback control for lcl-filtered grid converters with enhanced stability," *IEEE Transactions on Power Electronics*, vol. 32, no. 4, pp. 3216–3228, 2017. DOI: 10.1109/TPEL.2016.2580543 (cit. on p. 70).

[163] R. Teodorescu, F. Blaabjerg, M. Liserre, and P. C. Loh, "Proportional-resonant controllers and filters for grid-connected voltage-source converters," *IEE Proceedings-Electric Power Applications*, vol. 153, no. 5, pp. 750–762, 2006 (cit. on p. 71).

[164] Y. A.-R. I. Mohamed and E. F. El-Saadany, "Adaptive decentralized droop controller to preserve power sharing stability of paralleled inverters in distributed generation microgrids," *IEEE Transactions on Power Electronics*, vol. 23, no. 6, pp. 2806–2816, Nov. 2008. DOI: 10.1109/TPEL.2008.2005100 (cit. on p. 75).

[165] T. QORIA, "Grid-forming control to achieve a 100% power electronics interfaced power transmission systems," Theses, HESAM Université, Nov. 2020. [Online]. Available: https://pastel.archives-ouvertes.fr/tel-03078479 (cit. on p. 75).

[166] "Uninterruptible power systems (ups) - part 3 : Method of specifying the performance and test requirements," *IEC 62040-3*, 2021 (cit. on p. 83).

[167] X. Wang, F. Blaabjerg, and Z. Chen, "Autonomous control of inverter-interfaced distributed generation units for harmonic current filtering and resonance damping in an islanded microgrid," *IEEE Transactions on Industry Applications*, vol. 50, no. 1, pp. 452–461, Jan. 2014. DOI: 10.1109/TIA.2013.2268734 (cit. on p. 85).

[168] H. Gaztanaga, I. Etxeberria-Otadui, S. Bacha, and D. Roye, "Real-time analysis of the control structure and management functions of a hybrid microgrid system," in *IECON 2006 - 32nd Annual Conference on IEEE Industrial Electronics*, Nov. 2006, pp. 5137–5142. DOI: 10.1109/IECON.2006.347976 (cit. on p. 97).

[169] I. Etxeberria-Otadui, V. Manzo, S. Bacha, and F. Baltes, "Generalizedaverage modelling of facts for real time simulation in arene," in *IEEE 2002 28th AnnualConference of the Industrial Electronics Society.*, vol. 2, 2002 (cit. on p. 97).

[170] D. Ocnasu, C. Gombert, S. Bacha, D. Roye, F. Blache, and S. Mekhtoub, "Real-timehybrid facility for the study of distributed power generation systems.," *Journal of RenewableEnergies*, 2008 (cit. on p. 97).

[171] O. Crăciun, A. Florescu, S. Bacha, I. Munteanu, and A. I. Bratcu, "Hardware-in-the-loop testing of pv control systems using rt-lab simulator," in *14th International Power Electronics and Motion Control Conference EPE-PEMC IEEE*, 2010 (cit. on p. 97).

[172] "Low-voltage electrical installations - part 8-82: Functional aspects - prosumer's low-voltage electrical installations," *IEC 60364-8-82:2022*, 2022 (cit. on p. 122).

[173] G. J. Wakileh, "Harmonics in rotating machines," *Electric Power Systems Research*, vol. 66, no. 1, pp. 31–37, 2003, Power Quality. DOI: https://doi.org/10.1016/S0378-7796(03)00069-5. [Online]. Available: https://www.sciencedirect.com/science/article/pii/S0378779603000695 (cit. on p. 125).

[174] X. Han and H. Zhang, "Power system electromagnetic transient and electromechanical transient hybrid simulation based on pscad," 2015 (cit. on p. 135).

Résumé de la thèse

Nos efforts dans la lutte contre le changement climatique donnent un coup de pouce significatif aux technologies propres telles que les panneaux photovoltaïques (PV) sur les toits. Cependant, en raison de la nature intermittente de l'énergie PV, celle-ci doit être équilibrée à l'aide de systèmes de stockage d'énergie par batterie (BESS). L'intégration de ces technologies est facilitée par la technologie de micro-réseaux. De plus, les micro-réseaux peuvent fonctionner indépendamment du réseau électrique principal, fournissant une alimentation de secours lorsque le réseau principal subit des perturbations. Cependant, avec la technologie actuelle, les opérations des micro-réseaux ne peuvent pas garantir l'alimentation des charges critiques lors de la transition du réseau connecté à l'îlotage en cas de perturbation du réseau. Contrairement à l'alimentation sans interruption (ASI) qui fonctionne en série entre les charges électriques et le réseau, le BESS fonctionne en parallèle avec la charge et le réseau, de sorte que les perturbations du réseau auront toujours un impact sur les charges.

Ainsi, l'un des défis est d'isoler la perturbation du réseau. Avec un principe de sauvegarde de la charge critique, le micro-réseau doit s'isoler aussi rapidement que possible en cas de perturbation du réseau principal. À cet égard, la détection rapide et fiable des perturbations du réseau reste une question ouverte. Après avoir isolé le micro-réseau de la perturbation, un autre défi est de garantir l'alimentation en tension à partir du BESS. Le contrôle des onduleurs du BESS doit passer rapidement du mode grid-following au mode grid-forming. Bien que la transition entre ces modes ait été explorée dans de nombreuses études, les performances dynamiques de cette transition lors de perturbations du réseau restent sous-représentées dans la littérature. Dans ce contexte, cette thèse vise à améliorer la résilience de l'alimentation des micro-réseaux grâce à une exploitation DER locaux, protégeant efficacement les charges critiques face aux perturbations du réseau. Cette thèse est structurée en cinq chapitres.

Le Chapitre 1 introduire le contexte micro-réseaux pour les petits et moyens bâtiments, en particulier de l'intégration des sources d'énergie distribuées dans les bâtiments, ainsi que l'architecture et les modes de fonctionnement des micro-réseaux. L'alimentation sans coupure (UPS), la solution classique pour fournir l'alimentation aux charges critiques lors d'une panne de réseau, est également décrite. Les objectifs de la thèse, les questions de recherche, les contributions, telles que les publications et les brevets, et l'organisation de la thèse sont présentés.

Le Chapitre 2 décrit de décision d'îlotage en cas de perturbation du réseau. De plus, il explique en détail les problèmes de qualité de l'énergie, en particulier la chute de tension et l'interruption ; détermine les exigences de seamless transition, c'est-à-dire la période pendant laquelle la charge électrique peut supporter une chute de tension ou une interruption (10 millisecondes pour atteindre 73 % de la tension nominale); présente le code du réseau, en

particulier les exigences de maintien de la tension en cas de défaut ; et passe en revue les méthodes existantes pour la détection rapide de la perte de réseau.

Ensuite, une méthode de détection rapide de la perte de réseau est proposée et testée par simulation. La simulation démontre que cet algorithme est généralement précis pour déterminer la perte de réseau, même dans des conditions de tension polluée caractérisées par un THD de 10 %. Cependant, l'algorithme a une précision de 85 %, 93 % et 91 % pour déterminer les types de creux de tension I, II et III, respectivement, dans des conditions non polluées. Dans des conditions polluées, ces précisions sont légèrement réduites à 76 %, 83 % et 91 %, respectivement.

Le Chapitre 3 décrit la structure de contrôle de l'onduleur, y compris la grid forming et grid following, ainsi que le transfert entre les deux modes de fonctionnement. En cas de déconnexion du réseau, les onduleurs du BESS assurent la récupération de la tension. Nous avons proposé un contrôle d'onduleur adapté à transition *seamless*. Ce contrôle est basé sur une structure de contrôle à double boucle. Pour le mode de grid forming, la boucle de puissance externe est basée sur un régulateur PI dans le repère *dq*. En mode grid forming, la boucle de tension externe est basée sur un régulateur PR dans le repère *abc*. Un seul contrôle de courant interne basé sur un régulateur PR dans le repère *abc* est utilisé dans les deux modes. Trois stratégies ont été analysées pour leurs performances lors de la transition en îlotage sous une perte de réseau. La procédure de contrôle pour un micro-réseau en cas de perte de réseau a été proposée.

Le Chapitre 4 décrit le système de banc d'essai P-HIL et l'installation expérimentale. Nous rapportons et discutons les validations du contrôle des convertisseurs dans les modes de fonctionnement grid forming et grid-following respectivement, ainsi que operation *seamless* des micro-réseaux. L'algorithme de détection de perte de réseau a été prototypé sous le nom de Fast Islanding System (FIS). Le FIS a été validé pour détecter la perte de réseau selon les critères de performance, avec une tâche supplémentaire consistant à contrôler l'interrupteur statique et à commander d'îlotage au BESS. En outre, l'onduleur proposé a été mis en œuvre sur un banc d'essai d'onduleur de 5 kW utilisant DSPACE P-HIL. La *seamless* transition de micro-réseau a été testée sur une séquence de multiples scénarios de perte de réseau. Dans tous les cas, la tension a été rétablie à $0,52$ pu en $10ms$ et à $0,73$ pu en $20ms$. Le système a également démontré sa capacité à se reconnecter en *seamless* une fois la tension du réseau rétablie. Au cours de ces séquences de test, des équipements critiques tels que les ordinateurs et les moniteurs ont continué à fonctionner sans interruption, indiquant que le BESS protège efficacement les charges critiques contre les perturbations du réseau.

La conclusion fait l'objet du Chapitre 5. Elle rappelle l'objectif du mémoire, le contexte de la thèse, les divers points traités et le contribution de thèse ainsi les perspectives.